UNIVERSITÀ
DEGLI STUDI
DI UDINE
hic sunt futura

DOCTORAL PROGRAM IN

ENERGY AND ENVIRONMENTAL ENGINEERING SCIENCE

Cycle 32°

PHD THESIS

# RESONATOR-BASED MASS IDENTIFICATION IN NANOBEAMS

Doctoral Dissertation of
Marta Fedele Dell'Oste

Supervisor
Prof. Antonino Morassi

Co-Supervisor
Dr. Michele Dilena

**Anno 2021**

*to Federico...*
*be hungry, be foolish*

# Acknowledgments

I sincerely thank my Supervisor, Prof. Antonino Morassi, for giving me the opportunity to get in touch with the world of research and for having followed and trained me over the years. Thank you especially for taking a lot of him time to read and discuss the drafts of the thesis work.

I must also thank Dr. Michele Dilena not only for the technical support, but also for having been able to count on him in the moments of joy or discouragement of the PhD course.

I would also like to thank Prof. Ramón Zaera and, in particular, prof. José Fernández-Sáez of the Carlos III University of Madrid for welcoming and guiding me during my Spanish stay.

Finally, a dutiful and heartfelt thanks to my parents, Giuliana and Egidio, my son Federico, my friends, especially Arianna, who supported me and "endured" me unconditionally.

*Marta*

# Abstract

In this thesis we present a methodology for solving a finite inverse eigenvalue problem arising in the determination of added distributed mass in nanobeams by using the first lower resonant frequencies either of the axial or bending vibration under suitable sets of end conditions.

The nanobeams are modelled within a generalized continuum mechanics theory called modified strain gradient theory, to take into account the size-dependent behavior.

The inverse method is based on an iterative procedure that produces an approximation of the unknown mass variation as a generalized Fourier partial sum of order $N$. The Fourier coefficients of the added mass are evaluated from the first $N$ resonant frequencies belonging either to a single spectrum or two different spectra, for a mass variation with support contained in half of the nanobeam axis and for a general mass variation, respectively. The initial, unperturbed nanobeam is supposed to be uniform and the mass variation is assumed small with respect to the total mass of the nanoresonator. The reconstructive method takes advantage of a closed-form solution when the mass change is small, and a proof of local convergence of the iteration algorithm is provided for a family of finite dimensional mass coefficients.

An extended series of numerical simulations, also including cases with errors on the data, shows that the method is efficient and allows for accurate reconstruction of continuous mass coefficients. The accuracy deteriorates in presence of discontinuous mass coefficients. A constrained least-squares optimization filtering shows to be very effective to reduce the spurious oscillations near the discontinuity points of the rough coefficient. Surprisingly enough, in spite of its local character, the identification method performs well even for not necessarily small mass changes.

# Contents

# List of Figures

# List of Tables

# CHAPTER 1

# Introduction

In the last years, nanosensors based on nanoelectromechanical systems have gained interest in different physical, chemical and biological applications [6, 55]. The reason is connected with the promising features regarding a wide range of applications such as gas detection, early disease detection, gene mutation detection, DNA sequencing. In this respect, several reviews have been recently published showing the different capabilities of the nanostructures [5, 30, 77].

The main principle of a nanosensor is to obtain data from atomic scales and transfer them to the macroscopic world as analyzable data. The detection mechanism revolves identifying particular atoms or molecules accurately by measuring changes in volume, concentration, displacement, frequency, velocity, electricity, magnetic forces and temperature. According to the type of variables to be detected by nanosensors, they are typically classified into six groups [47]: mechanical, electrical, optical, magnetic, chemical and thermal.

In this thesis we are interested in mechanical nanoresonator sensors which, through their speed, reduced instrumentation size, increased sensitivity and label-free sensoring, have allowed to expand detection capabilities from the picogram ($10^{-12}$ g, Escherichia coli mass), reached in 2001, to the yoctogram ($10^{-24}$ g, proton mass), achieved in 2012 with a carbon nanotube [56, 65, 73]. The physical basis on which identification by means of mechanical nanoresonators is founded is that the adhesion of the analyte modifies the mass of the reference system, and monitoring the variations of the resonant frequencies provides cues for the determination of the unknown added mass [30, 39, 42]. This is the so-called *mass sensing principle* and in this thesis we will study inverse problems associated with it.

The identification problem of an attached mass by measurements of resonant frequency changes has been studied by several authors in the last years, see Eltaher et al. [29], Murmu et al. [66], and Li et al. [56]. Moreover, Bouchaala et al. [13] presented a method to determine the position and intensity of a concentrated mass attached to the surface of an electrostatically actuated clamped-clamped microbeam used as a mass sensor. Although these works are devoted to the study of microsensors, the laws of classical elasticity were used to model the nanostructure. Conversely, the experimental results of several authors [18, 21, 22, 53] pointed out that the consideration of size effects in the nanoscale components could be relevant to predict their mechanical response.

Therefore, since the classical continuum mechanics is a scale-free theory, other formulations based on generalized continuum mechanics approaches taking into account this size-dependent behavior must be explored.

Among the generalized continuum theories, we cite here three main groups: the *microcontinuum theory* by Eringen [33] including micropolar, microstretch and micromorphic ($3M$) theories (Cosserat micropolar elasticity [19] should be considered in this category, being the simplest formulation among $3M$ theories); the *strain gradient elasticity theory*, including the couple stress theory by Toupin and Mindlin [61,74,75], the first and second strain gradient theories of Mindlin [59,60], the modified couple stress theory by Yang et al. [79], and the modified strain gradient theory by Lam et al. [53]; the *nonlocal continuum mechanics theories* initiated by Kröner [50], Krumhansl [51] and Kunin [52], simplified subsequently by Eringen and coworkers [31, 32, 34], and formulated originally in integral form for linear homogeneous isotropic nonlocal elastic materials.

Although several scholars used the Eringen elasticity theory to asses the vibrational behavior of nanobeams with attached masses [29,56,66,80], and some attempts have been done to identify the added mass [56,66], the analyzed configurations are rather specific and a general formulation of the identification problem is still not available. Moreover, the main drawback using the fully nonlocal elasticity theory of Eringen has been pointed out by Romano et al. [68], who show that, in the majorities of the cases, the fully nonlocal elasticity theory leads to severely ill-posed problems that have no solution in general.

Other non-classical elasticity theories arise as attractive alternatives to overcome the difficulties associated with the fully nonlocal elasticity framework, particularly the modified strain gradient elasticity proposed by Lam et al. [53]. This approach needs new additional equilibrium equations to govern the behavior of higher-order stresses, and the corresponding three-dimensional model contains three non-classical constants in addition to the two classical ones for isotropic linear elastic materials. As the theory by Lam et al. [53] turned out to be in good agreement with experimental results, see, for example, the bending tests on micro-cantilevers performed in [45], in this thesis we shall use it to take into account the size effects in nanostructures and to model both axial and bending small vibrations in nanobeams. Chapter 2 presents a self-contained derivation of Lam's theory.

Starting from the paper by Kong et al. [49], who studied the static and dynamic bending behavior of nanobeams, and the research developed by Wang et al. [76], dealing with the analogous problem for Timoshenko nanobeams, the study of one-dimensional nanostructures using the modified strain gradient theory has led to numerous works. Akgoz and Civalek [2] derived analytical solutions for the buckling problem of axially loaded nanobeams with both uniform and variable cross section. The same authors used a non-classical sinusoidal shear deformation to study buckling of a nanobeam [3] and bending of a nanobeam embedded in an elastic medium [4]. Mohammadi and Mahzoon [62] investigated thermal effects on postbuckling of microbeams, considering Euler-Bernoulli theory and a nonlinear (Von-Kármán) strain measure. Miandoab et al. [58] estimated the Young's modulus and the length-scale parameters of the modified strain gradient model from experimental measurements of the voltages for static bending pull-in of different micro and nanobeams. Besides the previous analytical works, Kahrobaiyan et al. [45] developed an Euler-Bernoulli beam element, and Zhang et al. [81] developed a Timoshenko beam element for the study of static bending, free vibration and buckling behavior of microbeams.

The inverse problem of identifying added mass attached on nanobeams modelled within the modified strain gradient theory has been addressed only recently. Morassi et al. [64] developed a perturbation method for the identification of a single small mass attached to a nanobeam based on the measurement of the shifts of the first two resonant frequencies of the axial vibration. An extension of this result to nanobeams in bending vibration carrying a single small point mass was presented in [25]. However, added distributed mass representing the adsorbed analyte seems to be more realistic in several applications. The inverse eigenvalue problem is clearly more difficult, as the unknowns are no longer the position and intensity of the mass - as in the case of the point mass - but rather a function of a real variable describing the distribution of added mass. In this respect, much less effort to identify distributed mass on nanostructures has been given until now. For example, Roukes and Hanay and co-workers studied in a series of papers [42], [69], [46] the problem of identifying a distributed mass on transversely vibrating nanobeams under clamped end conditions. By using the Euler-Bernoulli model of the classical linear elasticity, they proposed an inertial imaging methodology which enables simultaneous identification of position and shape of distributed masses through measurements of resonant frequency shifts of the vibrational modes of the nanosensor. Bouchaala [12] analyzed the effect of a distributed added mass on the natural frequencies of an electrostatically actuated resonator modelled as a classical clamped-clamped Euler-Bernoulli beam with geometrical nonlinearities. A complete analysis of the published literature shows that a general formulation of the identification problem for distributed mass attached on nanostructures, described by generalized continuum mechanics theories and using resonant frequency data as input, is not given yet. The present thesis is a contribution on this topic.

From a mathematical point of view, the problem of the identification of a distributed added mass by using measurements of frequencies shifts falls into the class of *inverse problems with finite data*. Despite their importance and dissemination in many engineering and technological applications, general studies focused on these problems are relatively few. In this direction, the contribution by Barnes in [8] is illuminating. He shows that, to deal with this class of inverse problems, it is vital to determine the weakest topology in which the available set of eigenvalues are continuous (with respect to the unknown coefficient) since, otherwise, one would attempting to extract more information from the spectral data than it contains. The main difficulties of these problems are due to the non-uniqueness of the solution and to the difficulty in obtaining error estimates on the uniform approximation of the unknown coefficient. It can be shown that these estimates require the knowledge of infinite eigenvalues or, at least, of an accurate asymptotic formula and of sufficient spectral data to make good approximation to the infinite data, see, for example, [41]. In real cases, neither of this is available.

Extending an idea developed in [63] for the identification of structural damage in classical full-scale rods, the finite inverse problem is formulated in this thesis from a different point of view, see also Borg [11], Hald [40] and Knobel and Lowe [48]. Under the assumption that the added mass is a small perturbation of the reference mass distribution of a nanobeam, it is shown that the resonant frequency shifts caused by the mass change are correlated with certain generalized Fourier coefficients of the mass variation evaluated on a suitable family of functions. The method, which we call Generalized Fourier Coefficient Method (GFCM), leads to an iterative procedure of reconstruction of the unknown mass coefficient starting from the initial configuration of the structure which is assumed to be known.

In the first part of the thesis (Chapter 3), we study the inverse problem of determining the added mass from the knowledge of a finite number of lower natural frequencies of the axial vibration of a (initially) uniform nanobeam. Two main inverse problems are addressed.

We first consider the case in which the mass coefficient is *a priori known on half* of the nanobeam and the resonant frequency data belong to a single spectrum under clamped-clamped ends. Mathematically, this problem falls into the class of *mixed finite inverse problems* for fourth-order differential operators of Euler-Bernoulli's type, since a finite number of eigenvalues belonging to a single spectrum is known, and partial knowledge of the unknown coefficient is available. A celebrated uniqueness results for this class of problems can be traced back to Hochstadt and Lieberman [44]. Hochstadt-Lieberman's result holds for second-order differential operators of Sturm-Liouville type governing the axial vibration of classical straight elastic rods, i.e., $Lv = -\frac{1}{\rho(x)}v''(x)$, for a rod with unitary axial stiffness and linear mass density $\rho(x)$. Here, $v(x)$ expresses the longitudinal displacement at $x$ of the cross-section of the rod, $x \in [0, L]$, where $L$ is the rod length. It is shown that if $\rho(x)$ is prescribed over $\left[\frac{L}{2}, L\right]$, then all the infinite eigenvalues under clamped end conditions $v(0) = 0 = v(L)$ suffice to determine uniquely $\rho(x)$ on $\left[0, \frac{L}{2}\right]$. It should be remarked that there is another noticeable case in which the linear mass density of the rod can be uniquely determined from the single spectrum under clamped end conditions, namely when $\rho(x)$ is symmetric about the midpoint of the interval $(0, L)$ [43]. In the case of fourth-order operators, such as the one that governs the axial vibration of a nanorod, e.g., $Lv = \frac{1}{\rho}(bv^{IV} - av'')$, with $a$, $b$ constant positive stiffness coefficients and $\rho(x)$ unknown linear mass density function, the results of uniqueness for $\rho(x)$ are few and require the knowledge of an even larger infinite set of eigenvalues. For example, a classic result by Barcilon [7] shows that the unique determination of the coefficients $p(x)$, $q(x)$ of the Euler-Bernoulli operator $Lv = v^{IV} - (p(x)v')' + q(x)v$ requires knowledge of three complete spectra associated with three different boundary conditions, see the book of Gladwell [38] for a comprehensive analysis of this problem. We refer also to Schueller [70] for local uniqueness results related to an Euler-Bernoulli operator for a mixed-type inverse eigenvalue problem with two even coefficients, and to Caudill et al. [17] for the first systematic study of isospectral coefficient sets for Euler-Bernoulli operators.

In spite of the lack of general mathematical results on this class of inverse eigenvalue problems with finite data, application of the GFCM to the mass identification in axially vibrating nanobeams by finite number of lower resonant frequencies has led to encouraging results. The method has been tested on an extended class of coefficients, including smooth (e.g., continuous) and discontinuous mass variations, either with connected or disconnected support. Numerical simulations show good accuracy in approximating smooth coefficients when the first 9–12 eigenfrequencies are used. The reconstruction of discontinuous coefficients turns out to be less accurate, especially because of no negligible oscillations of the reconstructed mass variation near the discontinuity points, and typically requires the first 15–20 eigenfrequencies to obtain reasonable accuracy. In addition, we have also provided a convergence theorem for the iteration scheme for a particular family of finite dimensional mass coefficients. The result holds under the assumption that the eigenvalues of the perturbed and unperturbed nanobeam are close enough, and the mass variation is sufficiently small.

In the second part of the Chapter 3, the assumption that the mass variation is supported in half of the axis interval of the nanobeam is removed, and the GFCM is extended to the reconstruction of a *general* mass distribution. In this case, the reconstruction is based on the knowledge of a finite number of lower resonant frequencies belonging to two spectra corresponding to clamped-clamped and clamped-free end conditions. The results of the reconstruction confirm those already obtained by working with only one spectrum.

The second part of the thesis (Chapter 4) is devoted to analysis of the corresponding mass identification problems using resonant frequencies of the bending vibration. The nanobeam is modelled as in [49], and the eigenvalue problem consists of a 6th order ordinary differential equation with six end conditions. From the mathematical point of view, very few results are known for these operators and all of them concern uniqueness, not reconstruction. For example, Barcilon [7] announced that the unique determination of the three coefficients $\{p_i(x)\}_{1=1}^{3}$ in the 6th order differential equation $u^{VI} - (p_1 u'')'' + (p_2 u')' - p_3 u = \lambda u$, requires four full spectra associated with four distinct sets end conditions, see also [54] for more general analysis of inverse problems for ordinary differential operators of higher order. In spite of these not very reassuring premises, the application of the GFCM to the bending case proved unexpectedly encouraging. Adapting the procedure developed for the axial problem, we have first identified a distributed mass added on half of the nanobeam by using the first lower eigenfrequencies of the spectrum under supported end conditions. Next, we have extended the analysis to cover the more general case in which the mass variation may affect the entire length of the nanobeam. In this last case, resonant frequencies belonging to two spectra corresponding to supported-supported and supported-sliding end conditions have been used. The results of the reconstruction show that the solution of our inverse eigenvalue problem is very accurate at points which are far from the (possible) jump discontinuities of the mass coefficient, even when few first lower eigenfrequencies are available. Conversely, as it was expected, large oscillations may occur near discontinuity point, and they may obstruct the possibility to extract accurate pointwise information about the unknown added mass. In order to filter out these undesired oscillations, we have implemented an optimization filtering based on a least-squares minimization of the Euclidean norm between experimental and analytical eigenvalues (Section 4.4). Numerical results, both for a single spectrum and for two spectra, show that this constrained least squares filter eliminates most of the oscillations, giving significantly better results for discontinuous mass coefficients.

CHAPTER 2

# One-dimensional nanoresonators: mechanical models

Main goal of this Chapter is the presentation of the classical strain gradient theory for three-dimensional linear elasticity originally developed by Toupin [74] and Mindlin [59, 60], and later modified by Fleck and Hutchinson [35] and Lam et al. [53]. In particular, the theory by Lam et al. is applied in the second part of the Chapter to derive a strain gradient elastic theory for beams under either axial or bending small vibration. These mechanical models will be used in next chapters of the thesis to describe the dynamic behavior of one-dimensional nanosensors.

## 2.1 The Toupin-Mindlin strain gradient theory

Let us introduce a Cartesian reference frame $\{0, X_1, X_2, X_3\}$ of $\mathbb{R}^3$ with canonical basis $\{\mathbf{e}_i\}_{i=1}^3$, $\mathbf{e}_i \cdot \mathbf{e}_j = \delta_{ij}$, $\delta_{ij}$ being the Kronecker's symbol. Let us denote by $A_{ij},\ B_{ijk}$ the $(ij)$th, $(ijk)$th components of the second-order tensor $\mathbf{A}$ and the third-order tensor $\mathbf{B}$, respectively, $i, j, k = 1, 2, 3$. Unless otherwise stated, the usual summation convention applies to repeated indices.

Let $\Omega$ be a natural reference configuration of a solid, where $\Omega$ is an open, bounded continuum and connected subset of $\mathbb{R}^3$ having smooth boundary $\partial\Omega$. We denote by $\mathbf{u} = u_i \mathbf{e}_i$ a displacement field imposed to $\bar{\Omega}$, which induces the (infinitesimal) symmetric strain tensor

$$\varepsilon_{ij} = \frac{1}{2}\left(u_{i,j} + u_{j,i}\right) \tag{2.1}$$

and the second gradient of displacement

$$\eta_{ijk} = \frac{\partial^2 u_k}{\partial x_i \partial x_j}. \tag{2.2}$$

The strain tensor is symmetric, $\varepsilon_{ij} = \varepsilon_{ji}$, whereas the second gradient (or second-order deformation gradient) tensor is symmetric in the first two indices, $\eta_{ijk} = \eta_{jik}$.

Toupin [74] and Mindlin [60] developed a general theory for linear isotropic hyper-elastic solid material. Mindlin [60] developed a general higher-order stress theory, which includes higher-order strain gradients. Here, we shall consider his simplified version, where only the second-order deformation gradients are included as additional deformation metrics.

The strain energy density, $w$, defined in $\Omega$, is assumed to depend on the conventional strain $\epsilon_{ij}$ and on the second-order deformation gradient $\eta_{ijk}$, that is

$$w = w\left(\varepsilon_{ij}, \eta_{ijk}\right), \tag{2.3}$$

where a specific dependence of $w$ upon $\varepsilon_{ij}$ and $\eta_{ijk}$ was determined (see equation (2.38)). It should be noted that $\varepsilon_{ij}$ and $\eta_{ijk}$ have different dimensions; therefore, besides the traditional constants of the conventional elastic theory, additional constants including scale factors are expected to be present in the final constitutive equations.
The conventional symmetric *Cauchy stress* $\sigma_{ij}$ is defined as the work conjugate to $\varepsilon$, namely

$$\sigma_{ij} \equiv \frac{\partial w}{\partial \varepsilon_{ij}}, \quad \sigma_{ij} = \sigma_{ji}. \tag{2.4}$$

The *double stress tensor* $\tau_{ijk}$ is defined as the work conjugate to $\eta_{ijk}$ as

$$\tau_{ijk} \equiv \frac{\partial w}{\partial \eta_{ijk}}, \quad \tau_{ijk} = \tau_{jik}. \tag{2.5}$$

We now derive the formulation of the equilibrium problem of the body $\Omega$. Following the treatment of Toupin and Mindlin, we evaluate the first variation of the total strain energy stored in $\Omega$, that is

$$\mathscr{E}(\mathbf{u}) = \int_\Omega w\big(\varepsilon_{ij}(\mathbf{u}), \eta_{ijk}(\mathbf{u})\big) d\Omega, \tag{2.6}$$

where $\mathbf{u} = \mathbf{u}(\mathbf{x})$ is a regular displacement field assigned on $\Omega$. We start assuming that no geometrical conditions are imposed on $\partial\Omega$, and we evaluate the first variation of $\mathscr{E}$ at $\mathbf{u}$. Let

$$\mathbf{u}(\varepsilon) = \mathbf{u} + \varepsilon \mathbf{h},$$

with $\varepsilon \in [-\delta, \delta]$, $\delta$ being positive and small enough, and $\mathbf{h} = \mathbf{h}(\mathbf{x})$ is a smooth test function, $\mathbf{h} : \bar{\Omega} \to \mathbb{R}^3$. The function

$$\Phi(\varepsilon) = \mathscr{E}\left(\mathbf{u}(\varepsilon)\right), \quad \Phi : [-\delta, \delta] \to \mathbb{R}, \tag{2.7}$$

is a $C^1$-function in $[-\delta, \delta]$. Therefore, the stationarity of $\mathscr{E}$ at $\mathbf{u}$ implies $\delta\mathscr{E}[\mathbf{h}] \equiv \Phi'(\varepsilon)|_{\varepsilon=0} = 0$. A direct calculation shows that

$$\begin{aligned}
\delta\mathscr{E}[\mathbf{h}] &= \frac{d}{d\varepsilon} \int_\Omega w\left(\varepsilon_{ij}(\mathbf{u}+\varepsilon\mathbf{h}), \eta_{ijk}(\mathbf{u}+\varepsilon\mathbf{h})\right) d\Omega\big|_{\varepsilon=0} = \\
&= \int_\Omega \left( \frac{\partial w}{\partial \varepsilon_{ij}} \frac{d\varepsilon_{ij}(\mathbf{u}+\varepsilon\mathbf{h})}{d\varepsilon} + \frac{\partial w}{\partial \eta_{ijk}} \frac{d\eta_{ijk}(\mathbf{u}+\varepsilon\mathbf{h})}{d\varepsilon} \right) \Big|_{\epsilon=0} d\Omega = \\
&= \int_\Omega \left(\sigma_{ij}(\mathbf{u}+\varepsilon\mathbf{h})\varepsilon_{ij}(\mathbf{h}) + \tau_{ijk}(\mathbf{u}+\varepsilon\mathbf{h})\eta_{ijk}(\mathbf{h})\right) \big|_{\varepsilon=0} d\Omega = \\
&= \int_\Omega \left(\sigma_{ij}\varepsilon_{ij}(\mathbf{h}) + \tau_{ijk}\eta_{ijk}(\mathbf{h})\right) d\Omega,
\end{aligned} \tag{2.8}$$

where we have denoted $\sigma_{ij} = \sigma_{ij}(\mathbf{u}),\ \tau_{ijk} = \tau_{ijk}(\mathbf{u})$ to simplify the notation. By the symmetry of $\sigma_{ij}$, we have

$$\delta\mathscr{E}[\mathbf{h}] = \int_\Omega \left(\sigma_{ij} h_{i,j} + \tau_{ijk} h_{k,ij}\right) d\Omega = 0 \tag{2.9}$$

for every smooth test function $\mathbf{h}$.
We elaborate (2.9) by discharging the derivatives from $\mathbf{h}$ to $\sigma_{ij}$ and $\tau_{ijk}$ via integration by parts. The first integral of (2.9) becomes

$$\int_{\Omega} \sigma_{ij} h_{i,j} d\Omega = \int_{\partial\Omega} \sigma_{ij} n_j h_i da - \int_{\Omega} \sigma_{ij,j} h_i d\Omega, \tag{2.10}$$

where $\mathbf{n} = n_i \mathbf{e}_i$ is the unit exterior normal to $\partial\Omega$.
Let us elaborate the second integral in (2.9) by integrating by part twice:

$$\begin{aligned} \int_{\Omega} \tau_{ijk} h_{k,ij} d\Omega &= \int_{\partial\Omega} \tau_{ijk} n_i h_{k,j} da - \int_{\Omega} \tau_{ijk,i} h_{k,j} d\Omega = \\ &= \int_{\partial\Omega} \tau_{ijk} n_i h_{k,j} da - \int_{\partial\Omega} \tau_{ijk,i} n_j h_k da + \int_{\Omega} \tau_{ijk,ij} h_k d\Omega. \end{aligned} \tag{2.11}$$

By (2.10), (2.11), we have

$$\delta\mathscr{E}[\mathbf{h}] = -\int_{\Omega} \left(\sigma_{kj,j} - \tau_{ijk,ij}\right) h_k d\Omega + \int_{\partial\Omega} \left(\sigma_{kj} - \tau_{ijk,i}\right) n_j h_k da + \int_{\partial\Omega} \tau_{ijk} n_i h_{k,j} da = 0, \tag{2.12}$$

for every smooth test function $\mathbf{h}$.
Next, we elaborate the third (surface) integral on the right hand side of (2.12). This integral involves the full gradient of $\mathbf{h}$, whereas only the function $\mathbf{h}$ and its normal derivative can be independently assigned on $\partial\Omega$.
Let $f : \bar{\Omega} \to \mathbb{R}$ be a smooth scalar function. Then, its gradient $\nabla f$ can be decomposed as the sum of the normal part of the gradient $\nabla_n f$ and the tangential part of the gradient $\nabla_t f$:

$$\nabla f \equiv \nabla_n f + \nabla_t f, \tag{2.13}$$

where

$$\nabla_n f \equiv (\nabla f \cdot \mathbf{n})\, \mathbf{n} = (\mathbf{n} \otimes \mathbf{n})\, \nabla f, \tag{2.14}$$

$$\nabla_t f \equiv \nabla f - \nabla_n f = (\mathbf{1} - \mathbf{n} \otimes \mathbf{n})\, \nabla f. \tag{2.15}$$

and $(\mathbf{a} \otimes \mathbf{b})\mathbf{v} = (\mathbf{b} \cdot \mathbf{v})\mathbf{a}$ for every vectors $\mathbf{a}, \mathbf{b}, \mathbf{v}$. In Cartesian components, we have

$$\left(\nabla_n f\right)_j = \left(f_{,\ell} n_\ell\right) n_j \tag{2.16}$$

$$\left(\nabla_t f\right)_j = f_{,j} - \left(f_{,\ell} n_\ell\right) n_j. \tag{2.17}$$

We can generalize the above definitions to a vector-valued function $\mathbf{h} : \bar{\Omega} \to \mathbb{R}^3$ as

$$\underbrace{h_{k,j}}_{(\nabla \mathbf{h})_{kj}} = \underbrace{\left(\nabla_n h_k\right)_j}_{(\nabla_n \mathbf{h})_{kj}} + \underbrace{\left(\nabla_t h_k\right)_j}_{(\nabla_t \mathbf{h})_{kj}}, \tag{2.18}$$

where

$$\left(\nabla_n h_k\right)_j = h_{k,\ell} n_\ell n_j, \tag{2.19}$$

$$\left(\nabla_t h_k\right)_j = h_{k,j} - h_{k,\ell} n_\ell n_j. \tag{2.20}$$

Let us notice that the tangential and normal part of the gradient of $\mathbf{h}$ are orthogonal. In fact

$$\begin{aligned} (\nabla_n \mathbf{h}) \cdot (\nabla_t \mathbf{h}) &= (\nabla_n \mathbf{h})_{kj} (\nabla_t \mathbf{h})_{kj} \\ &= h_{k,m} n_m n_j \left(h_{k,j} - h_{k,\ell} n_\ell n_j\right) \\ &= h_{k,m} h_{k,j} n_m n_j - h_{k,m} h_{k,\ell} n_m n_\ell n_j n_j = 0. \end{aligned}$$

Using absolute notation, we have

$$\nabla_n \mathbf{h} = \nabla \mathbf{h} \left(\mathbf{n} \otimes \mathbf{n}\right), \tag{2.21}$$

$$\nabla_t \mathbf{h} = \left(\mathbf{1} - \mathbf{n} \otimes \mathbf{n}\right) \nabla \mathbf{h}, \tag{2.22}$$

and we define the *surface gradient operator*

$$\mathbf{D} = \left(\mathbf{1} - \mathbf{n} \otimes \mathbf{n}\right) \nabla, \tag{2.23}$$

with $\left(\nabla\right)_k = \partial_k$ and

$$D_j = \left(\delta_{jk} - n_j n_k\right) \partial_k. \tag{2.24}$$

The Green's theorem applied to a continuously differentiable function $\mathbf{f}$ over a smooth surface $S$ states (see [14], Chapter VI):

$$\int_S \big(\text{Div}\, \mathbf{f} - \text{Div}\, \mathbf{n} \left(\mathbf{n} \cdot \mathbf{f}\right) \big) dS = \int_{\partial\Omega} \mathbf{f} \cdot \boldsymbol{\nu}\, ds, \tag{2.25}$$

where Div $\mathbf{f}$ is the surface divergence of $\mathbf{f}$, $-$Div $\mathbf{n}$ is called the mean curvature of the surface, and the vector $\boldsymbol{\nu}$ is the unit normal to $\partial S$ tangent to $S$ and pointing outward.
Recalling that Div $\mathbf{f} = \nabla_t \cdot \mathbf{f}$, Div $\mathbf{n} = \nabla_t \cdot \mathbf{n}$, (2.25) takes the form

$$\int_S \left(\mathbf{1} - \mathbf{n} \otimes \mathbf{n}\right) \cdot \left(\nabla \mathbf{f} - \left(\mathbf{n} \cdot \mathbf{f}\right) \nabla \mathbf{n}\right) dS = \int_{\partial S} \mathbf{f} \cdot \boldsymbol{\nu}\, ds \tag{2.26}$$

or, in cartesian coordinates,

$$\int_S \left(\delta_{jk} - n_j n_k\right) f_{j,k} dS = \int_S \left(\delta_{jk} - n_j n_k\right) n_{j,k} n_\ell f_\ell dS + \int_{\partial S} f_j \nu_j ds$$

$$\int_S D_j f_j dS = \int_S \left(D_j n_j\right) n_\ell f_\ell dS + \int_{\partial S} f_j \nu_j ds. \tag{2.27}$$

Collecting the above results, we are in position to elaborate the third integral in (2.12). Expressing $h_{k,j}$ in terms of the normal and tangential part as in (2.18), using the definition (2.24) of $D_j$, and applying (2.27) with $f_j = n_i \tau_{ijk} h_k$, we have (for a *smooth boundary* $\partial\Omega$)

$$\begin{aligned}
\int_{\partial\Omega} \tau_{ijk} n_i h_{k,j} da &= \int_{\partial\Omega} \tau_{ijk} n_i \left(\nabla h_k \cdot \mathbf{n}\right) n_j da + \int_{\partial\Omega} \tau_{ijk} n_i \left(\nabla_t h_k\right)_j da \\
&= \int_{\partial\Omega} n_i n_j \tau_{ijk} \left(\nabla h_k \cdot \mathbf{n}\right) da + \int_{\partial\Omega} \tau_{ijk} n_i \left(h_{k,j} - h_{k,\ell} n_\ell n_j\right) da \\
&= \int_{\partial\Omega} n_i n_j \tau_{ijk} \left(\nabla h_k \cdot \mathbf{n}\right) da + \int_{\partial\Omega} \tau_{ijk} n_i D_j h_k da \\
&= \int_{\partial\Omega} n_i n_j \tau_{ijk} \left(\nabla h_k \cdot \mathbf{n}\right) da + \int_{\partial\Omega} D_j \left(\tau_{ijk} n_i h_k\right) da - \int_{\partial\Omega} h_k D_j \left(\tau_{ijk} n_i\right) da \\
&= \int_{\partial\Omega} n_i n_j \tau_{ijk} \left(\nabla h_k \cdot \mathbf{n}\right) da + \int_{\partial\Omega} \left(D_p n_p\right) n_i n_j \tau_{ijk} h_k da - \int_{\partial\Omega} h_k D_j \left(\tau_{ijk} n_i\right) da.
\end{aligned} \tag{2.28}$$

Replacing (2.28) in (2.12), and reordering the summands, we have

$$\begin{aligned}\delta\mathscr{E}[\mathbf{h}] &= -\int_{\Omega}\left(\sigma_{kj,j}-\tau_{ijk,ij}\right)h_k d\Omega + \int_{\partial\Omega} n_i n_j \tau_{ijk}\left(\nabla h_k\cdot\mathbf{n}\right)da+ \\ &\quad+\int_{\partial\Omega}\left(\sigma_{kj}-\tau_{ijk,i}\right)n_j h_k da+\int_{\partial\Omega} n_i n_j\tau_{ijk}\left(D_p n_p\right)h_k da-\int_{\partial\Omega} D_j\left(\tau_{ijk}n_i\right)h_k da = \\ &= -\int_{\Omega}\left(\sigma_{kj,j}-\tau_{ijk,ij}\right)h_k d\Omega+ \\ &\quad+\int_{\partial\Omega}\left\{\left[n_j(\sigma_{jk}-\tau_{ijk,i})+n_i n_j\tau_{ijk}(D_p n_p)-D_j(n_i\tau_{ijk})\right]h_k+n_i n_j\tau_{ijk}Dh_k\right\}da, \qquad (2.29)\end{aligned}$$

with $D$ such that

$$h_{k,\ell}n_l \equiv Dh_k. \qquad (2.30)$$

We assume that the functional of external loads is

$$\ell(\mathbf{h}) = \int_{\Omega}\mathbf{f}\cdot\mathbf{h}\,d\Omega+\int_{\partial\Omega}\left(\mathbf{h}\cdot\mathbf{h}+\mathbf{r}\cdot D\mathbf{h}\right)da, \qquad (2.31)$$

where $\mathbf{f}$ is the *body force* per unit volume, $\mathbf{t}$ is the *surface traction* on the surface $\partial\Omega$, and $\mathbf{r}$ is the *double- force traction* on $\partial\Omega$. Therefore, the final form of the stationarity of the total energy $(\mathscr{E}(\mathbf{h})-\ell(\mathbf{h}))$ is

$$\int_{\Omega}\left(\sigma_{ij}h_{i,j}+\tau_{ijk}h_{k,ij}\right)d\Omega=\int_{\Omega}f_k h_k d\Omega+\int_{\partial\Omega}\left(t_k h_k+r_k Dh_k\right)da \qquad (2.32)$$

for every test function $\mathbf{h}$.
The equilibrium equations are:

$$\sigma_{ik,i}-\tau_{ijk,ij}+f_k=0 \quad \text{in } \Omega, \qquad (2.33)$$

on $\partial\Omega$:

$$n_j\left(\sigma_{jk}-\tau_{ijk,i}\right)+n_i n_j\tau_{ijk}(D_p n_p)-D_i\left(n_j\tau_{ijk}\right)=\widehat{t}_k \qquad (2.34)$$

or

$$u_k=\widehat{u}_k \qquad (2.35)$$

and on $\partial\Omega$

$$n_i n_j\tau_{ijk}=\widehat{r}_k \qquad (2.36)$$

or

$$Du_k=\widehat{Du_k}. \qquad (2.37)$$

For the special case where the surface $\partial\Omega$ has edges, an additional term must be added to the right-hand side of (2.32) (see Mindlin [60], Fleck and Hutchinson [35]).

In order to complete the equilibrium problem, for linear elastic isotropic materials, Mindlin [60] proposed the density of strain energy $w$ as

$$w=\frac{1}{2}\lambda\varepsilon_{ii}\varepsilon_{jj}+\mu\varepsilon_{ij}\varepsilon_{ij}+a_1\eta_{ijj}\eta_{ikk}+a_2\eta_{iik}\eta_{kjj}+a_3\eta_{iik}\eta_{jjk}+a_4\eta_{ijk}\eta_{ijk}+a_5\eta_{ijk}\eta_{kji}, \qquad (2.38)$$

where $\lambda$ and $\mu$ are the classical Lamé moduli, and $a_n$ $(n=1,\dots,5)$ are the five additional elastic constants corresponding to the invariants of the second order deformation gradients. The energy density in (2.38) contains coupled terms involving both stretch and rotation gradients. The presence of this coupling makes it complicated the application of the equilibrium equations. In the next section we shall introduce a modified strain gradient elasticity theory that, under suitable assumptions, reduces the additional constants from five to three. This theory has been used to develop one-dimensional models of vibrating nanobeams, that we will use in next sections to formulate the inverse mass detection problem based on resonant frequency measurements.

## 2.2 The modified strain gradient theory by Lam et al.

The principle of stationarity of the total energy can be rearranged into forms which separate out the energy terms associated with the second-order deformation gradient $\eta_{ijk}$. These decompositions lead to more transparent reductions of the general framework to *couple-stress theory* when the constitutive behavior only depends on the rotation gradients. Fleck and Hutchinson [35, 36] reformulated Mindlin's simplified theory renaming it the *strain gradient theory*. In this theory, the second-order deformation gradient term is decomposed additively into two independent parts, namely, the *stretch gradient tensor* and the *rotation gradient tensor*, see also Smyshlyaev and Fleck [71].

Lam et al. [53], starting from the above previous works, proposed a stratifying decomposition scheme of the second-order deformation gradient terms to enable the application of new higher-order equilibrium relation [79]. Because of the requirement of the higher-order equilibrium conditions, it turns out that the anti-symmetric part of the rotation gradient does not contribute to the deformation energy. As a consequence, the number of the material length scale parameters is reduced from five (Mindlin's simplified theory) to three. Goal of this section is to present the so-called *modified* strain gradient theory by Lam et al. [53].

Following Fleck and Hotchinson [35], we define as the *symmetric part* of $\eta_{ijk}$ the term $\eta^S_{ijk}$

$$\begin{aligned}\eta^S_{ijk} &\equiv \frac{1}{3}\left(\eta_{ijk}+\eta_{jki}+\eta_{kij}\right)\\ &\equiv \frac{1}{3}\left(u_{k,ij}+u_{i,jk}+u_{j,ki}\right).\end{aligned} \tag{2.39}$$

Let us notice that, by definition (see Toupin [74]), $\eta^S_{ijk}$ is equal to the sum of all the possible permutations of the indices $i,\ j,\ k$ of $\eta_{ijk}$ – with plus sign – divided by 3! (and using the symmetry on the first two indices). Therefore, $\eta^S_{ijk}$ is symmetric with respect to every permutation of the indices $i,\ j,\ k$.

The *anti-symmetric part* $\eta^A_{ijk}$ of $\eta_{ijk}$ is

$$\eta^A_{ijk} \equiv \eta_{ijk} - \eta^S_{ijk}. \tag{2.40}$$

The symmetric part $\eta^S_{ijk}$ represents the stretch gradient tensor, and has ten independent components. The anti-symmetric part $\eta^A_{ijk}$, or rotation gradient tensor, has eight independent components and it is a measure of the curvature. To check this property, let us introduce the *curvature tensor* $\chi_{ij}$ as the spatial gradient of the material rotation $\boldsymbol{\omega} = \omega_i \mathbf{e}_i$:

$$\chi_{ij} = \omega_{i,j}. \tag{2.41}$$

Recalling that $\boldsymbol{\omega}$ is the axial vector associated to the anti-symmetric part of the displacement gradient, e.g. $\boldsymbol{\omega} \times \mathbf{a} = \mathbf{W}\mathbf{a}$ for every $\mathbf{a} \in \mathbb{R}^3$, $W_{ij} = \frac{1}{2}\left(u_{i,j} - u_{j,i}\right)$, we have

$$\omega_\ell = \frac{1}{2}\delta_{\ell ki} W_{ik}, \quad W_{ik} = \delta_{ijk}\omega_j, \tag{2.42}$$

and, therefore,

$$\omega_i = \frac{1}{2}\delta_{ijk} u_{k,j}. \tag{2.43}$$

Using this expression in (2.41), we have

$$\chi_{ij} = \frac{1}{2}\delta_{ipq}\eta_{jpq} \tag{2.44}$$

and we can evaluate $\eta^A_{ijk}$ as follows

$$\begin{aligned}\eta^A_{ijk} &= \eta_{ijk} - \eta^S_{ijk}\\ &= u_{k,ij} - \frac{1}{3}\left(u_{k,ij} + u_{i,jk} + u_{j,ki}\right)\\ &= \frac{1}{3}\left(u_{k,i} - u_{i,k}\right)_{,j} + \frac{1}{3}\left(u_{k,j} - u_{j,k}\right)_{,i}\\ &= \frac{2}{3}W_{ki,j} + \frac{2}{3}W_{kj,i}\\ &= \frac{2}{3}\left(\delta_{ik\ell}\chi_{\ell j} + \delta_{jk\ell}\chi_{\ell i}\right). \end{aligned} \tag{2.45}$$

This identity shows that $\eta^A_{ijk}$ is a curvature measure.

The components $\eta^S_{ijk}$ and $\eta^A_{ijk}$ are *orthogonal*, that is $\eta^S_{ijk}\eta^A_{ijk} = 0$. In fact, using (2.44) and (2.45), we have

$$\begin{aligned}\eta^S_{ijk}\eta^A_{ijk} &= \frac{2}{3}\eta^S_{ijk}\left(\delta_{ik\ell}\chi_{\ell j} + \delta_{jk\ell}\chi_{\ell i}\right)\\ &= \frac{2}{3}\eta_{ijk}\frac{1}{2}\left(\delta_{ik\ell}\delta_{\ell pq}\eta_{jpq} + \delta_{jk\ell}\delta_{\ell pq}\eta_{ipq}\right)\\ &= \frac{1}{3}\eta^S_{ijk}\left[\left(\delta_{ip}\delta_{kq} - \delta_{iq}\delta_{kp}\right)\eta_{jpq} + \left(\delta_{jp}\delta_{kq} - \delta_{jq}\delta_{kp}\right)\eta_{ipq}\right]\\ &= \frac{2}{3}\eta^S_{ijk}\left[\eta_{j[ik]} + \eta_{i[jk]}\right], \end{aligned} \tag{2.46}$$

where $\eta_{a[bc]} = \frac{1}{2}\left(\eta_{abc} - \eta_{acb}\right)$. For every $j, i$, $\eta_{j[ik]}$ and $\eta_{i[jk]}$ are anti-symmetric tensors. Therefore, since $\eta^S_{ijk}$ is symmetric (in every pair of indices), both terms in expression (2.46) vanish, and the orthogonality property follows.

Lam et al. [53] introduced a new, independent second-order strain metric by splitting the symmetric second-order deformation gradient $\eta^S_{ijk}$ into a *trace part*, $\eta^{(0)}_{ijk}$, and a *traceless part*, $\eta^{(1)}_{ijk}$:

$$\eta^S_{ijk} = \eta^{(0)}_{ijk} + \eta^{(1)}_{ijk}. \tag{2.47}$$

We recall that, by definition, the third order tensor $Q_{ijk}$ is named *traceless* if the sum of its components corresponding to a pair of indices is equal to zero, for every choice of the pair of indices, thus:

$$\begin{aligned} Q_{ijj} &= 0 \qquad \text{for every } i = 1,2,3,\\ Q_{iji} &= 0 \qquad \text{for every } j = 1,2,3,\\ Q_{iik} &= 0 \qquad \text{for every } k = 1,2,3, \end{aligned} \tag{2.48}$$

(repeated indices are summed). Therefore, we have

$$\eta^{(0)}_{ijk} = \frac{1}{5}\left[\delta_{ij}\eta^S_{mmk} + \delta_{jk}\eta^S_{mmi} + \delta_{ki}\eta^S_{mmj}\right]. \tag{2.49}$$

and

$$\eta^{(1)}_{ijk} \equiv \eta^S_{ijk} - \eta^{(0)}_{ijk}. \tag{2.50}$$

A direct calculation shows that

$$\begin{aligned}\eta^{(1)}_{ijk} = &-\frac{1}{15}\left[\delta_{ij}\left(\varepsilon_{mm,k} + 2\varepsilon_{mk,m}\right) + \delta_{jk}\left(\varepsilon_{mm,i} + 2\varepsilon_{mi,m}\right) + \delta_{ki}\left(\varepsilon_{mm,j} + 2\varepsilon_{mj,m}\right)\right] +\\ &+ \frac{1}{3}\left(\varepsilon_{jk,i} + \varepsilon_{ki,j} + \varepsilon_{ij,k}\right). \end{aligned} \tag{2.51}$$

Obviously, by definition, $\eta^{(1)}_{ijk}$ is a *traceless* tensor, as one can verify easily. Moreover, by Schwarz's theorem,

$$\eta^S_{mmk} = \frac{1}{3}\left(\eta_{mmk} + 2\eta_{kmm}\right). \tag{2.52}$$

The number of independent parameters is three and seven for $\eta^{(0)}_{ijk}$ and for $\eta^{(1)}_{ijk}$, respectively.

Let us split the curvature tensor $\chi_{ij}$ into the symmetric and anti-symmetric part

$$\chi_{ij} = \chi^S_{ij} + \chi^A_{ij}, \tag{2.53}$$

$$\chi^S_{ij} = \frac{1}{2}\left(\chi_{ij} + \chi_{ji}\right), \qquad \chi^A_{ij} = \frac{1}{2}\left(\chi_{ij} - \chi_{ji}\right). \tag{2.54}$$

The *trace part* $\eta^{(0)}_{ijk}$ of $\eta^S_{ijk}$ depends on the three quantities

$$\eta^S_{mmi}, \quad i = 1, 2, 3.$$

Let us evaluate $\eta^S_{mmi}$ in terms of the field displacement $\mathbf{u}$; by (2.52), we have

$$\begin{aligned}\eta^S_{mmi} &= \frac{1}{3}\left(u_{i,mm} + 2u_{m,im}\right)\\ &= \left(u_{m,m}\right)_{,i} + \frac{2}{3}W_{im,m}.\end{aligned} \tag{2.55}$$

By (2.42) and (2.44), we have

$$\eta^S_{mmi} = \varepsilon_{,i} + \frac{2}{3}\delta_{imn}\chi_{mn} = \varepsilon_{,i} + \frac{2}{3}\delta_{imn}\chi^A_{mn}, \tag{2.56}$$

where $\varepsilon = u_{m,m}$ is the *dilatation strain* and $\varepsilon_{,i}$ is the $i$th component of the *dilatation gradient*.

To summarize, we have decomposed an arbitrary strain gradient term $\eta_{ijk}$ into three components

$$\eta_{ijk} = \eta^{(0)}_{ijk} + \eta^{(1)}_{ijk} + \eta^A_{ijk}. \tag{2.57}$$

These three components are mutually orthogonal. In fact, by (2.46) we already known that

$$\left(\eta^{(0)}_{ijk} + \eta^{(1)}_{ijk}\right)\eta^A_{ijk} = 0. \tag{2.58}$$

Therefore, it is enough to verify that

$$\eta^{(0)}_{ijk}\eta^{(1)}_{ijk} = 0, \tag{2.59}$$

$$\eta^{(0)}_{ijk}\eta^A_{ijk} = 0. \tag{2.60}$$

Let us prove (2.59) first. By (2.49) and (2.50), we have

$$\begin{aligned}
\eta^{(0)}_{ijk}\eta^{(1)}_{ijk} &= \left(\delta_{ij}\eta^S_{mmk} + \delta_{jk}\eta^S_{mmi} + \delta_{ki}\eta^S_{mmj}\right)\left[\eta^S_{ijk} - \frac{1}{5}\left(\delta_{ij}\eta^S_{mmk} + \delta_{jk}\eta^S_{mmi} + \delta_{ki}\eta^S_{mmj}\right)\right] = \\
&= \left[\delta_{ij}\eta^S_{mmk}\eta^S_{ijk} - \frac{1}{5}\left(\delta_{ij}\delta_{ij}\eta^S_{mmk}\eta^S_{mmk} + \delta_{ij}\delta_{jk}\eta^S_{mmk}\eta^S_{mmi} + \delta_{ij}\delta_{ki}\eta^S_{mmk}\eta^S_{mmj}\right)\right] + \\
&+ \left[\delta_{jk}\eta^S_{mmi}\eta^S_{ijk} - \frac{1}{5}\left(\delta_{jk}\delta_{ij}\eta^S_{mmi}\eta^S_{mmk} + \delta_{jk}\delta_{jk}\eta^S_{mmi}\eta^S_{mmi} + \delta_{jk}\delta_{ki}\eta^S_{mmi}\eta^S_{mmj}\right)\right] + \\
&+ \left[\delta_{ki}\eta^S_{mmj}\eta^S_{ijk} - \frac{1}{5}\left(\delta_{ki}\delta_{ij}\eta^S_{mmj}\eta^S_{mmk} + \delta_{ki}\delta_{jk}\eta^S_{mmj}\eta^S_{mmi} + \delta_{ki}\delta_{ki}\eta^S_{mmj}\eta^S_{mmj}\right)\right] = \\
&= \eta^S_{mmk}\eta^S_{iik} - \frac{1}{5}\left(3\eta^S_{mmk}\eta^S_{mmk} + \eta^S_{mmk}\eta^S_{mmk} + \eta^S_{mmk}\eta^S_{mmk}\right) + \\
&+ \eta^S_{mmi}\eta^S_{ijj} - \frac{1}{5}\left(\eta^S_{mmi}\eta^S_{mmi} + 3\eta^S_{mmi}\eta^S_{mmi} + \eta^S_{mmi}\eta^S_{mmi}\right) + \\
&+ \eta^S_{mmj}\eta^S_{iji} - \frac{1}{5}\left(\eta^S_{mmj}\eta^S_{mmj} + \eta^S_{mmj}\eta^S_{mmj} + 3\eta^S_{mmj}\eta^S_{mmj}\right) = \\
&= \left[\left(\eta^S_{mmk}\right)^2 - \left(\eta^S_{mmk}\right)^2\right] + \left[\left(\eta^S_{mmi}\right)^2 - \left(\eta^S_{mmi}\right)^2\right] + \left[\left(\eta^S_{mmj}\right)^2 - \left(\eta^S_{mmj}\right)^2\right] = 0. \qquad (2.61)
\end{aligned}$$

We now prove (2.60). By (2.50) and (2.45), we have:

$$\begin{aligned}
\eta^{(0)}_{ijk}\eta^A_{ijk} &= \left(\delta_{ij}\eta^S_{mmk} + \delta_{jk}\eta^S_{mmi} + \delta_{ki}\eta^S_{mmj}\right)\left(\delta_{ik\ell}\chi_{\ell j} + \delta_{jk\ell}\chi_{\ell i}\right) = \\
&= \delta_{ij}\delta_{ik\ell}\eta^S_{mmk}\chi_{\ell j} + \delta_{ij}\delta_{jk\ell}\eta^S_{mmk}\chi_{\ell i} + \delta_{jk}\delta_{ik\ell}\eta^S_{mmi}\chi_{\ell j} \\
&+ \delta_{jk}\delta_{jk\ell}\eta^S_{mmi}\chi_{\ell i} + \delta_{ki}\delta_{ik\ell}\eta^S_{mmj}\chi_{\ell j} + \delta_{ki}\delta_{jk\ell}\eta^S_{mmj}\chi_{\ell i} = \\
&= \delta_{jk\ell}\eta^S_{mmk}\chi_{\ell j} + \delta_{ik\ell}\eta^S_{mmk}\chi_{\ell i} + \delta_{ik\ell}\eta^S_{mmi}\chi_{\ell k} + \delta_{ji\ell}\eta^S_{mmj}\chi_{\ell i} = \\
&= \eta^S_{mmk}\left(\delta_{jk\ell}\chi_{\ell j} + \delta_{ik\ell}\chi_{\ell i}\right) + \eta^S_{mmi}\left(\delta_{ik\ell}\chi_{\ell k} + \delta_{ik\ell}\chi_{\ell k}\right) = \\
&= \eta^S_{mmk}\left(\delta_{jk\ell}\chi_{\ell j} + \delta_{jk\ell}\chi_{\ell j}\right) + \eta^S_{mmk}\left(\delta_{kp\ell}\chi_{\ell p} + \delta_{kp\ell}\chi_{\ell p}\right) = \\
&= 2\eta^S_{mmk}\left(\delta_{jk\ell}\chi_{\ell j} + \delta_{kp\ell}\chi_{\ell p}\right) = \\
&= 2\eta^S_{mmk}\left(\delta_{k\ell j}\chi_{\ell j} + \delta_{kp\ell}\chi_{\ell p}\right) = \\
&= 2\eta^S_{mmk}\left(\delta_{k\ell j}\chi_{\ell j} + \delta_{kj\ell}\chi_{\ell j}\right) = \\
&= 2\eta^S_{mmk}\left(\delta_{k\ell j}\chi_{\ell j} - \delta_{k\ell j}\chi_{\ell j}\right) = 0. \qquad (2.62)
\end{aligned}$$

Following the analysis developed in Section 2.1 for the Toupin-Mindlin theory (and under the same assumptions), the second order term appearing on the first order variation of the total energy is

$$\int_\Omega \tau_{ijk}h_{k,ij}d\Omega \qquad (2.63)$$

for every smooth test function $\mathbf{h}$. Let us decompose the double stress term $\tau_{ijk}$ as we did for $\eta_{ijk}$, namely:

$$\tau_{ijk} = \tau^{(0)}_{ijk} + \tau^{(1)}_{ijk} + \tau^A_{ijk}, \qquad (2.64)$$

where

$$\tau^{(0)}_{ijk} \equiv \frac{1}{5}\left(\delta_{ij}\tau^S_{mmk} + \delta_{jk}\tau^S_{mmi} + \delta_{ki}\tau^S_{mmj}\right), \qquad (2.65)$$

$$\tau^{(1)}_{ijk} \equiv \tau^S_{ijk} - \tau^{(0)}_{ijk}, \qquad (2.66)$$

$\tau^S_{ijk}$ is the symmetric part of $\tau_{ijk}$, and $\tau^A_{ijk} \equiv \tau_{ijk} - \tau^S_{ijk}$ is the anti-symmetric part of $\tau_{ijk}$. Note that the above three components of $\tau_{ijk}$ are mutually orthogonal. Moreover, the following property holds.

Let $\delta\eta_{ijk} \equiv h_{k,ij}$. Then

$$\begin{aligned} &\tau^{(0)}_{ijk} && \text{is orthogonal to } \delta\eta^{(1)}_{ijk} \text{ and } \delta\eta^{A}_{ijk};\\ &\tau^{(1)}_{ijk} && \text{is orthogonal to } \delta\eta^{(0)}_{ijk} \text{ and } \delta\eta^{A}_{ijk};\\ &\tau^{A}_{ijk} && \text{is orthogonal to } \delta\eta^{(0)}_{ijk} \text{ and } \delta\eta^{(1)}_{ijk}. \end{aligned} \tag{2.67}$$

Let us prove, for instance, that $\tau^{(1)}_{ijk}\eta^{(0)}_{ijk} = 0$. We have (to simplify the notation, we write $\eta_{ijk}$ instead of $\delta\eta_{ijk}$):

$$\begin{aligned} \tau^{(1)}_{ijk}\eta^{(0)}_{ijk} = &\left[\tau^S_{ijk} - \frac{1}{5}\left(\delta_{ij}\tau^S_{mmk} + \delta_{jk}\tau^S_{mmi} + \delta_{ki}\tau^S_{mmj}\right)\right]\frac{1}{5}\left(\delta_{ij}\eta^S_{mmk} + \delta_{jk}\eta^S_{mmi} + \delta_{ki}\eta^S_{mmj}\right) =\\ =&\frac{1}{5}\left[\delta_{ij}\tau^S_{ijk}\eta^S_{mmk} + \delta_{jk}\tau^S_{ijk}\eta^S_{mmi} + \delta_{ki}\tau^S_{ijk}\eta^S_{mmj} - \frac{1}{5}\left(\delta_{ij}\delta_{ij}\tau^S_{mmk}\eta^S_{mmk} + \delta_{ij}\delta_{jk}\tau^S_{mmk}\eta^S_{mmi}\right)\right] +\\ &+\frac{1}{5}\left[-\frac{1}{5}\left(\delta_{ij}\delta_{ki}\tau^S_{mmk}\eta^S_{mmj} + \delta_{jk}\delta_{ij}\tau^S_{mmi}\eta^S_{mmk} + \delta_{jk}\delta_{jk}\tau^S_{mmi}\eta^S_{mmi} + \delta_{ik}\delta_{ki}\tau^S_{mmi}\eta^S_{mmj}\right)\right] +\\ &+\frac{1}{5}\left[-\frac{1}{5}\left(\delta_{ki}\delta_{ij}\tau^S_{mmj}\eta^S_{mmk} + \delta_{ki}\delta_{ij}\tau^S_{mmj}\eta^S_{mmk} + \delta_{ki}\delta_{ki}\tau^S_{mmj}\eta^S_{mmj}\right)\right] =\\ =&\frac{1}{5}\left[\tau^S_{iik}\eta^S_{mmk} + \tau^S_{ijj}\eta^S_{mmi} + \tau^S_{kjk}\eta^S_{mmj} - \frac{1}{5}\left(3\tau^S_{mmk}\eta^S_{mmk} + \delta_{ik}\tau^S_{mmk}\eta^S_{mmi} + \delta_{jk}\tau^S_{mmk}\eta^S_{mmj}\right)\right] +\\ &+\frac{1}{5}\left[-\frac{1}{5}\left(\delta_{ki}\tau^S_{mmi}\eta^S_{mmk} + 3\tau^S_{mmi}\eta^S_{mmi} + \delta_{ji}\tau^S_{mmi}\eta^S_{mmj} + \delta_{kj}\tau^S_{mmj}\eta^S_{mmk} + \delta_{kj}\tau^S_{mmj}\eta^S_{mmk}\right)\right] +\\ &+\frac{1}{5}\left[-\frac{1}{5}\left(3\tau^S_{mmj}\eta^S_{mmj}\right)\right] = \frac{1}{5}\left[3\tau^S_{iik}\eta^S_{mmk} - \frac{3}{5}\left(5\tau^S_{mmk}\eta^S_{mmk}\right)\right] = 0 \end{aligned} \tag{2.68}$$

By the above properties, the term in (2.63) takes the form (with $h_{k,ij} \equiv \delta\eta_{ijk}$)

$$\int_\Omega \tau_{ijk}h_{k,ij}d\Omega = \int_\Omega \tau_{ijk}\delta\eta_{ijk}d\Omega = \int_\Omega \left(\tau^{(0)}_{ijk}\delta\eta^{(0)}_{ijk} + \tau^{(1)}_{ijk}\delta\eta^{(1)}_{ijk} + \tau^{A}_{ijk}\delta\eta^{A}_{ijk}\right)d\Omega \tag{2.69}$$

and the set of stress metrics $\tau^{(0)}_{ijk}$, $\tau^{(1)}_{ijk}$, $\tau^{A}_{ijk}$ is work-conjugate to the strain of metrics $\eta^{(0)}_{ijk}$, $\eta^{(1)}_{ijk}$, $\eta^{A}_{ijk}$. The expression (2.69) was already present in the works by Fleck and Hutchinson [35]. In Lam el al. [53], the expression (2.69) is rearranged in terms of the new second-order strain metrics $\epsilon_{,i}$, $\eta^{(1)}_{ijk}$, $\chi_{ij}$.

Let us recall that, by (2.39), (2.49) and (2.53), $\eta^{(0)}_{ijk}$ depends on the quantities $\epsilon_{,i}$ and $\chi_{mm}$ only (see (2.45)). Therefore, we rewrite the second-order term of the stress energy density in (2.69) by separating the contribution associated to $\epsilon_{,i}$ to that due to $\chi_{ij}$, and by leaving unchanged the term associated to $\tau^{(1)}_{ijk}$. More precisely (writing $\eta_{ijk}$ instead of $\delta\eta_{ijk}$, for simplicity), we elaborate the first term on the right hand side of

$$\delta w = \tau^{(0)}_{ijk}\eta^{(0)}_{ijk} + \tau^{(1)}_{ijk}\eta^{(1)}_{ijk} + \tau^{A}_{ijk}\eta^{A}_{ijk}. \tag{2.70}$$

We have

$$\begin{aligned}
\tau^{(0)}_{ijk}\eta^{(0)}_{ijk} =& \frac{1}{5}\left(\delta_{ij}\tau^S_{mmk}+\delta_{jk}\tau^S_{mmi}+\delta_{ki}\tau^S_{mmj}\right)\frac{1}{5}\left(\delta_{ij}\eta^S_{mmk}+\delta_{jk}\eta^S_{mmi}+\delta_{ki}\eta^S_{mmj}\right) = \\
=& \frac{1}{25}\left[\tau^S_{mmk}\left(3\eta^S_{mmk}+\delta_{ki}\eta^S_{mmi}+\delta_{kj}\eta^S_{mmj}\right)+\tau^S_{mmi}\left(\delta_{ik}\eta^S_{mmk}+3\eta^S_{mmi}+\delta_{ji}\eta^S_{mmj}\right)\right]+ \\
&+\frac{1}{25}\tau^S_{mmj}\left(\delta_{kj}\eta^S_{mmk}+\delta_{ji}\eta^S_{mmi}+3\eta^S_{mmj}\right) = \\
=& \frac{1}{25}\left(5\tau^S_{mmk}\eta^S_{mmk}+5\tau^S_{mmi}\eta^S_{mmi}+5\tau^S_{mmj}\eta^S_{mmj}\right) = \qquad (2.71) \\
=& \frac{3}{5}\tau^S_{mmk}\eta^S_{mmk} = \\
=& \frac{3}{5}\tau^S_{mmk}\left(\epsilon_{,k}+\frac{2}{3}\delta_{kmn}\chi_{mn}\right) = \\
=& \frac{3}{5}\tau^S_{mmk}\epsilon_{,k}+\frac{2}{5}\delta_{kmn}\tau^S_{mmk}\chi_{mn}. \qquad (2.72)
\end{aligned}$$

Using (2.71) in (2.70), we obtain

$$\delta w = p_i\varepsilon_{,i}+\tau^{(1)}_{ijk}\eta^{(1)}_{ijk}+\left(\tau^A_{ijk}\eta^A_{ijk}+\frac{2}{5}\delta_{kmn}\tau^S_{mmk}\chi_{mn}\right), \tag{2.73}$$

with

$$p_i = \frac{3}{5}\tau^S_{mmi}. \tag{2.74}$$

Let us elaborate the term in brackets in (2.73). By (2.45), we have

$$\begin{aligned}
\tau^A_{ijk}\eta^A_{ijk}+\frac{2}{5}\delta_{kmn}\tau^S_{mmk}\chi_{mn} &= \tau^A_{ijk}\frac{2}{3}\left(\delta_{ik\ell}\chi_{\ell j}+\delta_{jk\ell}\chi_{\ell i}\right)+\frac{2}{5}\delta_{kmn}\tau^S_{mmk}\chi_{mn} = \\
&= \frac{2}{3}\tau^A_{ink}\delta_{ikm}\chi_{mn}+\frac{2}{3}\tau^A_{njk}\delta_{jkm}\chi_{mn}+\frac{2}{5}\delta_{kmn}\tau^S_{mmk}\chi_{mn} = \\
&= \left(\frac{2}{3}\tau^A_{ink}\delta_{ikm}+\frac{2}{3}\tau^A_{nik}\delta_{ikm}+\frac{2}{5}\delta_{mnk}\tau^S_{mnk}\right)\chi_{mn} = \\
&= \left(\frac{4}{3}\tau^A_{nik}\delta_{ikm}+\frac{2}{5}\delta_{mnk}\tau^S_{mmk}\right)\chi_{mn} \equiv m_{mn}\chi_{mn}, \qquad (2.75)
\end{aligned}$$

where

$$m_{mn} = \frac{4}{3}\tau^A_{nik}\delta_{mik}+\frac{2}{5}\delta_{mnk}\tau^S_{mmk}. \tag{2.76}$$

Therefore, (2.73) becomes (returning to variations)

$$\delta w = p_i\delta\epsilon_{,i}+\tau^{(1)}_{ijk}\delta\eta^{(1)}_{ijk}+m_{ij}\delta\chi_{ij}, \tag{2.77}$$

where $p_i$, $\tau^{(1)}_{ijk}$, $m_{ij}$ are work-conjugates quantities to $\epsilon_{,i}$, $\eta^{(1)}_{ijk}$, $\chi_{ij}$, respectively.

Next, we can repeat the analysis developed in Section 2.1 to derive the new formulation of the equilibrium problem in $\Omega$, namely (see Lam et al. [53])

$$\sigma_{ik,i}-\frac{1}{2}\delta_{j\ell k}m_{ij,i\ell}-p_{i,ik}-\tau^{(1)}_{ijk,ij}+f_k = 0 \qquad \text{in } \Omega, \tag{2.78}$$

with boundary conditions on (smooth) $\partial\Omega$ as

$$\begin{aligned}
&n_j\left(\sigma_{jk}-\frac{1}{2}\delta_{jk\ell}m_{i\ell,i}-\delta_{jk}p_{i,i}-\tau^{(1)}_{ijk,i}n_k\right)+\left(D_\ell n_\ell\right)\left(n_p p_p n_k+n_i n_j\tau^{(1)}_{ijk}+n_p n_q n_r\tau^{(1)}_{pqr}n_k\right)+ \\
&\quad -\frac{1}{2}\delta_{ijk}D_\ell\left(n_p n_q m_{pq} n_j\right)-D_k\left(p_p n_p\right)-D_j\left(n_i\tau^{(1)}_{ijk}\right)-D_\ell\left(n_i n_j\tau^{(1)}_{ij\ell}n_k\right) = \widehat{t_k} \qquad (2.79)
\end{aligned}$$

or

$$u_k = \widehat{u_k}, \tag{2.80}$$

and

$$n_i m_{ij} - (n_p m_{pq} n_q)\, n_j + 2\delta_{ijk} n_\ell n_p n_q \tau^{(1)}_{pqk} = \widehat{q_j}, \tag{2.81}$$

or

$$(\delta_{ij} - n_i n_j)\, \omega_i = \widehat{\omega_j}, \tag{2.82}$$

and

$$n_i p_i + n_i n_j n_k \tau^{(1)}_{ijk} = \widehat{r_k}, \tag{2.83}$$

or

$$\varepsilon_n \equiv n_i n_j \varepsilon_{ij} = \widehat{\varepsilon_n}. \tag{2.84}$$

Starting from the above stratifying decomposition scheme of the second-order deformation gradient terms, Lam et al. [53] proposed the adoption of a new higher-order equilibrium condition to show that the anti-symmetric part of the rotation gradient does not contribute to the deformation energy. As a consequence, the number of material length scale parameters is reduced from five (of Mindlin's theory) to three.

We follow the analysis in Yang et al. [79]. Let $\Omega'$, $\Omega' \subset\subset \Omega$, be a subset of $\Omega$ with smooth boundary $\partial\Omega'$. We denote $\mathbf{t}(\mathbf{x}, \mathbf{n})$, $\boldsymbol{\mu}(\mathbf{x}, \mathbf{n})$ respectively the force and couple per unit area transmitted through the surface $\partial\Omega'$ in a point $\mathbf{x} \in \partial\Omega'$, with unit external normal $\mathbf{n}$ to the surface. Let $\mathbf{f}$ and $\boldsymbol{\ell}$ be the boundary force and the body couple per unit volume, respectively. If the body is in statical equilibrium, then the Euler-Cauchy equations are satisfied:

$$\int_{\partial\Omega'} \mathbf{t}\, da + \int_{\Omega'} \mathbf{f}\, d\Omega' = \mathbf{0} \tag{2.85}$$

$$\int_{\partial\Omega'} (\mathbf{x} \times \mathbf{t} + \boldsymbol{\mu})\, da + \int_{\Omega'} (\mathbf{x} \times \mathbf{f} + \boldsymbol{\ell})\, d\Omega' = \mathbf{0}, \tag{2.86}$$

where $\mathbf{x}$ is the position vector of a material particle of continuum. The classical Cauchy's Lemma can be generalized to prove that, under suitable assumption, the dependence of $\mathbf{t}$ and $\boldsymbol{\mu}$ on the normal $\mathbf{n}$ is linear, that is

$$\mathbf{t}(\mathbf{x}, \mathbf{n}) = \mathbf{T}(\mathbf{x})\mathbf{n}, \qquad \boldsymbol{\mu}(\mathbf{x}, \mathbf{n}) = \mathbf{M}(\mathbf{x})\mathbf{n}, \tag{2.87}$$

where $\mathbf{T} = (t_{ij})$ is the stress tensor and $\mathbf{M} = (m_{ij})$ is the couple-stress tensor.
Using the divergence theorem to transform the surface integrals in (2.85), (2.86) to volume integrals, we obtain

$$\int_{\Omega'} (\mathrm{div}\mathbf{T} + \mathbf{f})\, d\Omega' = \mathbf{0}, \tag{2.88}$$

$$\int_{\Omega'} (\mathbf{x} \times (\mathrm{div}\mathbf{T} + \mathbf{f}) + \mathrm{div}\mathbf{M} + \boldsymbol{\ell} + \mathcal{a}\mathbf{T})\, d\Omega' = \mathbf{0}, \tag{2.89}$$

where $\mathcal{a}\mathbf{A}$ is the linear operator which associates to a second-order tensor $\mathbf{A}$ twice the axial vector of the anti-symmetric part of $\mathbf{A}$, e.g.,

$$(\mathcal{a}\mathbf{A})_k = \delta_{kji} A^A_{ij}, \quad k = 1, 2, 3. \tag{2.90}$$

By the arbitrariness of $\Omega'$, and under regularity assumptions on the integrands, from (2.89)–(2.90) we obtain the following differential equations of equilibrium:

$$\begin{cases} \mathrm{div}\mathbf{T} + \mathbf{f} = \mathbf{0} & \text{in } \Omega, \qquad (2.91) \\ \mathrm{div}\mathbf{M} + \boldsymbol{\ell} + \mathcal{a}\mathbf{T} = \mathbf{0} & \text{in } \Omega. \qquad (2.92) \end{cases}$$

The second equilibrium equation (2.92) indicates that the stress tensor $\mathbf{T}$ generates an equivalent body couple field $a\mathbf{T}$ which, acting together with $\boldsymbol{\ell}$, maintains the equilibrium of the continuum. In Yang et al. [79], it is proposed to introduce the following additional equilibrium equation to (2.88)–(2.89):

$$\int_{\partial\Omega'} \mathbf{x} \times \boldsymbol{\mu} da + \int_{\Omega'} \mathbf{x} \times (\boldsymbol{\ell} + a\mathbf{T})\, d\Omega' = \mathbf{0}. \tag{2.93}$$

This equation imposes the *equilibrium of moments of couples*. Using the divergence theorem, (2.93) can be rewritten as

$$\int_{\Omega'} (\mathbf{x} \times (\mathrm{div}\mathbf{M} + \boldsymbol{\ell} + a\mathbf{T}) + a\mathbf{M})\, d\Omega' = \mathbf{0}, \tag{2.94}$$

which implies, by (2.92) and using a standard localization procedure,

$$a\mathbf{M} = \mathbf{0}, \tag{2.95}$$

that is the couple stress tensor $\mathbf{M}$ is symmetric:

$$m_{ij} = m_{ji}. \tag{2.96}$$

As a result, the anti-symmetric part of the rotating gradient tensor does not contribute to the deformation energy (see(2.77)) and

$$m^A_{ij} = \frac{\partial\omega\left(\varepsilon_{ij}, \varepsilon_{,i}, \eta^{(1)}_{ijk}, \chi^S_{ij}, \chi^A_{ij}\right)}{\partial\chi^A_{ij}} = 0. \tag{2.97}$$

In conclusion, we have

$$w = w\left(\varepsilon_{ij}, \varepsilon_{,i}, \eta^{(1)}_{ijk}, \chi^S_{ij}\right) \tag{2.98}$$

and for linear elastic center-symmetric isotropic materials, the energy is a quadratic function of the invariant stress metrics:

$$w = \frac{1}{2}k\varepsilon_{ii}\varepsilon_{jj} + \mu\varepsilon^{\mathrm{Dev}}_{ij}\varepsilon^{\mathrm{Dev}}_{ij} + a'_0\varepsilon_{mm,i}\varepsilon_{nn,i} + a'_1\eta^{(1)}_{ij\ell}\eta^{(1)}_{ij\ell} + a'_2\chi^S_{ij}\chi^S_{ij}, \tag{2.99}$$

where $\boldsymbol{\varepsilon}^{\mathrm{Dev}} = \boldsymbol{\varepsilon} - \frac{1}{3}(\mathrm{tr}\,\boldsymbol{\varepsilon})\,\mathbf{1}$, $k$ and $\mu$ are the classical Lamé moduli, $a'_i$, $i = 0, 1, 2$, are three additional material parameters. Following Lam et al. [53], we rewrite the additional constants as

$$a'_0 = \mu\ell_0^2, \qquad a'_1 = \mu\ell_1^2 \qquad a'_2 = \mu\ell_2^2,$$

where $\ell_n$ $(n = 0, 1, 2)$ are *three material length scale parameters*. Finally, we have

$$\begin{aligned} \sigma_{ij} &= k\delta_{ij}\varepsilon_{mm} + 2G\varepsilon^{\mathrm{Dev}}_{ij}, \\ p_i &= 2G\ell_0^2\varepsilon_{mm,i} \\ \tau^{(1)}_{ij\ell} &= 2G\ell_1^2\eta^{(1)}_{ij\ell}, \\ m^S_{ij} &= 2G\ell_2^2\chi^S_{ij}, \end{aligned} \tag{2.100}$$

where $G = \mu > 0$ is the *shear modulus* and $k > 0$ is the *bulk modulus* of the material. In applications, we introduce the technical constants $E$ and $\nu$, where $E$ is the Young's modulus and $\nu$ the Poisson's coefficient, $k = E/(3(1 - 2\nu))$, $G = E/(2(1 + \nu))$, $\nu > 0$.

## 2.3 One-dimensional models of vibrating nanobeams

In this section free vibration of microbars has been investigated using modified strain gradient theory. The higher-order governing equation, initial and corresponding non-classical boundary conditions with classical boundary conditions for vibrating bar are obtained using Hamilton's principle.

### 2.3.1 Axial vibration

Following [3], let us consider the free longitudinal undamped vibrations of a slender straight uniform nanorod of length $L$, see Fig. 2.1. The components of displacement vector in $(x, y, z)$ directions are, respectively:

$$u_1 = u(x,t), \qquad u_2 = u_3 = 0. \tag{2.101}$$

The non zero component of dilatation gradient vector and of the deviatoric stretch gradient tensor are, respectively:

$$\varepsilon_{,i} = \frac{\partial^2 u}{\partial x^2}, \tag{2.102}$$

$$\eta^{(1)}_{ijk} = \frac{2}{5}\frac{\partial^2 u}{\partial x^2}, \qquad \text{if } (i,\ j,\ k = x) \tag{2.103}$$

$$\eta^{(1)}_{ijk} = -\frac{1}{5}\frac{\partial^2 u}{\partial x^2}, \qquad \text{in the other cases.} \tag{2.104}$$

All components of rotation vector, and therefore symmetric rotation gradient tensor, are equal to zero as

$$\omega_i = 0, \qquad (i = x,\ y,\ z) \tag{2.105}$$

$$\chi^S_{ij} = 0. \qquad (i,\ j = x,\ y,\ z). \tag{2.106}$$

The non-zero stress $\sigma_{ij}$, the non-zero higher-order stresses $p_i$ and $\tau^{(1)}_{ijk}$ can be expressed as

$$p_x = 2Gl_0^2\frac{\partial^2 u}{\partial x^2}, \tag{2.107}$$

$$\tau^{(1)}_{ijk} = \frac{4}{5}Gl_1^2\frac{\partial^2 u}{\partial x^2}, \qquad \text{if } (i = j = k = x) \tag{2.108}$$

$$\tau^{(1)}_{ijk} = -\frac{2}{5}Gl_1^2\frac{\partial^2 u}{\partial x^2}, \qquad \text{in the other cases.} \tag{2.109}$$

Finally, the equation of strain energy $\mathscr{E}(t)$ can be rewritten as:

$$\mathscr{E}(t) = \frac{1}{2}\int_0^L \left(a(u')^2 + b(u'')^2\right) dx, \tag{2.110}$$

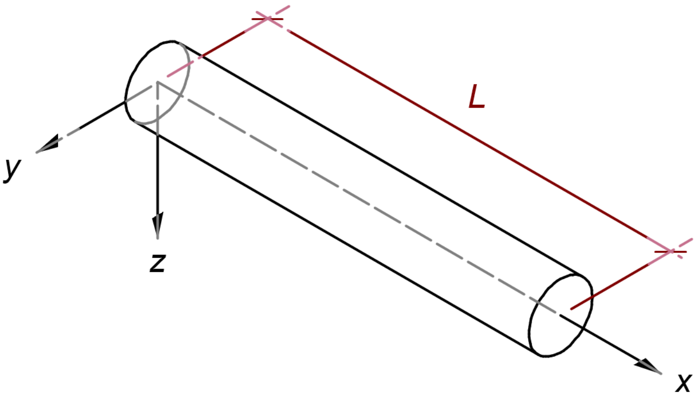

**Figure 2.1:** *Coordinate system*

where $u' = u'(x,t)$ indicates the first partial derivative of the function $u$ with respect to $x,\ x \in (0,L)$. The coefficient $a > 0$ is the axial stiffness of the nanorod and it can be expressed as

$$a = EA, \tag{2.111}$$

with $A$ a geometrical parameter that may be set to correspond with the cross-sectional area of the nanorod. The coefficient $b$ takes the expression

$$b = GA\Big(2\ell_0^2 + \frac{4}{5}\ell_1^2\Big). \tag{2.112}$$

The kinetic energy $\mathscr{T}(t)$ of the nanorod is equal to

$$\mathscr{T}(t) = \frac{1}{2}\int_0^L \rho(\dot{u})^2 dx, \tag{2.113}$$

where $\dot{u} = \dot{u}(x,t)$ denotes the first partial derivative of the function $u$ with respect to $t,\ t > 0$, and $\rho > 0$ is the mass coefficient per unit length.

In accordance with Hamilton's principle [37], the equations of free and undamped motion and their corresponding boundary conditions are obtained by imposing the stationarity of the action functional

$$\mathscr{I}(u) = \int_{t_1}^{t_2} \big(\mathscr{T}(t) - \mathscr{E}(t)\big) dt \tag{2.114}$$

on the following set of admissible configurations

$$\begin{aligned}\mathscr{H} = \big\{h \mid h(\cdot,t) \in C^2(0,L), h(x,\cdot) \in C^2(t_1,t_2),\\ h(x,t) \equiv 0 \text{ in } (0,L) \text{ for } t = t_1 \text{ and for } t = t_2\big\},\end{aligned} \tag{2.115}$$

where $C^2(\Omega)$ is the space of the functions defined on $\Omega$, being continuous and having partial continuous derivatives up to the 2nd order. We also assume that the displacement $u$ in the action functional (2.114) is as regular as is needed so that all the operations in which it is involved are meaningful, that is $u \in C^4(0,L)$.

Let $u(\varepsilon) = u + \varepsilon h$, with $\varepsilon > 0$ a small number and $h \in \mathscr{H}$ a test function. The stationarity condition on the action functional $\mathscr{I}$ at $u$ implies the vanishing of its first variation

$$\Phi'(\varepsilon)\big|_{\varepsilon=0} = \frac{d\mathscr{I}\big(u(\varepsilon)\big)}{d\varepsilon}\Big|_{\varepsilon=0} = 0. \tag{2.116}$$

We elaborate (2.116) by discharging the derivatives from $h$ to $u$ via integration by parts.

$$\begin{aligned}\Phi'(\varepsilon)\big|_{\varepsilon=0} =& \frac{1}{2}\frac{d}{d\varepsilon}\int_{t_1}^{t_2}\int_0^L \Big(\rho(\dot{u}+\varepsilon\dot{h})^2 - a(u'+\varepsilon h')^2 - b(u''+\varepsilon h'')^2\Big) dx\, dt\Big|_{\varepsilon=0} =\\ &= \int_{t_1}^{t_2}\int_0^L \big(\rho\dot{u}\dot{h} - au'h' - bu''h''\big)\, dx\, dt =\\ &= \int_{t_1}^{t_2}\int_0^L \big(-\rho\ddot{u} + au'' - bu''''\big)h\, dx\, dt + \int_0^L \rho\dot{u}h\big|_{t=t_1}^{t=t_2} dx +\\ &+ \int_{t_1}^{t_2}\big(-au' + bu'''\big)h\big|_{x=0}^{x=L} dt - \int_{t_1}^{t_2} bu''h'\big|_{x=0}^{x=L} dt = 0.\end{aligned} \tag{2.117}$$

With suitable choices of the test function $h$, the free vibrations of the uniform nanorod are governed by the following equation of motion

$$au'' - bu'''' = \rho\ddot{u}, \tag{2.118}$$

with boundary conditions

$$\begin{cases} u(0,t)=0 & \text{or} \quad -au'(0,t)+bu'''(0,t)=0 \\ u'(0,t)=0 & \text{or} \quad u''(0,t)=0 \\ u(L,t)=0 & \text{or} \quad -au'(L,t)+bu'''(L,t)=0 \\ u'(L,t)=0 & \text{or} \quad u''(L,t)=0 \end{cases} \qquad \text{for } t \geqslant 0. \tag{2.119}$$

Using the classical separation of variables method, the axial displacement $u(x,t)$ can be expressed as

$$u(x,t)=v(x)e^{i\omega t}, \tag{2.120}$$

where $v = v(x)$ is the amplitude of the normal mode (eigenfunction) associated to the natural (radian) frequency $\omega$ and $i = \sqrt{-1}$ is the imaginary unit. Substituting Eq.(2.120) into Eq.(2.118), the following ordinary differential equation is obtained:

$$-av''+bv''''=\lambda\rho v, \qquad x\in(0,L), \tag{2.121}$$

where $\lambda = \omega^2$ is the eigenvalue.

### 2.3.2 Bending vibration

Consider the straight nanobeam shown in Fig. 2.1, which cross-section is parallel to the $yz$ plane. According to the Euler-Bernoulli hypothesis, the displacement field of a beam in bending can be written as

$$u_1=-z\frac{\partial u(x,t)}{\partial x}, \qquad u_2=0, \qquad u_3=u(x,t), \tag{2.122}$$

where $u_1$, $u_2$, $u_3$, are the $x$-, $y$-, and $z$-components of the displacement vector, respectively.

By substituting (2.122) in the expression of the strain tensor $\varepsilon$ (2.1), then the non-zero component is

$$\varepsilon_{xx}=-z\frac{\partial^2 u}{\partial x^2}, \tag{2.123}$$

so

$$\varepsilon'_{xx}=\frac{2}{3}\varepsilon_{xx} \quad \varepsilon'_{yy}=\varepsilon'_{zz}=-\frac{1}{3}\varepsilon_{xx}. \tag{2.124}$$

and the components of dilatation gradient vector are

$$\varepsilon_{,x}=-z\frac{\partial^3 u}{\partial x^3}, \qquad \varepsilon_{,y}=0, \qquad \varepsilon_{,z}=-\frac{\partial^2 u}{\partial x^2}. \tag{2.125}$$

The non-zero components of the symmetric rotation gradient tensor $\chi^s_{ij}$ and of the deviatoric stretch gradient tensor $\eta^{(1)}_{ijk}$ are, respectively:

$$\chi^s_{xy}=\chi^s_{yx}=-\frac{1}{2}\frac{\partial^2 u}{\partial x^2}, \tag{2.126}$$

$$\eta^{(1)}_{xxx}=-\frac{2}{5}z\frac{\partial^3 u}{\partial x^3}, \tag{2.127}$$

$$\eta^{(1)}_{xxz}=\eta^{(1)}_{zxx}=\eta^{(1)}_{xzx}=-\frac{4}{15}\frac{\partial^2 u}{\partial x^2}, \tag{2.128}$$

$$\eta^{(1)}_{xyy}=\eta^{(1)}_{xzz}=\eta^{(1)}_{yyx}=\eta^{(1)}_{yxy}=\eta^{(1)}_{zxz}=\eta^{(1)}_{zzx}=\frac{1}{5}z\frac{\partial^3 u}{\partial x^3}, \tag{2.129}$$

$$\eta^{(1)}_{yyz}=\eta^{(1)}_{yzy}=\eta^{(1)}_{zyy}=\frac{2}{15}\frac{\partial^2 u}{\partial x^2}, \tag{2.130}$$

$$\eta^{(1)}_{zzz}=\frac{1}{5}\frac{\partial^2 u}{\partial x^2}. \tag{2.131}$$

Similarly, the non-zero higher-order stresses $\tau_{ijk}^{(1)}$ are

$$\tau_{xxx}^{(1)} = -\frac{4}{5} G \ell_1^2 z \frac{\partial^3 u}{\partial x^3}, \tag{2.132}$$

$$\tau_{xxz}^{(1)} = \tau_{zxx}^{(1)} = \tau_{xzx}^{(1)} = -\frac{8}{15} G \ell_1^2 \frac{\partial^2 u}{\partial x^2}, \tag{2.133}$$

$$\tau_{xyy}^{(1)} = \tau_{xzz}^{(1)} = \tau_{yxy}^{(1)} = \tau_{yyx}^{(1)} = \tau_{zxz}^{(1)} = \tau_{zzx}^{(1)} = \frac{2}{5} G \ell_1^2 z \frac{\partial^3 u}{\partial x^3}, \tag{2.134}$$

$$\tau_{yyz}^{(1)} = \tau_{yzy}^{(1)} = \tau_{zyy}^{(1)} = \frac{2}{15} G \ell_1^2 \frac{\partial^2 u}{\partial x^2}, \tag{2.135}$$

$$\tau_{zzz}^{(1)} = \frac{2}{5} G \ell_1^2 \frac{\partial^2 u}{\partial x^2}. \tag{2.136}$$

For a slender beam with a large aspect ratio, the Poisson effect is secondary and may be neglected. By setting $\nu = 0$, as was done in classical beam theories, the non-zero stresses $\sigma_{ij}$ are

$$\sigma_{ij} = E \varepsilon_{xx} = -E z \frac{\partial^2 u}{\partial x^2}. \tag{2.137}$$

Finally, the non-zero higher-order stresses $p_i$ and $m_{ij}^s$ are, respectively

$$p_x = -2G\ell_0^2 z \frac{\partial^3 u}{\partial x^3}, \quad p_y = 0, \quad p_z = -2G\ell_0^2 z \frac{\partial^2 u}{\partial x^2}, \tag{2.138}$$

$$m_{xy}^s = m_{yx}^s = 2G\ell_2^2 \left( -\frac{1}{2} \frac{\partial^2 u}{\partial x^2} \right) = -G\ell_2^2 \frac{\partial^2 u}{\partial x^2}. \tag{2.139}$$

Substituting the above relations in the expression of the strain energy $\mathscr{E}(t)$, we find

$$\mathscr{E}(t) = \frac{1}{2} \int_0^L \left[ S\,(u'')^2 + K\,(u''')^2 \right] dx, \tag{2.140}$$

$S$ and $K$ are constant coefficients ( [1,49])

$$K = I\left(2G\ell_0^2 + \frac{4}{5}G\ell_1^2\right), \quad S = EI + 2GA\ell_0^2 + \frac{8}{15}GA\ell_1^2 + GA\ell_2^2, \tag{2.141}$$

where $I$ is the second moment of area about the axis through the centroid of the cross-section, at right angles to the plane of vibration.

If we neglect the contribution associated with the rotation of the transversal sections, the kinetic energy $\mathscr{T}(t)$ of the nanobeam is equal to

$$\mathscr{T}(t) = \frac{1}{2} \int_0^L \rho(\dot{u})^2 dx. \tag{2.142}$$

The governing equation of the beam in bending as well as initial conditions and all boundary conditions can be determined with the aid of Hamilton's principle [37]

$$\mathscr{I}(u) = \int_{t_1}^{t_2} \big(\mathscr{T}(t) - \mathscr{E}(t)\big) dt \tag{2.143}$$

on the following set of admissible configurations

$$\begin{aligned} \mathscr{H} = \big\{ h \mid\, & h(\cdot,t) \in C^3(0,L), h(x,\cdot) \in C^2(t_1,t_2), \\ & h(x,t) \equiv 0 \text{ in } (0,L) \text{ for } t = t_1 \text{ and for } t = t_2 \big\}, \end{aligned} \tag{2.144}$$

where $C^m(\Omega)$ is the space of the functions defined on $\Omega$, being continuous and having partial continuous derivatives up to the $m$th order, $m = 2, 3$. We also assume that the displacement $u$ in the action functional (2.143) is as regular as is needed so that all the operations in which it is involved are meaningful, that is $u \in C^6(0, L)$.

Let $u(\varepsilon) = u + \varepsilon h$, with $\varepsilon > 0$ a small number and $h \in \mathscr{H}$ a test function. The stationarity condition on the action functional $\mathscr{I}$ at $u$ implies the vanishing of its first variation

$$\begin{aligned}
\Phi'(\varepsilon)\big|_{\varepsilon=0} =& \frac{1}{2}\frac{d}{d\varepsilon}\int_{t_1}^{t_2}\int_0^L \Big(\rho(\dot{u}+\varepsilon\dot{h})^2 - S(u''+\varepsilon h'')^2 - K(u'''+\varepsilon h''')^2\Big)dx\,dt\Big|_{\varepsilon=0} = \\
=& \int_{t_1}^{t_2}\int_0^L \big(\rho\dot{u}\dot{h} - Su''h'' - Ku'''h'''\big)\,dx\,dt = \\
=& \int_{t_1}^{t_2}\int_0^L \big(-\rho\ddot{u} - Su^{IV} + Ku^{VI}\big)h\,dx\,dt + \int_0^L \rho\dot{u}h\big|_{t=t_1}^{t=t_2}\,dx + \int_{t_1}^{t_2} Ku'''h''\big|_{x=0}^{x=L}\,dt \\
&+ \int_{t_1}^{t_2}\big(-Su'' + Ku^{IV}\big)h'\big|_{x=0}^{x=L}\,dt + \int_{t_1}^{t_2}\big(Su''' - Ku^{V}\big)h\big|_{x=0}^{x=L}\,dt = 0.
\end{aligned} \tag{2.145}$$

With suitable choices of the test function $h$, the free vibrations of the uniform nanorod are governed by the following equation of motion

$$-Su^{IV} + Ku^{VI} = \rho\ddot{u}, \tag{2.146}$$

with boundary conditions

$$\begin{cases}
u(0,t) = 0 & \text{or } Su'''(0,t) - Ku^{V}(0,t) = 0 \\
u'(0,t) = 0 & \text{or } -Su''(0,t) + Ku^{IV}(0,t) = 0 \\
u''(0,t) = 0 & \text{or } u'''(0,t) = 0 \\
u(L,t) = 0 & \text{or } Su'''(L,t) - Ku^{V}(L,t) = 0 \\
u'(L,t) = 0 & \text{or } -Su''(L,t) + Ku^{IV}(L,t) = 0 \\
u''(L,t) = 0 & \text{or } u'''(L,t) = 0
\end{cases} \qquad \text{for } t \geqslant 0. \tag{2.147}$$

Using the classical separation of variables method, the transversal displacement $u(x,t)$ can be expressed as

$$u(x,t) = v(x)e^{i\omega t}, \tag{2.148}$$

where $v = v(x)$ is the amplitude of the normal mode (eigenfunction) associated to the natural (radian) frequency $\omega$ and $i = \sqrt{-1}$ is the imaginary unit. Substituting Eq.(2.148) into Eq.(2.146), the following ordinary differential equation is obtained:

$$Sv^{IV} - Kv^{VI} = \lambda\rho v, \qquad x \in (0,L), \tag{2.149}$$

where $\lambda = \omega^2$ is the eigenvalue.

# CHAPTER 3

# Mass identification in axially vibrating nanobeams

## 3.1 Introduction

In this chapter a distributed mass reconstruction method for initially uniform nanorods based on measurements of the first lower resonant frequencies of the free axial vibration is presented. Two main inverse problems are addressed. In the first part (Sections 3.3–3.6), the mass variation is determined by using the first lower eigenfrequencies of a clamped-clamped nanorod, under the a priori assumption that the mass variation has support contained in half of the axis interval. The method is based on an iterative procedure that produces an approximation of the unknown mass density as a generalized Fourier partial sum of order $N$, whose coefficients are calculated from the first $N$ eigenvalues.

The assumption that the mass variation has support contained in half of the axis interval is needed to avoid trivial non-uniqueness due to the symmetry of the initial configuration of the nanorod. In the second part of the chapter, (Section 3.7), we remove this a priori assumption on the mass support, and we show how to extend the method to reconstruct a *general* mass distribution by adding to the input data the first $N$ lower eigenvalues of the nanorod under clamped-free end conditions.

The nanorod is modelled using the modified strain gradient theory to account for the microstructure and size effects. Moreover, the mass variation is supposed to be small with respect to the total mass of the initial nanorod.

An extended series of numerical examples shows that the method is efficient and gives excellent results in case of continuous mass variations. The determination of discontinuous coefficients exhibits no negligible oscillations near the discontinuity points, and requires more spectral data to obtain good reconstruction. A proof of local convergence of the iteration algorithm is provided for a family of finite dimensional mass coefficients. Surprisingly enough, in spite of its local character, the identification method performs well even for not necessarily small mass changes.

The results presented in this chapter have been obtained in collaboration with José Fernández-Sáez and Ramón Zaera (University Carlos III de Madrid, Spain) and Michele Dilena and Antonino Morassi (University of Udine, Italy), and have been published in [26], [24].

## 3.2 Inertial imaging in nanoresonators: an overview

As we stated in the Introduction, mass sensing with nanosystems has advanced significantly in the last decade. In this section we shall illustrate the methodology recently proposed by the research groups coordinated by M.L. Roukes (California Institute of Technology, Pasadena, USA) and M. Selim Hanay (Bilkent University, Ankara, Turkey) in a series of papers [42], [69], [46].

In spite of the fact that applications are for nanostructures, and particularly for nanobeams, the authors test their methodology on the classical Euler-Bernoulli model for transversely vibrating slender beams under clamped end conditions.

The infinitesimal free bending vibration at radian frequency $\sqrt{\lambda_n}$ of the unperturbed uniform nanobeam is governed by the following eigenvalue problem

$$\begin{cases} au_n^{IV} = \lambda_n \rho_0 u_n, \qquad x \in (0,L), & (3.1)\\ u_n(0)=0,\ u_n'(0)=0, & (3.2)\\ u_n(L)=0,\ u_n'(L)=0, & (3.3)\end{cases}$$

where $\lambda_n$ is the eigenvalue and $u_n = u_n(x)$ the associated eigenfunction, $n \geq 1$. The unperturbed mass density per unit length is $\rho_0$ =constant $> 0$; the bending stiffness is denoted by $a$, $a =$ constant $> 0$.

Let us assume that the mass density changes, and denote by

$$\rho(x) = \rho_0(x) + r(x) \tag{3.4}$$

the mass density for the perturbed beam, where $r = r(x)$ is the unknown mass change. We denote by $(\lambda_n(\rho), u_n(x,\rho))$ the $n$th eigenpair of the perturbed beam.
Under the assumption of "small" $r(x)$, Hanay et al. [42] argued that the first order change of the $n$th eigenvalue is given by

$$\delta\lambda_n \equiv 1 - \frac{\lambda_n(\rho)}{\lambda_n} = \int_0^l r(x) u_n^2(x)dx, \tag{3.5}$$

where the unperturbed eigenfunction is normalized as $\int_0^l \rho_0 u_n^2(x)dx = 1$.

The main idea of the method is to determine the first $N$ *moments* of the unknown mass variation $r(x)$ in terms of the measured shifts in the first $N$ eigenpair $\{\delta\lambda_n\}_{n=1}^N$.

Let us recall the classical form of the moment problem in a finite interval $[0,1]$. Given a sequence of real numbers $\{\mu_k\}_{k=0}^\infty$, to find a real-valued function $f(x),\ f:[0,1]\to\mathbb{R}$, such that

$$\int_0^1 x^k f(x)dx = \mu_k, \qquad k \geq 0. \tag{3.6}$$

This is called Hausdorff Moment Problem (HMP). The scalar products coupling $1, x, x^2, \ldots, x^k, \ldots$ with the function $f(x)$, e.g., $\int_0^1 x^k f(x)dx$, are called the moments of $f(x)$.
Several theoretical results on the HMP are well established, see, for example, Talenti [72] for a complete account. In brief, solutions to HMP that belong to $L^2(0,1)$ are unique, and a necessary and sufficient condition for $\{\mu_k\}_{k=0}^\infty$ to be the moments of a function $f(x) \in L^2(0,1)$ was established by Hausdorff. A crucial remark is that the HMP is an ill-posed problem in the sense of Hadamard. Talenti [72] proposed a theory and an algorithm for recovering a function from its moments for the case of a finite numbers of date contaminated by noise.

Returning to the mass determination problem, the unknowns are the real numbers $\left\{\alpha_n^{(k)}\right\}_{n=1}^N$, where $k$ is the order of the moment of $r(x)$ we want to determine, $k = 0, 1, \ldots, N$. Let $k$ be fixed,

$k = 0, 1, \dots, N$. We multiply (3.5) by $\alpha_n^{(k)}$ and sum over $n$:

$$\sum_{n=1}^{N} \alpha_n^{(k)} \delta\lambda_n = \sum_{n=1}^{N} \alpha_n^{(k)} \int_0^L r u_n^2 dx, \tag{3.7}$$

that is

$$\sum_{n=1}^{N} \alpha_n^{(k)} \delta\lambda_n = \int_0^L r g^{(k)} dx, \tag{3.8}$$

where

$$g^{(k)}(x) = \sum_{n=1}^{N} \alpha_n^{(k)} u_n^2(x). \tag{3.9}$$

Now, *if*

$$g^{(k)}(x) = x^k \qquad \text{in } [0,1], \tag{3.10}$$

then the right hand side of (3.8) is the $k$th moment of the mass variation $r$, say $\mu^{(k)}$. Simple examples show that condition (3.10) *cannot* be satisfied point-wise, e.g., in case of a clamped-clamped beam $u_n = 0$ at the boundary of the interval $[0, L]$, then $g_n^{(k)}(0) = g_n^{(k)}(L) = 0$. This aspect is briefly discussed in Hanay el al. (see [42], p. 4–5 of the Supplementary Information). Actually, the coefficients $\left\{\alpha_n^{(k)}\right\}_{n=1}^{N}$ are determinated via the following least-squares approach. For given $k,\ k = 0, 1, \dots, N$, to determine $\left\{\alpha_n^{(k)}\right\}_{n=1}^{N}$ such that

$$\min J\left(\alpha_1^{(k)}, \dots, \alpha_N^{(k)}\right), \qquad J = \int_0^L \left(g^{(k)}(x) - x^k\right)^2 dx. \tag{3.11}$$

The stationarity condition on $J$ requires $\frac{\partial J}{\partial \alpha_i^{(k)}} = 0,\ i = 1, \dots, N$, that is

$$\sum_{n=1}^{N} A_{in} \alpha_n^{(k)} = b_i^{(k)}, \qquad i = 1, \dots, N, \tag{3.12}$$

with

$$A_{in} = \int_0^L u_i^2 u_n^2 dx, \quad b_i^{(k)} = \int_0^L x^k u_i^2 dx, \quad i, n = 1, \dots, N. \tag{3.13}$$

A direct calculation shows that the matrix $A_{in}$ is not singular, and the coefficients $\left\{\alpha_n^{(k)}\right\}_{n=1}^{N}$ can be uniquely determinated (see [42], p. 9 of the Supplementary Information). Consequence of the approximation of $x^k$ by means of $g^k(x)$ on the inverse problem solution are not discussed by the authors.

Finally, assuming that the numbers $\left\{\alpha_n^{(k)}\right\}_{n=1}^{N}$ are known, one can determine the moments $\mu^{(k)} = \int_0^L r x^k dx$ in terms of the measured frequency shifts $\delta\lambda_n$. The knowledge of the first three moments $\mu^{(1)}, \mu^{(2)}, \mu^{(3)}$, and of the zeroth moment $\mu^{(0)}$, allows the authors to estimate the *center of mass* of the added distribution $r(x)$, the *size* $\int_0^L r(x)dx$, and the *asymmetry index* (skewness).

The approach was validated through detailed experimental data on a series of adsorbates and also by numerical simulation. We refer to the paper [42] for more details, and to subsequent papers [69] and [46] for generalization of the methodology and additional applications.

## 3.3 Formulation of the mass identification problem

We consider a straight uniform nanobeam in longitudinal vibration and under clamped end conditions. Using separation of variables, the axial displacement $u(x,t)$ can be expressed as (see section 2.3.1)

$$u(x,t) = v(x)e^{i\omega t}. \tag{3.14}$$

Then, the spatial variation of the infinitesimal free longitudinal vibration of the unperturbed or referential nanorod of length $L$ is governed by the following eigenvalue problem

$$\begin{cases} bv^{IV} - av'' = \lambda\rho_0 v, \quad x \in (0,L), & (3.15) \\ v(0) = 0, \ v''(0) = 0, & (3.16) \\ v(L) = 0, \ v''(L) = 0, & (3.17) \end{cases}$$

where $\lambda = \omega^2$ is the eigenvalue, $\omega$ is the (radian) frequency, and $v = v(x)$ is the corresponding eigenfunction. Moreover, $\rho_0 =$ const, $\rho_0 > 0$, is the unperturbed mass density per unit length, whereas the stiffness coefficients $a$ and $b$ are defined in ((2.111))–(2.112), with $a$ , $b$ positive constants.

The eigenpairs $\{\lambda_n, \ v_n(x)\}_{n=1}^{\infty}$ of (3.15)–(3.17) are

$$\lambda_n = \left(\frac{n\pi}{L}\right)^2 \left[\frac{1}{\rho_0}\left(a + b\left(\frac{n\pi}{L}\right)^2\right)\right], \tag{3.18}$$

$$v_n(x) = \sqrt{\frac{2}{\rho_0 L}} \sin\left(\frac{n\pi x}{L}\right), \tag{3.19}$$

where the following mass-normalization condition has been used

$$\int_0^L \rho_0 v_n^2(x) = 1, \quad n \geq 1. \tag{3.20}$$

Note that the sequence $\{\lambda_n\}_{n=1}^{\infty}$ of the unperturbed nanorod is *uniformly discrete*, that is, there exists a separation constant $\sigma > 0$, only depending on the parameters of the system, such that

$$|\lambda_n - \lambda_m| \geq \sigma, \tag{3.21}$$

for every $m, n \in \mathbb{N}$, with $m \neq n$. In particular, a direct calculation shows that

$$\sigma = \frac{1}{\rho_0}\left(\frac{\pi}{L}\right)^2 \left[a + 2b\left(\frac{\pi}{L}\right)^2\right]. \tag{3.22}$$

This property will be useful in proving the continuity of the eigenfunctions of the nanorod with respect to perturbations of the linear mass density.

Let us assume that the mass per unit length of the nanorod changes, and let us denote by

$$\rho(x) = \rho_0 + r_\epsilon(x), \quad x \in [0,L], \tag{3.23}$$

the mass density per unit length of the *perturbed* nanorod. We shall assume the following hypotheses on the perturbation $r_\epsilon$:

i) ($L^2$-perturbation and smallness)

$$\left(\frac{1}{L}\int_0^L (r_\epsilon(x))^2 dx\right)^{\frac{1}{2}} = \epsilon\rho_0, \tag{3.24}$$

where the perturbation parameter $\epsilon$ is a real number such that $0 < \epsilon \leq \widehat{\epsilon}$, with $\widehat{\epsilon} < 1$ a small number to be chosen later on.

ii) (Regularity)

$$r_\epsilon(x) \in L^\infty([0, L]), \tag{3.25}$$

where $L^\infty([0, L])$ is the space of (Lebesgue measurable) functions $f : [0, L] \to \mathbb{R}$ such that $\|f\|_\infty = ess\ sup_{x\in[0,L]}|f(x)| < \infty$ almost everywhere in $[0, L]$.

iii) (Uniform lower and upper bound)

$$0 < \rho^- \leq \rho(x) \leq \rho^+, \quad x \in [0, L], \tag{3.26}$$

with $\rho^-$, $\rho^+$, $\rho^+ \geq \rho_0 + \|r_\epsilon\|_\infty$, given constants independent of $\epsilon$.

*Remark* 3.3.1. The smallness of the mass variation $r_\epsilon(x)$ expressed in (3.24) allows to consider either perturbations of small amplitude given on large portions of the interval $[0, L]$ (e.g., diffuse mass change) or perturbation having large value concentrated in small parts of $[0, L]$. Moreover, it should be noticed that the mass identification problem in nanorods involves *positive* variations of the mass density $\rho_0$, that is

$$r_\epsilon(x) \geq 0, \quad x \in [0, L]. \tag{3.27}$$

However, it is difficult to include this constraint in our analysis, and condition (3.27) will be used in Section 3.6.3.4 to post-filtering the results of the proposed identification method.

Let us denote by $\{\lambda_n(\rho), v_n(x; \rho)\}_{n=1}^\infty$ the eigenpairs of (3.15)–(3.17) when the coefficient $\rho_0$ is replaced by $\rho(x)$, that is

$$\begin{cases} bv^{IV} - av'' = \lambda\rho v, \quad x \in (0, L), & (3.28) \\ v(0) = 0,\ v''(0) = 0, & (3.29) \\ v(L) = 0,\ v''(L) = 0. & (3.30) \end{cases}$$

Under our assumptions i)-iii), for any $\epsilon$, $0 < \epsilon \leq \widehat{\epsilon}$, the eigenvalue problem (3.28)–(3.30) still maintains the properties of the unperturbed eigenvalue problem, and we shall denote by $\{\lambda_n(\rho), v_n(x; \rho)\}_{n=1}^\infty$, the *perturbed eigenpairs*, with $0 < \lambda_1(\rho) < ... < \lambda_n(\rho) < ...$, $\lim_{n\to\infty} \lambda_n(\rho) = \infty$.
The main goal of this study is:

*Given the unperturbed nanorod, to recover the added mass $r_\epsilon(x)$ from the knowledge of the finite eigenvalue data $\{\lambda_n(\rho)\}_{n=1}^N$.*

Recalling that the knowledge of a single full spectrum is not enough to determine uniquely a general coefficient $r_\epsilon(x)$ (see [70] and, for Sturm-Liouville operators, [44]), here we formulate a mixed inverse problem of Hochstadt-Lieberman's type with finite data in which the mass coefficient is known in half of the nanorod, namely the mass variation $r_\epsilon(x)$ has support contained in $(0, L/2)$:

$$\text{supp}(r_\epsilon(x)) = \overline{\{x \in [0, L]|\ r_\epsilon(x) \neq 0\}} \subset \Big(0, \frac{L}{2}\Big). \tag{3.31}$$

## 3.4 An iterative first-order reconstruction procedure

In this section we shall present a reconstruction procedure which is inspired to the Generalized Fourier Coefficient Method introduced in [63] to deal with damage identification in (classical) beams and rods. In its essence, the method is based on the linearization of the inverse problem in a neighborhood of the referential configuration, and on using the eigenvalue sensitivity to the unknown perturbation (see next two subsections). An iterative version of the procedure will be presented in the third subsection. A formal study of the convergence is proposed in Section 3.5.

### 3.4.1 Eigenfrequency sensitivity to added mass

Let us introduce some notation. For any integer $m \geq 0$ and for any real numbers $\ell_1$, $\ell_2$, with $-\infty < \ell_1 < \ell_2 < +\infty$, $H^m(\ell_1, \ell_2)$ denotes the real-valued Hilbert space of the Lebesgue measurable functions $f : (\ell_1, \ell_2) \to \mathbb{R}$, such that $\int_{\ell_1}^{\ell_2} \left( f^2 + \sum_{i=1}^{m} \left( \frac{d^i f}{dx^i} \right)^2 \right) < +\infty$, where $\frac{d^i f}{dx^i}$ is the $i$th weak derivative of $f$ (see, for example, [15]). We notice that, when $m = 0$, $H^0(\ell_1, \ell_2)$ coincides with the space $L^2(\ell_1, \ell_2)$ of the square integrable functions in $(\ell_1, \ell_2)$, with norm $\|f\|_{L^2(\ell_1,\ell_2)} = \left( \int_{\ell_1}^{\ell_2} f^2(x) dx \right)^{\frac{1}{2}}$. In order to simplify the notation, the $L^2$ norm will be often denoted as $\|f\|_2$. Finally, let us set $\|f\|_\infty = \max_{x \in [0,L]} |f(x)|$ for any bounded function $f$, $f : [0, L] \to \mathbb{R}$. The characteristic function $\chi_I : \mathbb{R} \to \mathbb{R}$ of the closed interval $I$, $I \subset \mathbb{R}$, is defined as $\chi_I(x) = 1$ if $x \in I$, $\chi_I(x) = 0$ if $x \in \mathbb{R} \subset I$.

Let us rewrite the unperturbed eigenvalue problem (3.15)–(3.17) in the following form

$$F(v(x)) = \lambda M(v(x)), \tag{3.32}$$

where the operators $F : H^2(0, L) \to H^2(0, L)$, $M : H^2(0, L) \to H^2(0, L)$ are defined as

$$F(v(x)) = bv^{IV}(x) - av''(x), \tag{3.33}$$

$$M(v(x)) = \rho_0 v(x). \tag{3.34}$$

The perturbed eigenvalue problem (3.28)–(3.30) can be described similarly, that is

$$F(v(x; \rho)) = \lambda(\rho) M_\epsilon(v(x; \rho)), \tag{3.35}$$

where the operator $M_\epsilon : H^2(0, L) \to H^2(0, L)$ is defined as

$$M_\epsilon(v(x; \rho)) = \rho v(x; \rho), \qquad \rho = \rho_0 + r_\epsilon. \tag{3.36}$$

The set $\mathcal{H}$ of admissible configurations of the clamped nanorod is given by

$$\mathcal{H} = \{f : (0, L) \to \mathbb{R} \mid f \in H^2(0, L),\ f(x) = 0 \text{ at } x = 0 \text{ and at } x = L\}. \tag{3.37}$$

We introduce the following operations from $\mathcal{H} \times \mathcal{H}$ to $\mathbb{R}$:

$$\langle M(f), g \rangle = \int_0^L \rho_0 f g, \tag{3.38}$$

$$\langle F(f), g \rangle = \int_0^L (bf^{IV} - af'')g. \tag{3.39}$$

Integration by parts shows that both the operators $M$ and $F$ are self-adjoint in $\mathcal{H}$, that is, $\langle M(f), g \rangle = \langle f, M(g) \rangle$ and $\langle F(f), g \rangle = \int_0^L (bf''g'' + af'g') = \langle f, F(g) \rangle$ for every $f, g \in \mathcal{H}$.

In the sequel, we shall use an explicit expression of the first-order perturbation (with respect to the parameter $\epsilon$) of the eigenvalues. Note that, the $n$th unperturbed and perturbed eigenpair will be denoted by $\{\lambda_n, v_n(x)\}$ and $\{\lambda_n(\rho), v_n(x; \rho)\}$, respectively. In order to find the first-order change of the $n$th eigenvalue, we find convenient to define

$$\Delta\lambda_n = \lambda_n(\rho) - \lambda_n, \tag{3.40}$$

$$\Delta v_n = v_n(x; \rho) - v_n, \tag{3.41}$$

$$\Delta M = M_\epsilon - M, \tag{3.42}$$

and rewrite the normalization condition (3.20) as

$$\langle M(v_n), v_n\rangle = 1. \tag{3.43}$$

Let us multiply equation (3.32) (written for the $n$th unperturbed eigenfunction $v_n(x)$) and equation (3.35) (written for the $n$th perturbed eigenfunction $v_n(x;\rho)$) by $v_n(x;\rho)$ and $v_n(x)$, respectively. Integrating, subtracting side by side, using the self-adjointness property and condition (3.43), we deduce the *fundamental identity* between the states corresponding to mass coefficients $\rho_0$ and $\rho$:

$$\begin{aligned}\Delta\lambda_n = &-\lambda_n\langle \Delta M(v_n), v_n\rangle - \lambda_n\langle \Delta M(\Delta v_n), v_n\rangle - \Delta\lambda_n\langle M(\Delta v_n), v_n\rangle - \\ &-\Delta\lambda_n\langle \Delta M(v_n), v_n\rangle - \Delta\lambda_n\langle \Delta M(\Delta v_n), v_n\rangle.\end{aligned} \tag{3.44}$$

Next, we introduce the following theorem about the continuity of eigenvalues and eigenfunctions of the problem (3.28)–(3.30) with respect to $L^2$-perturbations of the mass coefficient. This result will be also useful in studying the convergence of the iterative identification method presented in Section 3.5.

Let us denote as *a priori data* the set $\mathcal{A}$ of quantities defining the unperturbed model (e.g., the coefficients $a$, $b$, $\rho_0$, $L$), and the uniform lower and upper bound of the mass density of the perturbed model $\rho(x)$:

$$\mathcal{A} = \{a, b, \rho_0, L, \rho^-, \rho^+\}. \tag{3.45}$$

Note that the separation constant $\sigma$ of the unperturbed nanorod depends on the a priori quantities belonging to $\mathcal{A}$, and therefore it will not be explicitly included in $\mathcal{A}$.

**Theorem 3.4.1.** *Under the above notation, let $\rho_i(x) = \rho_0 + r_{\epsilon,i}(x)$, where $r_{\epsilon,i}(x)$ satisfies* (3.24)–(3.26), *$i = 1, 2$. Let $\{\lambda_n(\rho_i),\ v_n(x;\rho_i)\}$, $n \geq 1$, be the nth eigenpair of* (3.28)–(3.30) *for $i = 1, 2$.*

*For every $n \geq 1$, there exists a constant $C_n^\lambda$, $C_n^\lambda > 0$, only depending on the a priori data $\mathcal{A}$ and $n$, such that*

$$|\lambda_n(\rho_1) - \lambda_n(\rho_2)| \leq C_n^\lambda \|\rho_1 - \rho_2\|_2. \tag{3.46}$$

*Let the eigenfunctions $v_n(x;\rho_1)$, $v_n(x;\rho_2)$ be normalized such that*

$$\int_0^L \rho_1 v_n^2(x;\rho_1) = \int_0^L \rho_1 v_n^2(x;\rho_2) = 1 \tag{3.47}$$

*and $v_n'(0;\rho_1)v_n'(0;\rho_2) > 0$, $n \geq 1$. For every $n \geq 1$, there exist a number $\widehat{\epsilon}$, $0 < \widehat{\epsilon} < 1$, and a constant $C_n^v$, $C_n^v > 0$, both only depending on the a priori data $\mathcal{A}$ and $n$, such that*

$$||v_n(x;\rho_1) - v_n(x;\rho_2)||_2 \leq C_n^v \|\rho_1 - \rho_2\|_2, \tag{3.48}$$

*for every $\rho_1$, $\rho_2$ satisfying $\|\rho_1 - \rho_2\|_2 \leq L^{\frac{1}{2}}\widehat{\epsilon}$.*

A proof of Theorem 3.4.1 is presented in Section 3.4.2.

By using inequalities (3.46), (3.48) into identity (3.44), for $0 < \epsilon \leq \widehat{\epsilon}$, the first order change with respect to $\epsilon$ of the $n$th eigenvalue is given by

$$\lambda_n(\rho) = \lambda_n - \lambda_n \int_0^{\frac{L}{2}} r_\epsilon(x) v_n^2(x)dx, \tag{3.49}$$

for every $n \geq 1$ and for $r_\epsilon$ satisfying (3.31).

To prove (3.49), we first start by showing that $|v_n(x)|$ is uniformly bounded in $[0, L]$ in terms of the a priori data $\mathcal{A}$ and $n$. By the definition of the eigenvalue problem for the unperturbed nanorod, by Hölder inequality and by using the normalization condition (3.20), for every $x \in [0, L]$ and every $n \geq 1$, we have

$$|v_n(x)| = \left| \int_0^x v_n'(s)ds \right| \leq L^{\frac{1}{2}} \left( \int_0^L (v_n'(x))^2 dx \right)^{\frac{1}{2}} \leq$$
$$\leq \left( \frac{L}{a} \right)^{\frac{1}{2}} \left( \int_0^L (b(v_n''(x))^2 + a(v_n'(x))^2) dx \right)^{\frac{1}{2}} \leq \left( \frac{L}{a} \right)^{\frac{1}{2}} \lambda_n^{\frac{1}{2}}. \tag{3.50}$$

Next, we show that all the terms on the right hand side of (3.44), but the first, are of higher order with respect to $\epsilon$. Let us consider the second term. By using (3.50), Hölder inequality and estimate (3.48) in Theorem 3.4.1, for $0 < \epsilon \leq \widehat{\epsilon}$, we have

$$|\lambda_n \langle \Delta M(\Delta v_n), v_n \rangle| \leq \lambda_n \left| \int_0^{\frac{L}{2}} r_\epsilon(x)(v_n(x; \rho_0 + r_\epsilon) - v_n(x)) v_n(x) dx \right| \leq$$
$$\leq \lambda_n \|v_n\|_\infty \|r_\epsilon\|_2 \|v_n(x; \rho_0 + r_\epsilon) - v_n(x)\|_2 \leq \lambda_n \|v_n\|_\infty C_n^v \|r_\epsilon\|_2^2 \leq C\epsilon^2, \tag{3.51}$$

where $C > 0$ is a constant only depending on the a priori data $\mathcal{A}$ and $n$.

The estimates of the third, fourth and fifth terms can be performed similarly, resulting, for $0 < \epsilon \leq \widehat{\epsilon}$,

$$|\Delta\lambda_n \langle M(\Delta v_n), v_n \rangle|, \ |\Delta\lambda_n \langle \Delta M(v_n), v_n \rangle| \leq C\epsilon^2, \ |\Delta\lambda_n \langle \Delta M(\Delta v_n), v_n \rangle| \leq C\epsilon^3, \tag{3.52}$$

where $C > 0$ is a constant only depending on the a priori data $\mathcal{A}$ and $n$. By using (3.51) and (3.52) in (3.44), and neglecting higher order terms with respect to $\epsilon$, we obtain (3.49).

Let us comment the expression (3.49). As expected by the general theory (see, for instance, [20]), expression (3.49) states that addition of mass causes decrease in all the eigenvalues. More precisely, the eigenvalue shift $(\lambda_n(\rho) - \lambda_n)$ turns out to be proportional to $\lambda_n$. This fact seems to have a certain importance in our inverse problem, since the relative variation of the eigenvalues appears to be significant also for large order $n$. Finally, it should be noticed that the expression (3.49) is independent of the boundary conditions of the eigenvalue problem and, therefore, the analysis could be extended also to other sets of boundary conditions of the nanorod.

### 3.4.2 Proof of Theorem 3.4.1

In this section we prove Theorem 3.4.1.

Let $n$ be a fixed integer, $n \geq 1$.

*Proof of estimate* (3.46).

We adapt the arguments shown in [8]. The Rayleigh quotient for the eigenvalue problem (3.28)–(3.30) is

$$R[u, \rho] = \frac{\int_0^L b(u'')^2 + a(u')^2}{\int_0^L \rho u^2}, \tag{3.53}$$

for every function $u \in \mathcal{H} \setminus \{0\}$, that is, $u \in H^2(0, L)$ satisfying the end conditions $u(0) = u(L) = 0$.

Let us recall the following variational characterization of the eigenvalues of (3.28)–(3.30). Let $v_n(x; \rho)$ denote the eigenfunction corresponding to $\lambda_n(\rho)$ and let $\mathcal{U}_n(\rho)$ be the subspace of $\mathcal{H}$ spanned by the first $n$ eigenfunctions $\{v_1(x; \rho), \ldots, v_n(x; \rho)\}$. Let $V_n$ be any other $n$-dimensional subspace of $\mathcal{H}$. We have

$$\lambda_n(\rho) \leq \max_{u \in V_n \setminus \{0\}} R[u, \rho], \qquad \lambda_n(\rho) = \max_{u \in \mathcal{U}_n(\rho) \setminus \{0\}} R[u, \rho]. \tag{3.54}$$

For every function $u \in \mathcal{H} \setminus \{0\}$ we have

$$R[u,\rho_2] = R[u,\rho_1]\left(1 + \frac{\int_0^L (\Delta\rho)u^2}{\int_0^L \rho_2 u^2}\right), \tag{3.55}$$

with $\Delta\rho = \rho_1 - \rho_2$.

Our main goal is to show that the numerator of the fraction appearing on the right hand side of (3.55) can be bounded from above by $const. \|\Delta\rho\|_2 \int_0^L u^2$ for every $u \in \mathcal{U}_n(\rho_1) \setminus \{0\}$, where $const.$ is a positive constant depending only on the a priori data and $n$. In fact, on assuming this bound available, and using the uniform lower bound (3.26), from (3.55) we have

$$R[u,\rho_2] \leq R[u,\rho_1]\left(1 + C\|\Delta\rho\|_2\right), \tag{3.56}$$

where the constant $C > 0$ only depends on the a priori data and $n$. Next, taking the maximum in (3.56) over the functions $u \in \mathcal{U}_n(\rho_1) \setminus \{0\}$ and using the variational characterization (3.54), we obtain

$$\lambda_n(\rho_2) \leq \lambda_n(\rho_1)\left(1 + C\|\Delta\rho\|_2\right). \tag{3.57}$$

Reversing the indexes 1 and 2, we also have

$$\lambda_n(\rho_1) \leq \lambda_n(\rho_2)\left(1 + C\|\Delta\rho\|_2\right). \tag{3.58}$$

From (3.57) and (3.58) we can derive the inequality

$$|\lambda_n(\rho_2) - \lambda_n(\rho_1)| \leq C \max\{\lambda_n(\rho_1), \lambda_n(\rho_2)\}\|\Delta\rho\|_2. \tag{3.59}$$

Recalling that, by definition of $\rho^-$ in (3.26) and by monotonicity results (see, for example, [20]), we have $\lambda_n(\rho_1) \leq \lambda_n(\rho^-)$ and $\lambda_n(\rho_2) \leq \lambda_n(\rho^-)$ for every $n \geq 1$, the wished estimate (3.46) follows from (3.59).

To complete the proof, it remains to control the numerator in the fraction on the right hand side of (3.55).

Let $u \in \mathcal{U}_n(\rho_1) \setminus \{0\}$, that is $u(x) = \sum_{i=1}^n c_i v_i(x;\rho_1)$ with $\sum_{i=1}^n c_i^2 > 0$, where $v_i(x;\rho_1)$ is normalized so that $\int_0^L \rho_1 v_1^2(x;\rho_1) = 1$, $i = 1, \dots, n$. By integrating by parts, we have:

$$\begin{aligned}\int_0^L \Delta\rho(x)u^2(x)dx = u^2(x)\int_0^x \Delta\rho(x_1)dx_1|_{x=0}^{x=L} - \\ -\int_0^L \left(\int_0^x \Delta\rho(x_1)dx_1\right)\left(u^2(x)\right)' dx = -2\int_0^L \left(\int_0^x \Delta\rho(x_1)dx_1\right)u(x)u'(x)dx.\end{aligned} \tag{3.60}$$

Using Hölder inequality, we obtain $|\int_0^x \Delta\rho(x_1)dx_1| \leq L^{\frac{1}{2}}\|\Delta\rho\|_2$, and then, inserting this estimate in (3.60), we get

$$|\int_0^L \Delta\rho(x)u^2(x)dx| \leq 2L^{\frac{1}{2}}\|\Delta\rho\|_2 \int_0^L |u(x)u'(x)|dx \leq 2L^{\frac{1}{2}}\|\Delta\rho\|_2\, \|u\|_2\, \|u'\|_2. \tag{3.61}$$

In order to estimate $\|v_i'\|_2$, by the weak formulation of the eigenvalue problem for $\{\lambda_i(\rho_1), v_i(x;\rho_1)\}$, and recalling that $\int_0^L \rho_1 v_i^2(x;\rho_1) = 1$, we have

$$\int_0^L (v_i'(x;\rho_1))^2 \leq \frac{\lambda_i(\rho_1)}{a}, \tag{3.62}$$

for every $i \geq 1$. Then, by Schwarz inequality and (3.62), we have

$$\int_0^L (u'(x))^2 \leq \sum_{i=1}^n c_i^2 \cdot \sum_{i=1}^n \int_0^L (v_i'(x;\rho_1))^2 \leq \frac{1}{a} \cdot \sum_{i=1}^n \lambda_i(\rho_1) \cdot \sum_{i=1}^n c_i^2. \tag{3.63}$$

By the orthogonality of the eigenfunctions $v_i(x;\rho_1)$ we also have

$$\int_0^L \rho_1 u^2(x) = \int_0^L \rho_1 \left( \sum_{i=1}^n c_i v_i(x;\rho_1) \right)^2 = \sum_{i=1}^n c_i^2, \tag{3.64}$$

and (3.63) becomes

$$\int_0^L (u'(x))^2 \leq \frac{\rho^+}{a} \cdot \sum_{i=1}^n \lambda_i(\rho_1) \int_0^L u^2(x). \tag{3.65}$$

Finally, using (3.65) in (3.61), we obtain

$$|\int_0^L \Delta\rho(x) u^2(x)dx| \leq 2L^{\frac{1}{2}} \|\Delta\rho\|_2 \left( \frac{\rho^+}{a} \cdot \sum_{i=1}^n \lambda_i(\rho_1) \right)^{\frac{1}{2}} \|u\|_2^2. \tag{3.66}$$

By monotonicity results, we have $\lambda_i(\rho_1) \leq \lambda_i(\rho^-) \leq \lambda_n(\rho^-)$, for every $i = 1, \ldots, n$. It follows that estimate (3.56) can be obtained from inequality (3.55), and the proof is complete.

*Proof of estimate* (3.48).

We now consider the continuity of the $n$th eigenfunction with respect to the mass coefficient.

Let us represent the $n$th eigenfunction $v_n(x;\rho_2)$ on the Hilbertian basis of $\mathcal{H}$ formed by the eigenfunctions $\{v_k(x;\rho_1)\}_{k=1}^\infty$:

$$v_n(x;\rho_2) = \sum_{k=1}^\infty c_n^k v_k(x;\rho_1), \tag{3.67}$$

where the series is uniformly convergent in $\mathcal{H}$ up to the second order derivatives.

Coefficients $\{c_n^k\}_{k=1}^\infty$ depend on $\rho_1, \rho_2$, e.g., $c_n^k = c_n^k(\rho_1, \rho_2)$. In view of the condition $v_n'(0;\rho_1)v_n'(0;\rho_2) > 0$ assumed in Theorem 3.4.1, we require that, for $i = 1, 2$, $c_n^n(\rho_i, \rho_i) = 1$ and $c_n^k(\rho_i, \rho_i) = 0$ if $k \neq n$.

Let us notice that, by (3.67), we have

$$v_n(x;\rho_2) - v_n(x;\rho_1) = \sum_{k=1, k\neq n}^\infty c_n^k v_k(x;\rho_1) + (c_n^n - 1)v_n(x;\rho_1). \tag{3.68}$$

Therefore, in order to estimate $\|v_n(x;\rho_2) - v_n(x;\rho_1)\|_2$, we need to control the sequence $\{c_n^k\}_{k=1,k\neq n}^\infty$ and the term $|c_n^n - 1|$.

Let us recall the weak formulation of the eigenvalue problem (3.28)–(3.30) for $\{\lambda_n(\rho_2), v_n(x;\rho_2)\}$:

$$\int_0^L (bv_n''(x;\rho_2)\varphi'' + av_n'(x;\rho_2)\varphi') = \lambda_n(\rho_2) \int_0^L \rho_2 v_n(x;\rho_2)\varphi, \tag{3.69}$$

for every $\varphi \in \mathcal{H}$. By inserting (3.67) in (3.69), choosing $\varphi = v_j(x;\rho_1)$, $j \geq 1$, and using the orthogonality conditions

$$\int_0^L \rho_1 v_k(x;\rho_1) v_j(x;\rho_1) = \delta_{kj}, \quad k, j \geq 1, \tag{3.70}$$

we have

$$c_n^j(\lambda_n(\rho_2) - \lambda_j(\rho_1)) = -\lambda_n(\rho_2) \int_0^L (\rho_2 - \rho_1) v_n(x;\rho_2) v_j(x;\rho_1), \tag{3.71}$$

for every $j \geq 1$.

In order to simplify the notation, in the sequel we shall denote by $C$ a positive constant that depends on the a priori data only and $n$, and that may change from line to line.

It should be noted that if $j = n$ in (3.71), then the left and the right hand side can be made very small for $\rho_1 \approx \rho_2$, and in the limit $\rho_2 = \rho_1$ equation (3.71) degenerates into a trivial identity. Therefore, we first assume $j \neq n$ and we estimate from below the quantity $(\lambda_n(\rho_2) - \lambda_j(\rho_1))$. The case $j = n$ shall be discussed later on.

We notice that, by asymptotic eigenvalue estimates, there exists $J_0^* \in \mathbb{N}$ and there exists a positive constant $C$ such that

$$\frac{C}{2} j^4 \leq \lambda_j(\rho_1) \leq C j^4, \qquad \text{for } j > J_0^*. \tag{3.72}$$

Let us distinguish two cases.

First, let $j > J_0^*$. By (3.72), one can show that there exists a number $J_0 \in \mathbb{N}$, $J_0$ possibly bigger than $J_0^*$ and $J_0 > n$, such that

$$|\lambda_n(\rho_2) - \lambda_j(\rho_1)| \geq C j^4, \qquad \text{for } j > J_0, \tag{3.73}$$

and, therefore,

$$\left| \frac{\lambda_n(\rho_2)}{\lambda_n(\rho_2) - \lambda_j(\rho_1)} \right| \leq \frac{C}{j^4}, \qquad \text{for } j > J_0. \tag{3.74}$$

In the other case, e.g., $j \leq J_0$ and $j \neq n$, we notice that there exists $\widehat{\epsilon}$, $\widehat{\epsilon}$, $0 < \widehat{\epsilon} < 1$ only depending on the a priori data and $n$, such that the sequences $\{\lambda_n(\rho_1)\}_{n=1}^{\infty}$, $\{\lambda_n(\rho_2)\}_{n=1}^{\infty}$ are uniformly discrete with separation constant $\sigma/2$, provided that $\|\rho_i - \rho_0\|_2 \leq \epsilon$ for $0 < \epsilon \leq \widehat{\epsilon}$, $i = 1, 2$. This property follows from the fact that the sequence $\{\lambda_n\}_{n=1}^{\infty}$ is uniformly discrete (with separation constant $\sigma$) and by using the continuity of the eigenvalues with respect to small $L^2$-perturbations of the referential linear mass density $\rho_0$ (e.g., for $\widehat{\epsilon}$ small enough).

Therefore, we can estimate from below as follows:

$$|\lambda_n(\rho_2) - \lambda_j(\rho_1)| \geq \min\{|\lambda_n(\rho_2) - \lambda_{n-1}(\rho_1)|, |\lambda_n(\rho_2) - \lambda_{n+1}(\rho_1)|\}, \tag{3.75}$$

where we have assumed $\lambda_0(\rho_1) = 0$. Let us consider the first term on the right hand side, the analysis of the second being similar. Since the sequence $\{\lambda_n(\rho_2)\}_{n=1}^{\infty}$ is uniformly discrete with separation constant $\sigma/2$, using estimate (3.46), and reducing the value of $\widehat{\epsilon}$ (where $\widehat{\epsilon}$ only depends on the a priori data and $n$), we have

$$\begin{aligned} |\lambda_n(\rho_2) - \lambda_{n-1}(\rho_1)| \geq |\lambda_n(\rho_2) - \lambda_{n-1}(\rho_2)| - |\lambda_{n-1}(\rho_2) - \lambda_{n-1}(\rho_1)| \geq \\ \geq \frac{\sigma}{2} - C_{n-1}^{\lambda} \|\rho_2 - \rho_1\|_2 \geq \frac{\sigma}{4}. \end{aligned} \tag{3.76}$$

Therefore, for every $j \leq J_0$ and $j \neq n$, we have

$$\left| \frac{\lambda_n(\rho_2)}{\lambda_n(\rho_2) - \lambda_j(\rho_1)} \right| \leq C. \tag{3.77}$$

By (3.74) and (3.77), we can compute $c_n^j$ for $j \neq n$:

$$c_n^j = -\frac{\lambda_n(\rho_2)}{\lambda_n(\rho_2) - \lambda_j(\rho_1)} \int_0^L (\rho_2 - \rho_1) v_n(x;\rho_2) v_j(x;\rho_1). \tag{3.78}$$

By adapting the arguments used to prove (3.50), $v_n(x;\rho_2)$ is uniformly bounded in $[0, L]$, i.e.,

$$\max_{x \in [0,L]} |v_n(x;\rho_2)| \leq C. \tag{3.79}$$

Then, by applying Hölder inequality to (3.78) and using (3.79), we have

$$|c_n^j| \leq C \left| \frac{\lambda_n(\rho_2)}{\lambda_n(\rho_2) - \lambda_j(\rho_1)} \right| \, \|\rho_2 - \rho_1\|_2, \tag{3.80}$$

that is, by (3.74) and (3.77),

$$|c_n^j| \leq C\|\rho_2 - \rho_1\|_2, \quad j \leq J_0, \; j \neq n, \tag{3.81}$$

$$|c_n^j| \leq \frac{C}{j^4}\|\rho_2 - \rho_1\|_2, \quad j > J_0. \tag{3.82}$$

We are now in position to estimate the $L^2$ norm (squared) of the first term appearing on the right hand side of (3.68):

$$\int_0^L \Big( \sum_{k=1,k\neq n}^{\infty} c_n^k v_k(x;\rho_1) \Big)^2 \leq$$

$$\leq 2\int_0^L \Big( \sum_{k=1,k\neq n}^{J_0} c_n^k v_k(x;\rho_1) \Big)^2 + 2\int_0^L \Big( \sum_{k=J_0+1}^{\infty} c_n^k v_k(x;\rho_1) \Big)^2 \equiv 2(I_{J_0} + I_\infty). \tag{3.83}$$

Let us first consider $I_{J_0}$. By Schwarz's inequality and (3.81), we have

$$I_{J_0} \leq \int_0^L \left( \sum_{k=1,k\neq n}^{J_0} (c_n^k)^2 \right) \cdot \left( \sum_{k=1,k\neq n}^{J_0} (v_k(x;\rho_1))^2 \right) \leq C\|\rho_2 - \rho_1\|_2^2. \tag{3.84}$$

Concerning the term $I_\infty$, we use the asymptotic estimate (3.82) and Schwarz inequality, obtaining

$$I_\infty \leq \int_0^L \left( \sum_{k=J_0+1}^{\infty} c_n^k v_k(x;\rho_1) \right)^2 \leq \int_0^L \left( \sum_{k=J_0+1}^{\infty} k^2 (c_n^k)^2 \right) \cdot \left( \sum_{k=J_0+1}^{\infty} \frac{1}{k^2}(v_k(x;\rho_1))^2 \right) \leq$$

$$\leq \sum_{k=J_0+1}^{\infty} k^2 \frac{C^2\|\rho_2 - \rho_1\|_2^2}{k^8} \cdot \sum_{k=J_0+1}^{\infty} \frac{1}{k^2} \int_0^L (v_k(x;\rho_1))^2 \leq$$

$$\leq C\|\rho_2 - \rho_1\|_2^2 \sum_{k=1}^{\infty} \frac{1}{k^6} \cdot \sum_{k=1}^{\infty} \frac{1}{k^2} \leq C\|\rho_2 - \rho_1\|_2^2. \tag{3.85}$$

Inserting (3.84) and (3.85) in (3.83), we obtain

$$\| \sum_{k=1,k\neq n}^{\infty} c_n^k v_k(x;\rho_1)\|_2 \leq C\|\rho_2 - \rho_1\|_2. \tag{3.86}$$

Finally, let us evaluate $c_n^n$. Recalling the normalization conditions (3.47), and using the representation (3.67), we have

$$(c_n^n)^2 \int_0^L \rho_1 v_n^2(x;\rho_1) + \sum_{j=1,j\neq n}^{\infty} c_n^n c_n^j \int_0^L \rho_1 v_n(x;\rho_1) v_j(x;\rho_1) +$$

$$+ \sum_{k=1,k\neq n}^{\infty} c_n^n c_n^k \int_0^L \rho_1 v_n(x;\rho_1) v_k(x;\rho_1) +$$

$$+ \sum_{k,j=1,\ (k,j)\neq(n,n)}^{\infty} c_n^k c_n^j \int_0^L \rho_1 v_k(x;\rho_1) v_j(x;\rho_1) = \int_0^L \rho_1 v_n^2(x;\rho_1). \tag{3.87}$$

By the orthogonality conditions (3.70), the above equation reduces to

$$(c_n^n)^2 - 1 = - \sum_{j=1, j\neq n}^{\infty} (c_n^j)^2, \tag{3.88}$$

where the right hand side can be estimated, as before, by using (3.81) and (3.82), that is

$$(c_n^n)^2 \leq 1 + C\|\rho_2 - \rho_1\|_2^2. \tag{3.89}$$

By choosing $\widehat{\epsilon} > 0$ small enough, and recalling that $c_n^n$ is expected to belong to a neighborhood of 1 (e.g., $c_n^n(\rho_i, \rho_i) = 1$, $i = 1, 2$), the above equality implies

$$|c_n^n - 1| \leq C\|\rho_2 - \rho_1\|_2^2, \tag{3.90}$$

that is the second term in (3.68) is an higher order term with respect to $\|\rho_2 - \rho_1\|_2$, and the thesis (3.48) follows.

*Remark* 3.4.2. We conclude this Appendix by proving that, under the assumptions of Theorem 3.4.1, the eigenfunctions are continuous in the $H^2$ norm with respect to mass perturbation. To show this, let us start with the following identity, which involves the energy norm $|||\cdot|||$ of the difference $(v_n(x;\rho_1) - v_n(x;\rho_2))$:

$$\begin{aligned}|||v_n(x;\rho_2) - v_n(x;\rho_1)|||^2 &\equiv \int_0^L b(v_n''(x;\rho_2) - v_n''(x;\rho_1))^2 + a(v_n'(x;\rho_2) - v_n'(x;\rho_1))^2 = \\ &= \int_0^L b(v_n''(x;\rho_1))^2 + a(v_n'(x;\rho_1))^2 - \int_0^L (bv_n''(x;\rho_1)v_n''(x;\rho_2) + av_n'(x;\rho_1)v_n'(x;\rho_2)) + \\ &+ \int_0^L (bv_n''(x;\rho_2)(v_n''(x;\rho_2) - v_n''(x;\rho_1)) + av_n'(x;\rho_2)(v_n'(x;\rho_2) - v_n'(x;\rho_1))) \equiv I_1 + I_2 + I_3,\end{aligned} \tag{3.91}$$

for every $n \geq 1$. By the weak formulation of the eigenvalue problem (see, for example, (3.69)), we have

$$I_1 = \lambda_n(\rho_1) \int_0^L \rho_1 v_n^2(x;\rho_1), \tag{3.92}$$

$$I_2 = -\lambda_n(\rho_1) \int_0^L \rho_1 v_n(x;\rho_1) v_n(x;\rho_2), \tag{3.93}$$

$$I_3 = \lambda_n(\rho_2) \int_0^L \rho_2 v_n(x;\rho_2)(v_n(x;\rho_2) - v_n(x;\rho_1)), \tag{3.94}$$

where the functions $v_n(x;\rho_2)$ and $(v_n(x;\rho_2) - v_n(x;\rho_1))$ have been chosen as test functions to obtain (3.93) and (3.94), respectively. Therefore, by inserting (3.92)–(3.94) in (3.91), we have

$$\begin{aligned}|||v_n(x;\rho_2) - v_n(x;\rho_1)|||^2 = \lambda_n(\rho_1) \int_0^L \rho_1 v_n(x;\rho_1)(v_n(x;\rho_1) - v_n(x;\rho_2)) + \\ + \lambda_n(\rho_2) \int_0^L \rho_2 v_n(x;\rho_2)(v_n(x;\rho_2) - v_n(x;\rho_1)).\end{aligned} \tag{3.95}$$

By using Hölder inequality, the normalization conditions (3.47) and estimate (3.48), we have

$$|||v_n(x;\rho_2) - v_n(x;\rho_1)|||^2 \leq C\|v_n(x;\rho_2) - v_n(x;\rho_1)\|_2 \leq C\|\rho_1 - \rho_2\|_2, \tag{3.96}$$

where $C > 0$ is a constant only depending on the a priori data and $n$. It should be noted that, if $\rho_1 = \rho_0$ (unperturbed nanorod) and $\rho_2 = \rho_0 + r_\epsilon(x)$ (see (3.24)), for $\epsilon > 0$ small enough, then the energy norm $|||v_n(x;\rho_0) - v_n(x;\rho_0 + r_\epsilon(x))|||$ is of order $\epsilon^{1/2}$ instead of order $\epsilon$, as for the norm $\|v_n(x;\rho_0) - v_n(x;\rho_0 + r_\epsilon(x))\|_2$. Finally, using (3.48) and (3.96), one can obtain the wished $H^2$ estimate:

$$||v_n(x;\rho_2) - v_n(x;\rho_1)||^2_{H^2(0,L)} \leq C\|\rho_1 - \rho_2\|_2, \tag{3.97}$$

where the constant $C > 0$ only depends on the a priori data and $n$.

### 3.4.3 The linearized inverse problem

In this section we shall use the eigenvalue sensitivity determined in (3.49) to formulate a linearized version of the inverse problem and to find an approximate solution.

Using the explicit expression of the unperturbed eigenfunctions (3.19) in (3.49), we have

$$\delta\lambda_n \equiv 1 - \frac{\lambda_n(\rho)}{\lambda_n} = \int_0^{\frac{L}{2}} r_\epsilon(x)\Phi_n(x)dx, \tag{3.98}$$

where

$$\Phi_n(x) \equiv (v_n(x))^2 = \frac{2}{\rho_0 L}\sin^2\left(\frac{n\pi x}{L}\right), \quad n \geq 1. \tag{3.99}$$

Equation (3.98) shows that the first-order relative shift of the $n$th eigenvalue coincides with the scalar product between the unknown mass variation $r_\epsilon(x)$ and the $n$th element of the family $\{\Phi_m(x)\}_{m=1}^\infty$.

In order to determine $r_\epsilon(x)$, a natural choice is to represent $r_\epsilon(x)$ on the family $\{\Phi_m(x)\}_{m=1}^\infty$ as

$$r_\epsilon(x) = \sum_{k=1}^\infty \beta_k \Phi_k(x)\chi_{[0,\frac{L}{2}]}, \tag{3.100}$$

where the convergence of the series should be understood in the mean, that is

$$\lim_{K\to\infty}\int_0^{\frac{L}{2}}\left(r_\epsilon(x) - \sum_{k=1}^K \beta_k\Phi_k(x)\right)^2 = 0. \tag{3.101}$$

Here, $\chi_I$, $\chi_I : \mathbb{R} \to \mathbb{R}$, is the characteristic function of the closed interval $I$, $I \subset \mathbb{R}$, defined as $\chi_I(x) = 1$ if $x \in I$, $\chi_I(x) = 0$ if $x \in \mathbb{R}\setminus I$.

The coefficients $(\beta_k)_{k=1}^\infty$ play the role of Generalized Fourier Coefficients of the unknown mass variation $r_\epsilon(x)$ evaluated on the family $\{\Phi_m(x)\}_{m=1}^\infty$. It should be noted that one cannot a priori exclude that the function $r_\epsilon(x)$ defined in (3.100) may change sign in the interval $(0, L/2)$; see also the remark after condition (3.27).

It is at this point that the a priori condition (3.31) can be mathematically justified. In fact, the family $\{\Phi_m(x)\}_{m=1}^\infty$ is a basis of the square integrable functions defined on *half* span of the nanorod, that is, the closed linear subspace spanned by $\{\Phi_m(x)\}_{m=1}^\infty$ is $L^2\left(0, \frac{L}{2}\right)$. To prove this property, we notice that the functions $\{\Phi_m(x)\}_{m=1}^\infty$ are *linearly independent* and form a *complete family* in $L^2\left(0, \frac{L}{2}\right)$. This last property is satisfied if, for any $r_\epsilon(x) \in L^2\left(0, \frac{L}{2}\right)$, the conditions $\int_0^{\frac{L}{2}} r_\epsilon(x)\Phi_m(x)dx = 0$ for every $n \geq 1$ imply $r_\epsilon(x) = 0$ in $\left(0, \frac{L}{2}\right)$. The above conditions can be rewritten as

$$0 = \int_0^{\frac{L}{2}} r_\epsilon(x)dx - \int_0^{\frac{L}{2}} r_\epsilon(x)\cos\left(\frac{2m\pi x}{L}\right)dx, \tag{3.102}$$

for every $m \geq 1$. Taking the limit in (3.102) as $m \to \infty$ and using the Riemann-Lebesgue Lemma (see, for instance, [78]), we have $\int_0^{\frac{L}{2}} r_\epsilon(x)dx = 0$ and, then, $\int_0^{\frac{L}{2}} r_\epsilon(x)\cos\left(\frac{2m\pi x}{L}\right)dx = 0$ for every

$m \geq 1$. Since the family $\{\cos\left(\frac{2m\pi x}{L}\right)\}_{m=1}^{\infty}$ is a basis for the set of functions belonging to $L^2\left(0, \frac{L}{2}\right)$ and having zero-mean, we have $r_\epsilon(x) = 0$ in $\left(0, \frac{L}{2}\right)$, and the thesis is proved.

Replacing (3.100) in (3.98), we obtain the infinite linear system

$$\delta\lambda_n = \sum_{k=1}^{\infty} A_{nk}\beta_k, \quad n = 1, 2, ..., \tag{3.103}$$

where

$$A_{nk} = \int_0^{\frac{L}{2}} \Phi_n(x)\Phi_k(x)dx = \frac{4}{(\rho_0 L)^2}\int_0^{\frac{L}{2}} \sin^2\left(\frac{n\pi x}{L}\right)\sin^2\left(\frac{k\pi x}{L}\right)dx, \tag{3.104}$$

$n, k = 1, 2....$ The coefficients $A_{nk}$ can be evaluated in closed form, and we have

$$A_{nk} = \frac{2}{4\rho_0^2 L} \quad \text{for } k \neq n, \quad A_{nn} = \frac{3}{4\rho_0^2 L}. \tag{3.105}$$

In real applications only a finite number of eigenvalues is available, typically the first $10 - 20$. This leads us to consider the $N$th finite dimensional approximation of the added mass, $(\beta_k^N)_{k=1}^N$ of (3.103), that is the $N \times N$ linear system

$$\delta\lambda_n = \sum_{k=1}^{N} A_{nk}\beta_k^N, \quad n = 1, ..., N. \tag{3.106}$$

A direct calculation shows that

$$\det(A_{nk}) = (2N+1)\left(\frac{1}{4\rho_0^2 L}\right)^N, \tag{3.107}$$

$$(A_{nk})^{-1} = (4\rho_0^2 L)\frac{2N-1}{2N+1} \text{ if } n = k, \quad (A_{nk})^{-1} = -(4\rho_0^2 L)\frac{2}{2N+1} \text{ if } n \neq k, \tag{3.108}$$

$n, k = 1, ..., M$. Therefore, the system (3.106) has the closed-form solution

$$\beta_k^N = 4\rho_0^2 L\left(\frac{2N-1}{2N+1}\delta\lambda_k - \frac{2}{2N+1}\sum_{j=1,\ j\neq k}^{N}\delta\lambda_j\right), \quad k = 1, ..., N, \tag{3.109}$$

and, finally,

$$r_\epsilon(x) = 8\rho_0\sum_{k=1}^{N}\left(\frac{2N-1}{2N+1}\delta\lambda_k - \frac{2}{2N+1}\sum_{j=1,\ j\neq k}^{N}\delta\lambda_j\right)\sin^2\left(\frac{k\pi x}{L}\right)\cdot\chi_{[0,\frac{L}{2}]}. \tag{3.110}$$

### 3.4.4 The reconstruction procedure

The estimation of $r_\epsilon$ given in (3.110) can be improved by iterating the identification procedure illustrated in the previous section. In order to simplify the notation, here the index $\epsilon$ has been omitted and $\lambda_n^{exp}$ denotes the measured value of the $n$th eigenvalue $\lambda_n(\rho)$ of the perturbed nanorod. Moreover, we shall write $\beta$ instead of $\beta^N$. The main steps of the reconstruction procedure and the corresponding numerical algorithm are illustrated in the sequel.

Let $\rho^{(0)}(x) = \rho_0$ be the mass per unit length of the referential nanorod. The unknown mass per unit length is determined on the interval $\left[0, \frac{L}{2}\right]$ by the iteration

$$\rho^{(j+1)}(x) = \rho^{(j)}(x) + r^{(j)}(x), \quad j \geq 0, \tag{3.111}$$

where the increment

$$r^{(j)}(x) = \sum_{k=1}^{N} \beta_k^{(j)} \Phi_k^{(j)}(x) \chi_{\left[0,\frac{L}{2}\right]} = \beta^{(j)} \cdot \Phi^{(j)}(x) \chi_{\left[0,\frac{L}{2}\right]} \tag{3.112}$$

is determined by solving the $N \times N$ linear system

$$\delta\lambda_n^{(j)} \equiv 1 - \frac{\lambda_n^{exp}}{\lambda_n(\rho^{(j)})} = \sum_{k=1}^{N} A_{nk}^{(j)} \beta_k^{(j)}, \tag{3.113}$$

$n = 1, ..., N$, or, equivalently, in compact form

$$\mathbf{A}^{(j)} \beta^{(j)} = \delta\lambda^{(j)}, \tag{3.114}$$

with $\beta^{(j)} = (\beta_1^{(j)}, \dots, \beta_N^{(j)})$. Here, $\{\lambda_n(\rho^{(j)}), v_n(x; \rho^{(j)})\}$ is the $n$th (mass normalized) eigenpair of the problem

$$\begin{cases} bv^{IV} - av'' = \lambda \rho^{(j)} v, \quad x \in (0, L), & (3.115) \\ v(0) = 0, \ v''(0) = 0, & (3.116) \\ v(L) = 0, \ v''(L) = 0. & (3.117) \end{cases}$$

Moreover, $\Phi_k^{(j)}(x) = v_k^2(x; \rho^{(j)})$ and the matrix $(A_{nk}^{(j)})$ is given by

$$A_{nk}^{(j)} = \int_0^{\frac{L}{2}} \Phi_n^{(j)}(x) \Phi_k^{(j)}(x) dx, \quad n, k = 1, ..., N. \tag{3.118}$$

Assuming the existence of $(\mathbf{A}^{(j)})^{-1}$ (see Section 3.5, Step i)), we have

$$r^{(j)}(x) = (\mathbf{A}^{(j)})^{-1} \delta\lambda^{(j)} \cdot \Phi^{(j)}(x) \chi_{\left[0,\frac{L}{2}\right]} \tag{3.119}$$

and, from (3.111), we have

$$\rho^{(j)}(x) = \rho_0 + \sum_{i=0}^{j-1} r^{(i)}(x), \quad j \geq 1. \tag{3.120}$$

In our application, the iterations go on until the updated mass coefficient satisfies the criterion

$$e \equiv \frac{1}{N} \left( \sum_{n=1}^{N} \left( \frac{\lambda_n^{exp} - \lambda_n(\rho^{(j+1)})}{\lambda_n^{exp}} \right)^2 \right)^{\frac{1}{2}} < \gamma, \tag{3.121}$$

for a small given number $\gamma$.

## 3.5 Convergence of the identification method

In this section we study the convergence of the iterative method shown in Section 3.4.4. We prove that, under suitable assumptions, there exists $\overline{\rho}(x) \in C^0\left(0, \frac{L}{2}\right)$ such that

$$\overline{\rho}(x) = \lim_{j \to \infty} \rho^{(j)}(x) = \rho_0 + \sum_{i=0}^{\infty} r^{(i)}(x), \tag{3.122}$$

where the series is uniformly convergent in $\left(0, \frac{L}{2}\right)$.

The proof is based on two main steps:
*Step i)* Existence of the inverse $(\mathbf{A}^{(j)})^{-1}$ and bound of $\|(\mathbf{A}^{(j)})^{-1}\|$ for every $j \geq 1$;
*Step ii)* Bound of $|\delta\lambda^{(j)}|$ to control $\|r^{(i)}\|_2$ for every $j \geq 1$.

In the sequel, we shall denote by $C$ positive constants which may change from line to line. Moreover, for every $N \times N$ matrix $\mathbf{B} \in \mathbb{R}^{N\times N}$, we denote by $\|\mathbf{B}\| = \left(\sum_{i,j=1}^{N}(B_{ij})^2\right)^{\frac{1}{2}}$ the Frobenius norm.

*Step i).* Let us consider the set of coefficients $\rho(x)$ given in (3.23), e.g., $\rho(x) = \rho_0 + r_\epsilon(x)$ in $[0, L]$, where $r_\epsilon$ satisfies conditions (3.23)–(3.26) and where $\epsilon > 0$ is a number small enough. We denote by $\mathbf{A}(\rho)$ the matrix defined in (3.118) corresponding to the coefficient $\rho(x)$.

We prove that there exists $\widehat{\epsilon}_\rho$, $0 < \widehat{\epsilon}_\rho < 1$, only depending on the a priori data $\mathcal{A}$ and $N$, such that, for every $\epsilon < \widehat{\epsilon}_\rho$, there exists $(\mathbf{A}(\rho))^{-1}$ and we have

$$\|(\mathbf{A}(\rho))^{-1}\| \leq C, \tag{3.123}$$

where $C > 0$ is a constant only depending on the a priori data $\mathcal{A}$ and $N$.

To prove (3.123), we shall write

$$\mathbf{A}(\rho) = \mathbf{A}(\rho_0) - \mathbf{P}, \tag{3.124}$$

where the inverse of $\mathbf{A}(\rho_0)$ is given explicitly in (3.108), and $\mathbf{P} = \mathbf{P}(\rho)$ is a perturbation due to the change of mass $r_\epsilon(x)$. Denoting $\Delta v_k(x) = v_k(x;\rho) - v_k(x;\rho_0) \equiv v_k(x;\rho) - v_k(x)$, for every $n, k = 1, \dots N$, by (3.118) we have

$$\begin{aligned}-P_{nk} =& 2\int_0^{\frac{L}{2}} \left(v_k v_n^2 \Delta v_k + v_n v_k^2 \Delta v_n\right) + \int_0^{\frac{L}{2}} \left(v_n^2(\Delta v_k)^2 + v_k^2(\Delta v_n)^2 + 4 v_n v_k \Delta v_n \Delta v_k\right) + \\ &+ 2\int_0^{\frac{L}{2}} \left(v_n \Delta v_n (\Delta v_k)^2 + v_k \Delta v_k (\Delta v_n)^2\right) + \int_0^{\frac{L}{2}} (\Delta v_n)^2 (\Delta v_k)^2.\end{aligned} \tag{3.125}$$

In order to simplify the analysis, we shall control the $L^\infty$ norm of all the quantities inside the integrals in (3.125). The norm $\|v_k\|_\infty$ (even in the whole interval $(0, L)$) can be bound via inequality (3.50), which holds for unperturbed eigenfunctions with a constant $C > 0$ only depending on the a priori data $\mathcal{A}$. In order to bound $\|\Delta v_k\|_\infty$, we use the Rellich-Kondrachov's Theorem (see [15], Theorem $IX.26$) and estimate (3.97): for every $k \geq 1$ we have

$$\|\Delta v_k\|_{L^\infty(0,L)} \leq C\|\Delta v_k\|_{H^2(0,L)} \leq C\|\rho - \rho_0\|_{L^2(0,L)}^{\frac{1}{2}} \leq C\epsilon^{\frac{1}{2}}, \tag{3.126}$$

for every $\epsilon \leq \widehat{\epsilon}(< 1)$, where $\widehat{\epsilon}$ has been introduced in Theorem 3.4.1, and $C > 0$ is a constant only depending on the a priori data $\mathcal{A}$ and $k$. Therefore, for every $n, k = 1, \dots, N$ and for every $\epsilon$ such that $\epsilon \leq \widehat{\epsilon}$, we have

$$|P_{nk}| \leq C(\epsilon^{\frac{1}{2}} + \epsilon + \epsilon^{\frac{3}{2}} + \epsilon^2) \leq C\epsilon^{\frac{1}{2}} \tag{3.127}$$

and

$$\|\mathbf{P}\| \leq C_P \epsilon^{\frac{1}{2}}, \tag{3.128}$$

where $C_P > 0$ is a constant only depending on the a priori data $\mathcal{A}$ and $N$.

Let us introduce the number

$$\widehat{\epsilon}_\rho = \min\left\{\widehat{\epsilon}, \left(\frac{1}{2C_P\|(\mathbf{A}(\rho_0))^{-1}\|}\right)^2\right\}. \tag{3.129}$$

Note that, possibly increasing $C_P$, the number $\left(\frac{1}{2C_P\|(\mathbf{A}(\rho_0))^{-1}\|}\right)^2$ is less than $1$. We now prove that if **P** satisfies (3.128) for every $\epsilon \leq \widehat{\epsilon}_\rho$, then $\mathbf{A}(\rho)$ is nonsingular, and

$$\|(\mathbf{A}(\rho))^{-1}\| \leq \frac{\|(\mathbf{A}(\rho_0))^{-1}\| \cdot \|\mathbf{I}\|}{1 - \|(\mathbf{A}(\rho_0))^{-1}\| \cdot \|\mathbf{P}\|}, \tag{3.130}$$

where **I** is the identity matrix in $\mathbb{R}^{N\times N}$. Let $\mathbf{x} \in \mathbb{R}^N \setminus \{\mathbf{0}\}$. Then, since $\mathbf{A}(\rho_0)$ is nonsingular, it is enough to prove that $(\mathbf{I} - (\mathbf{A}(\rho_0))^{-1}\mathbf{P})\mathbf{x} \neq \mathbf{0}$ for every $\mathbf{x} \in \mathbb{R}^N \setminus \{\mathbf{0}\}$. We have

$$\|(\mathbf{I} - (\mathbf{A}(\rho_0))^{-1}\mathbf{P})\mathbf{x}\| \geq (1 - \|(\mathbf{A}(\rho_0))^{-1}\| \cdot \|\mathbf{P}\|)\|\mathbf{x}\| > 0, \tag{3.131}$$

since, by (3.128) and (3.129), for every $\epsilon$, $0 < \epsilon \leq \widehat{\epsilon}_\rho$,

$$1 - \|(\mathbf{A}(\rho_0))^{-1}\| \cdot \|\mathbf{P}\| \geq 1 - \|(\mathbf{A}(\rho_0))^{-1}\| C_P \epsilon^{\frac{1}{2}} \geq \frac{1}{2} > 0. \tag{3.132}$$

Hence, if $\mathbf{x} \neq \mathbf{0}$, $(\mathbf{I} - (\mathbf{A}(\rho_0))^{-1}\mathbf{P})\mathbf{x} \neq \mathbf{0}$ or, equivalently, $(\mathbf{A}(\rho_0) - \mathbf{P})\mathbf{x} \neq \mathbf{0}$ and $\mathbf{A}(\rho) = \mathbf{A}(\rho_0) - \mathbf{P}$ is nonsingular.

Now, from the identity $(\mathbf{A}(\rho_0) - \mathbf{P})(\mathbf{A}(\rho_0) - \mathbf{P})^{-1} = \mathbf{I}$, it follows that

$$(\mathbf{I} - (\mathbf{A}(\rho_0))^{-1}\mathbf{P})^{-1} = \mathbf{I} + (\mathbf{A}(\rho_0))^{-1}\mathbf{P}(\mathbf{I} - (\mathbf{A}(\rho_0))^{-1}\mathbf{P})^{-1} \tag{3.133}$$

and, then,

$$\|(\mathbf{I} - (\mathbf{A}(\rho_0))^{-1}\mathbf{P})^{-1}\| \leq \frac{\|\mathbf{I}\|}{1 - \|(\mathbf{A}(\rho_0))^{-1}\| \cdot \|\mathbf{P}\|}. \tag{3.134}$$

Inequalities (3.134) and (3.130) are equivalent, and imply (3.123).

*Step ii).* In order to control $|\delta\lambda^{(i)}|$, we follow the steps of the iterative procedure shown in Section 3.4.4.

At step $\sharp 1$, we use the fundamental identity (3.44) between the unperturbed 0th state (corresponding to $\rho^{(0)}(x) = \rho_0$) and the state to be identified (corresponding to the unknown mass coefficient, say $\overline{\rho}(x)$, and target eigenvalues $\{\lambda_n^{exp}\}$, $n = 1, \dots, N$):

$$\lambda_n^{exp} = \lambda_n(\rho^{(0)}) - \lambda_n(\rho^{(0)})\langle \Delta M^{(0)} v_n(\rho^{(0)}), v_n(\rho^{(0)})\rangle + \widetilde{O}_n(\text{EXP-(0)}), \tag{3.135}$$

$n = 1, \dots, N$, where $\Delta M^{(0)} = \overline{\rho}(x) - \rho^{(0)}(x)$ and the higher order term $\widetilde{O}_n(\text{EXP-(0)})$ depends on the initial state $\rho^{(0)}$ and on the variations $\Delta M^{(0)}$, $\Delta\lambda_n^{(0)} = \lambda_n^{exp} - \lambda_n(\rho^{(0)})$, $\Delta v_n(x) = v_n(x;\overline{\rho}) - v_n(x;\rho^{(0)})$. The mass coefficient $\rho^{(0)}$ is updated at step $\sharp 1$ as

$$\rho^{(1)}(x) = \rho^{(0)}(x) + r^{(0)}(x), \tag{3.136}$$

where $r^{(0)}(x)$ (given in (3.112) for $j = 0$) is determined by neglecting the term $\widetilde{O}_n(\text{EXP-(0)})$ in (3.135), e.g., for every $n = 1, \dots, N$,

$$\lambda_n^{exp} - \lambda_n(\rho^{(0)}) = -\lambda_n(\rho^{(0)})\langle r^{(0)} v_n(\rho^{(0)}), v_n(\rho^{(0)})\rangle. \tag{3.137}$$

By using the updated value of the mass coefficient $\rho^{(1)}(x)$, we now estimate $\lambda_n(\rho^{(1)})$, $n = 1, \dots, N$. By applying the fundamental identity (3.44) between the states $\rho^{(0)}(x)$ and $\rho^{(1)}(x)$, we have

$$\lambda_n(\rho^{(1)}) - \lambda_n(\rho^{(0)}) = -\lambda_n(\rho^{(0)})\langle r^{(0)} v_n(\rho^{(0)}), v_n(\rho^{(0)})\rangle + \widetilde{O}_n(\text{(1)-(0)}). \tag{3.138}$$

The first term on the right hand side of (3.138) can be determined by (3.137), namely

$$\lambda_n(\rho^{(1)}) - \lambda_n(\rho^{(0)}) = \lambda_n^{exp} - \lambda_n(\rho^{(0)}) + \widetilde{O}_n(\text{(1)-(0)}), \tag{3.139}$$

that is

$$\lambda_n(\rho^{(1)}) - \lambda_n^{exp} = \widetilde{O}_n((1)\text{-}(0)), \quad n = 1, \dots, N. \tag{3.140}$$

Similarly, at step $\sharp 2$, the mass coefficient is updated as

$$\rho^{(2)}(x) = \rho^{(1)}(x) + r^{(1)}(x), \tag{3.141}$$

where $r^{(1)}(x)$ satisfies

$$\lambda_n^{exp} - \lambda_n(\rho^{(1)}) = -\lambda_n(\rho^{(1)})\langle r^{(1)} v_n(\rho^{(1)}), v_n(\rho^{(1)})\rangle, \tag{3.142}$$

$n = 1, \dots, N$. The identity (3.44) between the states $\rho^{(1)}(x)$ and $\rho^{(2)}(x)$ reads as

$$\lambda_n(\rho^{(2)}) - \lambda_n(\rho^{(1)}) = -\lambda_n(\rho^{(1)})\langle r^{(1)} v_n(\rho^{(1)}), v_n(\rho^{(1)})\rangle + \widetilde{O}_n((2)\text{-}(1)), \tag{3.143}$$

and, by (3.142) and (3.143), we obtain

$$\lambda_n(\rho^{(2)}) - \lambda_n^{exp} = \widetilde{O}_n((2)\text{-}(1)), \quad n = 1, \dots, N. \tag{3.144}$$

By iteration, at step $\sharp(i+1)$ we have

$$\lambda_n(\rho^{(i+1)}) - \lambda_n^{exp} = \widetilde{O}_n((i+1) - (i)), \quad n = 1, \dots, N. \tag{3.145}$$

At this point we need to bound the high order term $\widetilde{O}_n((i+1) - (i))$ appearing in (3.145).

Let us first estimate $\widetilde{O}_n((1)\text{-}(0))$. By (3.44) (written between the unperturbed state $\rho^{(0)}$ and the first updated state $\rho^{(1)}$) we have

$$\begin{aligned} |\widetilde{O}_n((1) - (0))| \leq \lambda_n |\langle \Delta M(\Delta v_n), v_n\rangle| + |\Delta\lambda_n| \cdot |\langle M(\Delta v_n), v_n\rangle| + \\ + |\Delta\lambda_n| \cdot |\langle \Delta M(v_n), v_n\rangle| + |\Delta\lambda_n| \cdot |\langle \Delta M(\Delta v_n), v_n\rangle| \equiv A_n + B_n + C_n + D_n. \end{aligned} \tag{3.146}$$

Let us consider the term $A_n$. By using Hölder inequality, we have

$$\begin{aligned} A_n \leq & \lambda_n ||v_n||_\infty \int_0^L |\Delta M(x)| \cdot |v_n(x; \rho^{(1)}) - v_n(x; \rho^{(0)})| dx \leq \\ \leq & \lambda_n ||v_n||_\infty ||\Delta M||_2 \cdot ||v_n(x; \rho^{(1)}) - v_n(x)||_2. \end{aligned} \tag{3.147}$$

Recalling that $\Delta M = r^{(0)}(x) = \sum_{k=1}^N \beta_k^{(0)} \Phi_k(x; \rho^{(0)}) \chi_{[0, \frac{L}{2}]}$, with $\Phi_k(x; \rho^{(0)}) = v_k^2(x; \rho^{(0)})$, and noticing that $||v_n||_\infty$ can be estimated via (3.50), we have

$$||\Delta M||_2 \leq \frac{L^{\frac{3}{2}}}{a} \Lambda |\beta^{(0)}|, \tag{3.148}$$

where the quantity

$$\Lambda^{(0)} = \left( \sum_{k=1}^N \lambda_k^2 \right)^{\frac{1}{2}} \tag{3.149}$$

can be calculated in terms of the unperturbed nanorod and, therefore, it depends on the a priori data set $\mathcal{A}$ only. By using (3.50), (3.148) and (3.48) in (3.147), we have

$$A_n \leq (\lambda_n)^{\frac{3}{2}} L \left( \frac{L}{a} \right)^{\frac{5}{2}} (\Lambda^{(0)})^2 C_n^v |\beta^{(0)}|^2. \tag{3.150}$$

The other terms in (3.146) can be evaluated similarly, namely

$$B_n \leq \rho_0^{\frac{1}{2}} L \left(\frac{L}{a}\right)^2 (\Lambda^{(0)})^2 C_n^\lambda C_n^v |\beta^{(0)}|^2, \tag{3.151}$$

$$C_n \leq \lambda_n L^{\frac{3}{2}} \left(\frac{L}{a}\right)^3 (\Lambda^{(0)})^2 C_n^\lambda |\beta^{(0)}|^2, \tag{3.152}$$

$$D_n \leq (\lambda_n)^{\frac{1}{2}} L^{\frac{3}{2}} \left(\frac{L}{a}\right)^{\frac{7}{2}} (\Lambda^{(0)})^3 C_n^\lambda C_n^v |\beta^{(0)}|^3. \tag{3.153}$$

Therefore, collecting the estimates (3.150)–(3.153), we have

$$|\widetilde{O}_n((1)\text{-}(0))| \leq C|\beta^{(0)}|^2(1 + C|\beta^{(0)}|), \tag{3.154}$$

where $C > 0$ is a constant only depending on the a priori data $\mathcal{A}$ and $n$, $n = 1, \dots, N$. By using (3.123) in (3.114) (for $j = 0$), we have

$$|\beta^{(0)}| \leq C|\delta\lambda^{(0)}|, \tag{3.155}$$

and (3.154) becomes

$$|\widetilde{O}_n((1)\text{-}(0))| \leq C|\delta\lambda^{(0)}|^2(1 + C|\delta\lambda^{(0)}|) \leq C|\delta\lambda^{(0)}|^2, \tag{3.156}$$

provided that $|\delta\lambda^{(0)}| \leq 1$, where $C > 0$ is a constant only depending on the a priori data $\mathcal{A}$ and $n$. Therefore, using (3.156) in (3.140), for every $n = 1, \dots, N$, we have

$$|\lambda_n(\rho^{(1)}) - \lambda_n^{exp}| \leq C|\delta\lambda^{(0)}|^2, \tag{3.157}$$

for $|\delta\lambda^{(0)}| \leq 1$, where $C > 0$ is a constant only depending on the a priori data $\mathcal{A}$ and $n$.

We proceed similarly in estimating $\widetilde{O}_n((2)\text{-}(1))$. By adapting the previous analysis to the states $\rho^{(2)}$ and $\rho^{(1)}$, we obtain

$$|\widetilde{O}_n((2)\text{-}(1))| \leq C|\beta^{(1)}|^2(1 + C|\beta^{(1)}|), \tag{3.158}$$

and, recalling (3.123) and (3.114),

$$|\widetilde{O}_n((2)\text{-}(1))| \leq C|\delta\lambda^{(1)}|^2, \tag{3.159}$$

that is, by (3.144),

$$|\lambda_n(\rho^{(2)}) - \lambda_n^{exp}| \leq C|\delta\lambda^{(1)}|^2, \tag{3.160}$$

for $|\delta\lambda^{(1)}| \leq 1$, where $C > 0$ is a constant only depending on the a priori data $\mathcal{A}$ and $n$. Using (3.157) in (3.160) (and noticing that $\lambda_n(\rho^{(1)})$ can be estimated from below by a positive quantity only depending on the a priori data $\mathcal{A}$ and $n$), we have

$$|\lambda_n(\rho^{(2)}) - \lambda_n^{exp}| \leq C|\delta\lambda^{(0)}|^{2\cdot 2}. \tag{3.161}$$

By iteration, for every $i \geq 1$ and $n = 1, \dots, N$, we obtain

$$|\lambda_n(\rho^{(i)}) - \lambda_n^{exp}| \leq C|\delta\lambda^{(0)}|^{2^i}, \tag{3.162}$$

where $C > 0$ is a constant only depending on the a priori data $\mathcal{A}$ and $n$, and $|\delta\lambda^{(0)}| \leq 1$.

*Conclusion of the proof.* By using the estimates (3.123) and (3.162), the series $\sum_{i=0}^{\infty} r^{(i)}(x)$ in (3.122) is $L^2$-uniformly convergent to a continuous function in $\left[0, \frac{L}{2}\right]$, since the $i$th term can be bounded as

$$\|r^{(i)}(x)\|_{L^2\left[0,\frac{L}{2}\right]} \leq C|\delta\lambda^{(0)}|^{2^i}, \quad i \geq 0, \tag{3.163}$$

where $C > 0$ is a constant only depending on the a priori data $\mathcal{A}$, and the numerical series $\sum_{i=0}^{\infty} |\delta\lambda^{(0)}|^{2^i}$ is convergent provided that $|\delta\lambda^{(0)}| \leq \widehat{\epsilon}_\lambda < 1$ (Weierstrass's criterion).

Summarizing, in this section we have proved the following result:

*If* $\epsilon \leq \widehat{\epsilon}_\rho$, *where* $\widehat{\epsilon}_\rho$ *is given in* (3.129), *and* $|\delta\lambda^{(0)}| \leq \widehat{\epsilon}_\lambda < 1$, *then the iterative procedure of identification converges uniformly to a continuous function in* $\left[0, \frac{L}{2}\right]$.

Our convergence result has local character, since the proof is built on the assumption that the mass variation is a small perturbation of the total mass of the unperturbed nanorod. It would be interesting, and also useful for practical applications, to determine or, at least, to find good approximation of the maximum value allowed for $\widehat{\epsilon}_\rho$. Moreover, the local character is also reflected on the condition $\widehat{\epsilon}_\lambda < 1$, which means that the first $N$ eigenvalues of the unperturbed nanorod must be close enough to the corresponding target eigenvalues.

## 3.6 Applications

### 3.6.1 Specimen

In order to illustrate the application of the identification method, reference is made to the geometrical and material properties of the nanorod used in [49]. In particular, the radius $r$ of the circular equivalent cross-section is equal to 50 $\mu$m ($= 50 \cdot 10^{-6}$ m) and the length $L$ is taken equal to $40r$; the material length scale parameters are assumed to be equal, and $\ell_0 = \ell_1 = \ell_2 = \ell = 17.6$ $\mu$m; the Young's modulus $E$ is equal to 1.44 GPa; the Poisson's coefficient is $\nu = 0.38$; and the volume mass density is equal to $\rho_{vol} = 1000$ kg/m$^3$. The coefficients $a$, $b$, $\rho_0$ corresponding to the above parameters take the value $a = 11.310$ N, $b = 3.554 \cdot 10^{-9}$ Nm$^2$, $\rho_0 = \rho_{vol} \cdot \pi r^2 = 7.854 \cdot 10^{-6}$ kg/m, respectively.

### 3.6.2 Discrete eigenvalue problem

The practical application of the mass identification method requires the development of a specific numerical code. The weak formulation of the eigenvalue problem (3.28)–(3.30) consists in determining a non-trivial function $v \in \mathcal{H}$ (see definition (3.37)), and a positive real number $\lambda$ such that

$$\int_0^L (bv''\varphi'' + av'\varphi') = \lambda \int_0^L \rho v \varphi, \tag{3.164}$$

for every $\varphi \in \mathcal{H}$. To find a finite element model of the weak formulation (3.164), we work on the finite-dimensional subspace of $\mathcal{H}$ formed by three-degree polynomial spline approximation of the axial displacement of the nanorod in each element. More precisely, let $\{x_0 = 0 < x_1 < x_2 < ... < x_{N_e} = L\}$ be the nodes of a mesh of the interval $[0, L]$, with $x_{i+1} - x_i = \Delta x = \frac{L}{N_e}$, for every $i = 0, 1, ..., N_e$. Therefore, the discrete version of (3.164) consists in finding the approximating eigenpair $(\widetilde{\lambda}, \widetilde{\mathbf{v}})$, $\widetilde{\mathbf{v}} \in \mathbb{R}^{2N_e} \setminus \{\mathbf{0}\}$, solution to

$$\widetilde{\mathbf{F}}\widetilde{\mathbf{v}} = \widetilde{\lambda}\widetilde{\mathbf{M}}\widetilde{\mathbf{v}}, \tag{3.165}$$

where $\widetilde{\mathbf{F}}$, $\widetilde{\mathbf{M}}$ is the $2N_e \times 2N_e$ real symmetric matrix of the stiffness and of the inertia of the nanorod, respectively.

The mass coefficient $\rho = \rho(x)$ is approximated by a continuous piecewise-linear function, that is, $\widetilde{\rho}(x) = \rho(x_i) + \{(\rho(x_{i+1}) - \rho(x_i))/(\Delta x)\}x$ for $x \in [x_i, x_{i+1}]$. Therefore, the $(n, k)$ entry of the local mass, $(\widetilde{M}_i^{nk})$, and stiffness, $(\widetilde{F}_i^{nk})$, matrix are given by

$$\widetilde{M}_i^{nk} = \int_{x_i}^{x_{i+1}} \widetilde{\rho}(x)\varphi_n(x)\varphi_k(x)dx, \quad \widetilde{F}_i^{nk} = \int_{x_i}^{x_{i+1}} (b\varphi_n''(x)\varphi_k''(x) + a\varphi_n'(x)\varphi_k'(x))dx, \tag{3.166}$$

$n, k = 1, \ldots, 4$, and are evaluated in exact form. Numerical integration of the quantities (3.118) was developed by means of a standard trapezoidal method. The discrete eigenvalue problem (3.165) was solved by using the Implicit Restarted Lanczos's method [16]. The identification procedure was built in Scilab environment (version $5.5.2$) by developing a specific numerical code. Regarding the computational burden, the time needed to complete a single iteration of the identification algorithm (for $N_e = 200$) was about $1$ second.

### 3.6.3 Results

In this section we present a selection of the results obtained in an extended series of applications of the Generalized Fourier Coefficient Method. Among other parameters, the procedure has been tested with respect to the number $N$ of the first eigenfrequencies used and to the geometry of the mass variation (e.g., position, intensity, regularity). In particular, the efficiency of the method has been evaluated on two main classes of mass variations corresponding to *smooth* (Section 3.6.3.1) or *discontinuous* (Section 3.6.3.2) function $r_\epsilon$. In both cases, the support of the mass variation coincides with an interval contained in $\left(0, \frac{L}{2}\right)$. We have first considered free-error data, i.e., the measurement errors are null with the exception of the errors induced by the numerical approximation via the finite element method. The analysis of *overlapping* mass variations, possibly having disconnected support, is also considered in Section 3.6.3.3. The application of suitable physical filtering to improve the accuracy of identification. The stability of the reconstruction in presence of noise are investigated in Section 3.6.3.5.

#### 3.6.3.1 Identification of smooth mass densities

In this series of simulations, the mass density of the perturbed nanorod is defined as

$$\rho(x) = \rho_0 + \rho_0 t \cos^2\left(\frac{\pi(x-s)}{c}\right)\chi_{[s-\frac{c}{2}, s+\frac{c}{2}]}, \tag{3.167}$$

where $s$ is the central point of the support of the mass variation, $c$ is the length of the support, $\rho_0 t$ is the maximum amplitude of variation, see Figure 3.1(a). Note that $\rho \in C^1[0, L]$.

The definition (3.167) allows to consider a wide family of coefficients, including either localized or diffuse mass variations. In the sequel, reference is made mainly to positions $\frac{s}{L} = 0.15,\ 0.25,\ 0.35$, extensions $\frac{c}{L} = 0.10,\ 0.20,\ 0.30$, and intensities $t = 0.10,\ 0.20,\ 0.50,\ 1.00$, for all the possible combinations of the parameters. Therefore, the global mass change ranges from $0.5$ percent to $15$ percent of the initial mass $\rho_0 L$, for ($\frac{c}{L} = 0.10,\ t = 0.10$) and ($\frac{c}{L} = 0.30,\ t = 1.0$), respectively.

In order to select a suitable mesh for the numerical solution of the eigenvalue problem, preliminary tests have been carried out on the uniform nanorod, for which analytical closed form expressions of the eigenpairs are available. The analysis suggests to assume a mesh with $N_e = 200$ equally spaced finite elements, which turns out to be a good compromise between accuracy (maximum error on the first $15$ eigenvalues less than $10^{-4}$ percent) and computational cost for all the cases studied, including the reconstruction procedure, see Table 3.1. Moreover, this set of preliminary tests suggests to choose $\gamma = 10^{-5}$ in the stopping criterion (3.121).

Regarding the influence of the number $N$ of eigenvalue data, here we will focus on the most two challenging cases. The first one ($\frac{s}{L} = 0.35$, $\frac{c}{L} = 0.1$, $t = 0.1$), see Figure 3.2, corresponds to small mass increase located in a small interval, which allows to assess the sensitivity of the method to the identification of the mass perturbation just as it occurs in the nanorod. The second case ($\frac{s}{L} = 0.35$, $\frac{c}{L} = 0.1$, $t = 1$, see Figure 3.3) deals with mass variation having the same support as before, but with an abrupt increase of mass with large $L^\infty$ amplitude. The first case is challenging since it involves a small mass perturbation and, therefore, it is an important test for evaluating the sensitivity of the identification method. The second case involves a sharp change in the coefficient, which reasonably requires a higher number of Fourier coefficients (and, therefore, eigenfrequency data) to be accurately reconstructed.

The analysis of Figure 3.2 shows that the identified coefficient agrees well with the exact one, and accuracy of reconstruction rapidly improves as $N$ increases. Similar properties can be deduced from the analysis of Figure 3.3, apart from the oscillatory character of the reconstructed coefficient, which is now more evident for $N = 6, 9$, whereas it becomes almost negligible when $N = 15$.

For the sake of completeness, it should be noted that part of our results involve not necessarily small mass variations, see, for example, Figure 3.4. This would suggest that the proposed reconstruction method has some unexpected potential, in spite of the fact that the proof of convergence presented in Section 3.5 requires to work in a sufficiently small neighborhood of the referential nanorod.

Finally, some synthetic numerical information concerning the sequence of iterations is reported in Table 3.2. Few iterations are sufficient to satisfy the convergence criterion, e.g., less than five in these cases. The quantity $e$ defined in (3.121), which can be considered at each iteration step as the average discrepancy between identified and target eigenvalues, is reduced by at least $3-4$ orders of magnitude with respect to the initial value. The errors on the mass coefficient, either evaluated on $L^2$ or $L^\infty$ norm, are reduced significantly through the iterations, albeit to a lesser extent than $e$. In particular, the relative error in $L^\infty$ norm is even more than one order of magnitude less than the initial value, so confirming the accuracy of the reconstruction of regular mass variations. It should also be noted that the matrix $\mathbf{A}^{(j)}$ remains well conditioned during the iterations, with condition number $\kappa(\mathbf{A}^{(j)}) = \|\mathbf{A}^{(j)}\| \, \|(\mathbf{A}^{(j)})^{-1}\|$ ranging between 30 and 120 in all the cases studied. Here, $\|\mathbf{A}^{(j)}\| = \max_{|\mathbf{y}|=1} |\mathbf{A}^{(j)}\mathbf{y}|$, where $|\mathbf{y}| = \sqrt{\mathbf{y}\cdot\mathbf{y}}$ is the Euclidean norm of the vector $\mathbf{y} \in \mathbb{R}^N$.

#### 3.6.3.2 Identification of discontinuous mass densities

The mass density to be determined is assumed equal to

$$\rho(x) = \rho_0 + \rho_0 t \cdot \chi_{[s-\frac{c}{2}, s+\frac{c}{2}]}, \tag{3.168}$$

where $s$, $c$, $t$ have the same meaning as in the previous section, see Figure 3.1(b).

Since the mass density $\rho$ has jump discontinuities at $x = s \pm \frac{c}{2}$, whereas the approximating functions $\Phi_n(x)$ are smooth functions of the axial coordinate $x$, it is expected that the reconstruction may fail near these points. Numerical simulations confirm this undesired behavior. Some representative cases are collected in Figures 3.5 and 3.6.

These cases correspond to perturbations both located near the left end of the nanorod ($\frac{s}{L} = 0.15$) and with small support ($\frac{c}{L} = 0.1$), but having either small ($t = 0.1$, case i)) or large ($t = 1.0$, case ii)) intensity, respectively. In case i) (see Figure 3.5), the results are accurate enough for $N = 15$, whereas the oscillations of the identified mass coefficient have appreciable amplitude in case ii) (see Figure 3.6), and propagate in the remaining part of the interval $\left[0, \frac{L}{2}\right]$. The support of the perturbation is slightly overestimated and, as it was expected, $L^\infty$ estimates fail near the jumps.

Figure 3.7 collects the results for large mass variations, both in $L^2$ and in $L^\infty$ norm, for $\frac{s}{L} = 0.35$, $\frac{c}{L} = 0.3$, $t = 1.0$. The support of the mass variation still is well estimated, even if oscillations with significant amplitude occur both within the support and in the remaining part of the interval $\left[0, \frac{L}{2}\right]$. The number of iterations needed to satisfy the stopping criterion (3.121) is slightly bigger than the smooth case, being however always less than 10.

Finally, it can be shown that results generally improve by considering larger $N$, say $N = 20, 25$. In order to reduce the numerical approximation error on higher order eigenvalues, all these cases have been developed on a numerical model of the nanorod having $N_e = 400$ equally spaced finite elements. As it can be seen by comparing Figures 3.7 and 3.8, the increase of $N_e$ shows beneficial effects, such as more accurate estimate of the actual support of the mass variation and reduction of the amplitude of the spurious oscillations of the identified coefficient around the exact value. However, the identification of large mass variations with left (respectively, right) jump position close to the left end (respectively, to the mid point) of the nanorod still remains problematic to some extent.

#### 3.6.3.3 Identification of overlapping added masses

The identification method has also been tested on mass distributions having less schematic profile than those considered in the previous sections. As an example, here we report some representative results related to two overlapping added mass profiles, one being regular (and belonging to the class of Section 3.6.3.1) and the other one having triangular shape, with a jump type discontinuity. More precisely, the mass density to be determined has the expression

$$\rho(x) = \rho_0 + \rho_0 \max\{t \cos^2\left(\frac{\pi(x-s)}{c}\right)\chi_{[s-\frac{c}{2},s+\frac{c}{2}]},\ \frac{t_1}{c_1}(x-(s_1-c_1))\chi_{[s_1-c_1,s_1]}\}, \qquad (3.169)$$

where $[s_1 - c_1, s_1] \subset \left[0, \frac{L}{2}\right]$ and $t_1\rho_0$, $t_1 > 0$, is the support and the maximum value of the triangular added mass profile, respectively; see Figure 3.1(c). Some of the results are summarized in the sequel. They have been obtained using $N_e = 200, 400$ equally spaced finite elements, for $N = 6, 9, 12, 15$ and $N = 20, 25$, respectively. In order to simplify the presentation of the results, the parameters $c$ and $c_1$ have been assumed equal to $0.2L$. It should be noted that, depending on the values of $s_1$ and $t_1$, the coefficient $\rho(x)$ in (3.169) can be either continuous or discontinuous. The latter case occurs, for example, when $s_1 \in \left(s - \frac{c}{2}, s + \frac{c}{2}\right)$ and $t_1$ is small enough with respect to $t$.

The determination of continuous mass coefficient turns out to be very accurate even when only the first $9 - 12$ eigenfrequencies are used in identification, as it was found for the class of smooth variations considered in Section 3.6.3.1. We refer to Figure 3.9 for a typical result.

In case of discontinuous coefficient, as it was already noticed in Section 3.6.3.2, spurious oscillations occur near the jump, with amplitude which turns out to be proportional to the intensity of the jump. As a consequence, identification of the smooth portion of the mass coefficient may become inaccurate for small values of $t$. At least $15 - 20$ first eigenfrequencies seem to be needed to obtain acceptable accuracy in these cases, see, for example, Figure 3.10. The method also shows good ability in identifying mass variations with disjoint supports, particularly when the values of $t_1$ and $t$ are close, see, for example, Figure 3.11.

#### 3.6.3.4 Physical post-filtering

In this section we show that, when the method is combined with additional information about the unknown mass coefficient, such as monotonicity or a priori information on the support of the mass variation, the reconstruction may further improve, leading to good uniform approximation of the solution. More precisely, we have considered in the sequel the following a priori information:

**F**$_1$) The mass variation is positive, e.g., the condition (3.27) holds.

As remarked in Section 3.3 (see Remark 3.3.1), this information is simply available from the physics of the problem. Actually, our identification algorithm produces a function $\rho(x)$ which may oscillate near the unperturbed linear mass density $\rho_0$. Basing on assumption $F_1$, we *filter* the results of identification by setting the mass density to be $\rho_0$ whenever the reconstructed value of $\rho(x)$ is greater than $\rho_0$.

**F**$_2$) There are situations in which it is a priori known that a *single* localized mass variation occurs in the nanosensor, that is, the support of the mass variation $r_\epsilon(x)$ is a closed (and possible small) interval compactly contained in $\left[0, \frac{L}{2}\right]$.

> In this case, under the assumption that the reconstructed coefficient $\rho(x)$ is a good uniform approximation of the actual mass, one can determine the interval of maximum mass increase and neglect all the other possible regions on which the mass density increases.

In order to check how the identification results improve by adding the above hypotheses $F_1$ and $F_2$, we tested the method in an extended series of simulations with error free data. As an example, Figure 3.12 reports the results obtained by applying filter $F_1$ and by combining in cascade $F_1 + F_2$. The cases considered correspond to discontinuous mass changes as in (3.168), with large mass variation ($t = 1.0$) localized either on a small or a large subinterval of $\left[0, \frac{L}{2}\right]$. The comparison with the corresponding unfiltered results clearly shows an improvement of accuracy of the reconstruction.

#### 3.6.3.5 Application to noisy data

An important aspect for applications is stability against noise in the given spectral data. In order to test the robustness of the method, the identification was carried out by perturbing the target noise-free eigenvalue $\lambda_n^{exp}$, $n = 1, \ldots, N$ as follows

$$\sqrt{\lambda_n^{exp-err}} = \sqrt{\lambda_n^{exp}} + \tau_n. \tag{3.170}$$

Here, $\tau_n$ is a random Gaussian variable with vanishing mean and standard deviation $\sigma$ such that $3\sigma = 2\pi\Pi$, where $\Pi$ is the maximum admitted error. The effect of errors was evaluated both for smooth and discontinuous mass distributions, by considering different profile of the coefficient and by varying the number $N$ of the first eigenfrequencies used in identification, for increasing values of $\Pi$ ranging from $100$ Hz to $5000$ Hz. A selected, though representative, set of results are presented in Figures 3.13 and 3.14, for smooth and discontinuous mass coefficients, respectively. For each position along the nanorod axis, and besides the exact mass profile, every subfigure contains three curves: the curve of the mean value and the two curves obtained by adding $\pm 3\sigma$ to the mean value. One thousand of simulations was performed for each case. It turns out that the three curves are almost indistinguishable for $\Pi = 100$ Hz. Appreciable discrepancy occurs for $\Pi = 1000$ Hz, and for $\Pi$ greater than $3000$ Hz the accuracy of the reconstruction is seriously compromised. In particular, for $\Pi$ less than $2000$ Hz, the effect of errors makes it possible to discriminate the presence of even minor variations of mass, either regular or discontinuous, and for which the influence of errors on data is expected to be more significant. It should be noted that $\Pi = 2000$ Hz corresponds to percentage errors ranging from $0.05$ (high frequency) to $0.65$ (low frequency) per cent of the unperturbed first fifteen resonant frequencies. Finally, the convergence speed of the iterative method is not significantly affected by the random noise, and the number of iterations needed to get convergence is slightly bigger than in the error-free case. The condition number $\kappa(\mathbf{A})$ takes values of the same order of those found in the analysis of the corresponding cases in absence of errors on the data.

**Table 3.1:** *First* $25$ *eigenvalues of the clamped-clamped uniform unperturbed nanorod in* (3.1)–(3.3)*, with physical parameters as in Section 3.6.1. Comparison between analytical (*$\lambda_n$*, column* $2$*) and numerical (*$\lambda_n^{FEM}$*) values obtained with* $N_e = 100, 200, 400$ *equally spaced finite elements. Percentage errors:* $e_n = 100 \times (\lambda_n^{FEM} - \lambda_n)/\lambda_n$ *for* $N_e = 100$ *(column* $3$*),* $N_e = 200$ *(column* $4$*),* $N_e = 400$ *(column* $5$*).*

| $n$ | $\lambda_n\ (rad/s)^2$ | $N_e = 100$ | $N_e = 200$ | $N_e = 400$ |
|---|---|---|---|---|
| 1 | $3.556 \cdot 10^{+12}$ | $1.4 \cdot 10^{-6}$ | $1.4 \cdot 10^{-6}$ | $1.4 \cdot 10^{-6}$ |
| 2 | $1.426 \cdot 10^{+13}$ | $1.4 \cdot 10^{-6}$ | $1.4 \cdot 10^{-6}$ | $1.4 \cdot 10^{-6}$ |
| 3 | $3.220 \cdot 10^{+13}$ | $1.5 \cdot 10^{-6}$ | $1.5 \cdot 10^{-6}$ | $1.5 \cdot 10^{-6}$ |
| 4 | $5.755 \cdot 10^{+13}$ | $5.0 \cdot 10^{-7}$ | $5.0 \cdot 10^{-7}$ | $5.0 \cdot 10^{-7}$ |
| 5 | $9.055 \cdot 10^{+13}$ | $1.6 \cdot 10^{-6}$ | $5.2 \cdot 10^{-7}$ | $5.2 \cdot 10^{-7}$ |
| 6 | $1.315 \cdot 10^{+14}$ | $8.1 \cdot 10^{-6}$ | $5.2 \cdot 10^{-7}$ | $5.2 \cdot 10^{-7}$ |
| 7 | $1.807 \cdot 10^{+14}$ | $1.3 \cdot 10^{-5}$ | $2.4 \cdot 10^{-6}$ | $2.4 \cdot 10^{-6}$ |
| 8 | $2.387 \cdot 10^{+14}$ | $2.6 \cdot 10^{-5}$ | $1.2 \cdot 10^{-6}$ | $1.2 \cdot 10^{-6}$ |
| 9 | $3.059 \cdot 10^{+14}$ | $5.3 \cdot 10^{-5}$ | $3.9 \cdot 10^{-6}$ | $6.6 \cdot 10^{-7}$ |
| 10 | $3.829 \cdot 10^{+14}$ | $9.9 \cdot 10^{-5}$ | $4.9 \cdot 10^{-6}$ | $-2.8 \cdot 10^{-7}$ |
| 11 | $4.703 \cdot 10^{+14}$ | $1.7 \cdot 10^{-4}$ | $1.1 \cdot 10^{-5}$ | $2.6 \cdot 10^{-7}$ |
| 12 | $5.688 \cdot 10^{+14}$ | $2.9 \cdot 10^{-4}$ | $1.7 \cdot 10^{-5}$ | $1.3 \cdot 10^{-6}$ |
| 13 | $6.792 \cdot 10^{+14}$ | $4.6 \cdot 10^{-4}$ | $2.7 \cdot 10^{-5}$ | $2.5 \cdot 10^{-6}$ |
| 14 | $8.022 \cdot 10^{+14}$ | $7.0 \cdot 10^{-4}$ | $4.4 \cdot 10^{-5}$ | $2.4 \cdot 10^{-6}$ |
| 15 | $9.389 \cdot 10^{+14}$ | $1.0 \cdot 10^{-3}$ | $6.4 \cdot 10^{-5}$ | $3.9 \cdot 10^{-6}$ |
| 16 | $1.090 \cdot 10^{+15}$ | $1.5 \cdot 10^{-3}$ | $9.1 \cdot 10^{-5}$ | $8.2 \cdot 10^{-6}$ |
| 17 | $1.257 \cdot 10^{+15}$ | $2.1 \cdot 10^{-3}$ | $1.3 \cdot 10^{-4}$ | $9.6 \cdot 10^{-6}$ |
| 18 | $1.440 \cdot 10^{+15}$ | $2.9 \cdot 10^{-3}$ | $1.8 \cdot 10^{-4}$ | $1.4 \cdot 10^{-5}$ |
| 19 | $1.642 \cdot 10^{+15}$ | $3.9 \cdot 10^{-3}$ | $2.4 \cdot 10^{-4}$ | $1.5 \cdot 10^{-5}$ |
| 20 | $1.862 \cdot 10^{+15}$ | $5.2 \cdot 10^{-3}$ | $3.2 \cdot 10^{-4}$ | $2.0 \cdot 10^{-5}$ |
| 21 | $2.103 \cdot 10^{+15}$ | $6.8 \cdot 10^{-3}$ | $4.2 \cdot 10^{-4}$ | $2.4 \cdot 10^{-5}$ |
| 22 | $2.365 \cdot 10^{+15}$ | $8.8 \cdot 10^{-3}$ | $5.4 \cdot 10^{-4}$ | $3.2 \cdot 10^{-5}$ |
| 23 | $2.651 \cdot 10^{+15}$ | $1.1 \cdot 10^{-2}$ | $6.9 \cdot 10^{-4}$ | $4.2 \cdot 10^{-5}$ |
| 24 | $2.961 \cdot 10^{+15}$ | $1.4 \cdot 10^{-2}$ | $8.7 \cdot 10^{-4}$ | $5.6 \cdot 10^{-5}$ |
| 25 | $3.297 \cdot 10^{+15}$ | $1.7 \cdot 10^{-2}$ | $1.1 \cdot 10^{-3}$ | $6.7 \cdot 10^{-5}$ |

**Table 3.2:** *Some results of the reconstruction of smooth mass changes as in* (3.167) *versus iteration number $j$ (up to convergence), with (a): $\frac{s}{L} = 0.35$, $\frac{c}{L} = 0.10$, $t = 0.10$ (Figure 3.2); (b): $\frac{s}{L} = 0.35$, $\frac{c}{L} = 0.10$, $t = 1.00$ (Figure 3.3); (c): $\frac{s}{L} = 0.35$, $\frac{c}{L} = 0.30$, $t = 1.00$ (Figure 3.4), using the first $N = 6$ (columns $2-5$), $N = 15$ (columns $6-9$) eigenfrequencies. The quantity $e$ is defined in* (3.121)*; $e_{L^2} = \frac{\|\rho^{ident} - \rho^{exact}\|_{L^2}}{\|\rho^{exact}\|_{L^2}}$, $e_{L^\infty} = \frac{\|\rho^{ident} - \rho^{exact}\|_{L^\infty}}{\|\rho^{exact}\|_{L^\infty}}$, where $\rho^{ident} = \rho^{ident}(x)$, $\rho^{exact} = \rho^{exact}(x)$ are the identified and the exact mass density per unit length, respectively. $\kappa(\mathbf{A}^{(j)})$ is the condition number of the matrix $\mathbf{A}^{(j)}$. The unperturbed nanorod corresponds to $j = 0$.*

(a)

| $j$ | $e$ | $\kappa(\mathbf{A}^{(j)})$ | $e_{L^2}$ | $e_{L^\infty}$ | $e$ | $\kappa(\mathbf{A}^{(j)})$ | $e_{L^2}$ | $e_{L^\infty}$ |
|---|---|---|---|---|---|---|---|---|
| 0 | $2.40 \cdot 10^{-3}$ | $1.30 \cdot 10^{+1}$ | $1.92 \cdot 10^{-2}$ | $9.09 \cdot 10^{-2}$ | $1.44 \cdot 10^{-3}$ | $3.10 \cdot 10^{+1}$ | $1.92 \cdot 10^{-2}$ | $9.09 \cdot 10^{-2}$ |
| 1 | $3.11 \cdot 10^{-5}$ | $1.31 \cdot 10^{+1}$ | $1.04 \cdot 10^{-2}$ | $3.95 \cdot 10^{-2}$ | $3.84 \cdot 10^{-5}$ | $3.12 \cdot 10^{+1}$ | $1.58 \cdot 10^{-3}$ | $5.34 \cdot 10^{-3}$ |
| 2 | $5.12 \cdot 10^{-8}$ | $1.41 \cdot 10^{+1}$ | $1.04 \cdot 10^{-2}$ | $3.88 \cdot 10^{-2}$ | $3.35 \cdot 10^{-7}$ | $3.64 \cdot 10^{+1}$ | $1.31 \cdot 10^{-3}$ | $4.43 \cdot 10^{-3}$ |

(b)

| $j$ | $e$ | $\kappa(\mathbf{A}^{(j)})$ | $e_{L^2}$ | $e_{L^\infty}$ | $e$ | $\kappa(\mathbf{A}^{(j)})$ | $e_{L^2}$ | $e_{L^\infty}$ |
|---|---|---|---|---|---|---|---|---|
| 0 | $2.33 \cdot 10^{-2}$ | $1.30 \cdot 10^{+1}$ | $1.81 \cdot 10^{-1}$ | $5.00 \cdot 10^{-1}$ | $1.29 \cdot 10^{-2}$ | $3.10 \cdot 10^{+1}$ | $1.81 \cdot 10^{-1}$ | $5.00 \cdot 10^{-1}$ |
| 1 | $2.52 \cdot 10^{-3}$ | $1.31 \cdot 10^{+1}$ | $1.00 \cdot 10^{-1}$ | $2.43 \cdot 10^{-1}$ | $2.23 \cdot 10^{-3}$ | $3.12 \cdot 10^{+1}$ | $5.70 \cdot 10^{-2}$ | $1.47 \cdot 10^{-1}$ |
| 2 | $9.00 \cdot 10^{-5}$ | $2.36 \cdot 10^{+1}$ | $9.68 \cdot 10^{-2}$ | $2.02 \cdot 10^{-1}$ | $2.63 \cdot 10^{-4}$ | $8.16 \cdot 10^{+1}$ | $1.14 \cdot 10^{-2}$ | $2.55 \cdot 10^{-2}$ |
| 3 | $3.37 \cdot 10^{-7}$ | $2.60 \cdot 10^{+1}$ | $9.68 \cdot 10^{-2}$ | $2.02 \cdot 10^{-1}$ | $7.77 \cdot 10^{-6}$ | $1.14 \cdot 10^{+2}$ | $7.17 \cdot 10^{-3}$ | $1.50 \cdot 10^{-2}$ |

(c)

| $j$ | $e$ | $\kappa(\mathbf{A}^{(j)})$ | $e_{L^2}$ | $e_{L^\infty}$ | $e$ | $\kappa(\mathbf{A}^{(j)})$ | $e_{L^2}$ | $e_{L^\infty}$ |
|---|---|---|---|---|---|---|---|---|
| 0 | $6.42 \cdot 10^{-2}$ | $1.30 \cdot 10^{+1}$ | $2.82 \cdot 10^{-1}$ | $5.00 \cdot 10^{-1}$ | $3.64 \cdot 10^{-2}$ | $3.10 \cdot 10^{+1}$ | $2.82 \cdot 10^{-1}$ | $5.00 \cdot 10^{-1}$ |
| 1 | $1.24 \cdot 10^{-2}$ | $1.31 \cdot 10^{+1}$ | $9.46 \cdot 10^{-2}$ | $1.74 \cdot 10^{-1}$ | $7.03 \cdot 10^{-3}$ | $3.12 \cdot 10^{+1}$ | $9.57 \cdot 10^{-2}$ | $1.84 \cdot 10^{-1}$ |
| 2 | $9.08 \cdot 10^{-4}$ | $2.44 \cdot 10^{+1}$ | $1.53 \cdot 10^{-2}$ | $3.54 \cdot 10^{-2}$ | $6.14 \cdot 10^{-4}$ | $5.89 \cdot 10^{+1}$ | $1.44 \cdot 10^{-2}$ | $3.08 \cdot 10^{-2}$ |
| 3 | $2.20 \cdot 10^{-5}$ | $3.25 \cdot 10^{+1}$ | $9.97 \cdot 10^{-3}$ | $2.79 \cdot 10^{-2}$ | $1.54 \cdot 10^{-5}$ | $7.92 \cdot 10^{+1}$ | $4.64 \cdot 10^{-3}$ | $1.78 \cdot 10^{-2}$ |
| 4 | $4.89 \cdot 10^{-8}$ | $3.30 \cdot 10^{+1}$ | $9.96 \cdot 10^{-3}$ | $2.80 \cdot 10^{-2}$ | $9.11 \cdot 10^{-8}$ | $8.11 \cdot 10^{+1}$ | $4.62 \cdot 10^{-3}$ | $1.75 \cdot 10^{-2}$ |

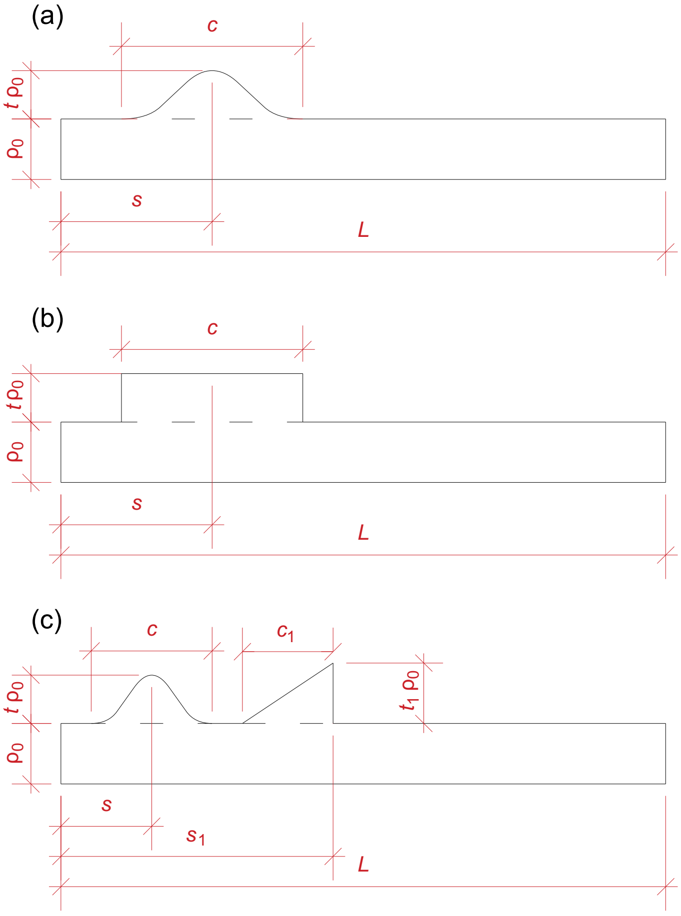

**Figure 3.1:** *Mass density per unit length* $\rho = \rho(x)$ *to be identified in* $\left[0, \frac{L}{2}\right]$. *(a) Smooth mass changes as in* (3.167)*; (b) discontinuous mass changes as in* (3.168)*; (c) overlapping mass changes as in* (3.169)*.*

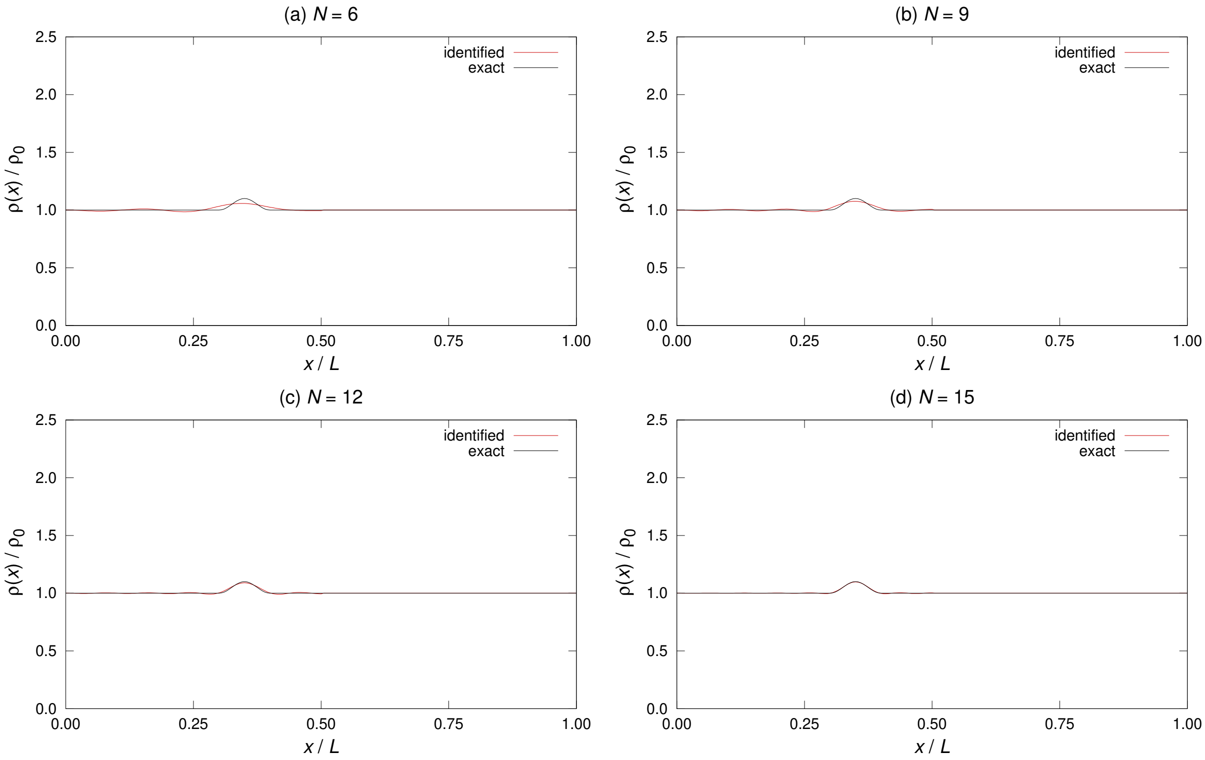

**Figure 3.2:** *Reconstruction of smooth mass changes as in* (3.167)*, with* $\frac{s}{L} = 0.35$*,* $\frac{c}{L} = 0.10$*,* $t = 0.10$*, using the first* $N = 6, 9, 12, 15$ *eigenfrequencies.*

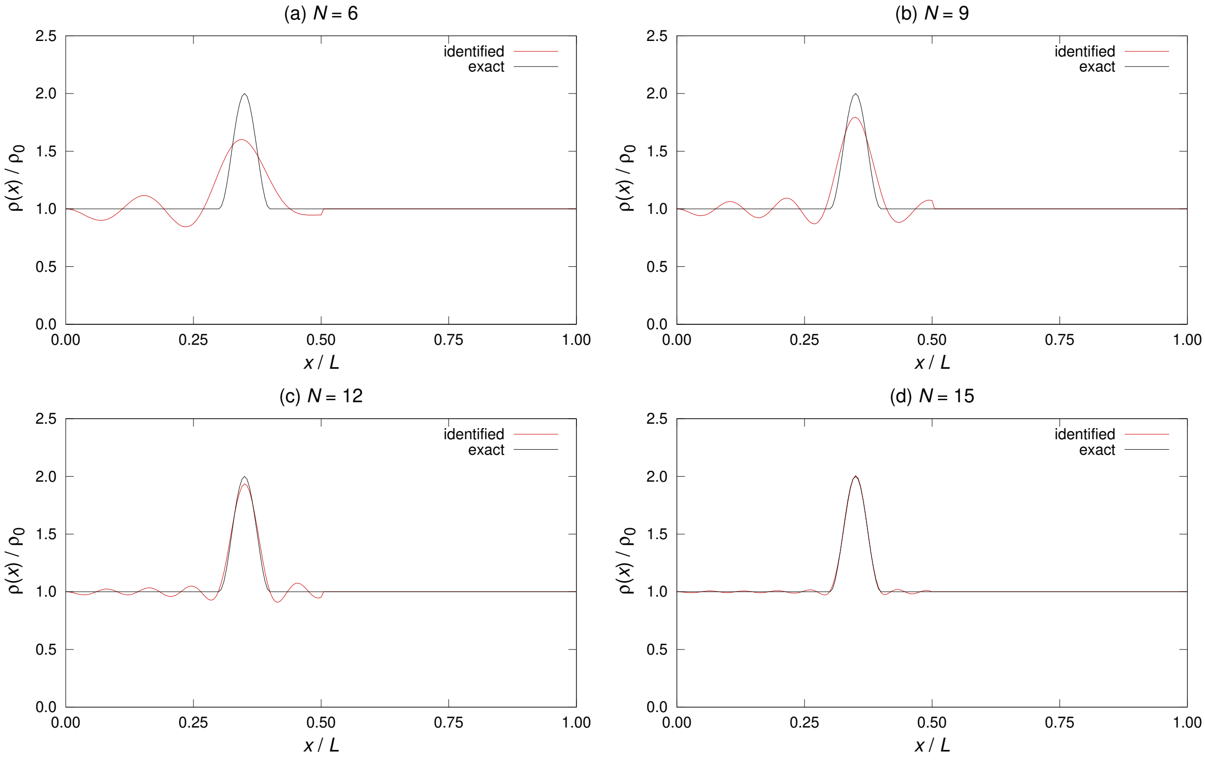

**Figure 3.3:** *Reconstruction of smooth mass changes as in* (3.167)*, with* $\frac{s}{L} = 0.35$*,* $\frac{c}{L} = 0.10$*,* $t = 1.00$*, using the first* $N = 6, 9, 12, 15$ *eigenfrequencies.*

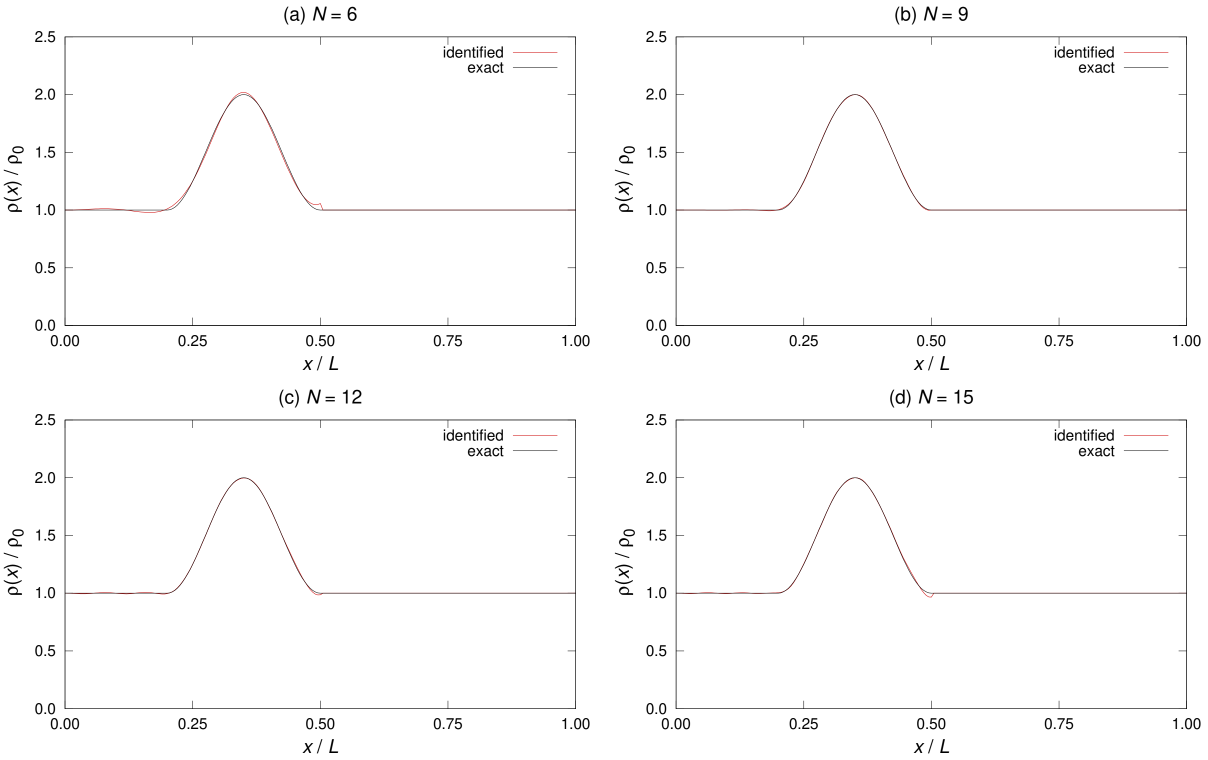

**Figure 3.4:** *Reconstruction of smooth mass changes as in* (3.167)*, with* $\frac{s}{L} = 0.35$*,* $\frac{c}{L} = 0.30$*,* $t = 1.00$*, using the first* $N = 6, 9, 12, 15$ *eigenfrequencies.*

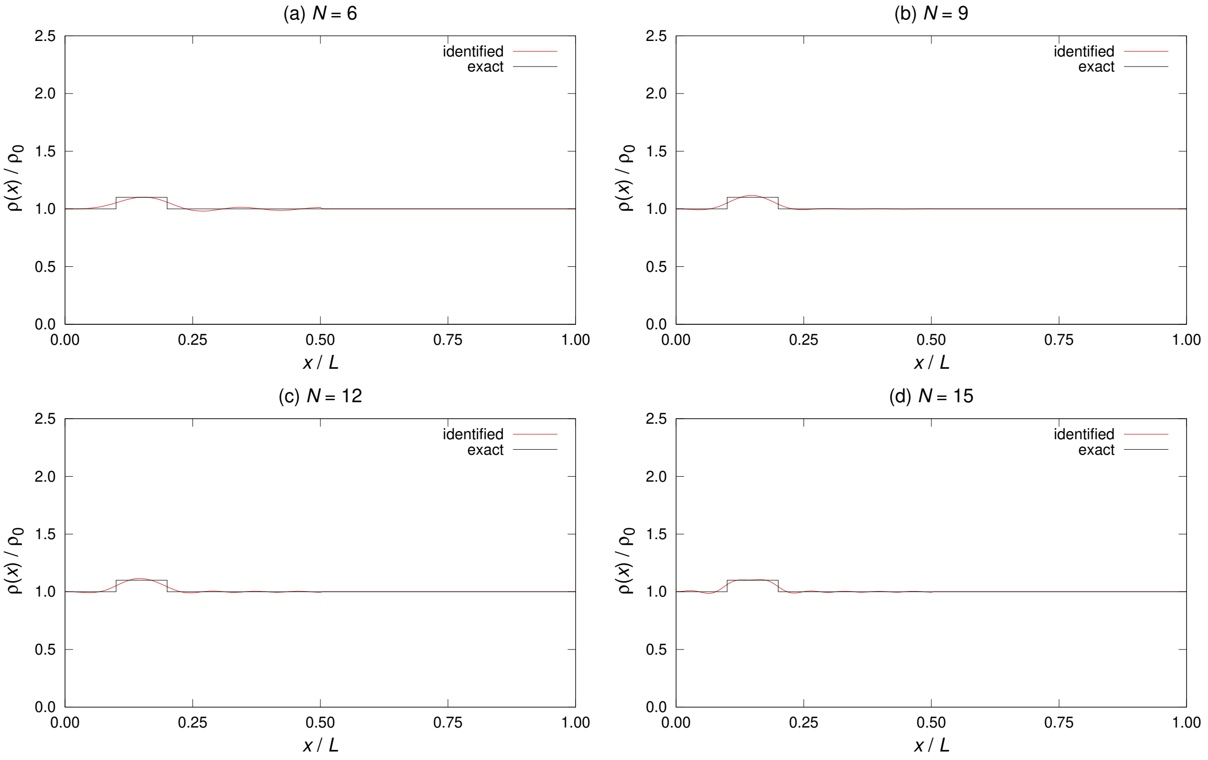

**Figure 3.5:** *Reconstruction of discontinuous mass changes as in* (3.168)*, with* $\frac{s}{L} = 0.15$*,* $\frac{c}{L} = 0.10$*,* $t = 0.10$*, using the first* $N = 6, 9, 12, 15$ *eigenfrequencies.*

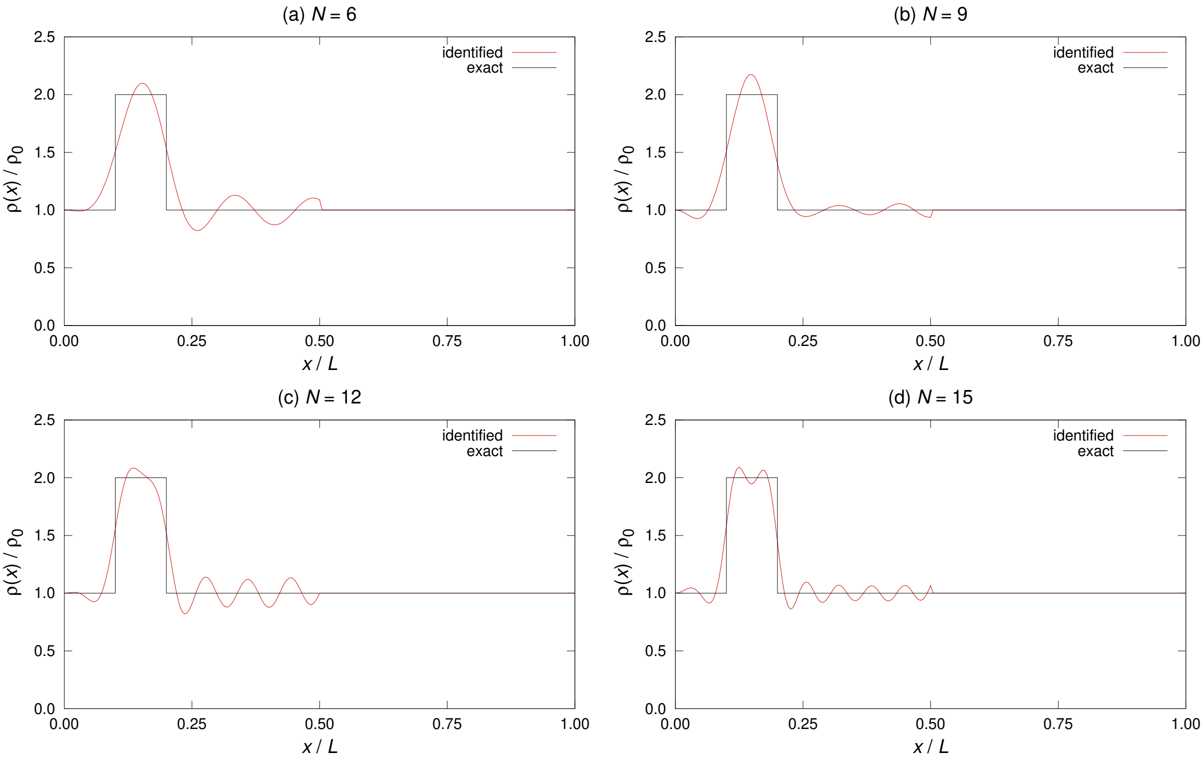

**Figure 3.6:** *Reconstruction of discontinuous mass changes as in* (3.168)*, with* $\frac{s}{L} = 0.15$*,* $\frac{c}{L} = 0.10$*,* $t = 1.00$*, using the first* $N = 6, 9, 12, 15$ *eigenfrequencies.*

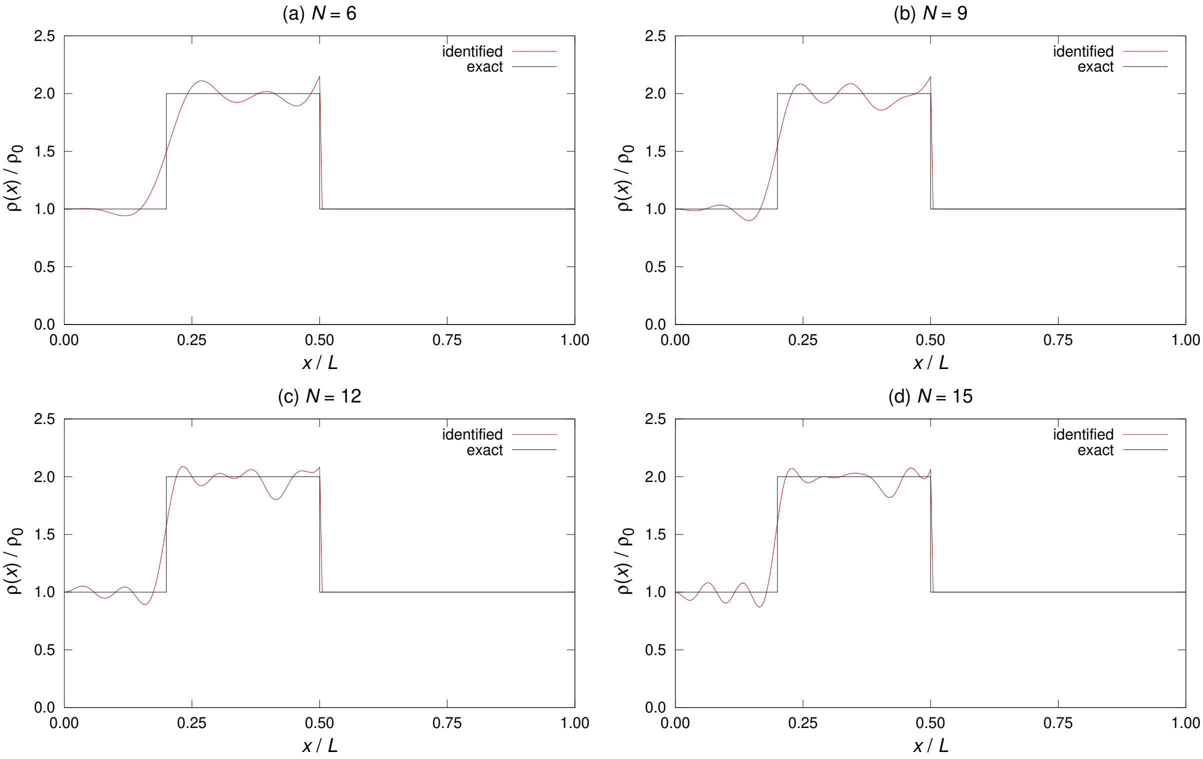

**Figure 3.7:** *Reconstruction of discontinuous mass changes as in* (3.168)*, with* $\frac{s}{L} = 0.35$*,* $\frac{c}{L} = 0.30$*,* $t = 1.00$*, using the first* $N = 6, 9, 12, 15$ *eigenfrequencies.*

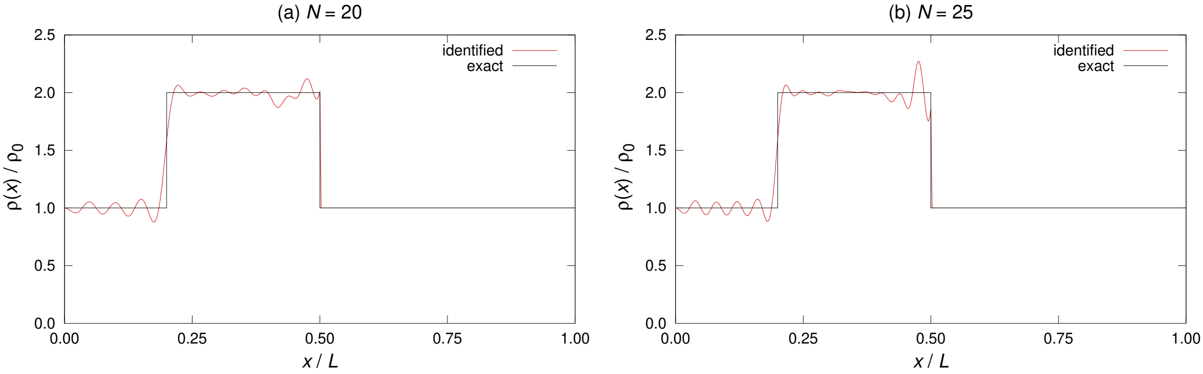

**Figure 3.8:** *Reconstruction of discontinuous mass changes as in* (3.168)*, with* $\frac{s}{L} = 0.35$*,* $\frac{c}{L} = 0.30$*,* $t = 1.00$*, using the first* $N = 20, 25$ *eigenfrequencies.*

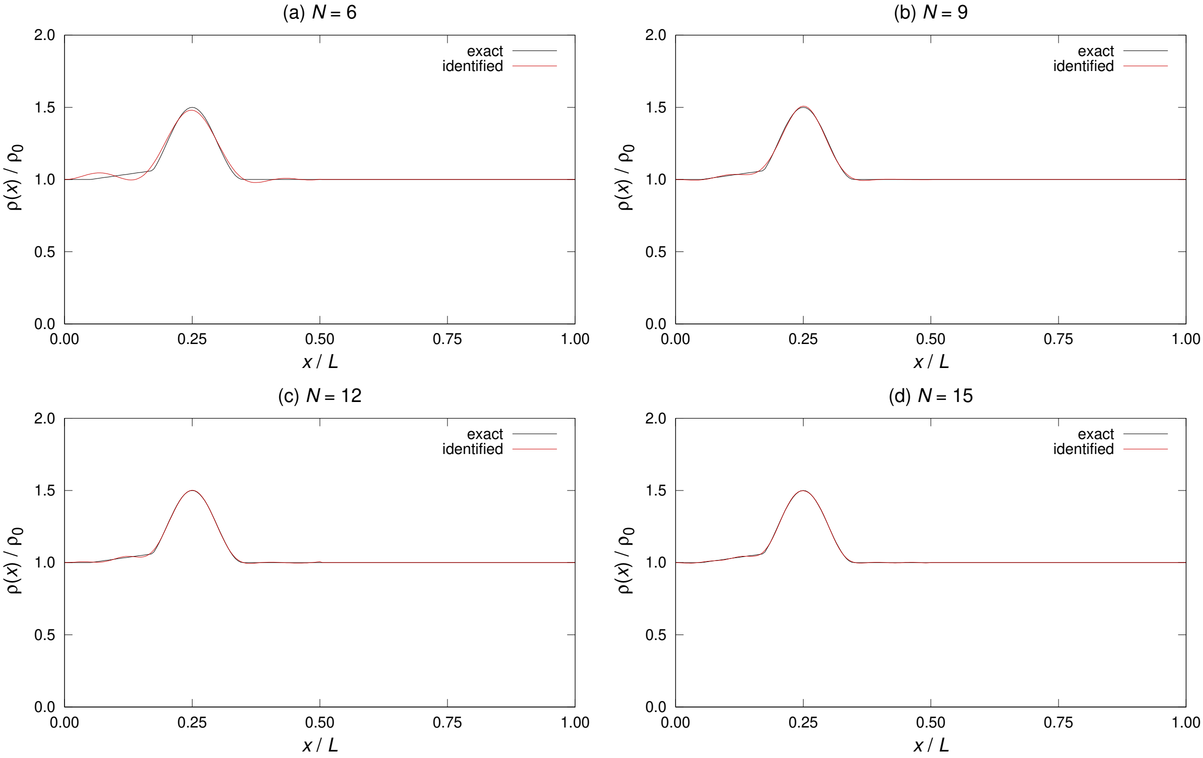

**Figure 3.9:** *Reconstruction of overlapping mass changes as in* (3.169)*, with* $\frac{s}{L} = 0.25$*,* $t = 0.50$*,* $\frac{s_1}{L} = 0.25$*,* $t_1 = 0.10$*, using the first* $N = 6$ *to* 15 *eigenfrequencies.*

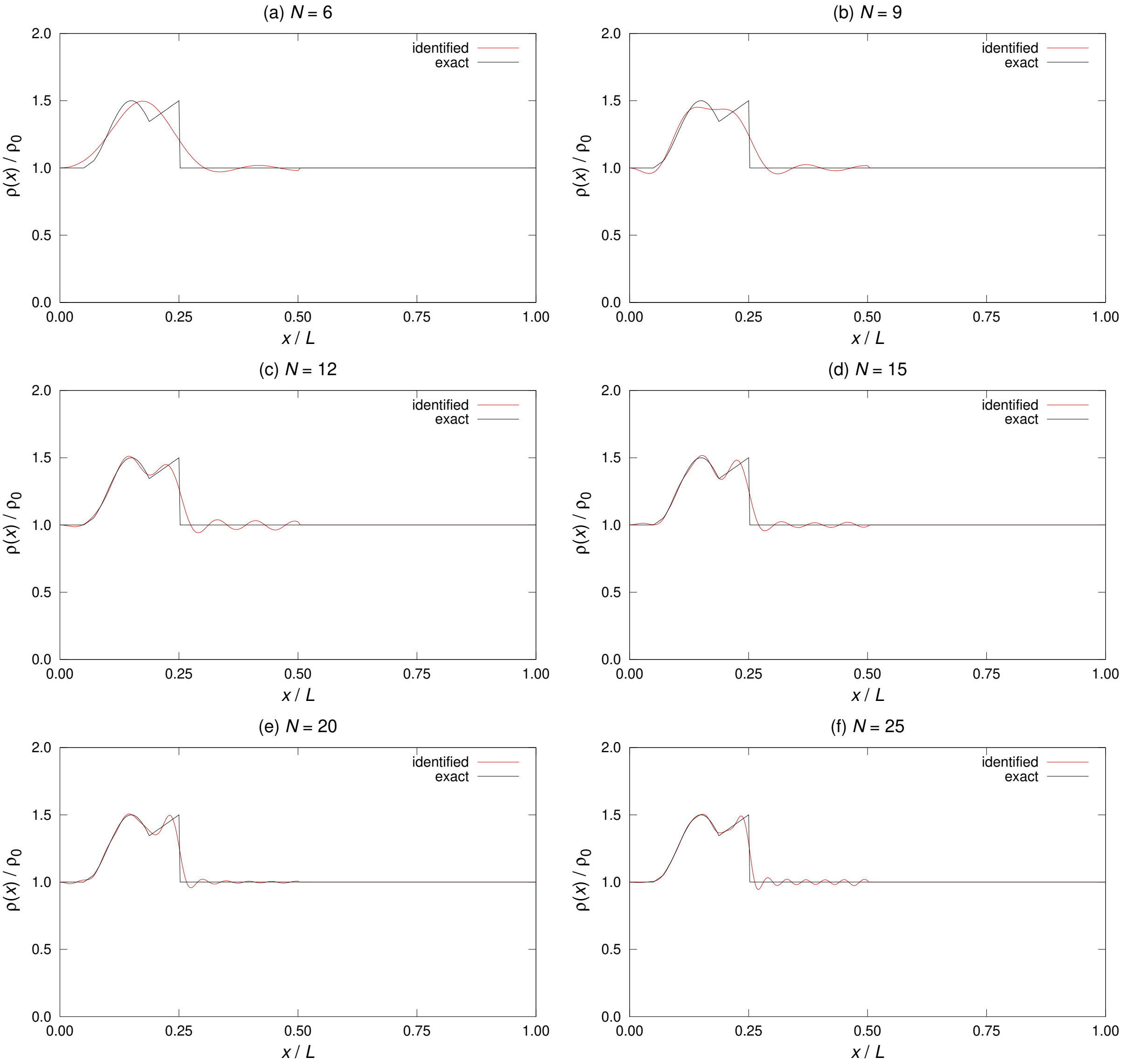

**Figure 3.10:** *Reconstruction of overlapping mass changes as in* (3.169)*, with* $\frac{s}{L} = 0.15$*,* $t = 0.50$*,* $\frac{s_1}{L} = 0.25$*,* $t_1 = 0.50$*, using the first* $N = 6$ *to* $25$ *eigenfrequencies.*

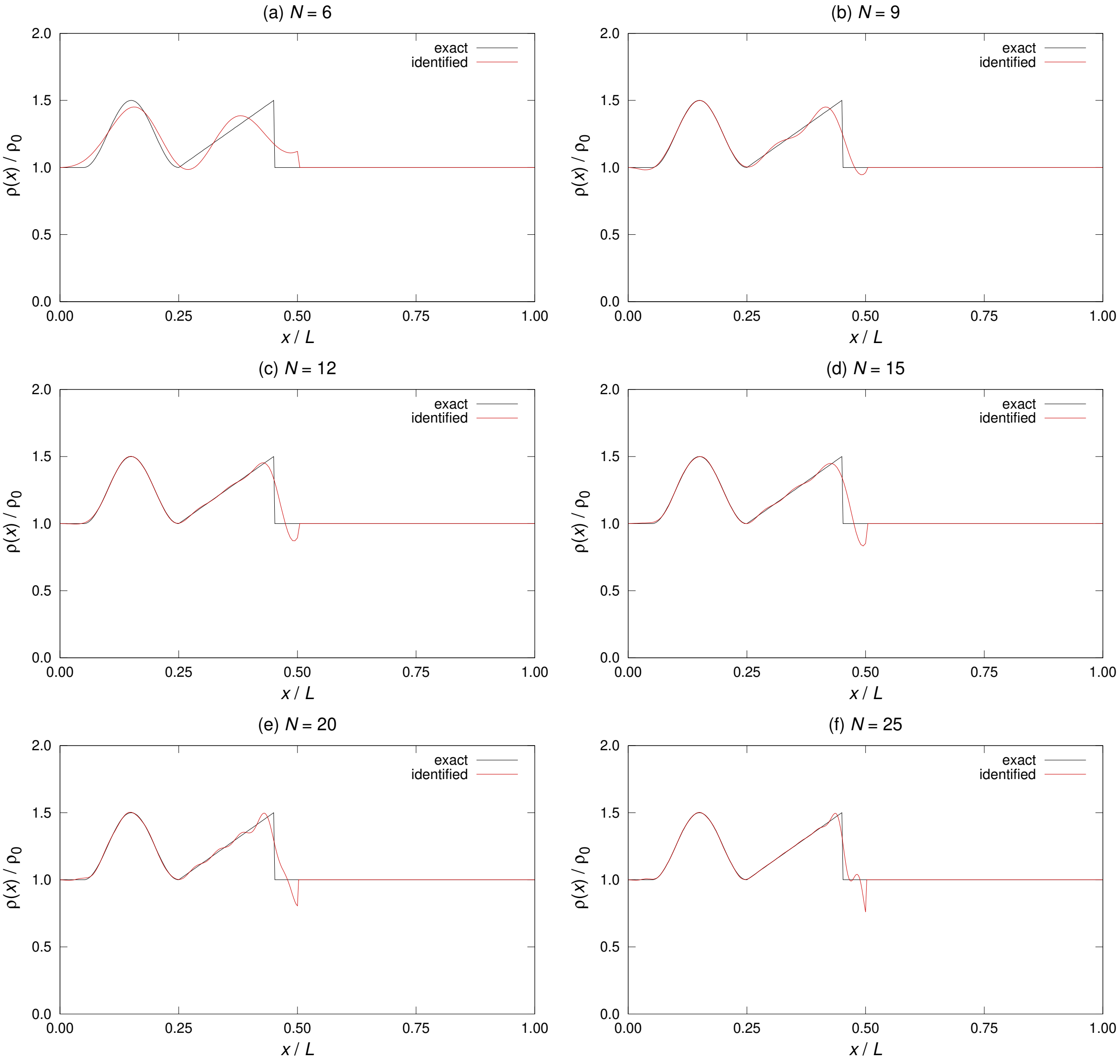

**Figure 3.11:** *Reconstruction of overlapping mass changes as in* (3.169)*, with* $\frac{s}{L} = 0.15$*,* $t = 0.50$*,* $\frac{s_1}{L} = 0.45$*,* $t_1 = 0.50$*, using the first* $N = 6$ *to* $25$ *eigenfrequencies.*

(a) Without filtering

(b) Without filtering

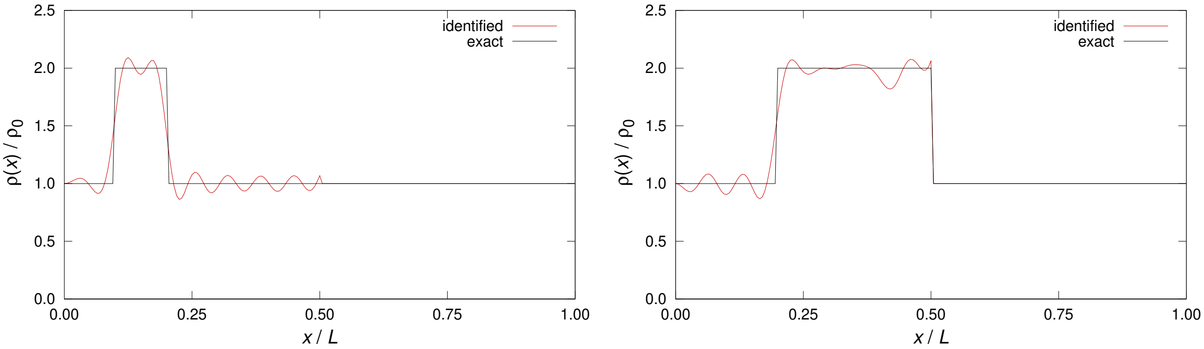

(c) Filter $F_1$

(d) Filter $F_1$

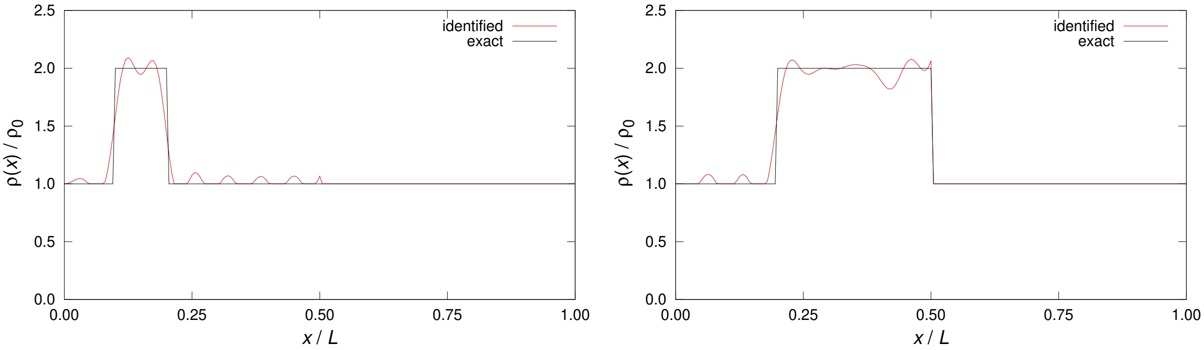

(e) Filter $F_1 + F_2$

(f) Filter $F_1 + F_2$

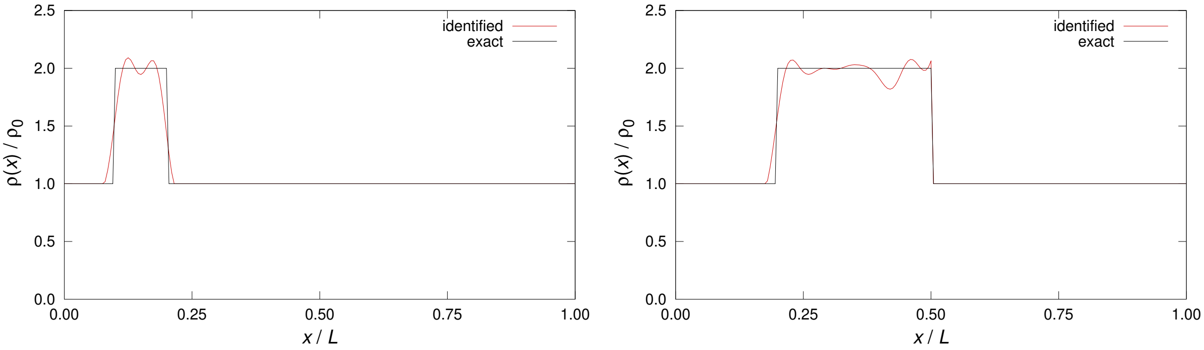

**Figure 3.12:** *Filtering effects on identification. Reconstruction of discontinuous mass changes as in* (3.168)*, with* $\frac{s}{L} = 0.15$, $\frac{c}{L} = 0.10$, $t = 1.00$, *using the first* $N = 15$ *eigenfrequencies.*

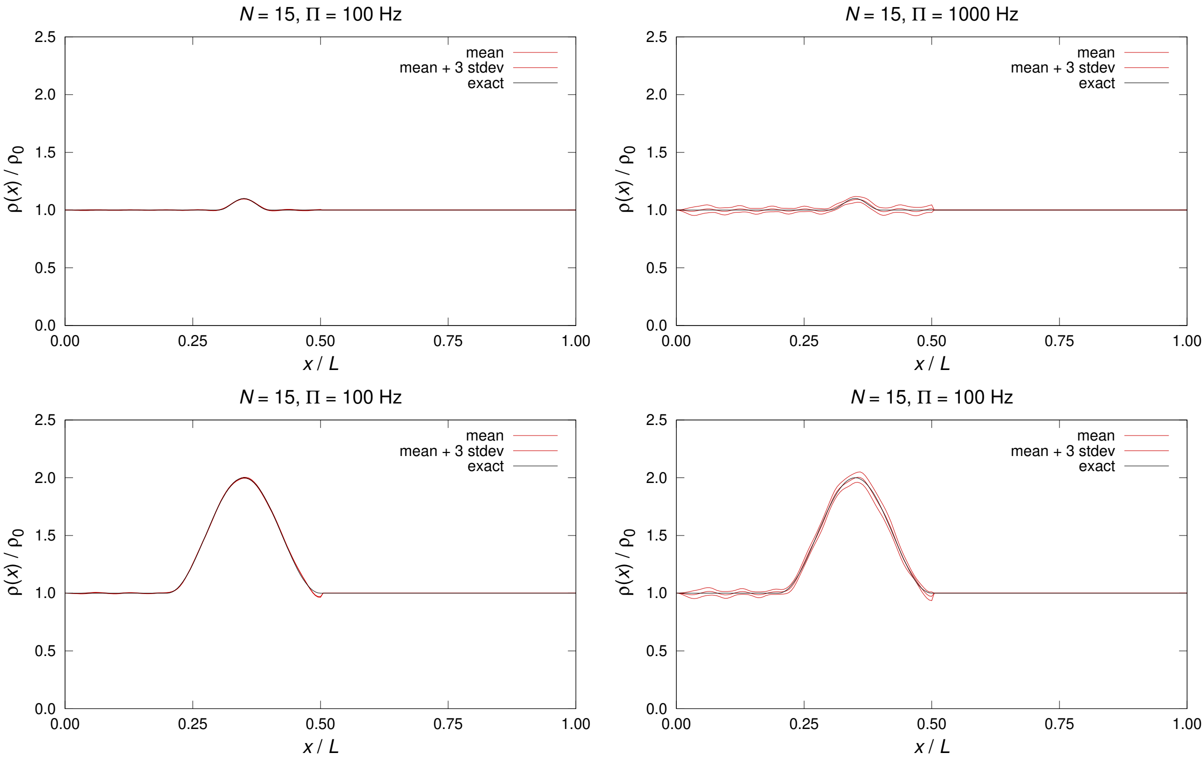

**Figure 3.13:** *Noise effects on identification of smooth mass changes. Upper row: mass changes as in* (3.167)*, with* $\frac{s}{L} = 0.35$, $\frac{c}{L} = 0.10$, $t = 0.10$. *Lower row: mass changes as in* (3.167)*, with* $\frac{s}{L} = 0.35$, $\frac{c}{L} = 0.30$, $t = 1.00$.

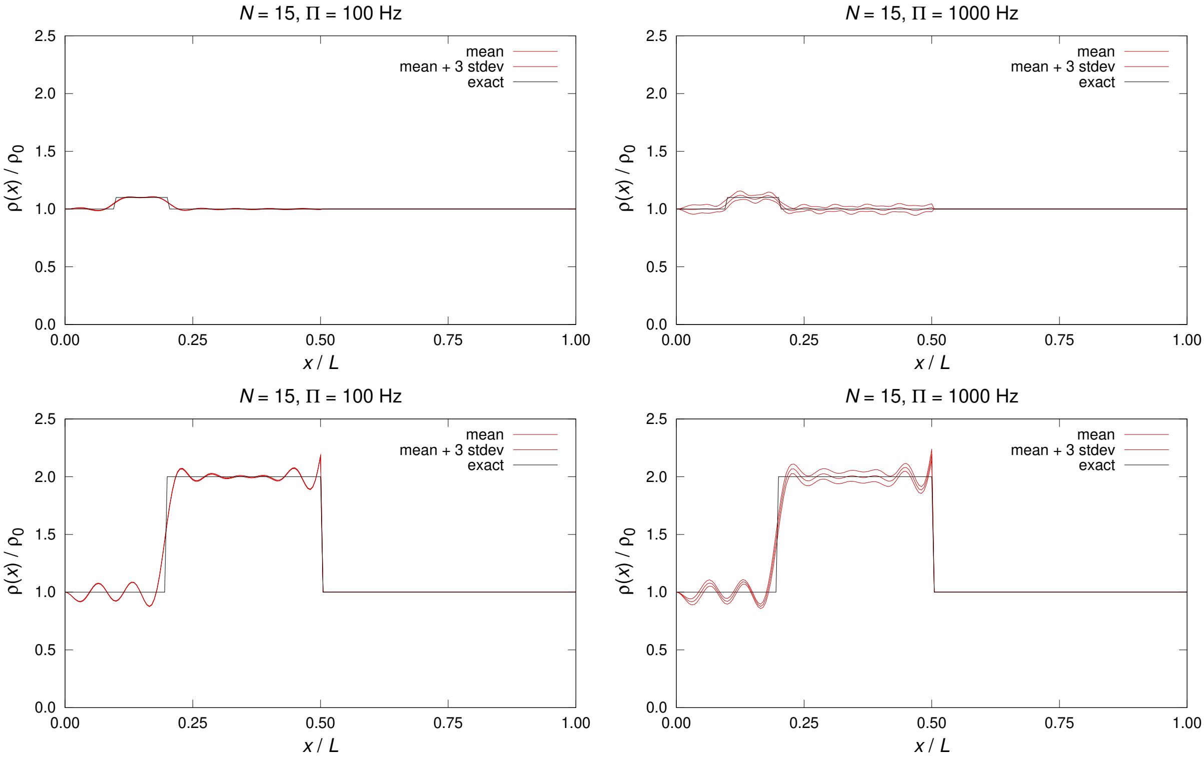

**Figure 3.14:** *Noise effects on identification of discontinuous mass changes. Upper row: mass changes as in* (3.168)*, with* $\frac{s}{L} = 0.15$, $\frac{c}{L} = 0.10$, $t = 0.10$. *Lower row: mass changes as in* (3.168)*, with* $\frac{s}{L} = 0.35$, $\frac{c}{L} = 0.30$, $t = 1.00$.

## 3.7 Formulation of the mass identification from two-spectra finite data

We have seen in Section 3.3 that the spatial variation of the infinitesimal free axial vibration at radian frequency $\sqrt{\lambda}$ of the *unperturbed* uniform nanorod, of length $L$ and under clamped end conditions, is governed within the modified strain gradient theory by the following eigenvalue problem [3, 64]

$$\begin{cases} bv^{IV} - av'' = \lambda\rho_0 v, \quad x \in (0, L), & (3.171)\\ v(0) = 0,\ v''(0) = 0, & (3.172)\\ v(L) = 0,\ v''(L) = 0, & (3.173)\end{cases}$$

where $\lambda$ is the eigenvalue and $v = v(x)$ is the corresponding eigenfunction. The coefficient $\rho_0 = const.$, $\rho_0 > 0$, is the unperturbed mass density per unit length.

The eigenpairs $\{\lambda_n^C, v_n^C(x)\}_{n=1}^{\infty}$ of (3.171)–(3.173) are denoted here by

$$\lambda_n^C = \left(\frac{n\pi}{L}\right)^2 \left[\frac{1}{\rho_0}\left(a + b\left(\frac{n\pi}{L}\right)^2\right)\right], \tag{3.174}$$

$$v_n^C(x) = \sqrt{\frac{2}{\rho_0 L}} \sin\left(\frac{n\pi x}{L}\right), \tag{3.175}$$

and the eigenfunctions are mass-normalized such that

$$\int_0^L \rho_0 (v_n^C(x))^2 = 1, \quad n \geq 1. \tag{3.176}$$

If in (3.171)–(3.173) the boundary conditions (3.173) are replaced by

$$v'(L) = 0, \quad v'''(L) = 0, \tag{3.177}$$

then the nanorod is said to be under *clamped-free* end conditions, and the eigenvalues of (3.171), (3.172), (3.177) are

$$\lambda_n^F = \left(\frac{(2n-1)\pi}{2L}\right)^2 \left[\frac{1}{\rho_0}\left(a + b\left(\frac{(2n-1)\pi}{2L}\right)^2\right)\right], \tag{3.178}$$

$$v_n^F(x) = \sqrt{\frac{2}{\rho_0 L}} \sin\left(\frac{(2n-1)\pi x}{2L}\right), \tag{3.179}$$

with $\int_0^L \rho_0 (v_n^F(x))^2 = 1$ for every $n \geq 1$.

Let us assume that the mass density changes, and denote by

$$\rho(x) = \rho_0 + r_\epsilon(x), \quad x \in [0, L], \tag{3.180}$$

the mass density per unit length of the *perturbed* nanorod. The mass change $r_\epsilon$ is such that

$$\left(\frac{1}{L}\int_0^L (r_\epsilon(x))^2 dx\right)^{\frac{1}{2}} = \epsilon\rho_0, \tag{3.181}$$

$$r_\epsilon(x) \in L^\infty([0, L]), \tag{3.182}$$

$$0 < \rho^- \leq \rho(x) \leq \rho^+, \quad x \in [0, L], \tag{3.183}$$

where $\epsilon$, $0 < \epsilon \leq \widehat{\epsilon}_\rho$, for a given small number $\widehat{\epsilon}_\rho$, and $\rho^-$, $\rho^+$ are given constants (with $\rho^+ \geq \rho_0 + \|r_\epsilon\|_\infty$) independent of $\epsilon$.

Let us denote by $\{\lambda_n^C(\rho), v_n^C(x;\rho)\}_{n=1}^{\infty}$, $\{\lambda_n^F(\rho), v_n^F(x;\rho)\}_{n=1}^{\infty}$ the eigenpairs of the problems (3.171)–(3.173) and (3.171), (3.172), (3.177), respectively, when $\rho_0$ is replaced by $\rho(x)$.

In this section we wish to construct an approximation to $\rho(x)$ (or, equivalently, to $r_\epsilon(x)$) using a finite amount of spectral data belonging to the clamped-clamped and clamped-free spectra, namely, the set

$$\{\lambda_n^C(\rho)\}_{n=1}^{N} \bigcup \{\lambda_m^F(\rho)\}_{m=1}^{M}, \tag{3.184}$$

where $N$, $M$ are given integers.

### 3.7.1 The reconstruction method

The reconstruction method is obtained as a generalization of the method shown in previous sections.

The key mathematical tool in our analysis is the explicit expression of the first order change with respect to the smallness parameter $\varepsilon$ of an eigenvalue of the nanorod. With reference to the initial uniform nanorod, we have

$$\delta\lambda_n^C \equiv 1 - \frac{\lambda_n^C(\rho)}{\lambda_n^C} = \int_0^L r_\epsilon(x)\Phi_n^C(x)dx, \tag{3.185}$$

$$\delta\lambda_m^F \equiv 1 - \frac{\lambda_m^F(\rho)}{\lambda_m^F} = \int_0^L r_\epsilon(x)\Phi_m^F(x)dx, \tag{3.186}$$

where $\Phi_n^C(x) \equiv (v_n^C(x))^2$, $\Phi_m^F(x) \equiv (v_m^F(x))^2$, $n = 1, \ldots, N$, $m = 1, \ldots, M$. This result has been proved in Section 3.4 for clamped end conditions and can be generalized to clamped-free end conditions.

We first present the linearization of the inverse problem in a neighborhood of the unperturbed nanorod. A simple calculation shows that (up to an inessential multiplicative constant)

$$\{\Phi_n^C(x), \Phi_m^F(x)\}_{n,m=1}^{\infty} = \{1 - \cos(k\pi x/L)\}_{k=1}^{\infty}, \tag{3.187}$$

which is a basis of $L^2(0,L)$. This property enables us to introduce the representation

$$r_\epsilon(x) = \sum_{k=1}^{\infty} \beta_k^C \Phi_k^C(x) + \beta_k^F \Phi_k^F(x), \tag{3.188}$$

where the coefficients $\{\beta_k^C, \beta_k^F\}_{k=1}^{\infty}$ play the role of Generalized Fourier Coefficients of the mass variation $r_\epsilon(x)$. Replacing the above series expansion of $r_\epsilon(x)$ in (3.185) and (3.186), and taking the finite approximation of order $(N+M)$ of $r_\epsilon(x)$ in (3.188), we obtain the $(N+M)\times(N+M)$ linear system

$$\mathbf{A}\boldsymbol{\beta} = \boldsymbol{\delta\lambda}, \tag{3.189}$$

or, more explicitly,

$$\begin{pmatrix} A_{11}^{C-C} & \cdots & A_{1N}^{C-C} & A_{11}^{C-F} & \cdots & A_{1M}^{C-F} \\ \cdots & & \cdots & \cdots & & \cdots \\ A_{N1}^{C-C} & \cdots & A_{NN}^{C-C} & A_{N1}^{C-F} & \cdots & A_{NM}^{C-F} \\ A_{11}^{F-C} & \cdots & A_{1N}^{F-C} & A_{11}^{F-F} & \cdots & A_{1M}^{F-F} \\ \cdots & & \cdots & \cdots & & \cdots \\ A_{M1}^{F-C} & \cdots & A_{MN}^{F-C} & A_{M1}^{F-F} & \cdots & A_{MM}^{F-F} \end{pmatrix} \begin{pmatrix} \beta_1^C \\ \cdots \\ \beta_N^C \\ \beta_1^F \\ \cdots \\ \beta_M^F \end{pmatrix} = \begin{pmatrix} \delta\lambda_1^C \\ \cdots \\ \delta\lambda_N^C \\ \delta\lambda_1^F \\ \cdots \\ \delta\lambda_M^F \end{pmatrix}, \tag{3.190}$$

with

$$A_{nk}^{C-C} = \int_0^L \Phi_n^C(x)\Phi_k^C(x)dx, \quad n,k = 1,\cdots N, \tag{3.191}$$

$$A_{nk}^{C-F} = \int_0^L \Phi_n^C(x)\Phi_k^F(x)dx, \quad n = 1, \cdots N, \ k = 1, \cdots M, \tag{3.192}$$

$$A_{mk}^{F-C} = \int_0^L \Phi_k^C(x)\Phi_m^F(x)dx, \quad k = 1, \cdots N, \ m = 1, \cdots, M, \tag{3.193}$$

$$A_{mk}^{F-F} = \int_0^L \Phi_m^F(x)\Phi_k^F(x)dx, \quad m, k = 1, \cdots, M. \tag{3.194}$$

A direct calculation based on the explicit expressions of the eigenfunctions (3.175) and (3.179), shows that the entries of the matrix $\mathbf{A}$ are given by

$$A_{mn} = \frac{1}{\rho_0^2 L} \text{ for } m \neq n, \quad A_{nn} = \frac{3}{2\rho_0^2 L}, \tag{3.195}$$

$m, n = 1, \cdots, M + N$, and

$$\det(\mathbf{A}) = (2M + 2N + 1)\left(\frac{1}{2\rho_0^2 L}\right)^{M+N}, \tag{3.196}$$

$$(\mathbf{A})_{mn}^{-1} = -(2\rho_0^2 L)\frac{2}{2M + 2N + 1} \text{ for } m \neq n, \quad (\mathbf{A})_{nn}^{-1} = (2\rho_0^2 L)\frac{2M + 2N - 1}{2M + 2N + 1}, \tag{3.197}$$

$m, n = 1, \cdots, M + N$. Therefore, the unknown vector $\boldsymbol{\beta}$ in (3.190) has the following expression

$$\beta_n^C = \frac{2\rho_0^2 L}{2M + 2N + 1}\left((2M + 2N - 1)\delta\lambda_n^C - 2\left(\sum_{k=1, k\neq n}^{N} \delta\lambda_k^C + \sum_{j=1}^{M} \delta\lambda_j^F\right)\right), \tag{3.198}$$

$$\beta_m^F = \frac{2\rho_0^2 L}{2M + 2N + 1}\left((2M + 2N - 1)\delta\lambda_m^F - 2\left(\sum_{k=1, k\neq m}^{M} \delta\lambda_k^F + \sum_{j=1}^{N} \delta\lambda_j^C\right)\right) \tag{3.199}$$

$n = 1, ..., N, m = 1, ..., M$, and the first-order mass variation can be obtained by means of equation (3.188) (truncated series).

Next, we shall introduce the iteration of the previous analysis. Let us denote by $\{\lambda_n^{C(exp)}\}_{n=1}^N$, $\{\lambda_m^{F(exp)}\}_{m=1}^M$ the measured (or *target*) values of the eigenvalues $\{\lambda_n^C(\rho)\}_{n=1}^N$, $\{\lambda_m^F(\rho)\}_{m=1}^M$ of the perturbed nanorod with mass density $\rho(x) = \rho_0 + r_\epsilon(x)$. The function $\rho(x)$ is determined in $[0, L]$ by the iterative process

$$\rho^{(j+1)}(x) = \rho^{(j)}(x) + r^{(j)}(x), \quad j \geq 0, \tag{3.200}$$

with $\rho^{(0)}(x) \equiv \rho_0$. The subscript $\epsilon$ has been omitted to simplify the notation. The increment

$$r^{(j)}(x) = \sum_{k=1}^{N} \beta_k^{C(j)}\Phi_k^{C(j)}(x) + \sum_{k=1}^{M} \beta_k^{F(j)}\Phi_k^{F(j)}(x) \tag{3.201}$$

is evaluated by solving the $(N + M) \times (N + M)$ linear system

$$\boldsymbol{A}^{(j)}\boldsymbol{\beta}^{(j)} = \boldsymbol{\delta\lambda}^{(j)}, \tag{3.202}$$

in which $\boldsymbol{\delta\lambda}^{(j)} = (\delta\lambda_1^{C(j)}, \cdots, \delta\lambda_N^{C(j)}, \delta\lambda_1^{F(j)}, \cdots, \delta\lambda_M^{C(j)})$, with

$$\delta\lambda_n^{C(j)} \equiv 1 - \frac{\lambda_n^{C(exp)}}{\lambda_n^C(\rho^{(j)})}, \quad n = 1, \cdots, N, \tag{3.203}$$

$$\delta\lambda_m^{F(j)} \equiv 1 - \frac{\lambda_m^{F(exp)}}{\lambda_m^F(\rho^{(j)})}, \quad m = 1, \cdots, M. \tag{3.204}$$

The entries of the matrix $\mathbf{A}^{(j)}$ are as in (3.191)–(3.194), with the functions $\Phi_n^C(x)$, $\Phi_m^F(x)$ replaced by $\Phi_n^{C(j)}(x) = (v_n^C(x;\rho^{(j)}))^2$, $\Phi_m^{F(j)}(x) = (v_m^F(x;\rho^{(j)}))^2$, $n = 1, \cdots, N$, $m = 1, \cdots, M$. Here, $\{\lambda_n^C(\rho^{(j)}), v_n^C(x;\rho^{(j)})\}$, $\{\lambda_m^F(\rho^{(j)}), v_m^F(x;\rho^{(j)})\}$ are the $n$th and $m$th (mass normalized) eigenpairs of the clamped and clamped-free nanobeam with mass density $\rho^{(j)}(x)$, respectively. By solving (3.202) and using (3.200), (3.201), one has

$$\rho^{(j+1)}(x) = \rho_0 + \sum_{i=0}^{j} r^{(i)}(x), \quad j \geq 0, \tag{3.205}$$

and the iterations are stopped when the condition

$$e \equiv \frac{1}{N}\left(\sum_{n=1}^{N}\left(\frac{\lambda_n^{C(exp)} - \lambda_n^C(\rho^{(j)})}{\lambda_n^{C(exp)}}\right)^2\right)^{\frac{1}{2}} + \frac{1}{M}\left(\sum_{m=1}^{M}\left(\frac{\lambda_m^{F(exp)} - \lambda_m^F(\rho^{(j)})}{\lambda_m^{F(exp)}}\right)^2\right)^{\frac{1}{2}} < \gamma \tag{3.206}$$

is satisfied for a small given number $\gamma$.

The convergence of the iterative procedure described above can be studied by extending the methods discussed in Section 3.5, see also [26], where finite eigenvalue data coming from a single spectrum only were used. Here, we recall the main result for the present reconstruction method in case of smooth mass variations. There exists a positive number $\widehat{\epsilon}_\rho$, $\widehat{\epsilon}_\rho$ only depending on the a priori data of the inverse problem, such that if $\epsilon \leq \widehat{\epsilon}_\rho$, then the iterative procedure of identification converges uniformly to a continuous function in $[0, L]$, provided that $|\boldsymbol{\delta\lambda}^{(0)}| \leq \widehat{\varepsilon}_\lambda < 1$, where $|\boldsymbol{\delta\lambda}^{(0)}|$ is the Euclidean norm of the vector $\boldsymbol{\delta\lambda}^{(0)}$. The convergence result clearly has local character, since its proof holds on the assumption that the mass variation is a small perturbation of the total mass of the unperturbed nanorod. It should be noticed, in addition, that the local character is also reflected on the condition $|\boldsymbol{\delta\lambda}^{(0)}| \leq \widehat{\varepsilon}_\lambda < 1$, which requires that the first $N$, $M$ eigenvalues of the unperturbed nanorod under clamped and clamped-free end conditions, respectively, must be close enough to the corresponding target eigenvalues.

### 3.7.2 Applications

#### 3.7.2.1 Numerical setting and test specimen

In order to evaluate the performance of the reconstruction method, we have used an extended version of the numerical code originally developed in [26]. The code is based on a finite element model of the nanobeam, with third-degree polynomial spline approximation of the axial displacement in each finite element. The spatial mesh consists of $N_e$ equally spaced finite elements, and the mass coefficient is approximated by a continuous, piecewise linear function on each finite element. Most of the simulations have been performed taking $N_e = 200$ and using the same number of frequencies from both spectra, e.g., $M = N$, with $N$ up to 15. Local mass and stiffness matrices were evaluated in exact form, and the entries of the matrix $\mathbf{A}$ were determined by a trapezoidal rule of integration. The entire procedure, both for the direct and the inverse problem, was built in Scilab environment (version $5.5.2$). The computation time needed for a single iteration of the identification algorithm (for $N_e = 200$ and with $N = M = 15$) was about 1 second. We refer to [26] (Section $5.2$) for more details on the numerical procedure.

Concerning the test specimen, reference is made to the geometrical and material properties of the nanorod used in [49] and [26]. The radius $R$ of the circular equivalent cross-section is equal to $50\ \mu$m and the length $L$ is taken equal to $40\,R$; the material length scale parameters are assumed to be equal, and $\ell_0 = \ell_1 = 17.6$ $\mu$m; the Young's modulus $E$ is equal to $1.44$ GPa; the Poisson's coefficient is $\nu = 0.38$; and the volume mass density is equal to $\rho_{vol} = 1000$ kg/m$^3$. The coefficients $a$, $b$, $\rho_0$ corresponding to the above parameters take the value $a = 11.310$ N, $b = 3.554 \cdot 10^{-9}$ Nm$^2$, $\rho_0 = \rho_{vol} \cdot \pi R^2 = 7.854 \cdot 10^{-6}$ kg/m.

The method has been tested on an extended series of simulations, by varying, among other parameters, the number $M$, $N$ of the first eigenfrequencies and the geometry of the mass variation (e.g., position, intensity, regularity). In particular, two main classes of mass variations will be considered hereinafter, namely, smooth or discontinuous mass functions $r_\epsilon(x)$, see Figure 3.15. The results of identification for free-error data are presented first, that is, only errors due to numerical approximation are included in the following analysis.

Before presenting the results, we recall that a preliminary series of tests were carried out in order to select a suitable mesh size for the numerical solution of the direct and inverse eigenvalue problem. The analysis suggests to assume a mesh with $N_e = 200$ equally spaced finite elements, which turns out to be a good compromise between accuracy (maximum error on the first $N = M = 15$ eigenvalues less than $6.4 \cdot 10^{-5}$ percent) and computational cost for all the cases studied, including the reconstruction procedure. Moreover, preliminary tests suggest to choose $\gamma = 10^{-5}$ in the stopping criterion (3.206).

### 3.7.3 Identification of smooth mass coefficients

The identification of smooth coefficients (e.g., continuous mass distribution) leads to good results. Figures 3.16-3.18 show typical reconstructions of the mass density

$$\rho(x) = \rho_0 + \rho_0 t \cos^2\left(\frac{\pi(x-s)}{c}\right) \chi_{[s-\frac{c}{2}, s+\frac{c}{2}]}, \tag{3.207}$$

where $\chi_{[L_1,L_2]}$ is the characteristic function of the interval $[L_1, L_2]$, $s$ is the central point of the support of the mass variation, $c$ is the length of the support, $\rho_0 t$ is the maximum amplitude of variation, see Figure 3.15(a). For the sake of completeness, let us recall that the characteristic function $\chi_I : \mathbb{R} \to \mathbb{R}$ of the closed interval $I$, $I \subset \mathbb{R}$, is defined as $\chi_I(x) = 1$ if $x \in I$, $\chi_I(x) = 0$ if $x \in \mathbb{R} \setminus I$. The results for the two challenging cases corresponding to small mass increase and large mass increase, both supported in a small interval, (e.g., $s/L = 0.35$, $c/L = 0.1$, $t = 0.1$ and $s/L = 0.35$, $c/L = 0.1$, $t = 1$, respectively) are presented for $N = M$ in Figure 3.16 and 3.17. The global mass change ranges from $0.5\%$ to $5.0\%$ of the initial mass $\rho_0 L$, for $(\frac{c}{L} = 0.10,\ t = 0.10)$ and $(\frac{c}{L} = 0.10,\ t = 1.0)$, respectively.

We see that, in the first case, the identified coefficient agrees well with the exact one, and accuracy of reconstruction rapidly improves as $N$ increases. Similar properties hold for the second case, apart from the oscillatory character of the reconstructed coefficient around the actual mass value, which is more evident for $N = 9$, whereas it becomes almost negligible when $N = 15$. Few iterations are sufficient to satisfy the convergence criterion (3.206) with $\gamma = 10^{-5}$, e.g., less than five in the present cases. For the sake of completeness, it should be noted that part of our results involve not necessarily small mass variations, see, for example, Figure 3.18, with mass change equal to $15$ per cent of the initial mass $\rho_0 L$.

In Table 3.3 some synthetic information concerning the sequence of iterations is reported. At most four iterations are required to fulfill the convergence criterion in all the cases considered. The quantity $e$ defined as the average difference between identified and target eigenvalues, see equation (3.206), is reduced at each step of $1-2$ orders of magnitude. The $L^2$ and $L^\infty$ errors on the mass coefficient estimate are both reduced through the iterations. In particular, for $M = N = 15$ the relative errors in $L^2$ and $L^\infty$ norm are less than $7\%$ and $5\%$ of the initial values, respectively, confirming the accuracy in reconstructing smooth mass distributions. It should be also pointed out that the matrix $\mathbf{A}^{(j)}$ is always well conditioned during the iterations, with condition number $\kappa(\mathbf{A}^{(j)}) = \|\mathbf{A}^{(j)}\| \, \|(\mathbf{A}^{(j)})^{-1}\|$ ranging between 30 and 200 in all the cases studied. Here, $\|\mathbf{A}^{(j)}\| = \max_{|\mathbf{y}|=1} |\mathbf{A}^{(j)}\mathbf{y}|$, where $|\mathbf{y}| = \sqrt{\mathbf{y} \cdot \mathbf{y}}$ is the Euclidean norm of the vector $\mathbf{y} \in \mathbb{R}^{N+M}$.

We briefly discuss the results of the reconstruction when a different number of resonant frequencies belonging to the two spectra is chosen. The closed-form solution of the inverse linearized problem in the neighborhood of the uniform nanorod presented above shows that, in the extreme case in which the frequency data belong to the single spectrum under clamped end conditions, only the even generalized Fourier coefficients of the first-order mass variation can be determined. As a consequence, the reconstructed mass variation is symmetric with respect to the mid-point $x = L/2$ and shows an appreciable increase of the mass density exactly inside the actual region of the interval $[0, L/2]$ affected by the mass change, see, for instance, Figure 3.19. The estimate of the mass density amplitude, however, is rather inaccurate, showing an underestimate of about $50\%$. This indeterminacy is typical of the identification in symmetrical systems by eigenvalue data only, and it has been found also in other contexts, see, for example, the identification of damage in full-scale beams performed in [10] (see Figure 9 of this reference). When, on the other hand, only the resonant frequencies of the clamped-free spectrum are used, our numerical simulations show that the graph of the mass variation is approximately odd with respect to $x = L/2$. Therefore, in case of positive mass variations (i.e., $r_\epsilon(x) \geq 0$), this implies a significant difference between identified and exact coefficient, as it is shown in Figure 3.20. Finally, significant discrepancy was also found in the intermediate cases in which $N \neq M$, primarily since some generalized Fourier coefficients are missing in the expression of $r_\epsilon(x)$, see Figure 3.21. Basing on the above considerations and results, our experience suggests that it is preferable to use the same number of first frequencies in both spectra. It can be shown that similar conclusions can be drawn in determining discontinuous mass variations.

### 3.7.4 Identification of discontinuous mass coefficients

The determination of discontinuous mass coefficients is more problematic, since it is expected that the reconstruction may fail near the jump discontinuities. Some representative results are shown for the coefficient

$$\rho(x) = \rho_0 + \rho_0 t \cdot \chi_{[s-\frac{c}{2}, s+\frac{c}{2}]}, \tag{3.208}$$

where $s$, $c$, $t$ have the same meaning as in the previous section, see Figure 3.15(b). These cases correspond to perturbation located near the left end of the nanorod ($s/L = 0.15$) and with small support ($c/L = 0.1$), but having either small ($t = 0.1$, case i)) or large ($t = 1.0$, case ii)) intensity, respectively. In case i) (see Figure 3.22), the results are accurate enough for $N = 12 - 15$, whereas oscillations of the identified mass coefficient have appreciable amplitude in case ii) (see Figure 3.23), and propagate in the remaining part of the interval. As it was expected, pointwise estimates of the mass change fail near the jumps. The support of the mass perturbation is slightly overestimated, whereas it turns out that the mean value of the mass change is estimated with good accuracy.

Numerical results also show that the reconstruction of large mass variations is accurate enough, see Figure 3.24, although a large number of frequencies (e.g., $M = N = 20 - 25$ with $N_e = 400$) and more iterations (less than $10$) are needed to reduce the oscillatory character of the identified mass profile, see Figure 3.25. Regarding this point, we recall that when the present method is combined with the physical a priori information that the mass variation is positive, the reconstruction of discontinuous distributions may further be improved, leading to better uniform approximation of the actual solution. We refer to [26] (Section $5.3.4$) for more details and applications.

### 3.7.5 Application to noisy data

In order to test the robustness of the method, the identification was carried out by perturbing the target noise-free resonant frequencies belonging to the two spectra $\sqrt{\lambda_n^{exp}}$ as follows

$$\sqrt{\lambda_n^{exp-err}} = \sqrt{\lambda_n^{exp}} + \tau_n. \tag{3.209}$$

Here, $\tau_n$ is a random Gaussian variable with vanishing mean and standard deviation $\sigma$ such that $3\sigma = 2\pi\Pi$, where $\Pi$ is the maximum admitted error in the frequency measurements. The effect of errors was evaluated both for smooth and discontinuous mass distributions, by considering different profile of the coefficient and by varying the number $N = M$ of the first eigenfrequencies used in identification, for increasing values of $\Pi$ ranging from $100$ Hz to $5000$ Hz. A selected, though representative, set of results is shown in Figures 3.26 and 3.27, for smooth and discontinuous mass coefficients, respectively. For each position along the nanorod axis, and besides the exact mass coefficient, every subfigure contains three curves: the curve of the mean value and the two curves obtained by adding $\pm 3\sigma$ to the mean value. One thousand of simulations was performed for each case. It turns out that the three curves are almost indistinguishable for $\Pi = 100$ Hz. Appreciable discrepancy occurs for $\Pi = 1000$ Hz, and for $\Pi$ greater than $3000$ Hz the quality of the reconstruction is poor. In particular, for $\Pi$ less than $2000$ Hz, the effect of errors makes it possible to discriminate the presence of even minor variations of mass, either regular or discontinuous, and for which the influence of errors on the data is expected to be more significant. It should be noted that $\Pi = 2000$ Hz corresponds to percentage errors ranging approximately from $0.05$ (high frequency) to $0.65$ (low frequency) per cent of the unperturbed first fifteen resonant frequencies. Finally, the convergence speed of the iterative method is not significantly affected by the random noise, and the number of iterations needed to get convergence is slightly bigger than in the error-free case.

**Table 3.3:** *Some results of the reconstruction of smooth mass changes as in* (3.207) *versus iteration number* $j$ *(up to convergence), with (a):* $\frac{s}{L} = 0.35$, $\frac{c}{L} = 0.10$, $t = 0.10$ *(Figure 3.16); (b):* $\frac{s}{L} = 0.35$, $\frac{c}{L} = 0.10$, $t = 1.00$ *(Figure 3.17); (c):* $\frac{s}{L} = 0.35$, $\frac{c}{L} = 0.30$, $t = 1.00$ *(Figure 3.18), using the first* $N = 6$ *(columns* $2-5$*),* $N = 15$ *(columns* $6-9$*) eigenfrequencies. The quantity* $e$ *is defined in* (3.206)*;* $e_{L^2} = \frac{\|\rho^{ident}-\rho^{exact}\|_{L^2}}{\|\rho^{exact}\|_{L^2}}$, $e_{L^\infty} = \frac{\|\rho^{ident}-\rho^{exact}\|_{L^\infty}}{\|\rho^{exact}\|_{L^\infty}}$*, where* $\rho^{ident} = \rho^{ident}(x)$, $\rho^{exact} = \rho^{exact}(x)$ *are the identified and the exact mass density per unit length, respectively.* $\kappa(\mathbf{A}^{(j)})$ *is the condition number of the matrix* $\mathbf{A}^{(j)}$*. The unperturbed nanorod corresponds to* $j = 0$*.*

(a)

| $j$ | $e$ | $\kappa(\mathbf{A}^{(j)})$ | $e_{L^2}$ | $e_{L^\infty}$ | $e$ | $\kappa(\mathbf{A}^{(j)})$ | $e_{L^2}$ | $e_{L^\infty}$ |
|---|---|---|---|---|---|---|---|---|
| 0 | $1.69 \cdot 10^{-3}$ | $2.50 \cdot 10^{+1}$ | $1.92 \cdot 10^{-2}$ | $9.09 \cdot 10^{-2}$ | $1.01 \cdot 10^{-3}$ | $6.10 \cdot 10^{+1}$ | $1.92 \cdot 10^{-2}$ | $9.09 \cdot 10^{-2}$ |
| 1 | $2.50 \cdot 10^{-5}$ | $2.50 \cdot 10^{+1}$ | $1.01 \cdot 10^{-2}$ | $3.84 \cdot 10^{-2}$ | $2.69 \cdot 10^{-5}$ | $6.10 \cdot 10^{+1}$ | $1.66 \cdot 10^{-3}$ | $5.57 \cdot 10^{-3}$ |
| 2 | $4.27 \cdot 10^{-8}$ | $2.75 \cdot 10^{+1}$ | $1.01 \cdot 10^{-2}$ | $3.74 \cdot 10^{-2}$ | $2.32 \cdot 10^{-7}$ | $7.42 \cdot 10^{+1}$ | $1.39 \cdot 10^{-3}$ | $4.24 \cdot 10^{-3}$ |

(b)

| $j$ | $e$ | $\kappa(\mathbf{A}^{(j)})$ | $e_{L^2}$ | $e_{L^\infty}$ | $e$ | $\kappa(\mathbf{A}^{(j)})$ | $e_{L^2}$ | $e_{L^\infty}$ |
|---|---|---|---|---|---|---|---|---|
| 0 | $1.63 \cdot 10^{-2}$ | $2.50 \cdot 10^{+1}$ | $1.81 \cdot 10^{-1}$ | $5.00 \cdot 10^{-1}$ | $9.03 \cdot 10^{-3}$ | $6.10 \cdot 10^{+1}$ | $1.81 \cdot 10^{-1}$ | $5.00 \cdot 10^{-1}$ |
| 1 | $1.89 \cdot 10^{-3}$ | $2.50 \cdot 10^{+1}$ | $9.86 \cdot 10^{-2}$ | $2.45 \cdot 10^{-1}$ | $1.53 \cdot 10^{-3}$ | $6.10 \cdot 10^{+1}$ | $5.89 \cdot 10^{-2}$ | $1.55 \cdot 10^{-1}$ |
| 2 | $9.03 \cdot 10^{-5}$ | $5.34 \cdot 10^{+1}$ | $9.40 \cdot 10^{-2}$ | $1.95 \cdot 10^{-1}$ | $1.95 \cdot 10^{-4}$ | $1.93 \cdot 10^{+2}$ | $1.30 \cdot 10^{-2}$ | $2.52 \cdot 10^{-2}$ |
| 3 | $4.19 \cdot 10^{-7}$ | $6.27 \cdot 10^{+1}$ | $9.40 \cdot 10^{-2}$ | $1.95 \cdot 10^{-1}$ | $6.09 \cdot 10^{-6}$ | $3.17 \cdot 10^{+2}$ | $8.40 \cdot 10^{-3}$ | $1.53 \cdot 10^{-2}$ |

(c)

| $j$ | $e$ | $\kappa(\mathbf{A}^{(j)})$ | $e_{L^2}$ | $e_{L^\infty}$ | $e$ | $\kappa(\mathbf{A}^{(j)})$ | $e_{L^2}$ | $e_{L^\infty}$ |
|---|---|---|---|---|---|---|---|---|
| 0 | $4.46 \cdot 10^{-2}$ | $2.50 \cdot 10^{+1}$ | $2.82 \cdot 10^{-1}$ | $5.00 \cdot 10^{-1}$ | $2.56 \cdot 10^{-2}$ | $6.10 \cdot 10^{+1}$ | $2.82 \cdot 10^{-1}$ | $5.00 \cdot 10^{-1}$ |
| 1 | $8.44 \cdot 10^{-3}$ | $2.50 \cdot 10^{+1}$ | $1.01 \cdot 10^{-1}$ | $1.92 \cdot 10^{-1}$ | $4.73 \cdot 10^{-3}$ | $6.10 \cdot 10^{+1}$ | $1.02 \cdot 10^{-1}$ | $1.97 \cdot 10^{-1}$ |
| 2 | $8.70 \cdot 10^{-4}$ | $5.25 \cdot 10^{+1}$ | $1.99 \cdot 10^{-2}$ | $3.38 \cdot 10^{-2}$ | $5.20 \cdot 10^{-4}$ | $1.29 \cdot 10^{+2}$ | $1.91 \cdot 10^{-2}$ | $3.80 \cdot 10^{-2}$ |
| 3 | $2.90 \cdot 10^{-5}$ | $7.91 \cdot 10^{+1}$ | $1.05 \cdot 10^{-2}$ | $1.68 \cdot 10^{-2}$ | $1.85 \cdot 10^{-5}$ | $1.95 \cdot 10^{+2}$ | $2.16 \cdot 10^{-3}$ | $3.15 \cdot 10^{-3}$ |
| 4 | $7.49 \cdot 10^{-8}$ | $8.17 \cdot 10^{+1}$ | $1.05 \cdot 10^{-2}$ | $1.65 \cdot 10^{-2}$ | $8.27 \cdot 10^{-8}$ | $2.03 \cdot 10^{+2}$ | $2.05 \cdot 10^{-3}$ | $2.92 \cdot 10^{-3}$ |

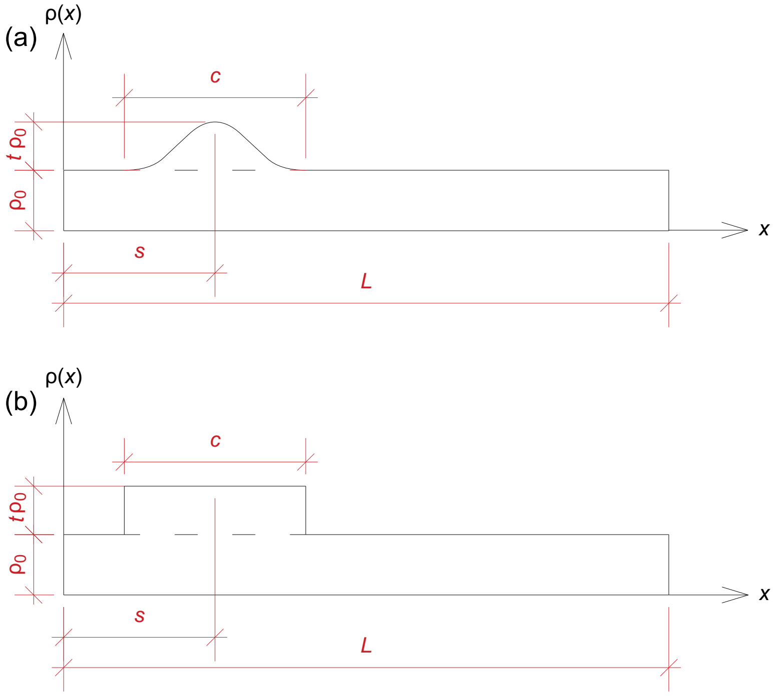

**Figure 3.15:** *Mass density per unit length* $\rho = \rho(x)$ *to be identified in* $[0, L]$*. (a) Smooth mass changes as in* (3.207)*; (b) discontinuous mass changes as in* (3.208)*.*

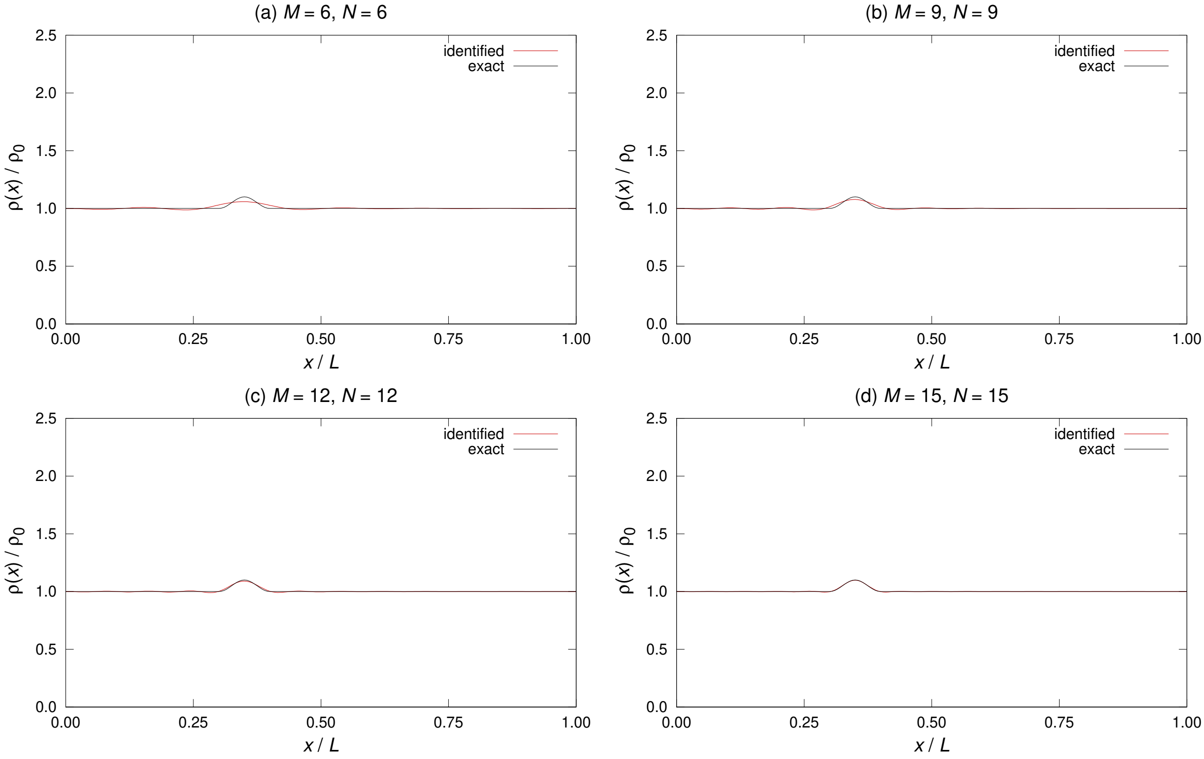

**Figure 3.16:** *Reconstruction of smooth mass changes as in* (3.207)*, with* $\frac{s}{L} = 0.35$*,* $\frac{c}{L} = 0.10$*,* $t = 0.10$*, using the first* $N = M = 6, 9, 12, 15$ *eigenfrequencies of both spectra.*

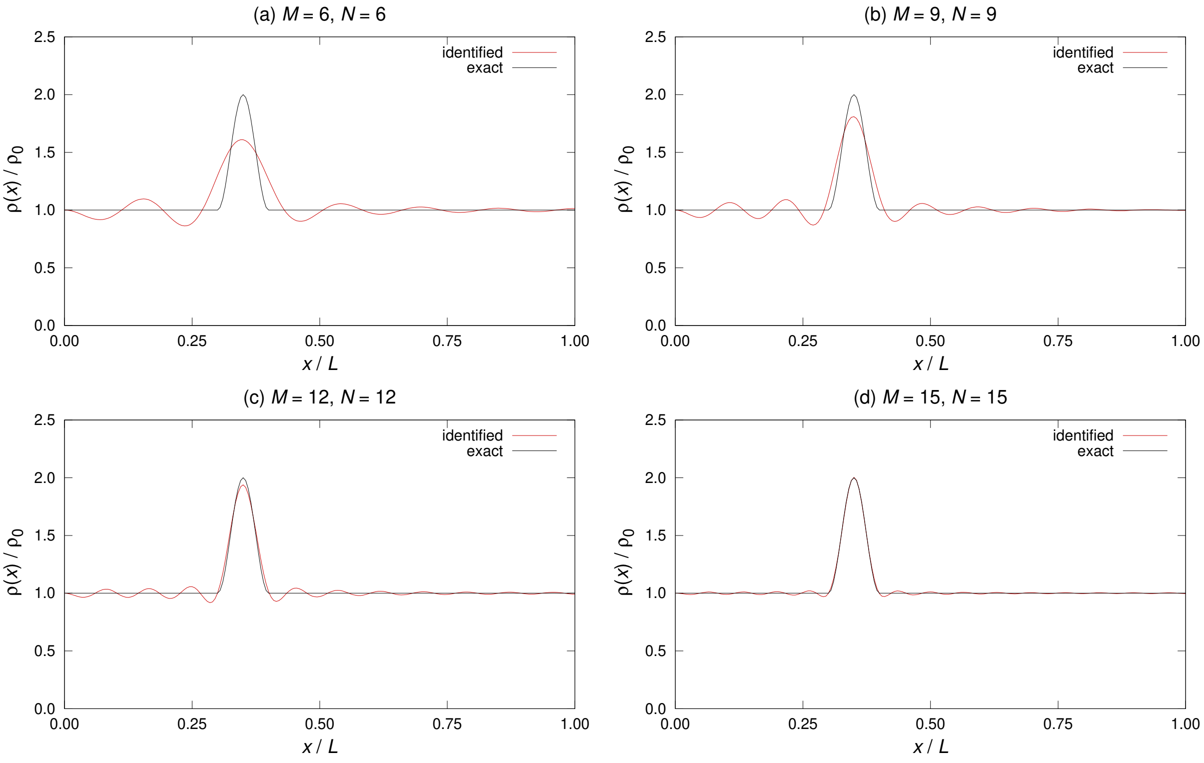

**Figure 3.17:** *Reconstruction of smooth mass changes as in* (3.207)*, with* $\frac{s}{L} = 0.35$*,* $\frac{c}{L} = 0.10$*,* $t = 1.00$*, using the first* $N = M = 6, 9, 12, 15$ *eigenfrequencies of both spectra.*

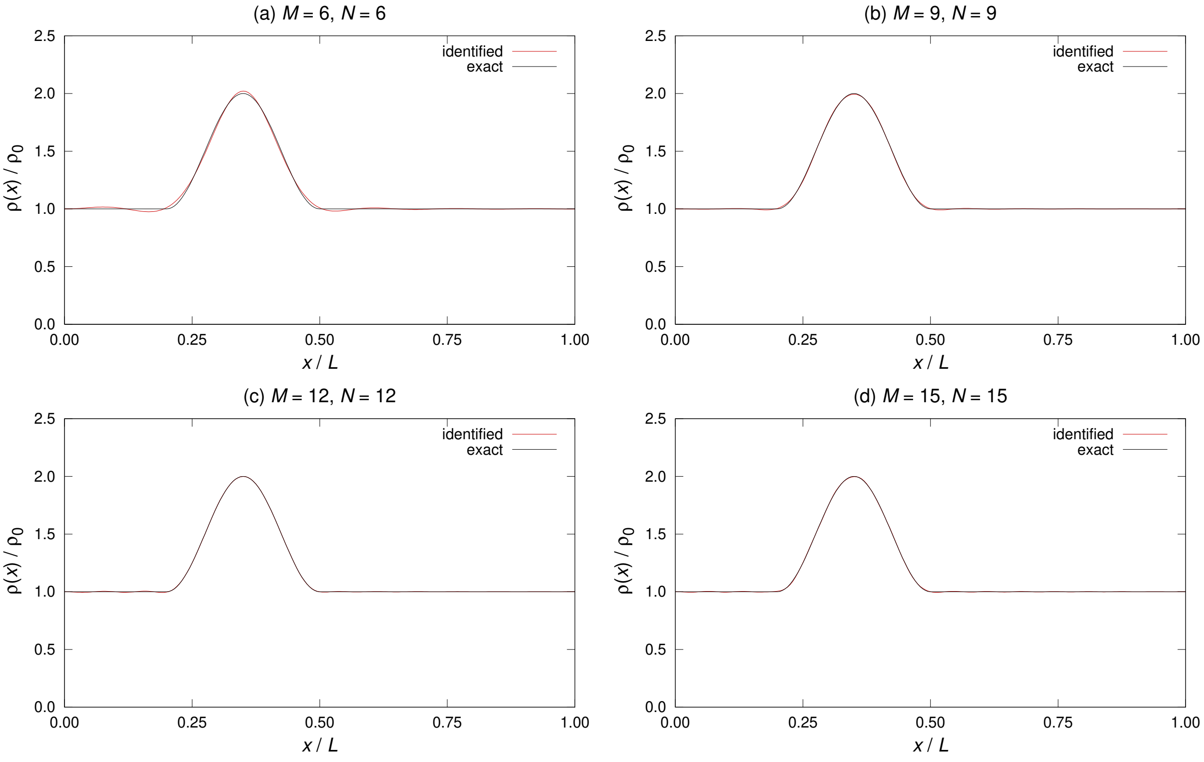

**Figure 3.18:** *Reconstruction of smooth mass changes as in* (3.207)*, with* $\frac{s}{L} = 0.35$*,* $\frac{c}{L} = 0.30$*,* $t = 1.00$*, using the first* $N = M = 6, 9, 12, 15$ *eigenfrequencies of both spectra.*

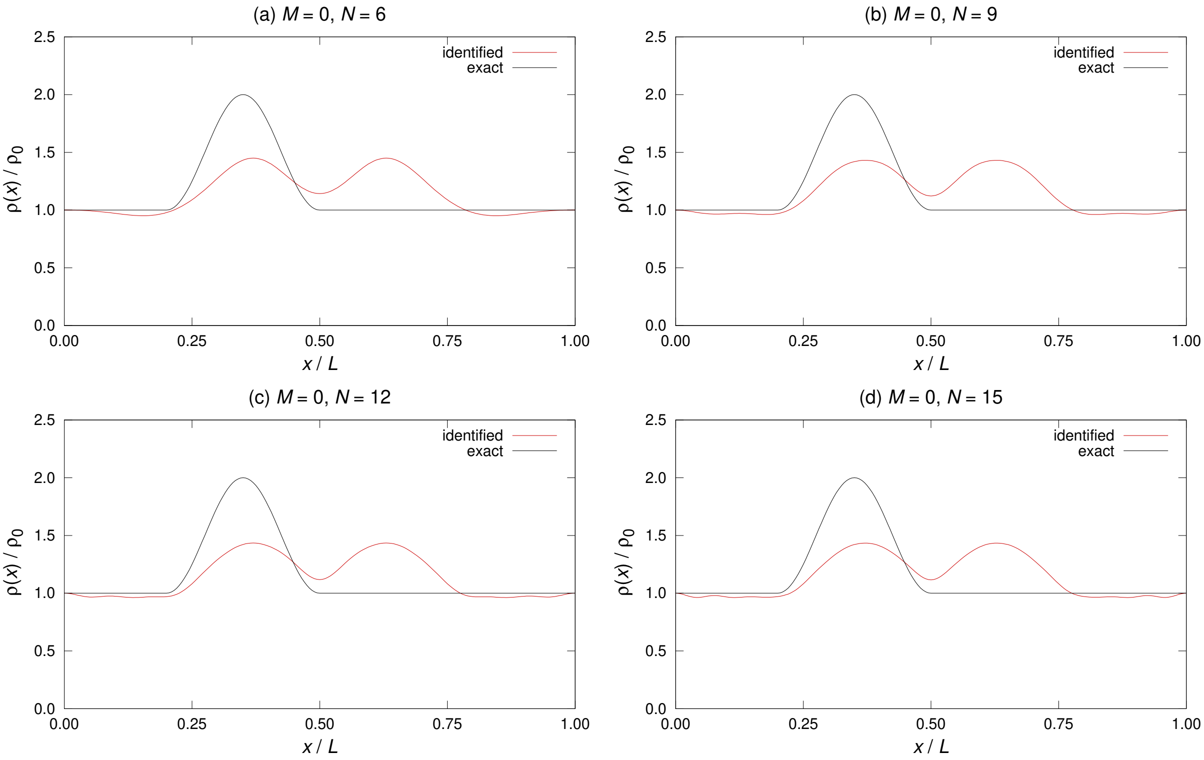

**Figure 3.19:** *Reconstruction of smooth mass changes as in* (3.207)*, with* $\frac{s}{L} = 0.35$*,* $\frac{c}{L} = 0.30$*,* $t = 1.00$*, using only the first* $N = 6, 9, 12, 15$ *eigenfrequencies of the clamped nanorod.*

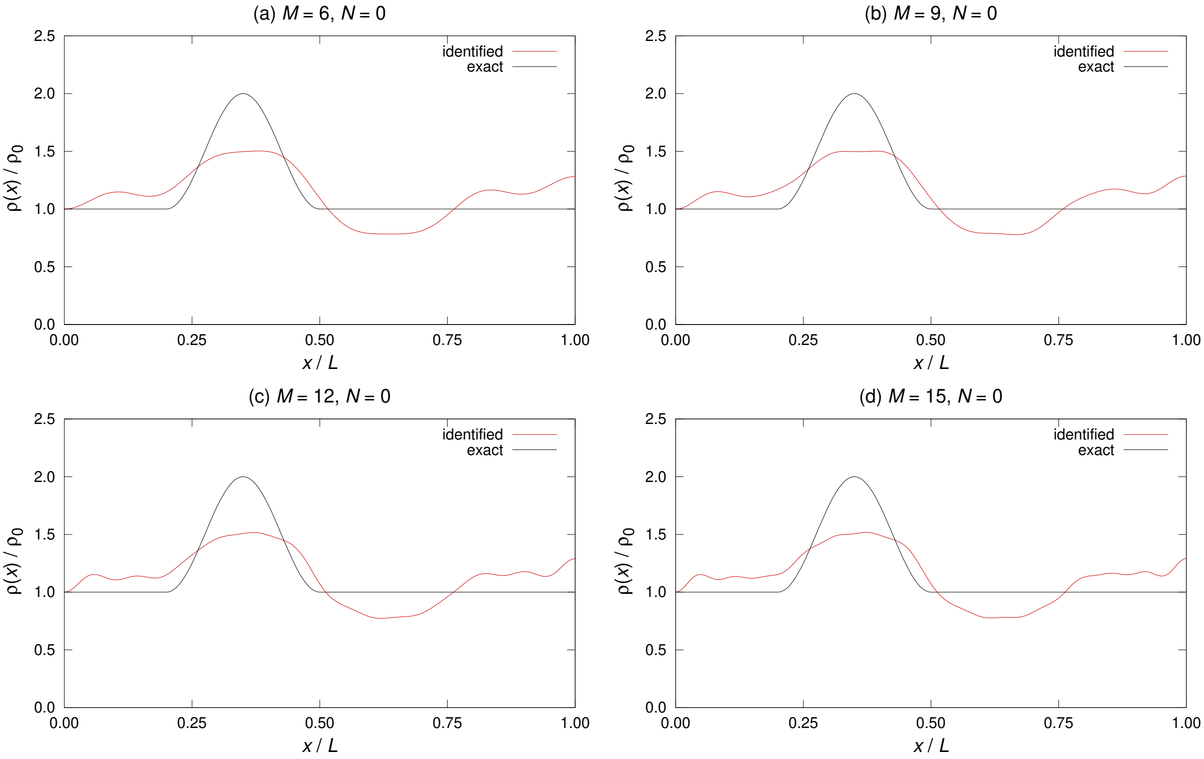

**Figure 3.20:** *Reconstruction of smooth mass changes as in* (3.207)*, with* $\frac{s}{L} = 0.35$*,* $\frac{c}{L} = 0.30$*,* $t = 1.00$*, using only the first* $M = 6, 9, 12, 15$ *eigenfrequencies of the clamped-free nanorod.*

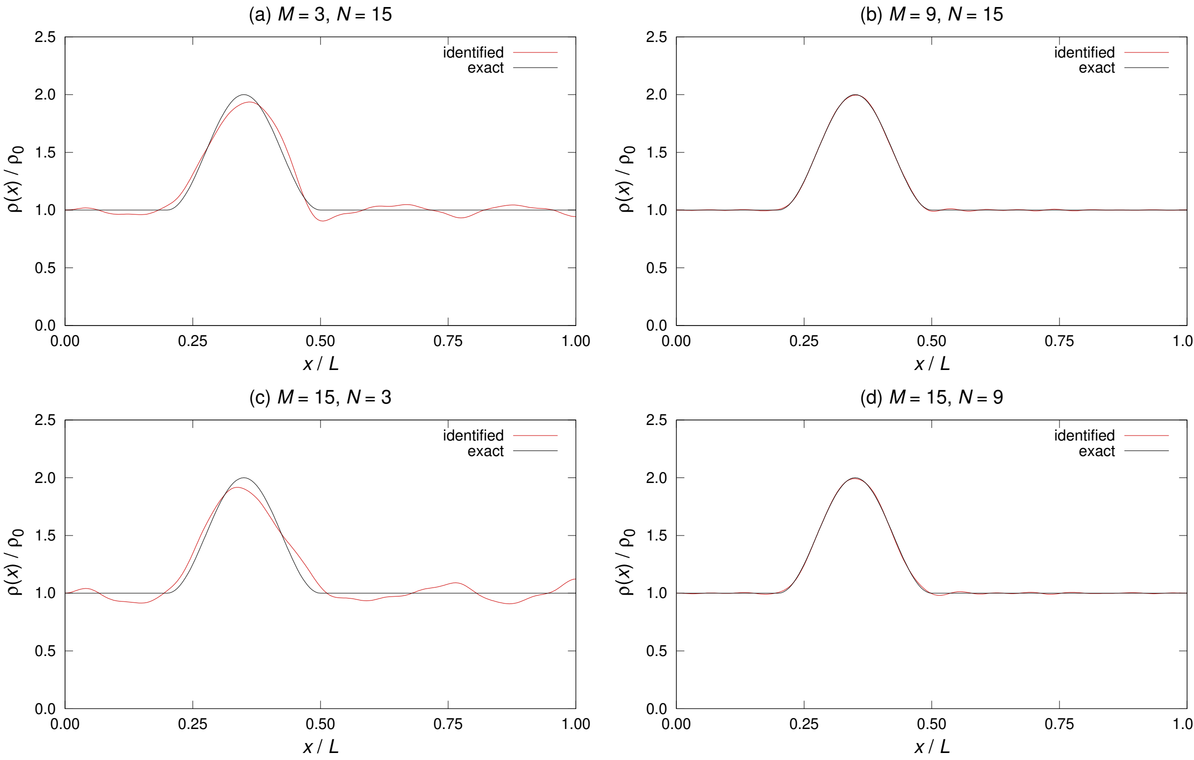

**Figure 3.21:** *Reconstruction of smooth mass changes as in* (3.207)*, with* $\frac{s}{L} = 0.35$*,* $\frac{c}{L} = 0.30$*,* $t = 1.00$*, using the first* $(M, N) = (3, 15)$*,* $(M, N) = (9, 15)$*,* $(M, N) = (15, 3)$*,* $(M, N) = (15, 9)$ *eigenfrequencies of the two spectra.*

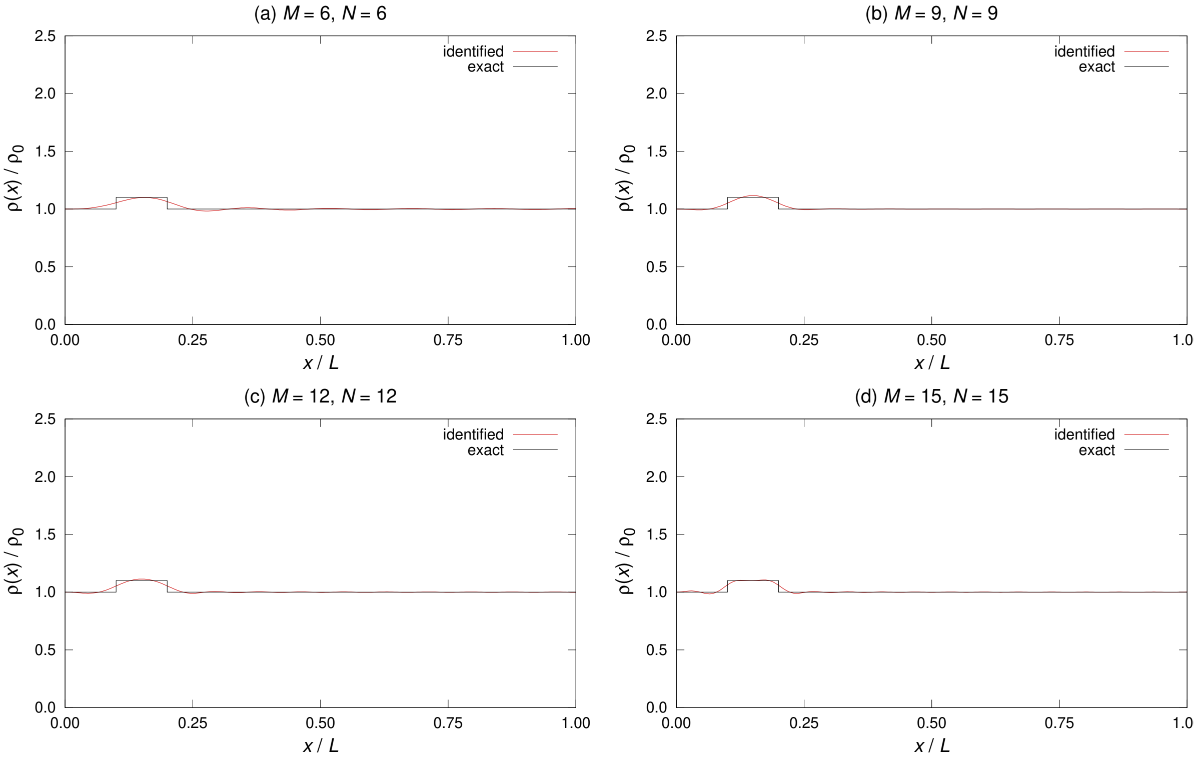

**Figure 3.22:** *Reconstruction of discontinuous mass changes as in* (3.208)*, with* $\frac{s}{L} = 0.15$*,* $\frac{c}{L} = 0.10$*,* $t = 0.10$*, using only the first* $N = M = 6, 9, 12, 15$ *eigenfrequencies of both spectra.*

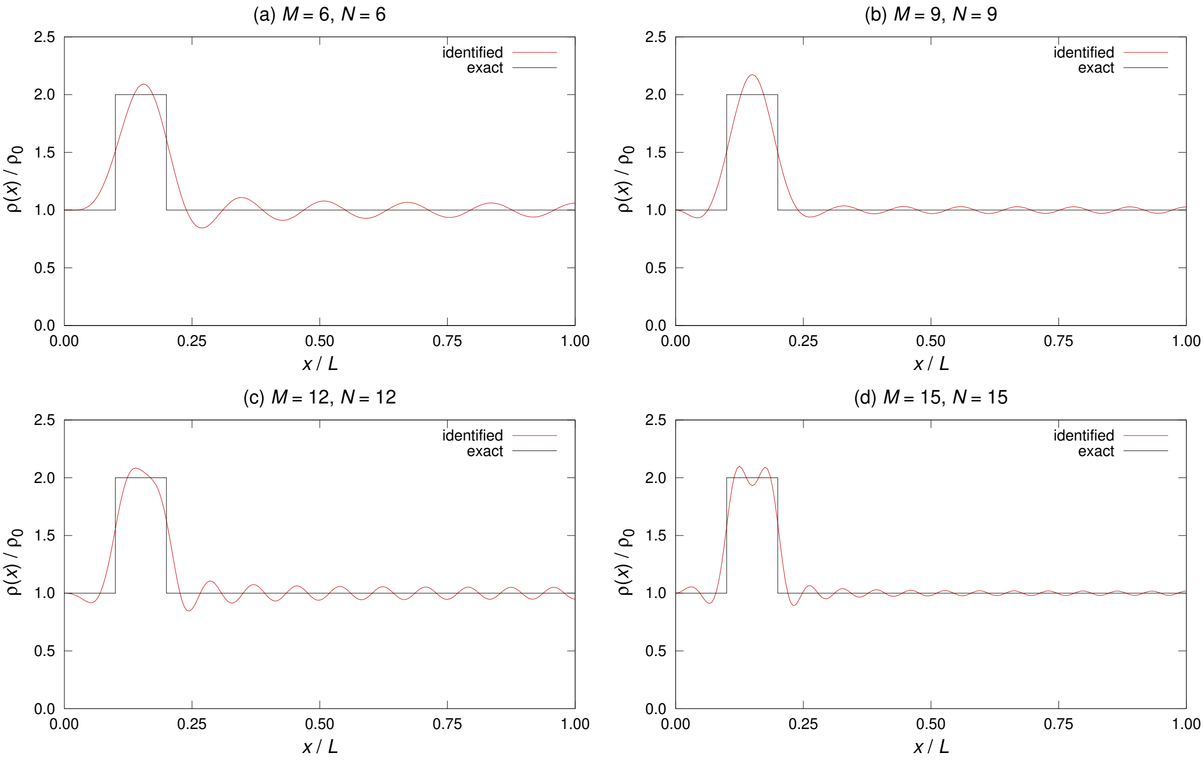

**Figure 3.23:** *Reconstruction of discontinuous mass changes as in* (3.208)*, with* $\frac{s}{L} = 0.15$*,* $\frac{c}{L} = 0.10$*,* $t = 1.00$*, using the first* $N = M = 6, 9, 12, 15$ *eigenfrequencies of both spectra.*

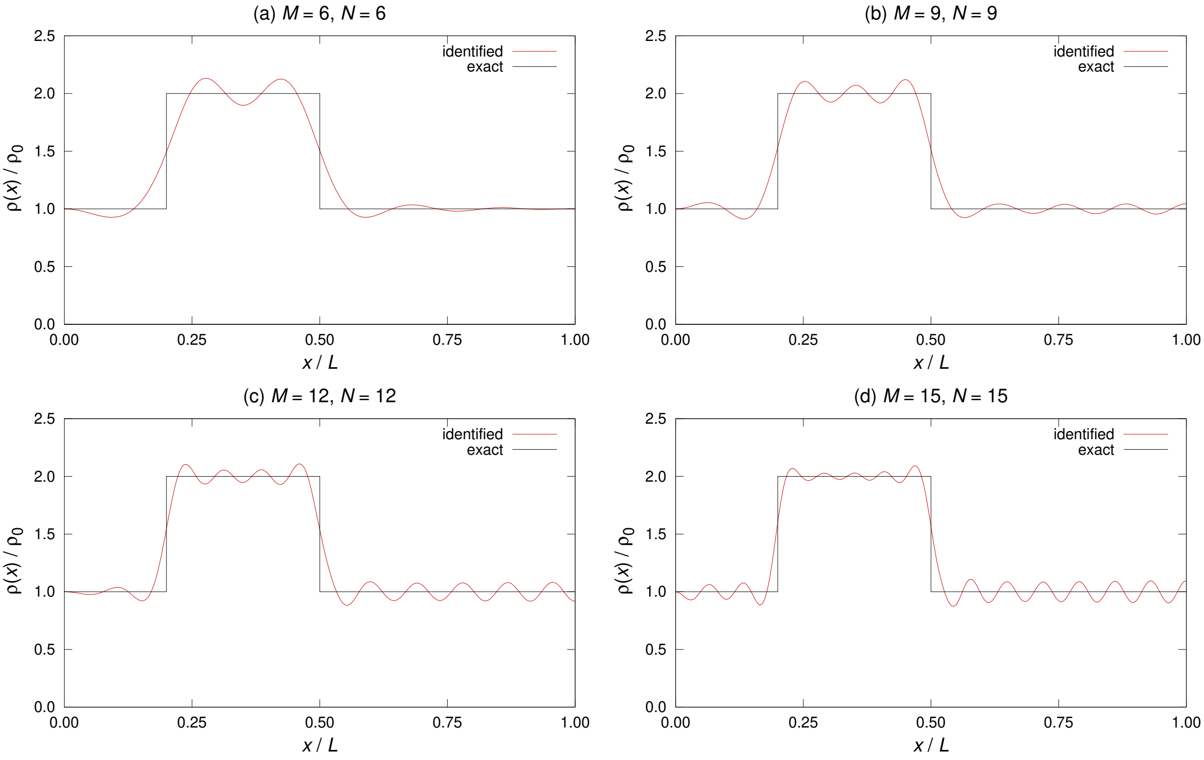

**Figure 3.24:** *Reconstruction of discontinuous mass changes as in* (3.208)*, with* $\frac{s}{L} = 0.35$*,* $\frac{c}{L} = 0.30$*,* $t = 1.00$*, using the first* $N = M = 6, 9, 12, 15$ *eigenfrequencies of both spectra.*

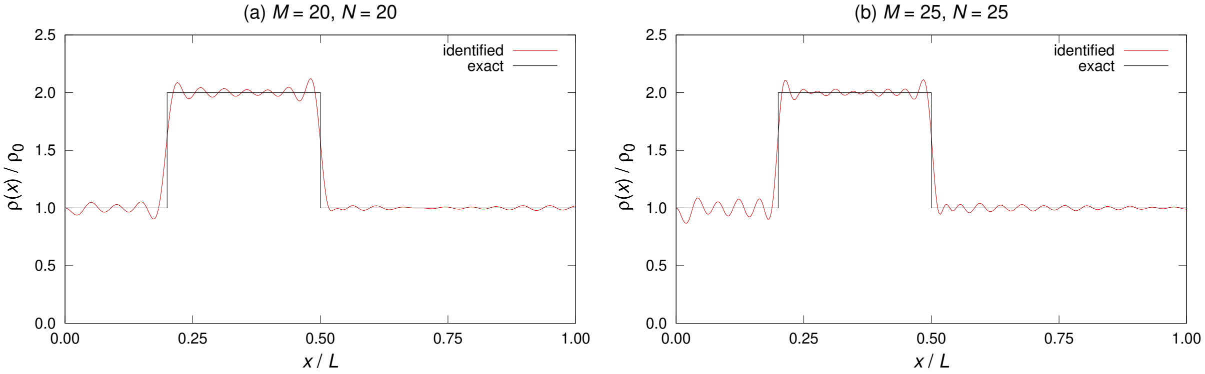

**Figure 3.25:** *Reconstruction of discontinuous mass changes as in* (3.208)*, with* $\frac{s}{L} = 0.35$*,* $\frac{c}{L} = 0.30$*,* $t = 1.00$*, using the first* $N = M = 20, 25$ *eigenfrequencies.*

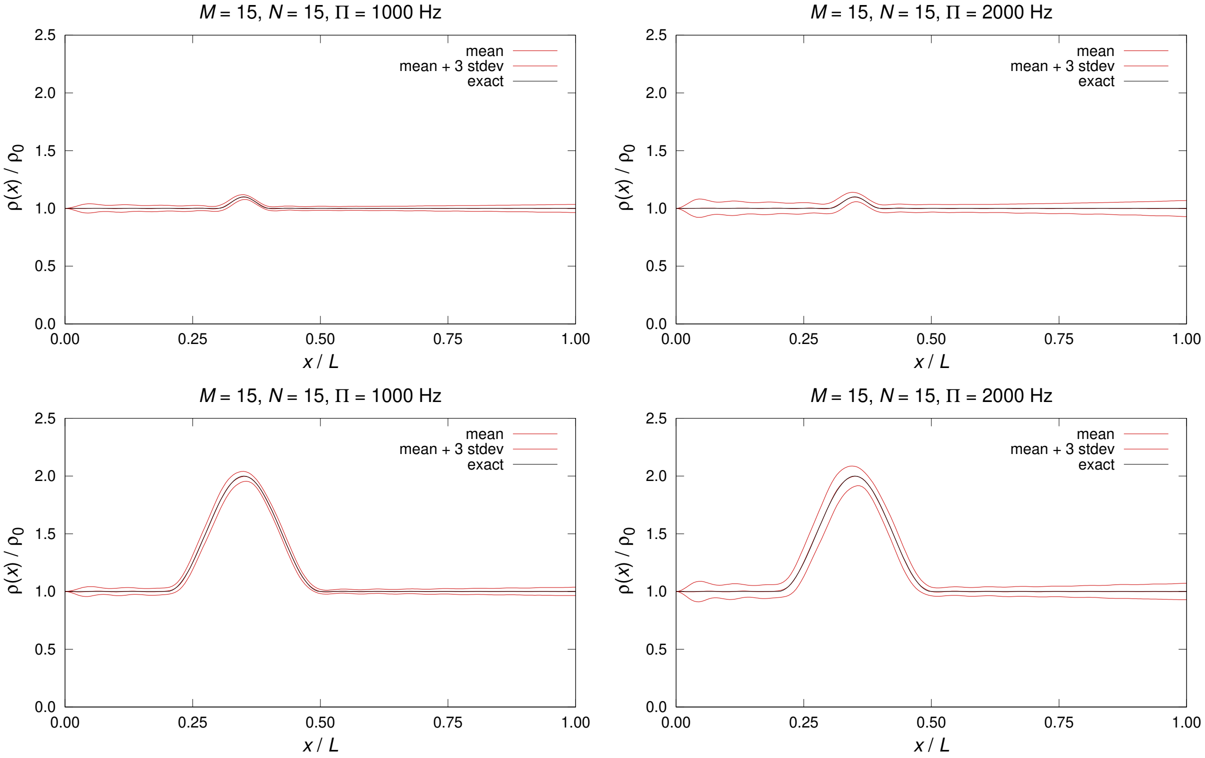

**Figure 3.26:** *Noise effects on identification of smooth mass changes. Upper row: mass changes as in* (3.207)*, with* $\frac{s}{L} = 0.35$*,* $\frac{c}{L} = 0.10$*,* $t = 0.10$*. Lower row: mass changes as in* (3.207)*, with* $\frac{s}{L} = 0.35$*,* $\frac{c}{L} = 0.30$*,* $t = 1.00$*.*

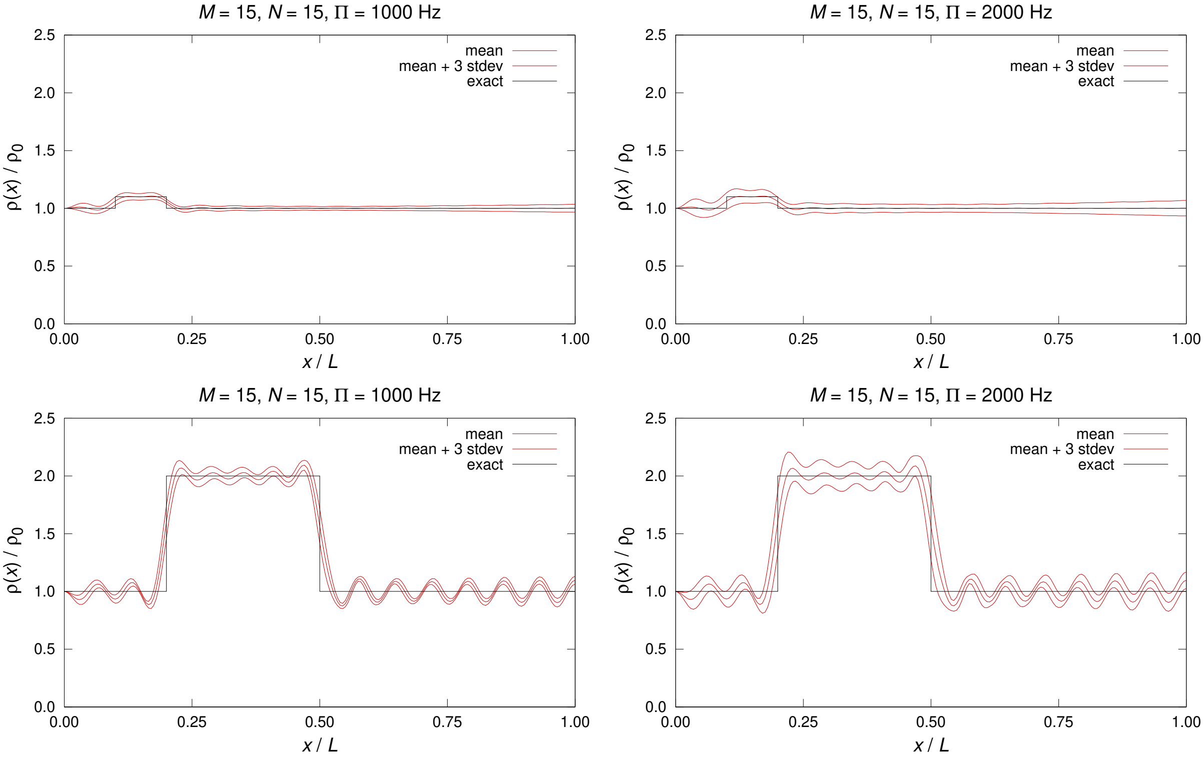

**Figure 3.27:** *Noise effects on identification of discontinuous mass changes. Upper row: mass changes as in* (3.208)*, with* $\frac{s}{L} = 0.15$, $\frac{c}{L} = 0.10$, $t = 0.10$. *Lower row: mass changes as in* (3.208)*, with* $\frac{s}{L} = 0.35$, $\frac{c}{L} = 0.30$, $t = 1.00$.

CHAPTER 4

# Mass identification using bending vibrations

## 4.1 Introduction

In this chapter, we extend the analysis of the inverse problem to the determination of distributed added mass in nanobeams under *bending vibration*. The nanobeam is modeled as in [49], and the eigenvalue problem consists of a 6th order ordinary differential equation with six end conditions.
In Section 4.2, we study an inverse problem analogous to that considered in in the first part of Section 3, that is, we try to identify a distributed mass added on half of the nanobeam by using the first lower eigenfrequencies of the spectrum under supported end conditions. Next, in Section 4.3, we extend the analysis to cover the more general case in which the mass vibration may affect the entire length of the nanobeam. We will see that two partial spectra (at least), corresponding to different end conditions, should be used in that case.
The results obtained via the Fourier Generalized Coefficient Method (GFCM) show that, for a discontinuous mass distribution, the solution of the inverse problem obtained using the first lower eigenfrequencies is very accurate at points which are far from the (possible) jump discontinuities of the mass coefficient. In fact, the large oscillations occurring near a discontinuity may obstruct the possibility to extract accurate point wise information about the unknown added mass. In order to filter out these undesired oscillations, we have implemented an optimization filtering based on a least-squares minimization of the Euclidean norm between experimental and analytical eigenvalues. Minimization is performed by assuming the corresponding solution of the GFCM as starting point, and the method allows to take into account the positivity constraint on the added mass. Numerical results, both for a single spectrum and for two spectra, show that this constrained least squares filter eliminates most of the oscillations produced by the GFCM, giving significantly better results for discontinuous mass coefficients.

The results presented in this chapter have been obtained in collaboration with José Fernández-Sáez and Ramón Zaera (University Carlos III de Madrid, Spain) and Michele Dilena and Antonino Morassi (University of Udine, Italy), and have been published in [27].

## 4.2 Reconstruction of mass variation supported on half interval from one partial spectrum

### 4.2.1 Formulation of the inverse problem and reconstruction method

We consider the inverse problem of determining a small distributed mass added to a referential nanobeam under supported end conditions by using the first $N$ eigenfrequency shifts of the bending vibration. We will see later on that additional a priori assumptions must be included in the analysis, particularly, the hypothesis that the support of the mass variation must be compactly contained in half interval of the nanobeam axis.

The spatial variation of the infinitesimal free bending vibration of the uniform, *unperturbed* or referential nanobeam of length $L$ is governed by the following eigenvalue problem (see, for instance, [49] and Section 2.3.2)

$$\begin{cases} Sv^{IV} - Kv^{VI} = \lambda\rho_0 v, \quad x \in (0,L), & (4.1)\\ v(0) = 0, \quad -Sv''(0) + Kv^{IV}(0) = 0, \quad v''(0) = 0, & (4.2)\\ v(L) = 0, \quad -Sv''(L) + Kv^{IV}(L) = 0, \quad v''(L) = 0, & (4.3) \end{cases}$$

where $\lambda$ is the eigenvalue and $v = v(x)$ the associated eigenfunction. The coefficient $\rho_0$=const., $\rho_0 > 0$, is the unperturbed mass density per unit length. The coefficients $K$ and $S$ are defined in (2.141), $K = \text{const} > 0$, $S = \text{const} > 0$. The set of non-classical boundary conditions selected above are only one of the two possible ones for nanobeam models based on strain gradient theories. However, the explicit expression of the sensitivity of the eigenvalues to the added mass (see, for example, (4.11)), our analysis could be extended also to other sets of non-classical boundary condition. In Section 4.3.1 the problem corresponding to the (non-classical) supported-sliding case is addressed.

The eigenpairs $\{\lambda_n^S,\, u_n^S(x)\}_{n=1}^{\infty}$ of (4.1)–(4.3) are

$$\lambda_n^S = \left(\frac{n\pi}{L}\right)^6 \left[\frac{1}{\rho_0}\left(K + \frac{S}{(\frac{n\pi}{L})^2}\right)\right], \tag{4.4}$$

$$u_n^S(x) = \sqrt{\frac{2}{\rho_0 L}} \sin\left(\frac{n\pi x}{L}\right), \quad n \geq 1, \tag{4.5}$$

where the mass-normalization condition $\int_0^L \rho_0 (u_n^S(x))^2 dx = 1$ has been taken into account.

We now assume that the mass density changes, and we denote by

$$\rho(x) = \rho_0 + r_\epsilon(x), \quad x \in [0,L], \tag{4.6}$$

the mass density per unit length of the perturbed nanobeam. On the mass variation $r_\epsilon = r_\epsilon(x)$, we assume:

$$\left(\frac{1}{L}\int_0^L (r_\epsilon(x))^2 dx\right)^{\frac{1}{2}} = \epsilon\rho_0, \tag{4.7}$$

$$r_\epsilon(x) \in L^\infty([0,L]), \tag{4.8}$$

$$0 < \rho^- \leq \rho(x) \leq \rho^+, \quad x \in [0,L], \tag{4.9}$$

$$supp\,(r_\epsilon(x)) = \overline{\{x \in [0,L] \mid r_\epsilon(x) \neq 0\}} \subset\subset \left[0, \frac{L}{2}\right], \tag{4.10}$$

where $\epsilon$, $0 < \epsilon \leq \widehat{\epsilon}_\rho$, for a given small number $\widehat{\epsilon}_\rho$, and $\rho^-$, $\rho^+$ are given constants independent of $\epsilon$. The eigenpairs of the problem (4.1)–(4.3), with $\rho_0$ replaced by $\rho(x)$, are denoted by $\left\{\lambda_n^S(\rho),\, u_n^S(x;\rho)\right\}_{n=1}^{\infty}$.

The inverse problem is linearized in a neighborhood of the unperturbed nanobeam. The normalized first order change of an eigenvalue of the nanobeam, evaluated with respect to the smallness parameter $\epsilon$, takes the explicit expression

$$\delta\lambda_n^S \equiv 1 - \frac{\lambda_n^S(\rho)}{\lambda_n^S} = \int_0^{\frac{L}{2}} r_\epsilon(x)\Phi_n^S(x)dx, \tag{4.11}$$

where

$$\Phi_n^S \equiv (u_n^S(x))^2 = \frac{2}{\rho_0 L}\sin^2\left(\frac{n\pi x}{L}\right), \quad n \geq 1. \tag{4.12}$$

Since $\left\{\Phi_n^S(x)\right\}_{n=1}^{\infty}$ is a basis of the square integrable functions defined on the interval $\left[0, \frac{L}{2}\right]$, we look for a $N$th order dimensional approximation of the added mass in the form

$$r_\epsilon(x) = \sum_{k=1}^{N} \beta_k^S \Phi_k^S(x) \cdot \chi_{[0,\frac{L}{2}]}, \tag{4.13}$$

Replacing (4.13) in (4.11), we obtain the $N \times N$ linear system

$$\delta\lambda_n = \sum_{k=1}^{N} A_{nk}\beta_k^S, \quad n = 1, ...., N, \tag{4.14}$$

with $A_{nk} = \int_0^{\frac{L}{2}} \Phi_n^S(x)\Phi_k^S(x)dx$, $n, k = 1, ..N$. A direct calculation shows that

$$A_{nk} = \frac{2}{4\rho_0^2 L} \quad \text{for } k \neq n, \quad A_{nn} = \frac{3}{4\rho_0^2 L}, \tag{4.15}$$

for $n, k = 1, 2, ..., N$,

$$\det(\mathbf{A}) = (2N+1)\left(\frac{1}{4\rho_0^2 L}\right)^N, \tag{4.16}$$

$$(\mathbf{A}^{-1})_{nk} = (4\rho_0^2 L)\frac{2N-1}{2N+1} \text{ for } n = k, \quad (\mathbf{A}^{-1})_{nk} = -(4\rho_0^2 L)\frac{2}{2N+1} \text{ for } n \neq k, \tag{4.17}$$

$n, k = 1, ..., N$. By using (4.17), the linear system (4.14) has the closed-form solution

$$\beta_k^S = 4\rho_0^2 L\left(\frac{2N-1}{2N+1}\delta\lambda_k^S - \frac{2}{2N+1}\sum_{j=1,\ j\neq k}^{N}\delta\lambda_j^S\right), \quad k = 1, ..., N, \tag{4.18}$$

and, by (4.13), we obtain

$$r^{(0)}(x) = 8\rho_0 \sum_{k=1}^{N}\left(\frac{2N-1}{2N+1}\delta\lambda_k^S - \frac{2}{2N+1}\sum_{j=1,j\neq k}^{N}\delta\lambda_j^S\right)\sin^2\left(\frac{k\pi x}{L}\right)\chi_{[0,\frac{L}{2}]}, \tag{4.19}$$

where the index $\epsilon$ has been omitted to simplify the notation.

The accuracy in the determination of $r(x)$ can be improved by using the following iterative procedure, already illustrated in Section 3.4 and for which $r^{(0)}(x)$ in (4.19) is the 0th-step approximation of $r(x)$. The analysis of the convergence of the iterative procedure can be carried out by adapting the arguments used in Section 3.5 to study the analogous inverse problem for longitudinal vibration. Here, we do not discuss the mathematical details of the proof of convergence, rather, we recall the main result in case of small, smooth mass variation. There exists a positive number $\widehat{\varepsilon}_\rho$,

$\widehat{\varepsilon}_\rho$ only depending on the a priori data of the inverse problem, such that, if $\varepsilon \le \widehat{\varepsilon}_\rho$, then the iterative procedure of identification converges uniformly to a continuous function in $[0, \frac{L}{2}]$ with the wished spectral properties, provided that $|\delta\boldsymbol{\lambda}^{S(0)}| \ge \widehat{\varepsilon_\lambda} < 1$, where $\delta\boldsymbol{\lambda}^{S(0)} = (\delta\lambda_1^{S(0)}, \dots, \delta\lambda_N^{S(0)})$ and $|\delta\boldsymbol{\lambda}^{S(0)}|^2 = \sum_{n=1}^{N}(\delta\lambda_n^{S(0)})^2$. The convergence result is of local character, since convergence is ensured only if the mass variation is a (smooth) small perturbation of the total mass of the unperturbed nanorod.

## 4.2.2 Applications

### 4.2.2.1 Numerical setting

The practical application of the reconstruction method needs the implementation of a numerical algorithm. The corresponding numerical code is based on the weak formulation of the eigenvalue problem (4.1)–(4.3). Let the set of admissible configurations defined as

$$\mathcal{H} = \{f : (0, L) \to \mathbb{R} |\ f \in H^3(0, L),\ f = f'' = 0 \text{ at } x = 0 \text{ and at } x = L\} \tag{4.20}$$

Here, $H^3(0, L)$ denotes the real-valued Hilbert space of the Lebesgue measurable functions $f$ with $\int_0^L \left( f^2 + \sum_{i=1}^{3} \left( \frac{d^i f}{dx^i} \right)^2 \right) < \infty$, where $\frac{d^i f}{dx^i}$ is the $i$th weak derivative of $f$ (see, for example, [15]).

The weak formulation of (4.1)–(4.3) consists in finding $\{u \in \mathcal{H} \setminus \{0\},\ \lambda \in \mathbb{R}\}$ such that

$$\int_0^L (Su''\varphi'' + Ku'''\varphi''')\, dx = \lambda \int_0^L \rho\, u\, \varphi\, dx, \quad \text{for every } \varphi \in \mathcal{H}. \tag{4.21}$$

In order to find a finite element model of the weak formulation (4.21), we select the finite-dimensional subspace of $\mathcal{H}$ formed by five-degree Hermite polynomial approximation of the transverse displacement of the nanobeam in each finite element. The interval $[0, L]$ is divided in $N_e$ equally spaced elements, with nodes at the points $x_i = i \cdot \Delta x,\ \Delta x = \frac{L}{N_e},\ i = 0, 1, ...N_e$. Therefore, the discrete version of (4.21) consists in determining the approximating eigenpair $\{\widetilde{\boldsymbol{u}} \in \mathbb{R}^{2N_e} \setminus \{\boldsymbol{0}\},\ \widetilde{\lambda} \in \mathbb{R}\}$ solution to

$$\widetilde{\boldsymbol{F}}\widetilde{\boldsymbol{u}} = \widetilde{\lambda}\widetilde{\boldsymbol{M}}\widetilde{\boldsymbol{u}}, \tag{4.22}$$

where the $(n, k)$-entry of the local mass, $\widetilde{M}_i^{nk}$, and stiffness, $\widetilde{F}_i^{nk}$, matrix in the $i$th finite element $[x_i, x_{i+1}]$ take the expressions

$$\begin{aligned} \widetilde{M}_i^{nk} &= \int_{x_i}^{x_{i+1}} \widetilde{\rho}(x)\varphi_n(x)\varphi_k(x)dx, \\ \widetilde{F}_i^{nk} &= \int_{x_i}^{x_{i+1}} \left(S\varphi_n''(x)\varphi_k''(x) + K\varphi_n'''(x)\varphi_k'''(x)\right) dx, \end{aligned} \tag{4.23}$$

$n, k = 1, ..., 6$. The mass density per unit length $\rho = \rho(x)$ is approximated by a continuous piecewise linear function, e.g., $\widetilde{\rho}(x) = \rho(x_i) + \frac{\rho(x_{i+1}) - \rho(x_i)}{\Delta x} \cdot x$ for $x \in [x_i, x_{i+1}]$, and the integrals (4.23) were evaluated in exact form.

It should be noted that the use of the five-degree Hermite polynomials as shape functions, instead of the more complex functions corresponding to exact solution of the transverse displacement for a static bending problem [45], permits, despite of the simplicity of this approximation, a proper description of the vibrational behavior of the nanobeam, as it can be seen through the results presented in next sections.

Concerning the identification procedure, a standard trapezoidal method was used to evaluate the entries of the matrix **A**, and the discrete eigenvalue problem (4.22) was solved by means of the Implicit Restarted Lanczos's method [16]. The numerical procedure was built in Scilab environment (version 5.5.2).

#### 4.2.2.2 Test specimen

The material properties of the specimen correspond to epoxy and they have been used in [53,57,67], i.e., Young's modulus $E = 1.44$ GPa, Poisson's coefficient $\nu = 0.38$, volume mass density $\rho_{vol} = 1220\ kg/m^3$, and material length scale parameters $\ell_0 = \ell_1 = \ell_2 = \ell = 17.6\ \mu$m.

The equivalent cross-section is assumed to be rectangular, as in [25], with thickness $h = 50$ $\mu$m, width $b = 2h$, area $A = bh$, moment of inertia $I = bh^3/12$, and length $L = 20$h. The above parameters lead to the following coefficients: $S = 4.36 \cdot 10^{-9}\ Nm^2$, $K = 4.71 \cdot 10^{-19}\ Nm^4$, $\rho_0 = \rho_{vol} \cdot A = 6.1 \cdot 10^{-6}\ kg/m$.

#### 4.2.2.3 Reconstruction results

The performance of the reconstruction procedure has been tested on the class of *overlapping* mass variations shown in Figure 4.1. More precisely, the mass density to be determined has the expression

$$\rho(x) = \rho_0 + \rho_0 \max \left\{ t \cos^2 \left( \frac{\pi(x-s)}{c} \right) \chi_{[s-\frac{c}{2}, s+\frac{c}{2}]},\ t_1 \frac{x-(s_1-c_1)}{c_1} \chi_{[s_1-c_1, s_1]} \right\}, \tag{4.24}$$

where the intervals $[s-\frac{c}{2},\ s+\frac{c}{2}]$ and $[s_1-c_1,\ s_1]$ belong to $(0, \frac{L}{2})$; $s$ is the central point of the smooth mass variation term (e.g., the first term in brackets in (4.24)) and $c$ is its length support; $\rho_0 t$ and $\rho_0 t_1$, with $t$ and $t_1$ positive numbers, are the maximum amplitude of variation for the regular and the discontinuous term (e.g., the second term in brackets in (4.24)). It should be noted that, depending on the values of the parameters $c,\ c_1,\ t,\ t_1,\ s,\ s_1$, the definition (4.24) allows to obtain a wide family of coefficients, including regular (e.g., continuous) or discontinuous mass density $\rho(x)$ with jump discontinuity at $x = s_1$.

A preliminary series of numerical tests suggested to assume a mesh with $N_e = 200$ equally spaced finite elements to manage cases with $N$ up to 15. The maximum error in estimating the first fifteen eigenvalues of the unperturbed nanobeam was, in fact, less than $1.2 \cdot 10^{-4}$ percent. The only exception is represented by the cases with larger number of resonant frequencies, e.g., $N = 20,\ 25$, for which the choice $N_e = 400$ was implemented. Finally, this set of simulations suggests to choose $\gamma = 10^{-5}$ in the stopping criterion (3.121).

Some results of the identification are summarized in the sequel. They are representative of a large set of simulations. In order to simplify the presentation, we have assumed $c = c_1 = 0.2L$ in this analysis.

The determination of continuous coefficients shows high degree of accuracy in $L^\infty$-norm, even when only the first 9–12 frequencies are used as input data. This holds true even when the mass variation is not necessarily small. We refer to Figure 4.2 for a typical result of the reconstruction. For the sake of completeness, in Figure 4.3 we exploited the information contained in the very few first eigenfrequencies. It can be seen that for small mass variation, even the first $4 - -5$ eigenfrequencies are sufficient for acceptable reconstruction of the coefficient. Accuracy decreases in case of large amplitude mass variation.

In case of discontinuous coefficients, spurious oscillations around the target coefficient occur near the discontinuity point, see Figures 4.4 and 4.5. Our simulations show that the maximum amplitude of these oscillations is proportional to the intensity of the jump, and the effect decays moving away from the discontinuity. In case of large jump, the oscillatory character of the identified coefficient may compromise the accuracy of the reconstruction either in the whole or in a significant part of the interval $[0, \frac{L}{2}]$. At least 20–25 first resonant frequencies are needed to get acceptable accuracy in these cases, for which $N_e = 400$ equally spaced finite elements were used.

Finally, the results show that at most eight to fifteen iterations are required to fulfill the convergence criterion for continuous or discontinuous coefficients, respectively. The corresponding calculation time for each iteration step of the reconstruction procedure is approximately 2 and 4 s.

#### 4.2.2.4 An experimental validation

Experimental data on eigenfrequency induced changes due to added mass in nanobeams are not numerous. In this section, we test our method on the experimental results reported in [42]. We refer to this paper for a complete description of the experiment. In brief, liquid droplets were deposited on a single-crystal Si cantilever, with length $L = 397\ \mu m$ and rectangular cross-section having $b = 29\ \mu m$ in width and $h = 2\ \mu m$ in thickness. Array droplets were deposited in pairs, beginning from the free end of the cantilever, and the six configurations shown in Figure 4.6 were considered. The eigenfrequencies of the first four bending modes were measured for the referential (U) and perturbed (Pi) configurations, $i = 1, \dots, 6$; see Table 4.1, which was deduced from Table 1 in [42] (Supplementary Information).

The small transverse vibrations of the reference cantilever are described by the eigenvalue problem

$$
\begin{cases}
Sv^{IV} - Kv^{VI} = \lambda\rho_0 v, \quad x \in (0, L) & (4.25)\\
v(0) = 0, \quad v'(0) = 0, \quad v''(0) = 0, & (4.26)\\
-Sv''(L) + Kv^{IV}(L) = 0, & (4.27)\\
-Sv'''(L) + Kv^{V}(L) = 0, & (4.28)\\
Kv'''(L) = 0, & (4.29)
\end{cases}
$$

where $S$ and $K$ are defined in (2.141). We assumed Poisson's ratio $\nu = 0.2$; volume mass density $\rho_{vol} = 2330\ kgm^{-3}$; and $l_0 = l_1 = l_2$. The Young's modulus $E$ of the material and the scale parameter $l_0$ have been determined by a constrained least-squares fitting of the first four measured resonant frequencies $\{f_n^{U,exp}\}_{n=1}^4$, i.e., by solving the optimization problem

$$
\min_Q \sum_{n=1}^{4} \left( 1 - \frac{f_n^{U,exp}}{f_n^{U,th}(E, l_0)} \right)^2, \tag{4.30}
$$

where $Q = \{(E, l_0) \mid 170 \text{ GPa} \le E \le 185 \text{ GPa},\ 0.02h \le l_0 \le 0.04h\}$. The upper and lower bounds on $E$ were chosen as small perturbations (around $\pm 4\%$) of the guess value $E_g = 177.4$ GPa. The latter was obtained by imposing the first natural frequency determined via the classical Euler-Bernoulli cantilever model coincident with the corresponding experimental value. The upper and lower bounds of the scale parameter $l_0$ were selected by considering the first two natural frequencies of the problem (4.25)–(4.29) with $E = E_g$. A numerical analysis of the optimization problem (4.30) provided the following (unique) solution: $E^{opt} = 175$ GPa, $l_0^{opt} = 0.032$h. Table 4.1 shows that the mass-induced frequency shifts are, in average, larger than the modelling errors evaluated on the reference configuration. Experience developed by the authors on other inverse eigenvalue problems based on experimental finite data (e.g., damage identification in classical full-scale beams, see, for example, [63]) suggests that this is an essential necessary condition for the success of the identification.

The reconstruction method presented in Section 4.2.1 was applied to the present experimental case. A selected set of results is shown in Figure 4.7. The reconstructed mass coefficients shown in Figures 4.7(a,b) were determined by assuming *a priori* that the support of the unknown mass variation belongs to the right half of the cantilever, e.g., the subinterval $(0.5L, L)$. It should be noted that this ambiguity can be resolved only having additional frequency data belonging (at least) to a second spectrum under different boundary conditions at disposal. The reconstructed density function correctly exhibits large positive increments within the end quarter of the cantilever. The maximum of the mass change increases for cases $P1$ to $P5$, as it was expected, and the support of the positive mass variation also extends from the free end inwards. It is interesting to note that the mass profile reconstructed in case $P6$ is close to that of case $P2$ in $[0.85L, L]$, and shows additional positive increment proceeding towards the center of the cantilever. For the sake of completeness, the reconstruction has been carried out by gradually reducing the size of the interval. Figures 4.7(c,d) show the case $[0.7L, L]$, which essentially confirms the results obtained working on half interval. Further reduction of the interval in which the mass variation is expected to occur does not improve the results of identification. In all the cases studied, a maximum of six iterations were needed to satisfy the error criterion (3.206), with $\gamma = 10^{-7}$.

Table 4.2 collects the global added mass, evaluated by integrating the reconstructed function $r(x)$ (columns 2 and 3, for the interval $[0.5L, L]$ and $[0.7L, L]$, respectively) and by considering the positive mass change defined as $r^{+}(x) = \max\{r(x), 0\}$ (columns 4 and 5). The estimates provided working on $[0.5L, L]$ or on $[0.7L, L]$ are comparable, and maximum difference of about $5\%$ was found in cases $P2$ and $P3$.

In conclusion, the proposed technique was effective despite the small number of available experimental eigenfrequencies. The results of the numerical simulations developed in previous sections suggest that the accuracy of the reconstruction would significantly improve, even in $L^{\infty}$ norm, if a slightly larger number of first eigenfrequencies (six-eight) had been available. Furthermore, the encouraging results obtained in this experimental test seem to suggest that the previous theory - developed for identification in supported nanobeams from a single partial spectrum - could also be extended to different end conditions (such as those of the cantilever, for example). This aspect requires further theoretical investigation.

## 4.3 Reconstruction of general mass variation from two partial spectra

In this section, we extend the reconstruction method presented in Section 4.2 to the determination of a general mass variation, e.g., $r_{\epsilon}(x)$ not necessarily supported in half of the nanobeam axis. As in the axial case, the main idea is to include as input data also the lower eigenfrequencies of a second spectrum obtained by changing one end condition.

### 4.3.1 Formulation of the reconstruction method

Let us consider the free transverse vibration of the nanobeam introduced at the beginning of Section 4.2.1. If in (4.1)–(4.3) the boundary conditions (4.3) are changed into

$$v'(L) = 0, \ -Sv'''(L) + Kv^{V}(L) = 0, \ Kv'''(L) = 0, \tag{4.31}$$

then the nanobeam is said to be under (non classical) *supported-sliding* end conditions. Note that conditions (4.31) imply (from the left to the right, respectively) the vanishing of the rotation of the end cross-section, the vanishing of the shear and the vanishing of the higher-order resultant caused by higher-order stresses at the same cross-section. The eigenpairs $\left\{\lambda_n^{S\ell}, v_n^{S\ell}(x)\right\}_{n=1}^{\infty}$ of (4.1), (4.2), (4.31) are

$$\lambda_n^{S\ell} = \left(\frac{(2n-1)\pi}{2L}\right)^6 \left[\frac{1}{\rho_0}\left(K + \frac{S}{\left(\frac{(2n-1)\pi}{2L}\right)^2}\right)\right], \tag{4.32}$$

$$v_n^{S\ell}(x) = \sqrt{\frac{2}{\rho_0 L}} \sin\left(\frac{(2n-1)\pi x}{2L}\right), \tag{4.33}$$

with $\int_0^L \rho_0 (v_n^{S\ell}(x))^2 dx = 1$ for every $n \geq 1$.

Assume that the mass change $r_{\epsilon}(x)$ introduced in (4.6) satisfies (4.7), (4.8), (4.9), but not necessarily (4.10), e.g., the support of $r_{\epsilon}(x)$ now is a subset of the *whole* interval $[0, L]$. Let us denote by

$\left\{\lambda_n^{S\ell}(\rho),\ v_n^{S\ell}(x;\rho)\right\}_{n=1}^{\infty}$ the eigenpairs of (4.1), (4.2), (4.31) with $\rho_0$ replaced by $\rho(x)=\rho_0+r_\epsilon(x)$. In the sequel, we use the set of spectral data

$$\left\{\lambda_n^{S}(\rho)\right\}_{n=1}^{N} \cup \left\{\lambda_m^{S\ell}(\rho)\right\}_{m=1}^{M}, \tag{4.34}$$

where $N,\ M$ are given integers, and we adapt the reconstructive procedure shown in Section 3.4.4 to reconstruct an approximation of the mass change $r_\varepsilon(x)$.

The stopping criterion of the iterative procedure was set as

$$e^{S-S\ell}=\frac{1}{N}\left(\sum_{n=1}^{N}\left(\frac{\lambda_n^{S(exp)}-\lambda_n^{S}(\rho^{(j)})}{\lambda_n^{S(exp)}}\right)^2\right)^{\frac{1}{2}}+\frac{1}{M}\left(\sum_{m=1}^{M}\left(\frac{\lambda_m^{S\ell(exp)}-\lambda_m^{S\ell}(\rho^{(j)})}{\lambda_m^{S\ell(exp)}}\right)^2\right)^{\frac{1}{2}}<\gamma, \tag{4.35}$$

for a small given number $\gamma$ ($\gamma=10^{-5}$).

### 4.3.2 Application and results

The reconstruction method has been tested on an extended series of simulations with the *overlapping* mass variation defined in (4.24). In the sequel, we briefly discuss the salient results. Note that, based on our previous experience on the longitudinal vibration case (see also [25]), the same number of first natural frequencies in both spectra was used, e.g., $N=M$.

The identification of continuous mass variation gives good results, and accuracy rapidly improves as $N$ increases. The determination of discontinuous, coefficients, as it was expected, leads to discrepancies analogous to these encountered in Section 4.2.2.3. For the sake of brevity, here we will focus only on cases in which the discontinuous mass variation in (4.24) is supported on two disjoint intervals of $(0,L)$. In case of $L^{\infty}$-small mass variation (and, then, also small jump magnitude), the results are accurate enough for $N=12-15$, with the exception of a small interval close to the discontinuity, see Figure 4.8. When the mass variation is not necessarily small and the jump magnitude is comparable with the maximum value of the smooth term of the mass variation (or even larger), for $N$ up to $15$ undesired oscillations appear and propagate throughout the whole interval, with amplitude that typically decays away from the jump, see Figures 4.9 and 4.10. Better accuracy is reached in these cases by increasing $N$, e.g., $N$ up to $20-25$. Finally, in spite of the fact that convergence of the identification procedure has local character and requires to work in a sufficiently small neighborhood of the referential nanobeam, it should be noted that the method shows unexpected potential in dealing with not necessarily small mass variation, see Figure 4.11.

### 4.3.3 Stability to noisy data

The robustness of the reconstruction to errors on the data was tested by perturbing the noise-free resonant frequencies corresponding to the target eigenvalues. The following two kinds of errors were considered:

$$\sqrt{\lambda_k^{err}}=\sqrt{\lambda_k}+\tau_k^{A}, \tag{4.36}$$

$$\sqrt{\lambda_k^{err}}=\sqrt{\lambda_k}(1+\tau_k^{R}), \tag{4.37}$$

where $\lambda_k$ belongs to the set $\left\{\lambda_n^{S(exp)}\right\}_{n=1}^{N} \cup \left\{\lambda_m^{S\ell(exp)}\right\}_{m=1}^{M}$. In (4.36), the frequency noise is assumed to be constant (in absolute terms) for all the modes, and $\tau_k^{A}$ is a random Gaussian variable with vanishing mean and standard deviation $\sigma^{A}$ such that $3\sigma^{A}=2\pi\Pi^{A}$, where $\Pi^{A}$ is the maximum admitted error. In (4.37), a constant relative error is assumed for all the resonant frequencies, and $\tau_k^{R}$ is a random Gaussian variable with vanishing mean and standard deviation $\sigma^{R}$ such that $3\sigma^{R}=\Pi^{R}$, where $\Pi^{R}$ is the maximum eigenfrequency percentage uncertainty.

A selected, although representative, set of results is presented below for discontinuous mass coefficients belonging to the family (4.24).

Figure 4.12 shows the results for errors as in (4.36). In each subfigure, besides the exact mass profile, three curves are shown, namely, the curve of the mean value and the two curves obtained by adding $\pm 3\sigma^A$ to the mean value. For each case, a thousand of simulations was performed. The effect of errors on the data is not important for $\Pi^A = 100$ Hz, whereas appreciable discrepancy occurs for $\Pi^A = 200$ Hz. When $\Pi^A$ is greater than $300 - 400$ Hz, the accuracy of the reconstruction is seriously compromised. It should be noted that $\Pi^A = 200$ Hz corresponds to percentage errors ranging approximately from $0.0019$ (high frequency) to $0.4763$ (low frequency) percent of the unperturbed first fifteen resonant frequencies.

The results of the error analysis based on (4.37) are collected in Figure 4.13. The notation is the same of the previous case. It turns out that the effects of errors are almost negligible for $\Pi^R$ up to $0.05$ percent, and differences become significant starting from $\Pi^R = 0.20$ percent.

Finally, we notice that similar results have been obtained for continuous mass coefficients. The number of iterations needed to get convergence is slightly larger than the corresponding error-free cases.

## 4.4 A constrained least squares-based filtering

### 4.4.1 The method and its application using one partial spectrum

The mass identification problem in nanobeams involves *positive* variations of the mass density $\rho_0$, that is

$$r_\epsilon(x) \geq 0. \tag{4.38}$$

However, it would be very difficult to take advantage of this positivity constraint using a global basis such as the family of functions $\left\{\Phi_n^S\right\}_{n=1}^N$ or $\left\{\Phi_n^S(x), \Phi_m^{S\ell}(x)\right\}_{n,m=1}^N$ adopted in our GFCM in Section 4.2 or 4.3, respectively. On the other hand, it is expected that the a priori information contained in (4.38) is of great importance, since this constraint can be used to eliminate the large oscillations in the identified mass coefficient, like those occuring near a discontinuity point of $r_\epsilon(x)$.

Taking into account these considerations, we implemented a filtering method based on a constrained least-squares optimization procedure which permits to enforce the reconstructed added mass $r_\epsilon^{(j)}(x)$ to fulfill condition (4.38), $j$ being the iteration index at which the iterative process converged according to the stopping criterion adopted for the GFCM. For the sake of simplicity, here we refer to the inverse problem with one partial spectrum considered in Section 4.2. The case with two partial spectra will be analyzed in next section.

In order to allow for discontinuities in the mass coefficient and, simultaneously, to take into account the constraint (4.38) in $[0, L/2]$, as in [8] we adopt the representation

$$r^{(j+1)}(x) = \sum_{k=1}^{Q} \vartheta_k \Psi_k(x), \tag{4.39}$$

where the piecewise constant functions $\{\Psi_k(x)\}_{k=1}^Q$, $\Psi_k(x) : [0, L/2] \to \mathbb{R}$, are defined as

$$\Psi_k(x) = 1 \ \text{ if } x_{k-1} \leq x \leq x_k, \quad \Psi_k(x) = 0 \ \text{ otherwise}, \quad k = 1, ..., Q, \tag{4.40}$$

where

$$x_k = k\frac{L}{2N}, \quad k = 1, ..., Q, \tag{4.41}$$

is a given subdivision of the interval $[0, L/2]$. Note that, to simplify the notation, we have omitted the index $\epsilon$. The coefficients $\vartheta_k$, $k = 1, ..., Q$, are the unknowns of the optimization problem, and the index $j+1$ in expression (4.39) refers to the additional filtering step performed after the iterative reconstruction method described in Section 4.2.

Using (4.39), the first order approximation of the $n$th eigenvalue of the perturbed nanobeam can be calculated as

$$\lambda_n^S(\rho^{(j+1)}) = \lambda_n^S(\rho^{(j)}) + \sum_{k=1}^{Q} \Gamma_{nk}^S \vartheta_k, \tag{4.42}$$

with

$$\Gamma_{nk}^S = -\lambda_n^S(\rho^{(j)}) \int_{x_{k-1}}^{x_k} \Phi_n^{S(j)}(x)dx. \tag{4.43}$$

Typically the number $Q$ of unknowns $\boldsymbol{\vartheta} = (\vartheta_1, \cdots, \vartheta_Q)$ is chosen large enough to enhance the mass reconstruction. In addition, it should be noticed that the number of eigenvalues measured in experiments $\{\lambda_n^{S(exp)}\}_{n=1}^N$ is usually less than the number of unknowns, i.e., $N < Q$ or even $N << Q$. This leads us to formulate the inverse problem as the following constrained optimization problem.

$$\text{To minimize} \quad F(\boldsymbol{\vartheta}) = \|\boldsymbol{\lambda}^{S(exp)} - (\boldsymbol{\lambda}^S + \boldsymbol{\Gamma}^S \boldsymbol{\vartheta})\|^2 \tag{4.44}$$

$$\text{subject to} \quad \vartheta_k \geq 0, \ k = 1, ..., Q, \tag{4.45}$$

where the $N$-vectors $\boldsymbol{\lambda}^{S(exp)} = (\lambda_1^{S(exp)}, ..., \lambda_N^{S(exp)})$, $\boldsymbol{\lambda}^S = (\lambda_1^S(\rho^{(j)}), ..., \lambda_N^S(\rho^{(j)}))$ are the target and analytical eigenvalues, respectively, $\boldsymbol{\Gamma}^{\mathbf{S}}$ is the $N \times Q$ matrix with $\left(\boldsymbol{\Gamma}^{\mathbf{S}}\right)_{nk} = \Gamma_{nk}^S$, and

$$\|\boldsymbol{\varphi}\|^2 = \sum_{n=1}^{N} \left( \frac{\varphi_n}{\lambda_n^{S(exp)}} \right)^2 \quad \text{for every } \boldsymbol{\varphi} \in \mathbb{R}^N. \tag{4.46}$$

Notice that each $\varphi_n$ has been normalized with the corresponding $\lambda_n^{S(exp)}$ in expression (4.46) in order to avoid an excessive weight of the higher eigenvalues in the objective function.

The optimization problem (4.44)-(4.45) has been solved iteratively based on an *optimized* steepest descent method. More precisely, the vector $\boldsymbol{\vartheta}$ at the $(i+1)$th step is updated as

$$\boldsymbol{\vartheta}^{(i+1)} = \boldsymbol{\vartheta}^{(i)} - t_{opt}^{(i)} \nabla F\left(\boldsymbol{\vartheta}^{(i)}\right), \tag{4.47}$$

where $\nabla F\left(\boldsymbol{\vartheta}^{(i)}\right)$ is the gradient of the objective function $F$ at $\boldsymbol{\vartheta}^{(i)}$, and the real number $t_{opt}^{(i)}$ is chosen so as to minimize $F$ in the direction $\nabla F\left(\boldsymbol{\vartheta}^{(i)}\right)$. In order to ease computation, however, the value of $t^{(i)}$ that minimizes the quadratic approximation of $F$ has been used, see, for example, [23] for an application to damage identification in classical beams. In a small neighborhood of $\boldsymbol{\vartheta}^{(i)}$, using (4.47) and neglecting higher order terms, we can write

$$\begin{aligned} F\left(\boldsymbol{\vartheta}^{(i+1)}\right) \simeq F\left(\boldsymbol{\vartheta}^{(i)}\right) - t_{opt}^{(i)} \nabla F\left(\boldsymbol{\vartheta}^{(i)}\right) \cdot \nabla F\left(\boldsymbol{\vartheta}^{(i)}\right) + \\ + \frac{\left(t_{opt}^{(i)}\right)^2}{2} \nabla F\left(\boldsymbol{\vartheta}^{(i)}\right) \cdot H\left(\boldsymbol{\vartheta}^{(i)}\right) \nabla F\left(\boldsymbol{\vartheta}^{(i)}\right), \end{aligned} \tag{4.48}$$

$H\left(\boldsymbol{\vartheta}^{(i)}\right)$ being the Hessian of the objective function $F$ at $\boldsymbol{\vartheta}^{(i)}$. Here, the symbol $'\cdot'$ denotes the usual scalar product between vectors. Minimization of $F\left(\boldsymbol{\vartheta}^{(i+1)}\right)$ with respect to $t_{opt}^{(i)}$ leads to

$$t_{opt}^{(i)} = \frac{\nabla F\left(\boldsymbol{\vartheta}^{(i)}\right) \cdot \nabla F\left(\boldsymbol{\vartheta}^{(i)}\right)}{\nabla F\left(\boldsymbol{\vartheta}^{(i)}\right) \cdot H\left(\boldsymbol{\vartheta}^{(i)}\right) \nabla F\left(\boldsymbol{\vartheta}^{(i)}\right)}. \tag{4.49}$$

According to the definition of $F$ in (4.44), the components of gradient and Hessian of the objective function are given by the expressions

$$\left(\nabla F\left(\boldsymbol{\vartheta}^{(i)}\right)\right)_r = \frac{\partial F}{\partial \vartheta_r}\left(\boldsymbol{\vartheta}^{(i)}\right) = -\sum_{n=1}^{N} \frac{2\left[\lambda_n^{S(exp)} - \lambda_n^S(\rho^{(j+1)})\right]\Gamma_{nr}^S}{\left(\lambda_n^{S(exp)}\right)^2}, \tag{4.50}$$

$$\left(H\left(\boldsymbol{\vartheta}^{(i)}\right)\right)_{rs} = \frac{\partial^2 F}{\partial \vartheta_r \partial \vartheta_s}\left(\boldsymbol{\vartheta}^{(i)}\right) = \sum_{n=1}^{N} \frac{2\,\Gamma_{nr}^S \Gamma_{ns}^S}{\left(\lambda_n^{S(exp)}\right)^2}. \tag{4.51}$$

The algorithm checks that, with this choice of $t_{opt}^{(i)}$, $\boldsymbol{\vartheta}^{(i+1)}$ does not violate the constraints (4.45). Otherwise, the algorithm takes the point on the boundary of the feasible domain along the the maximal descent direction. The iteration continues until the relative variations of both $F$ and $\boldsymbol{\vartheta}$ satisfy a chosen criterion of smallness. For the objective function, the criterion $\left(F^{(i+1)} - F^{(i)}\right)/F^{(i)} < 10^{-3}$ holds, whereas for the unknown coefficients the criterion $\|\boldsymbol{\vartheta}^{(i+1)} - \boldsymbol{\vartheta}^{(i)}\|_\infty / \|\boldsymbol{\vartheta}^{(i)}\|_\infty < 5 \cdot 10^{-4}$ was considered.

Some results of the filtering method described above are summarized next, which are representative of a large set of performed simulations. In particular, the cases with discontinuous coefficients, for which spurious oscillations occur (see Figures 4.4 and 4.5), have been considered the most relevant to be presented. As it can be seen in Figures 4.14 and 4.15, obtained with a number of piecewise constant functions $Q = 200$, the filtering process permits to ensure the monotonicity property (4.38), and reduces or even eliminates the oscillations outside of the support of $r_\epsilon(x)$. Additionally, it improves the reconstruction near the discontinuity point $x = s_1$. For the presented cases, the average number of iterations and CPU time were 1250 and 14 seconds, respectively.

### 4.4.2 Application using two partial spectra

Having extended, in the case of the use of two partial spectra, the reconstruction method to the determination of a general mass variation $r_\epsilon(x)$ not necessarily supported in half of the nanobeam axis, the monotonicity constraint now reads

$$r_\epsilon(x) \geq 0, \qquad x \in [0, L]\,. \tag{4.52}$$

Then, $r_\epsilon(x)$ is represented as

$$r^{(j+1)}(x) = \sum_{k=1}^{Q} \vartheta_k \Upsilon_k(x), \tag{4.53}$$

where the piecewise constant functions $\{\Upsilon_k(x)\}_{k=1}^{Q}$, $\Upsilon_k(x) : [0, L] \to \mathbb{R}$, are given by

$$\Upsilon_k(x) = 1 \text{ if } \tilde{x}_{k-1} \leq x \leq \tilde{x}_k, \quad \Upsilon_k(x) = 0 \text{ otherwise}, \quad k = 1, ..., Q, \tag{4.54}$$

and

$$\tilde{x}_k = k\frac{L}{N}, \quad k = 1, ..., Q. \tag{4.55}$$

The coefficients $\vartheta_k$, $k = 1, ..., Q$, are again the unknowns of the optimization problem.

The first order approximation of the $n$th eigenvalue of the perturbed nanobeam, for supported ($S$) and supported-sliding ($S\ell$) end conditions, respectively, are now calculated as

$$\lambda_n^S(\rho^{(j+1)}) = \lambda_n^S(\rho^{(j)}) + \sum_{k=1}^{Q} \Gamma_{nk}^S \vartheta_k, \tag{4.56}$$

with

$$\Gamma_{nk}^{S} = -\lambda_n^S(\rho^{(j)}) \int_{\tilde{x}_{k-1}}^{\tilde{x}_k} \Phi_n^{S(j)}(x)dx, \tag{4.57}$$

and

$$\lambda_n^{S\ell}(\rho^{(j+1)}) = \lambda_n^{S\ell}(\rho^{(j)}) + \sum_{k=1}^{Q} \Gamma_{nk}^{S\ell}\vartheta_k, \tag{4.58}$$

with

$$\Gamma_{nk}^{S\ell} = -\lambda_n^{S\ell}(\rho^{(j)}) \int_{\tilde{x}_{k-1}}^{\tilde{x}_k} \Phi_n^{S\ell(j)}(x)dx. \tag{4.59}$$

Hence, the constrained optimization problem is formulated as follows:

$$\text{to minimize} \quad \mathring{F}\,(\boldsymbol{\vartheta}) = \|\mathring{\boldsymbol{\lambda}}^{(exp)} - (\mathring{\boldsymbol{\lambda}} + \mathring{\boldsymbol{\Gamma}}\boldsymbol{\vartheta})\|_{S\cup S\ell}^2 \tag{4.60}$$

$$\text{subject to} \quad \vartheta_k \geq 0,\ k = 1, ..., Q, \tag{4.61}$$

Here, the $(N+M)$-vectors $\mathring{\boldsymbol{\lambda}}^{(exp)} = (\lambda_1^{S(exp)}, ..., \lambda_N^{S(exp)}, \lambda_1^{S\ell(exp)}, ..., \lambda_M^{S\ell(exp)})$, $\mathring{\boldsymbol{\lambda}} = (\lambda_1^S(\rho^{(j)}), ..., \lambda_N^S,$ $\lambda_1^{S\ell}(\rho^{(j)}), ..., \lambda_M^{S\ell}(\rho^{(j)}))$ are the target and analytical eigenvalues corresponding to both spectra, $\mathring{\boldsymbol{\Gamma}}$ is a $(N+M) \times Q$ matrix with $\left(\mathring{\boldsymbol{\Gamma}}\right)_{ik} = \Gamma_{ik}^S$ if $i \leq N$, and $\left(\mathring{\boldsymbol{\Gamma}}\right)_{ik} = \Gamma_{i-N,k}^{S\ell}$ if $i > N$, and

$$\|\boldsymbol{\varphi}\|_{S\cup S\ell}^2 = \sum_{n=1}^{N} \left(\frac{\varphi_n}{\lambda_n^{S(exp)}}\right)^2 + \sum_{m=1}^{M} \left(\frac{\varphi_{N+m}}{\lambda_m^{S\ell(exp)}}\right)^2 \quad \text{for every } \boldsymbol{\varphi} \in \mathbb{R}^{N+M}. \tag{4.62}$$

Following the iteration method described in Section 4.4.1, the vector $\boldsymbol{\vartheta}$ at the $(i+1)$th step is updated according to equation (4.47), where the direction defined by the gradient of $\mathring{F}$ (instead of $F$) has to be used. Likewise, the optimal step $t_{opt}^i$ is obtained with expression (4.49), now considering the objective function $\mathring{F}$. The components of gradient and Hessian of $\mathring{F}$ are given by

$$\left(\nabla\mathring{F}\left(\boldsymbol{\vartheta}^{(i)}\right)\right)_r = -\sum_{n=1}^{N} \frac{2\left[\lambda_n^{S(exp)} - \lambda_n^S(\rho^{(j+1)})\right]\Gamma_{nr}^S}{\left(\lambda_n^{S(exp)}\right)^2} - \sum_{m=1}^{M} \frac{2\left[\lambda_m^{S\ell(exp)} - \lambda_m^{S\ell}(\rho^{(j+1)})\right]\Gamma_{mr}^{S\ell}}{\left(\lambda_m^{S\ell(exp)}\right)^2}, \tag{4.63}$$

$$\left(H\left(\boldsymbol{\vartheta}^{(i)}\right)\right)_{rs} = \sum_{n=1}^{N} \frac{2\,\Gamma_{nr}^S\Gamma_{ns}^S}{\left(\lambda_n^{S(exp)}\right)^2} + \sum_{m=1}^{M} \frac{2\,\Gamma_{mr}^{S\ell}\Gamma_{ms}^{S\ell}}{\left(\lambda_m^{S\ell(exp)}\right)^2}. \tag{4.64}$$

Figures 4.16 and 4.17 present some selected results of the filtering method with $Q = 200$ for the case of two partial spectra, which correspond to the results shown in Figures 4.10 and 4.11 for (unfiltered) reconstructions obtained by standard application of the Generalized Fourier Coefficients Method. Once again, the process permits to ensure the monotonicity property (4.52) and reduces the oscillations outside the support of $r_\epsilon(x)$, and improves the reconstruction near the discontinuity point $x = s_1$. For the presented cases, the average number of iterations and CPU time were $1740$ and 23 seconds, respectively.

## 4.5 A convergence result for small and smooth mass perturbations

### 4.5.1 Theory

By adapting the arguments shown in Section 3.5 and under the assumptions (4.7)–(4.10) on $r_\varepsilon(x)$, for $\varepsilon$ small enough, it can be shown that the iterative reconstructive procedure converges to a continuous function $\bar{\rho}(x)$ with the wished spectral behavior of the first $N$ resonant frequencies. The numerical results presented in Section 4.2.2.3 show that, under our assumptions, the function $\bar{\rho}(x)$ actually is a very good approximation of the target (unknown) mass coefficient $\rho(x)$, as the number $N$ of first natural frequencies included in identification increases. This is confirmed, for example, by the analysis of Figure 4.2, and also by other simulations performed by varying the mass profile, whose results are not reported here for the sake of brevity. However, up to now, the mathematical theory behind the present inverse problem does not explain why $\bar{\rho}(x)$ turns out to be close to the actual mass coefficient $\rho(x)$.

In this section, we tackle this issue and we present a partial answer to this question. More precisely, for small mass change and under suitable additional assumptions on $r_\epsilon(x)$, we shown that

$$\lim_{N\to+\infty} r_\epsilon^{(0)}(x) = r(x), \qquad \text{for } x \in \left(0, \frac{L}{2}\right), \tag{4.65}$$

where $r_\epsilon^{(0)}(x)$ denotes the mass variation determined at the first step of the iterative procedure by expression (4.19).

Before embarking in calculations, we wish to illustrate the main idea behind the proof of (4.65). We know that, for $\epsilon$ small enough, the first-order variation of the nth eigenvalue $\lambda_n^S$ is given by (4.11). Therefore, if we insert the expression (4.11) of $\delta\lambda_n^S$ into the expression of the first-order mass variation and we neglect higher order terms in $\epsilon$, then we obtain

$$r^N(x) = \int_0^{\frac{L}{2}} K^N(x,s) r(s) ds, \tag{4.66}$$

where, hereinafter, we shall write $r_\epsilon^{(0)}(x) \equiv r^N(x)$ and $r_\epsilon(x) \equiv r(x)$ to simplify the notation and to emphasize the dependence on $N$. The kernel $K^N(x,s)$ is given by

$$\begin{aligned} K^N(x,s) &= 4\rho_0^2 L \left\{ \sum_{k=1}^{N} \Phi_k^S(s)\Phi_k^S(x) - \frac{2}{2N+1} \sum_{k,j=1}^{N} \Phi_k^S(s)\Phi_j^S(x) \right\} \\ &\equiv 4\rho_0^2 L \left\{ \widetilde{K}^N(x,s) - \widetilde{\widetilde{K}}^N(x,s) \right\}, \end{aligned} \tag{4.67}$$

where $\Phi_k^S(x)$ are defined as in (4.12). The key point is to prove that, in a suitable sense, for every $x \in \left(0, \frac{L}{2}\right)$ and every $s \in \left(0, \frac{L}{2}\right)$, we have

$$\lim_{N\to+\infty} K^N(x,s) = \delta(x-s), \tag{4.68}$$

where, for fixed $x \in \left(0, \frac{L}{2}\right)$, $\delta(x-s)$ is the Dirac's delta distribution supported at $x$, e.g., $\int_{-\infty}^{+\infty} \delta(x-s)\varphi(s)ds = \varphi(x)$ for every $\varphi \in C_c^\infty(\mathbb{R}) = \{f\colon \mathbb{R} \to \mathbb{R} \,|\, f \in C^\infty(\mathbb{R}), \text{supp}(f) = \text{compact set} \subset \mathbb{R}\}$. In fact, using (4.68) in (4.66), at least formally, we have

$$\lim_{N\to+\infty} r^N(x) = \int_0^{L/2} \delta(x-s) r(s) ds = r(x), \tag{4.69}$$

assuming that $r(x)$ is a smooth function, with compact support contained in $[0, \frac{L}{2}]$, and extended to 0 in $\mathbb{R}$ outside $[0, \frac{L}{2}]$.

By using the explicit expression (4.12) for $\Phi_k^S(x)$, by writing $\sin^2(\frac{k\pi x}{L}) = \frac{1}{2}(1 - \cos(\frac{2k\pi s}{L}))$, and recalling the identity $\frac{1}{2}+\cos\xi+\cdots+\cos(N\xi)=\frac{1}{2}\frac{\sin\frac{2N+1}{2}\xi}{\sin\frac{\xi}{2}}$ for $\xi\in\mathbb{R}\setminus\{0\}$, we have

$$\begin{aligned}\frac{(\rho_0 L)^2}{4}\widetilde{K}^N(x,s) = \frac{N+1}{4} &- \frac{1}{8}\frac{\sin((2N+1)\pi\frac{s}{L})}{\sin(\pi\frac{s}{L})} \\ &- \frac{1}{8}\frac{\sin((2N+1)\pi\frac{x}{L})}{\sin(\pi\frac{x}{L})} + \frac{1}{16}\frac{\sin((2N+1)\pi(\frac{s+x}{L}))}{\sin(\pi(\frac{s+x}{L}))} \\ &+ \frac{1}{16}\frac{\sin((2N+1)\pi(\frac{s-x}{L}))}{\sin(\pi(\frac{s-x}{L}))} - \frac{1}{8}\end{aligned} \tag{4.70}$$

and

$$\begin{aligned}\frac{(\rho_0 L)^2}{4}\widetilde{\widetilde{K}}^N(x,s) = \frac{1}{2N+1}\cdot\frac{1}{2}\Bigg\{ &N(N+1) - \frac{N}{2}\cdot\frac{\sin((2N+1)\pi\frac{s}{L})}{\sin(\pi\frac{s}{L})} \\ &-\frac{N}{2}\cdot\frac{\sin((2N+1)\pi\frac{x}{L})}{\sin(\pi\frac{x}{L})} + \sum_{k=1}^{N}\sum_{j=1}^{N}\cos\left(2k\pi\frac{s}{L}\right)\cos\left(2j\pi\frac{x}{L}\right)\Bigg\}.\end{aligned} \tag{4.71}$$

By (4.70) and (4.71), after simple algebra, we obtain

$$\begin{aligned}K^N(x,s) = \frac{16}{L}\Bigg\{ &\frac{1}{8(2N+1)} - \frac{1}{8(2N+1)}\cdot\frac{\sin((2N+1)\pi\frac{s}{L})}{\sin(\pi\frac{s}{L})} \\ &- \frac{1}{8(2N+1)}\cdot\frac{\sin((2N+1)\pi\frac{x}{L})}{\sin(\pi\frac{x}{L})} + \frac{1}{16}\cdot\frac{\sin((2N+1)\pi(\frac{s-x}{L}))}{\sin(\pi(\frac{s-x}{L}))} \\ +\frac{1}{16}\cdot\frac{\sin((2N+1)\pi(\frac{s+x}{L}))}{\sin(\pi(\frac{s+x}{L}))} &- \frac{1}{2(2N+1)}\cdot\sum_{k,j=1}^{N}\cos(2k\pi\frac{s}{L})\cos(2j\pi\frac{x}{L})\Bigg\} \equiv \sum_{i=1}^{6}K_i^N(x,s).\end{aligned} \tag{4.72}$$

In what follows, we first prove that

$$\lim_{N\to+\infty}\int_0^{L/2} r^N(x)\varphi(x)dx = \int_0^{L/2} r(x)\varphi(x)dx, \quad \text{for every } \varphi\in C_c^\infty\left(\left(0,\frac{L}{2}\right)\right), \tag{4.73}$$

that is $r^N(x)$ (given in (4.66), with $K^N(x,s)$ as in (4.67)) converges to $r(x)$ in the sense of distributions as $N\to+\infty$. Condition (4.73) is satisfied under specific conditions on $r(x)$ that will be introduced throughout the analysis.

By linearity, we can consider separately the six terms in (4.72). Concerning $K_1^N(x,s)$, it is easy to see that, for every $\varphi\in C_c^\infty\left(\left(0,\frac{L}{2}\right)\right)$, we have

$$\left|\int_0^{L/2}\left(\int_0^{L/2}K_1^N(x,s)r(s)ds\right)\varphi(x)dx\right| \le \frac{2}{L}\cdot\frac{1}{2N+1}\|r\|_{L^1}\|\varphi\|_{L^1}, \tag{4.74}$$

where $\| r \|_{L^1}=\int_0^{L/2} \mid r(x)\mid dx$.

To control the term involving $K_2^N(x,s)$, we assume that

$$\text{there exists } \delta>0,\ \delta<\frac{L}{2}, \text{ such that supp } (r(x))\subset\left[\delta,\frac{L}{2}\right]. \tag{4.75}$$

Then, we have

$$\left| \int_0^{L/2} \left( \int_0^{L/2} K_2^N(x,s) r(s) ds \right) \varphi(x) dx \right| =$$

$$= \frac{2}{L(2N+1)} \left| \int_0 \varphi(x) dx \int_\delta^{L/2} \frac{\sin((2N+1)\pi \frac{s}{L})}{\sin(\pi \frac{s}{L})} r(s) ds \right| \leq$$

$$\leq \frac{2}{L(2N+1)} \cdot \frac{1}{\sin \frac{\pi\delta}{L}} \cdot \|\varphi\|_{L^1} \cdot \|r\|_{L^1}, \quad (4.76)$$

for every $\varphi \in C_c^\infty\left((0, \frac{L}{2})\right)$.

By definition, there exists $\widetilde{\delta} > 0$, $\widetilde{\delta} < \frac{L}{2}$, such that $\varphi(x) = 0$ in $[0, \widetilde{\delta}]$. Then, for every $\varphi \in C_c^\infty\left((0, \frac{L}{2})\right)$, we have

$$\left| \int_0^{L/2} \left( \int_0^{L/2} K_3^N(x,s) r(s) ds \right) \varphi(x) dx \right| \leq \frac{2}{L(2N+1)} \cdot \frac{1}{\sin \frac{\pi\widetilde{\delta}}{L}} \cdot \|r\|_{L^1} \cdot \|\varphi\|_{L^1} \cdot \quad (4.77)$$

We now consider the key term involving $K_4^N(x,s)$. By introducing the change of variables

$$\xi = \frac{x+s}{L}, \; \eta = \frac{x-s}{L}, \quad (4.78)$$

we have, for every $\varphi \in C_c^\infty\left((0, \frac{L}{2})\right)$,

$$\int_0^{L/2} \left( \int_0^{L/2} K_4^N(x,s) r(s) ds \right) \varphi(x) dx =$$

$$= \frac{1}{L} \int_0^{L/2} \int_0^{L/2} \frac{\sin((2N+1)\pi(\frac{s-x}{L}))}{\sin(\pi(\frac{s-x}{L}))} \cdot r(s)\varphi(x) ds dx$$

$$= \frac{L}{2} \int \int_\Omega \frac{\sin((2N+1)\pi\eta)}{\sin(\pi\eta)} r\left(\frac{L}{2}(\xi-\eta)\right) \varphi\left(\frac{L}{2}(\xi+\eta)\right) d\xi d\eta, \quad (4.79)$$

where $\Omega = \{(\xi,\eta) \in \mathbb{R}^2 \mid \xi = \frac{x+s}{L}, \eta = \frac{x-s}{L}, \text{ with } x \in [0, \frac{L}{2}], s \in [0, \frac{L}{2}]\}$. Here, we further assume that the support of $r(s)$ is compactly contained in $[0, \frac{L}{2}]$, e.g.,

$$\text{supp}(r(s)) \subset\subset \left[0, \frac{L}{2}\right]. \quad (4.80)$$

Then

$$\text{supp}\left( r\left(\frac{L}{2}(\xi-\eta)\right) \cdot \varphi\left(\frac{L}{2}(\xi+\eta)\right)\right) \subset\subset \Omega \quad (4.81)$$

and we extend the function $r\left(\frac{L}{2}(\xi-\eta)\right)\varphi\left(\frac{L}{2}(\xi+\eta)\right)$ to 0 in $\mathbb{R}^2 \setminus \bar{\Omega}$. The extended function is continuous on $\mathbb{R}^2$, and the extension of $r$, $\varphi$ will be denoted by $\bar{r}$, $\bar{\varphi}$, respectively. Next, we rewrite the first factor inside the integral in (4.79) as

$$\frac{\sin((2N+1)\pi\eta)}{\sin(\pi\eta)} = \frac{\sin((2N+1)\pi\eta)}{\pi\eta} \cdot \frac{\pi\eta}{\sin(\pi\eta)}, \quad (4.82)$$

where the function $f(\eta) = \frac{\pi\eta}{\sin(\pi\eta)}$, originally defined in the interval $[-\frac{1}{2}, \frac{1}{2}]$, can be extended to a continuous function $\bar{f} : \mathbb{R} \to \mathbb{R}$ by taking $\bar{f}(\eta) = f(\frac{1}{2})$ in $\mathbb{R} \setminus [-\frac{1}{2}, \frac{1}{2}]$. At this stage we recall the well known result

$$\lim_{T \to +\infty} \frac{\sin Tx}{\pi x} = \delta(x), \quad (4.83)$$

which holds in the sense of distributions, see, for example, [9]. By using the above properties of $r$, $\varphi$, $f$, and those of their extensions to $\mathbb{R}$ $\bar{r}$, $\bar{\varphi}$, $\bar{f}$, and by (4.83), for $r(x) \in C^0\left(\left[0, \frac{L}{2}\right]\right)$, we have

$$\lim_{N\to+\infty} \int_0^{L/2} \left( \int_0^{L/2} K_4^N(x,s) r(s) ds \right) \varphi(x) dx =$$

$$= \lim_{N\to+\infty} \frac{L}{2} \int_{-\infty}^{+\infty} \int_{-\infty}^{+\infty} \frac{\sin((2N+1)\pi\eta)}{\pi\eta} \cdot \bar{f}(\eta) \cdot \bar{r}\left(\frac{L}{2}(\xi-\eta)\right) \bar{\varphi}\left(\frac{L}{2}(\xi+\eta)\right) d\xi d\eta =$$

$$= \frac{L}{2} \int_{-\infty}^{+\infty} \delta(\eta) \bar{f}(\eta) \bar{r}\left(\frac{L}{2}(\xi-\eta)\right) \bar{\varphi}\left(\frac{L}{2}(\xi-\eta)\right) d\xi d\eta =$$

$$= \frac{L}{2} \int_{-\infty}^{+\infty} f(0) \bar{r}\left(\frac{L}{2}\xi\right) \bar{\varphi}\left(\frac{L}{2}\xi\right) = \frac{L}{2} \int_0^1 r\left(\frac{L}{2}\xi\right) \varphi\left(\frac{L}{2}\xi\right) d\xi =$$

$$= \int_0^{L/2} r(x)\varphi(x) dx, \quad (4.84)$$

where, in the last step, we have reversed the change of variables (4.78).

The term involving $K_5^N(x,s)$ can be treated as the previous one, obtaining

$$\lim_{N\to+\infty} \int_0^{L/2} \left( \int_0^{L/2} K_5^N(x,s) r(s) ds \right) \varphi(x) dx = \int_0^{L/2} \bar{r}(-x)\varphi(x) dx = 0, \quad (4.85)$$

since the extension $\bar{r}$, $\bar{r}: \mathbb{R} \to \mathbb{R}$, of the function $r$, $r: \left[0, \frac{L}{2}\right] \to \mathbb{R}$, vanishes in $\mathbb{R} \setminus [0, \frac{L}{2}]$.
In order to control the last term, we shall assume the following additional hypotheses on $r(x)$:

$$r \in C^1\left(\left[0, \frac{L}{2}\right]\right), \qquad \|r''\|_{L^1} \text{ finite.} \quad (4.86)$$

For every $\varphi \in C_c^\infty\left(\left(0, \frac{L}{2}\right)\right)$, we have

$$\int_0^{L/2} \left( \int_0^{L/2} K_6^N(x,s) r(s) ds \right) \varphi(x) dx =$$

$$= -\frac{1}{2} \cdot \frac{1}{2N+1} \cdot \sum_{k,j=1}^{N} \int_0^{L/2} \cos\frac{2k\pi s}{L} r(s) ds \cdot \int_0^{L/2} \cos\frac{2j\pi x}{L} \varphi(x) dx. \quad (4.87)$$

Let us consider the first integral of the sum in (4.87). Since $r \in C^1\left(\left[0, \frac{L}{2}\right]\right)$ and has compact support contained in $[0, \frac{L}{2}]$, integrating by parts twice gives

$$\left| \int_0^{L/2} \cos\frac{2k\pi s}{L} r(s) ds \right| = \left| -\frac{L^2}{4k^2\pi^2} \int_0^{L/2} \cos\frac{2k\pi s}{L} r''(s) ds \right| \le \frac{L^2}{4k^2\pi^2} \|r''\|_{L^1}, \quad (4.88)$$

for every $k \ge 1$. Similarly, for every $\varphi \in C_c^\infty\left(\left(0, \frac{L}{2}\right)\right)$ and for every $j \ge 1$, we have

$$\left| \int_0^{L/2} \cos\frac{2j\pi x}{L} \varphi(x) dx \right| \le \frac{L^2}{4j^2\pi^2} \|\varphi''\|_{L^1}. \quad (4.89)$$

Then

$$\sum_{k,j=1}^{N} \int_0^{L/2} \cos\frac{2k\pi s}{L} r(s) ds \int_0^{L/2} \cos\frac{2j\pi x}{L} \varphi(x) dx \le \frac{L^4}{16\pi^4} \|r''\|_{L^1} \|\varphi''\|_{L^1} \sum_{k,j=1}^{N} \frac{1}{k^2 j^2}. \quad (4.90)$$

By simple calculation, we have

$$\sum_{k,j=1}^{N} \frac{1}{k^2 j^2} \leq \sum_{k=1}^{\infty} \frac{1}{k^2} + \sum_{j=1}^{\infty} \frac{1}{j^2} + \sum_{k,j=2}^{+\infty} \frac{1}{k^2 j^2}$$
$$\leq \frac{\pi^2}{3} + \int_2^{+\infty} \int_2^{+\infty} \frac{1}{(x-1)^2 (y-1)^2} dx dy = \frac{\pi^3}{3} + 1. \quad (4.91)$$

Therefore, by (4.86), (4.87), (4.89), (4.90), (4.91), we have

$$\lim_{N \to +\infty} \int_0^{L/2} \left( \int_0^{L/2} K_6^N(x,s) r(s) ds \right) \varphi(x) dx = 0, \quad (4.92)$$

for every $\varphi \in C_c^\infty \left( (0, \frac{L}{2}) \right)$.

Finally, by using (4.74), (4.76), (4.77), (4.84), (4.85), (4.92) in (4.73), we obtain the weak convergence result (4.73). To derive the point-wise convergence (4.65), we can proceed by contradiction. Let us assume that there exists $x_0 \in \left(0, \frac{L}{2}\right)$ such that $\lim_{N \to +\infty} (r^N(x_0) - r(x_0)) \neq 0$, say, $\lim_{N \to +\infty} (r^N(x_0) - r(x_0)) > 0$. Therefore, there exists $\tau > 0$ such that, for every $N_0 > 0$, $N_0 \in \mathbb{N}$, (up to subsequences) $(r^N(x_0) - r(x_0)) > \tau$ for every $N \geq N_0$. Since $(r^N(x) - r(x)) \in C^0 \left( \left[0, \frac{L}{2}\right] \right)$, there exists $\delta > 0$, $\delta$ small enough, such that $(r^N(x) - r(x)) > \frac{\tau}{2}$ in $(x_0 - \delta, x_0 + \delta) \subset\subset [0, \frac{L}{2}]$. Let us choose $\varphi(x) = \exp\left( \frac{1}{(x-x_0)^2 - (\frac{\delta}{2})^2} \right)$ in $\left(x_0 - \frac{\delta}{2}, x_0 + \frac{\delta}{2}\right)$ and $\varphi(x) = 0$ otherwise in $\left[0, \frac{L}{2}\right]$. Then, we have

$$0 = \lim_{N \to +\infty} \int_0^{L/2} (r^N(x) - r(x)) \varphi(x) dx =$$
$$= \lim_{N \to +\infty} \int_{x_0 - \frac{\delta}{2}}^{x_0 + \frac{\delta}{2}} (r^N(x) - r(x)) \varphi(x) dx > \frac{\tau}{2} \int_{x_0 - \frac{\delta}{2}}^{x_0 + \frac{\delta}{2}} \exp\left( \frac{1}{(x-x_0)^2 - (\frac{\delta}{2})^2} \right) dx > 0, \quad (4.93)$$

a contradiction.

In conclusion, we have proved that if $r(x)$ is *small*, $r(x) \in C^1([0, \frac{L}{2}])$, $\|r''\|_{L^1}$ is finite, supp$(r(x))$ is compactly contained in $[0, \frac{L}{2}]$, then $\lim_{N \to +\infty} r_N(x) = r(x)$ for every $x \in [0, \frac{L}{2}]$.

The above convergence result gives some insights on our reconstruction method and, in particular, it shows that, in case of small smooth mass perturbations, a good approximation of the solution can be obtained even at the first step of the procedure (in which $r_N(x)$ is given by closed form expression), provided that the number of eigenfrequencies is large enough.

In the next section, we shall provide some examples in support of the above theoretical result.

### 4.5.2 Numerical applications

In the first example, the first order formula (4.19) is used to construct an approximation of the mass variation $r(x) = h_1(x)$, where the function $h_1(x) \equiv h_1(x; a_1, b_1, k_1, t_1) : [0, L/2] \to \mathbb{R}$ is defined as

$$h_1(x) = t_1 \rho_0 \exp\left( -\frac{k_1}{d_1(x)} + \frac{k_1}{d_1(b_1)} \right) \text{ if } d_1(x) > 0, \quad h_1(x) = 0 \text{ otherwise}, \quad (4.94)$$

with $d_1(x) = a_1^2 - \left(\frac{x}{L} - b_1\right)^2$, $a_1 > 0$, $b_1 > 0$, $a_1 + b_1 < 1/2$, $b_1 - a_1 > 0$, $k_1 > 0$, $t_1 > 0$, and $t_1$ small. It is easy to verify that $r \in C_c^\infty([0, L/2])$, $r(x) \geq 0$ in $[0, L/2]$, $r = r(x)$ is an even function with respect to $x/L = b_1$, and $\max_{x \in [0, L/2]} r(x) = r(b_1) = \rho_0 t_1$. A plot of the reconstruction for $t_1 = 0.01,\ 0.02,\ 0.05,\ 0.10$ is shown in Figure 4.18 for $a_1 = 0.20$, $b_1 = 0.25$ and $k_1 = 0.10$. It can be seen that, even for $N$ small, $N = 6$, say, the approximation is good and the accuracy improves as $t_1$ decreases. It can be shown that the reconstruction is almost perfect when $N$ is bigger than $15$ and $t_1$ is up to $0.05$.

In the second example, we construct an approximation to a mass variation $r(x)$ which is a linear combination of two $C_c^\infty([0, L/2])$ functions with form similar to $h_1(x)$ of the last example. Precisely, we define

$$r(x) = h_1(x) - h_2(x), \tag{4.95}$$

where $h_2(x) \equiv h_2(x; a_2, b_2, k_2, t_2) : [0, L/2] \to \mathbb{R}$ is defined as $h_1(x)$ in (4.94) with $d_1(x)$, $a_1$, $b_1$, $k_1$, $t_1$ replaced by $d_2(x), a_1, b_1, k_1, t_1$, respectively, and $a_2 > 0$, $b_2 > 0$, $a_2 + b_2 < 1/2$, $b_2 - a_2 > 0$, $k_2 > 0$, $t_2 > 0$, $t_2$ small. A plot of the reconstruction for $a_1 = 0.20$, $a_2 = 0.10$, $b_1 = b_2 = 0.25$, $k_1 = k_2 = 0.10$, $t_2 = 0.8t_1$, and $t_1 = 0.01,\ 0.02,\ 0.05,\ 0.10$ is shown in Figure 4.19. The results confirm that the reconstructed coefficient for $N = 15$ is almost coincident with the target coefficient for small $t_1$, say for $t_1$ up to $0.05$. A small difference is still present, as expected, for $t_1 = 0.10$.

Finally, Table 4.3 contains the $L^\infty$-norm of the normalized error for the cases considered in Figures 4.18 and 4.19, for increasing value of $N$. It can be seen that when the perturbation is very small, e.g., $t_1 = 0.01 - 0.02$, the error is practically negligible for $N = 18 - 21$. These results lead to the conjecture that the convergence can be stronger than the point-wise convergence proved here. This aspect will be explored in future studies.

## 4.6 Tables and Figures

**Table 4.1:** *Experimental eigenfrequency values of the cantilever shown in Figure 4.6. $U$=unperturbed configuration; absolute values in Hz and percentage modeling errors $U\% = 100 \cdot (f_n^{U,th} - f_n^{U,exp})/f_n^{U,exp}$. $Pi$= $i$th perturbed configuration, $i = 1, \dots, 6$; percentage mass-induced eigenfrequency shifts $Pi\% = 100 \cdot (f_n^{U,exp} - f_n^{Pi,exp})/f_n^{U,exp}$. $f_n^{U,th}$=$n$th theoretical unperturbed eigenfrequency; $f_n^{U,exp}$=$n$th experimental unperturbed eigenfrequency; $f_n^{Pi,exp}$=$n$th experimental eigenfrequency of the perturbed $Pi$ cantilever. Experimental data taken from [42].*

| | Unperturbed | | | | Perturbed | | | |
|---|---|---|---|---|---|---|---|---|
| Mode | U | U% | P1% | P2% | P3% | P4% | P5% | P6% |
| 1 | 17883 | 0.31 | 0.59 | 1.14 | 1.53 | 2.18 | 2.67 | 1.36 |
| 2 | 112465 | -0.04 | 0.49 | 0.77 | 0.87 | 0.94 | 0.94 | 0.74 |
| 3 | 315158 | -0.12 | 0.41 | 0.53 | 0.54 | 0.58 | 0.75 | 0.60 |
| 4 | 617728 | -0.15 | 0.33 | 0.36 | 0.38 | 0.67 | 1.07 | 0.60 |

**Table 4.2:** *Mass identification for the cantilever shown in Figure 4.6. Total added mass (in percentage) for two choices of the interval of identification. $r^+(x) = \max\{r(x), 0\}$.*

| Case | $100 \cdot \left(\int_0^L r(x)dx\right) / (\rho_0 L)$ | | $100 \cdot \left(\int_0^L r^+(x)dx\right) / (\rho_0 L)$ | |
|---|---|---|---|---|
| | $[0.5L, L]$ | $[0.7L, L]$ | $[0.5L, L]$ | $[0.7L, L]$ |
| P1 | 0.64 | 0.62 | 0.68 | 0.64 |
| P2 | 1.00 | 0.96 | 1.13 | 1.06 |
| P3 | 1.24 | 1.25 | 1.43 | 1.36 |
| P4 | 1.73 | 1.80 | 1.85 | 1.83 |
| P5 | 2.18 | 2.31 | 2.35 | 2.34 |
| P6 | 1.23 | 1.19 | 1.24 | 1.19 |

**Table 4.3:** *First-order reconstruction of the mass variation as in Figures 4.18 and 4.19. Values of the normalized error $\rho_0^{-1} \parallel \rho^{reconstr} - \rho^{target} \parallel_\infty = \rho_0^{-1} \max_{x\in(0,L/2)} \mid \rho^{reconstr}(x) - \rho^{target}(x) \mid$ for increasing values of $N$.*

| Mass variation as in Figure 4.18 | | | | | | | | | |
|---|---|---|---|---|---|---|---|---|---|
| $t_1$ | $t_2$ | $N=3$ | $N=6$ | $N=9$ | $N=12$ | $N=15$ | $N=18$ | $N=21$ | $N=24$ |
| 0.01 | 0.00 | 0.0022 | 0.0003 | 0.0002 | 0.0001 | 0.0001 | 0.0001 | 0.0001 | 0.0001 |
| 0.02 | 0.00 | 0.0044 | 0.0007 | 0.0005 | 0.0003 | 0.0003 | 0.0003 | 0.0003 | 0.0003 |
| 0.05 | 0.00 | 0.0106 | 0.0018 | 0.0021 | 0.0018 | 0.0018 | 0.0017 | 0.0017 | 0.0018 |
| 0.10 | 0.00 | 0.0203 | 0.0063 | 0.0074 | 0.0067 | 0.0069 | 0.0067 | 0.0067 | 0.0067 |
| Mass variation as in Figure 4.19 | | | | | | | | | |
| $t_1$ | $t_2$ | $N=3$ | $N=6$ | $N=9$ | $N=12$ | $N=15$ | $N=18$ | $N=21$ | $N=24$ |
| 0.01 | 0.008 | 0.0043 | 0.0029 | 0.0017 | 0.0006 | 0.0003 | 0.0001 | 0.0001 | 0.0001 |
| 0.02 | 0.016 | 0.0085 | 0.0057 | 0.0034 | 0.0013 | 0.0007 | 0.0003 | 0.0003 | 0.0003 |
| 0.05 | 0.04 | 0.0208 | 0.0139 | 0.0083 | 0.0039 | 0.0023 | 0.0013 | 0.0014 | 0.0013 |
| 0.10 | 0.08 | 0.0406 | 0.0266 | 0.0184 | 0.0098 | 0.0067 | 0.0048 | 0.0049 | 0.0049 |

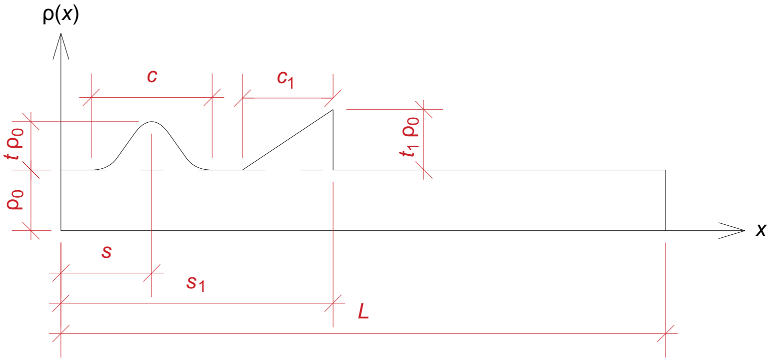

**Figure 4.1:** *Mass density per unit length $\rho = \rho(x)$ to be identified. Overlapping mass change as in* (4.24)*.*

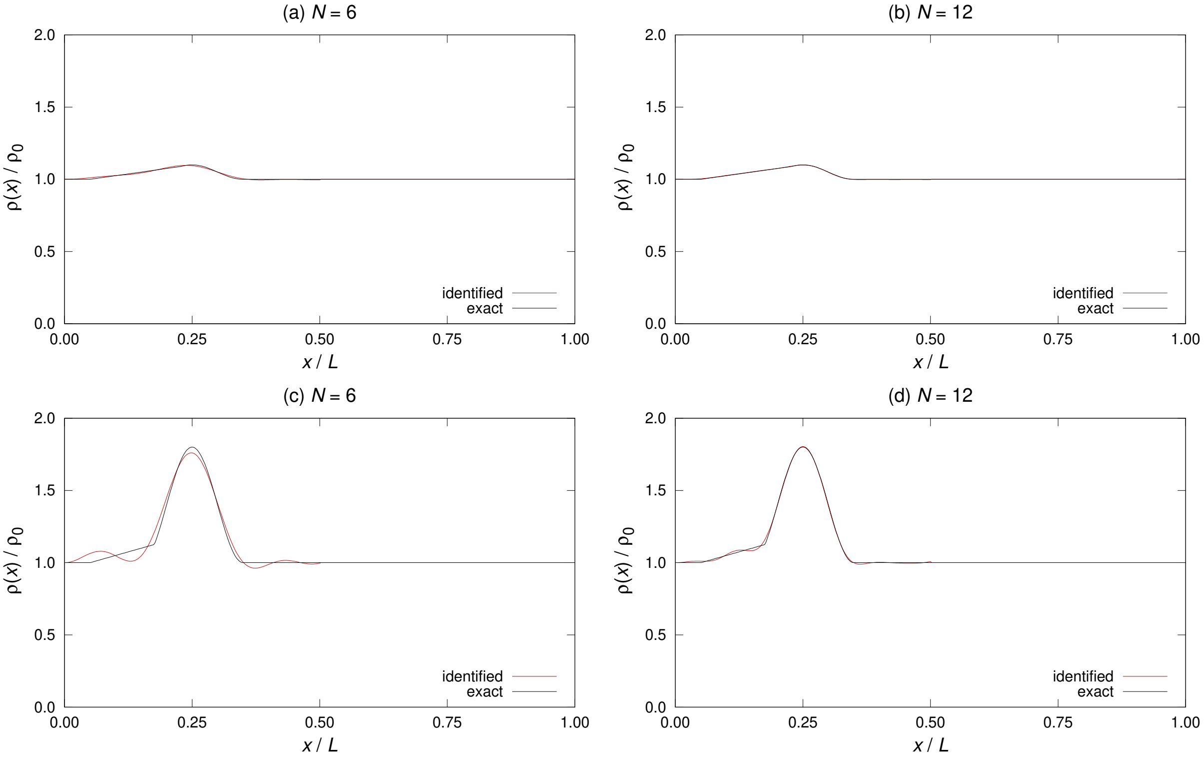

**Figure 4.2:** *Reconstruction of continuous overlapping mass changes as in* (4.24) *in* $\left[0, \frac{L}{2}\right]$*. Parameters:* $\frac{s}{L} = 0.25$, $t = 0.10$, $\frac{s_1}{L} = 0.25$, $t_1 = 0.10$, *with* $N = 6$ *(a),* $N = 12$ *(b). Parameters:* $\frac{s}{L} = 0.25$, $t = 0.80$, $\frac{s_1}{L} = 0.25$, $t_1 = 0.20$, *with* $N = 6$ *(c),* $N = 12$ *(d).*

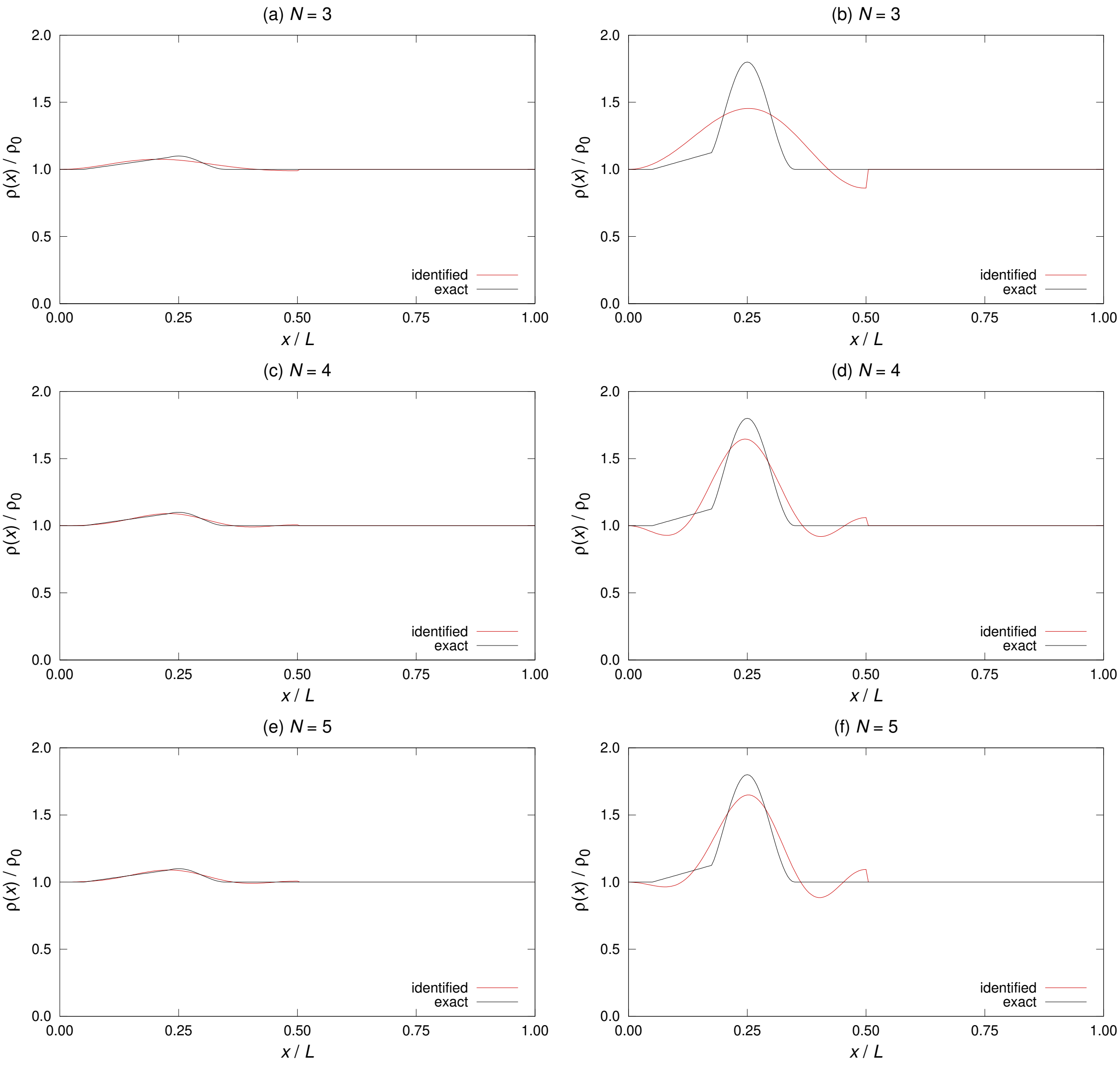

**Figure 4.3:** *Reconstruction of continuous overlapping mass changes as in* (4.24) *in* $\left[0, \frac{L}{2}\right]$ *using the first* $N = 3 - 5$ *resonant frequencies. Parameters:* $\frac{s}{L} = 0.25$, $t = 0.10$, $\frac{s_1}{L} = 0.25$, $t_1 = 0.10$, *with* $N = 3$ *(a),* $N = 4$ *(c),* $N = 5$ *(e). Parameters:* $\frac{s}{L} = 0.25$, $t = 0.80$, $\frac{s_1}{L} = 0.25$, $t_1 = 0.20$, *with* $N = 3$ *(b),* $N = 4$ *(d),* $N = 5$ *(f).*

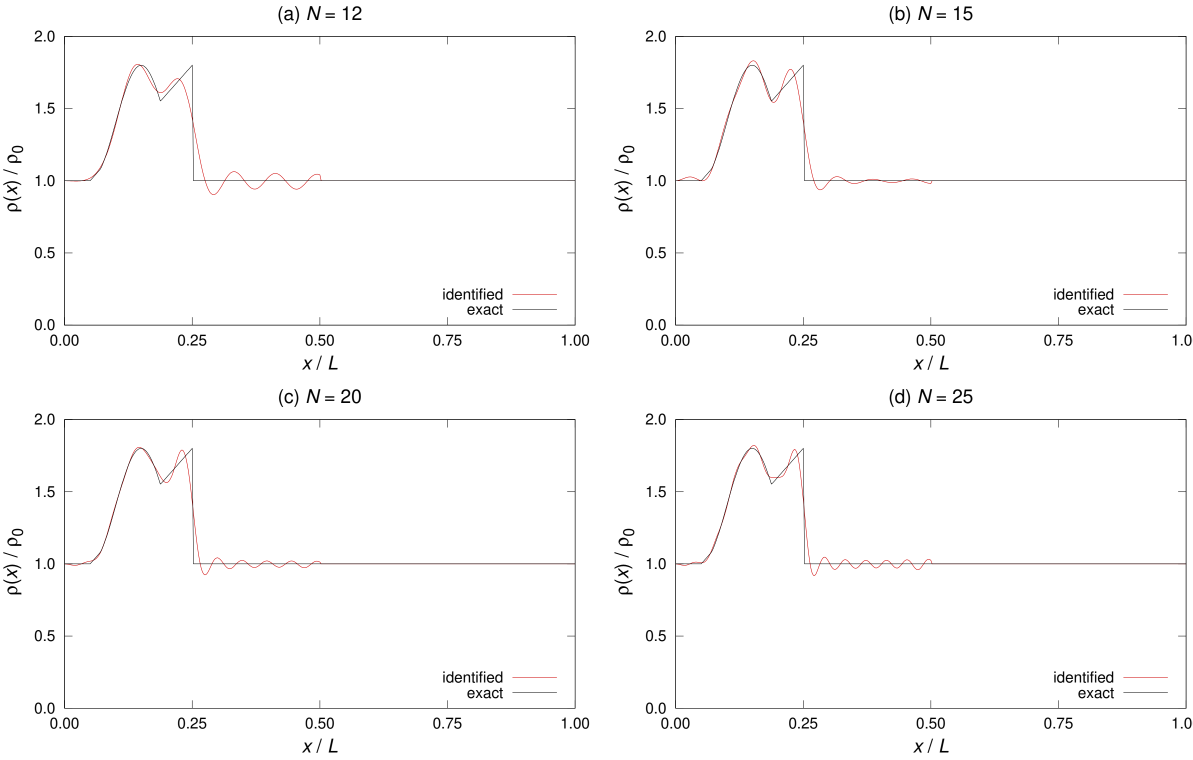

**Figure 4.4:** *Reconstruction of discontinuous overlapping mass changes as in* (4.24) *in* $\left[0, \frac{L}{2}\right]$. *Parameters:* $\frac{s}{L} = 0.15$, $t = 0.80$, $\frac{s_1}{L} = 0.25$, $t_1 = 0.80$, *with* $N = 12$ *(a),* $N = 15$ *(b),* $N = 20$ *(c),* $N = 25$ *(d).*

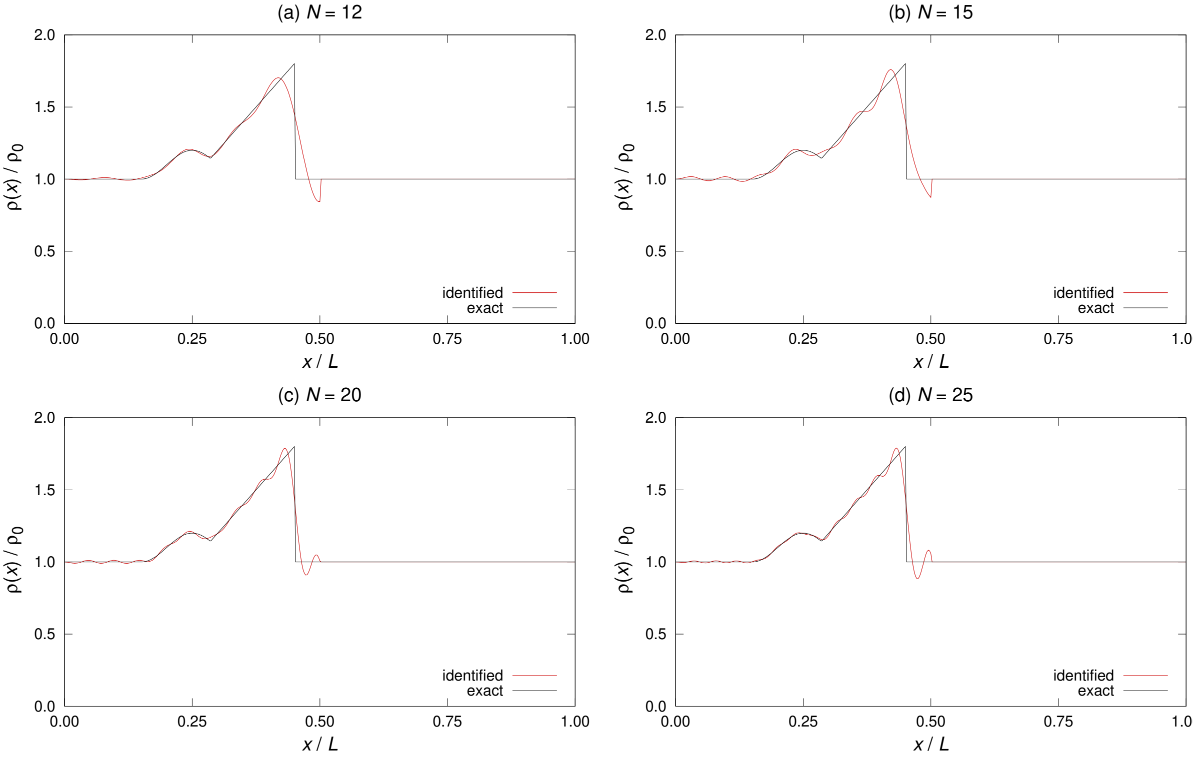

**Figure 4.5:** *Reconstruction of discontinuous overlapping mass changes as in* (4.24) *in* $\left[0, \frac{L}{2}\right]$. *Parameters:* $\frac{s}{L} = 0.25$, $t = 0.20$, $\frac{s_1}{L} = 0.45$, $t_1 = 0.80$, *with* $N = 12$ *(a),* $N = 15$ *(b),* $N = 20$ *(c),* $N = 25$ *(d).*

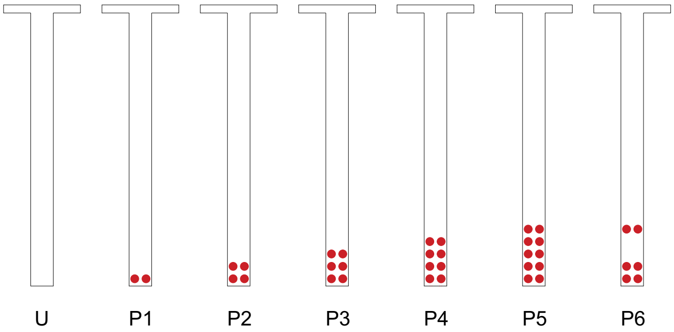

**Figure 4.6:** *Experimental specimen: unperturbed (U) and mass-perturbed configurations (Pi,* $i = 1, \ldots, 6$*) obtained by liquid droplet arrays deposition. Reproduction from [42].*

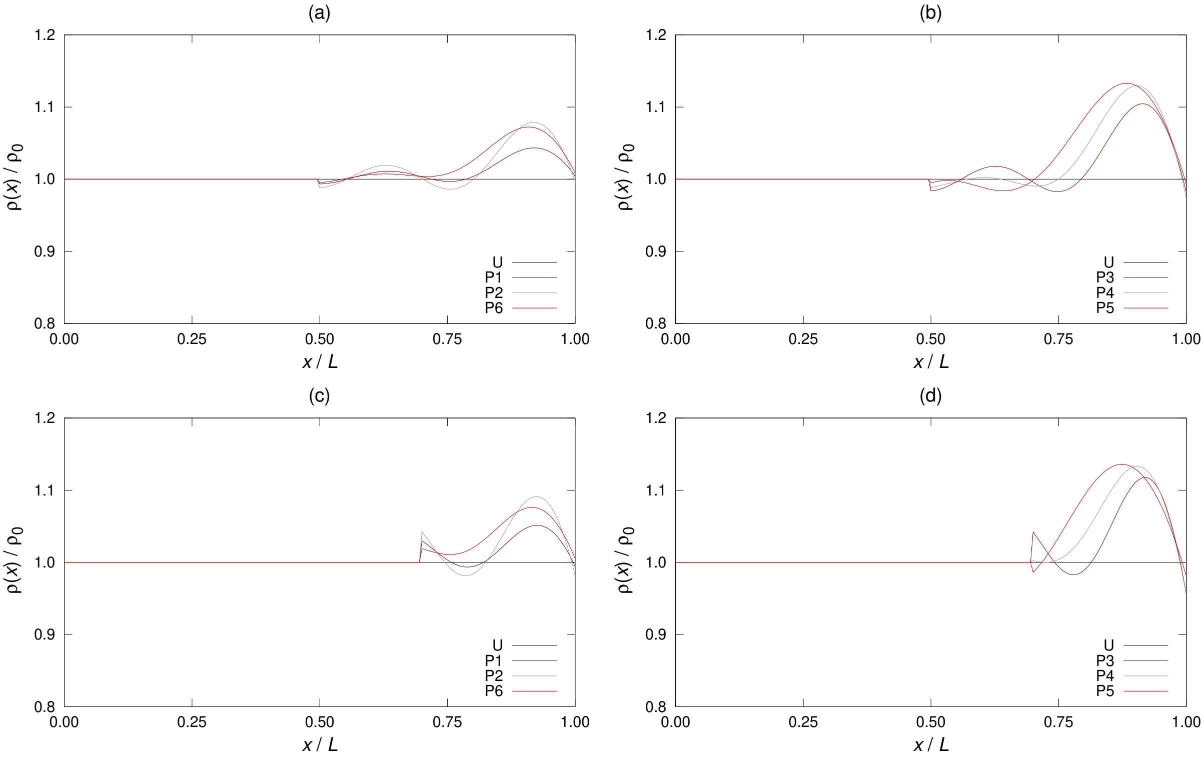

**Figure 4.7:** *Mass reconstruction for the cantilever shown in Figure 4.18 using the first four experimental eigenfrequencies and for different choices of the interval of identification. Upper row:* $[0.5L, L]$*; lower row:* $[0.7L, L]$.

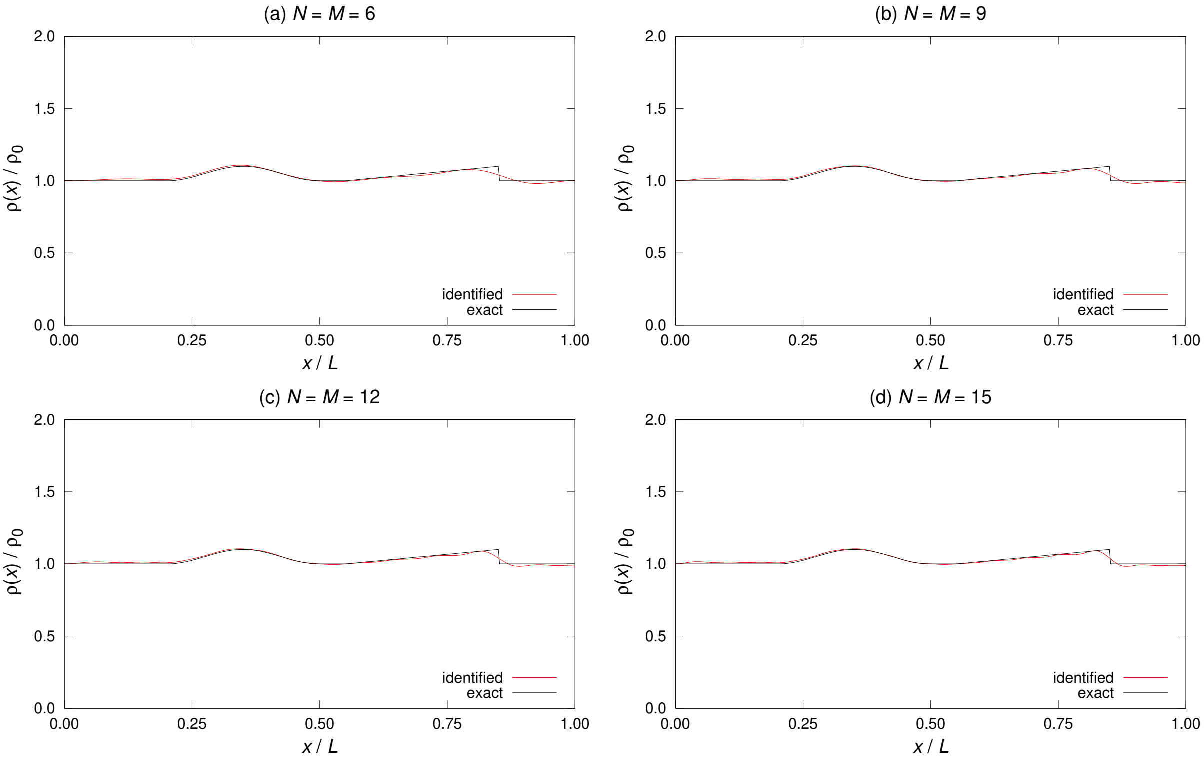

**Figure 4.8:** *Reconstruction of discontinuous overlapping mass changes as in* (4.24) *in* $[0, L]$. *Parameters:* $\frac{s}{L} = 0.35$, $\frac{c}{L} = 0.30$, $t = 0.10$, $\frac{s_1}{L} = 0.85$, $\frac{c_1}{L} = 0.30$, $t_1 = 0.10$, *with* $N = M = 6$ *(a)*, $N = M = 9$ *(b)*, $N = M = 12$ *(c)*, $N = M = 15$ *(d)*.

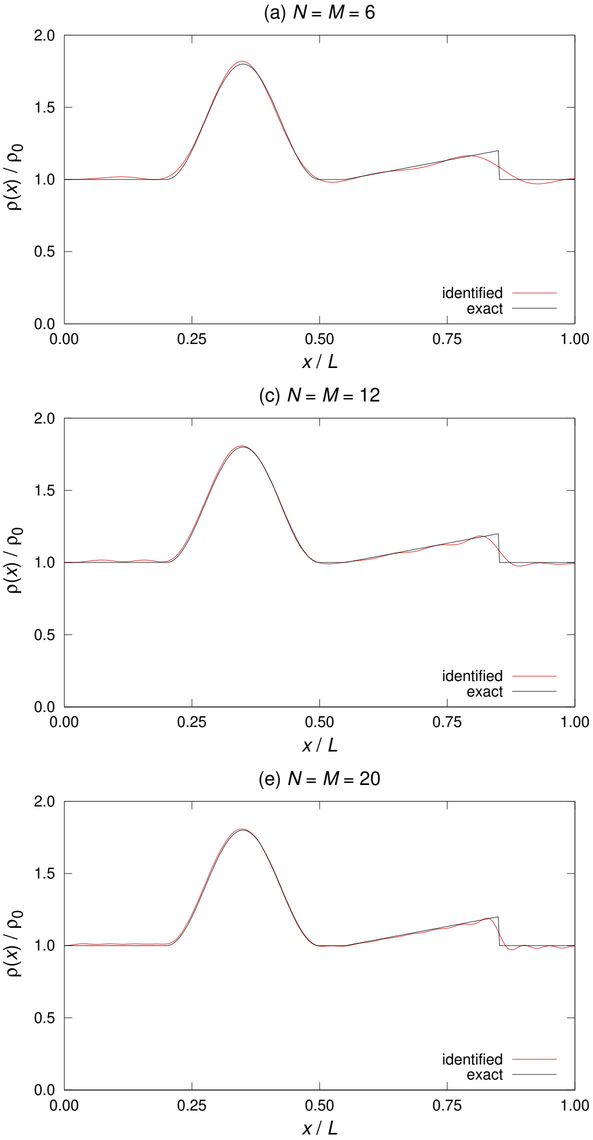

**Figure 4.9:** *Reconstruction of discontinuous overlapping mass changes as in* (4.24) *in* $[0, L]$. *Parameters:* $\frac{s}{L} = 0.35$, $\frac{c}{L} = 0.30$, $t = 0.80$, $\frac{s_1}{L} = 0.85$, $\frac{c_1}{L} = 0.30$, $t_1 = 0.20$, *with* $N = M = 6, 9, 12, 15, 20, 25$ *eigenfrequencies.*

Note: box covers both columns.

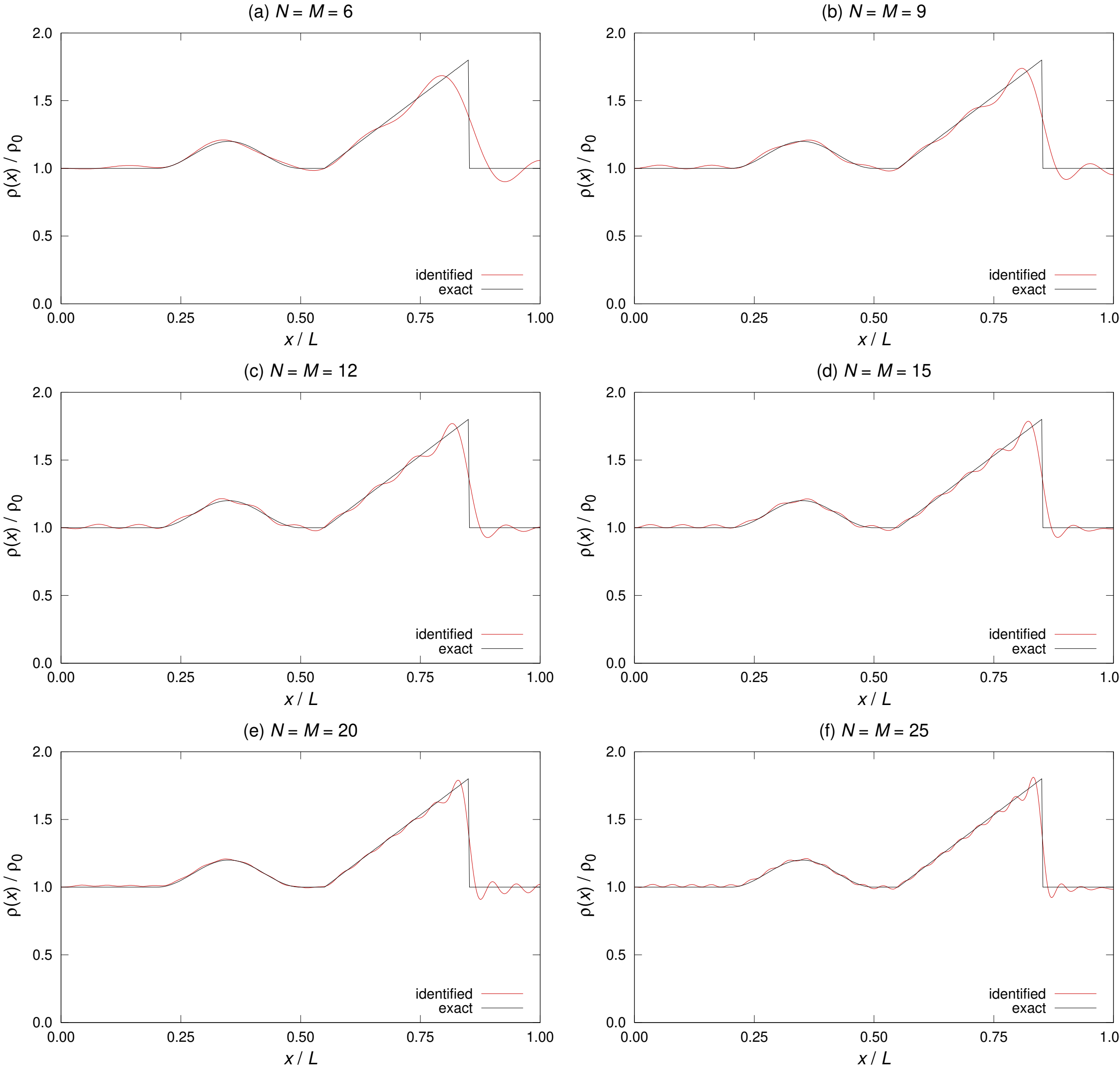

**Figure 4.10:** *Reconstruction of discontinuous overlapping mass changes as in* (4.24) *in* $[0, L]$. *Parameters:* $\frac{s}{L} = 0.35$, $\frac{c}{L} = 0.30$, $t = 0.20$, $\frac{s_1}{L} = 0.85$, $\frac{c_1}{L} = 0.30$, $t_1 = 0.80$, *with* $N = M = 6, 9, 12, 15, 20, 25$ *eigenfrequencies.*

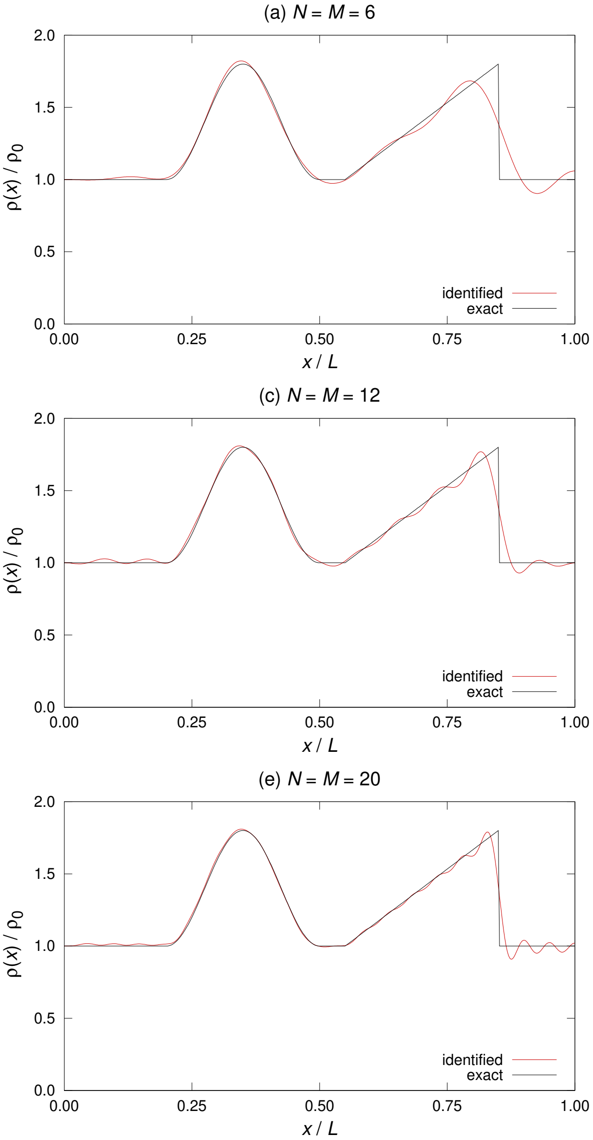

**Figure 4.11:** *Reconstruction of discontinuous overlapping mass changes as in* (4.24) *in* $[0, L]$. *Parameters:* $\frac{s}{L} = 0.35$, $\frac{c}{L} = 0.30$, $t = 0.80$, $\frac{s_1}{L} = 0.85$, $\frac{c_1}{L} = 0.30$, $t_1 = 0.80$, *with* $N = M = 6, 9, 12, 15, 20, 25$ *eigenfrequencies.*

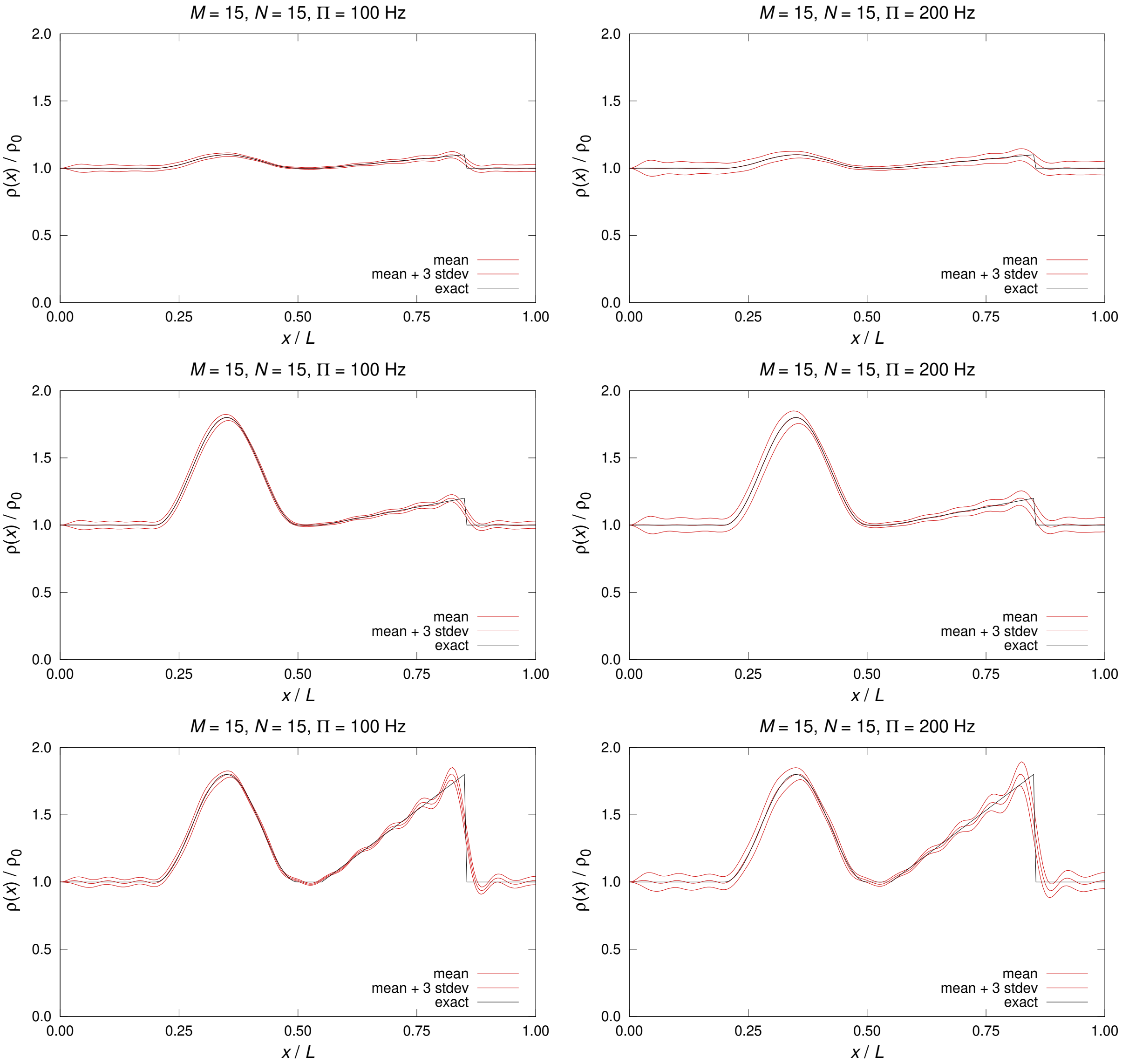

**Figure 4.12:** *Effect of noise* (4.36) *on identification of discontinuous mass changes as in* (4.24)*. Upper row:* $\frac{s}{L} = 0.35$, $\frac{c}{L} = 0.30$, $t = 0.10$, $\frac{s_1}{L} = 0.85$, $\frac{c_1}{L} = 0.30$, $t_1 = 0.10$*. Central row:* $\frac{s}{L} = 0.35$, $\frac{c}{L} = 0.30$, $t = 0.80$, $\frac{s_1}{L} = 0.85$, $\frac{c_1}{L} = 0.30$, $t_1 = 0.20$*. Lower row:* $\frac{s}{L} = 0.35$, $\frac{c}{L} = 0.30$, $t = 0.80$, $\frac{s_1}{L} = 0.85$, $\frac{c_1}{L} = 0.30$, $t_1 = 0.80$.

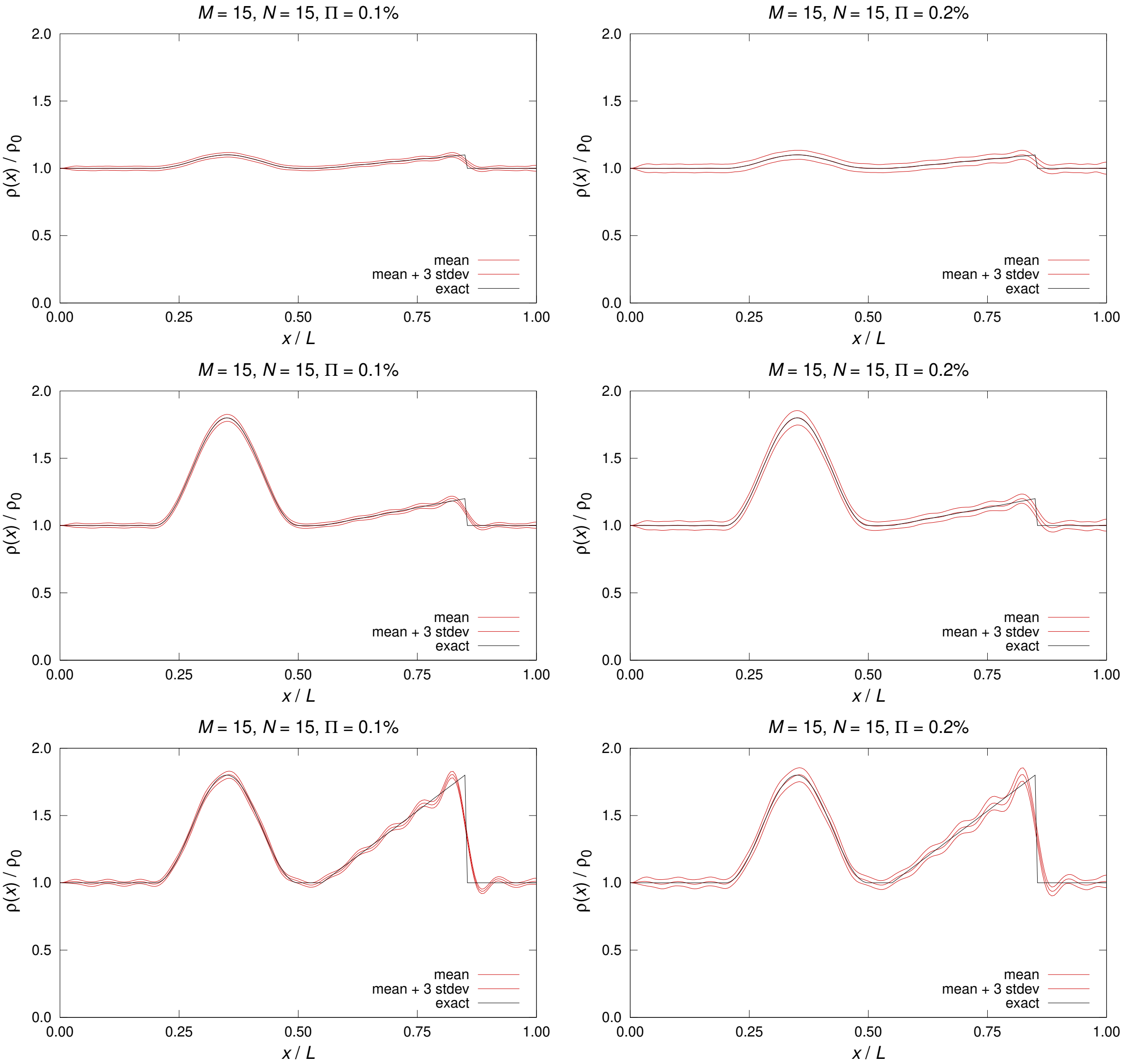

**Figure 4.13:** *Effect of noise* (4.37) *on identification of discontinuous mass changes as in* (4.24). *Upper row:* $\frac{s}{L} = 0.35$, $\frac{c}{L} = 0.30$, $t = 0.10$, $\frac{s_1}{L} = 0.85$, $\frac{c_1}{L} = 0.30$, $t_1 = 0.10$. *Central row:* $\frac{s}{L} = 0.35$, $\frac{c}{L} = 0.30$, $t = 0.80$, $\frac{s_1}{L} = 0.85$, $\frac{c_1}{L} = 0.30$, $t_1 = 0.20$. *Lower row:* $\frac{s}{L} = 0.35$, $\frac{c}{L} = 0.30$, $t = 0.80$, $\frac{s_1}{L} = 0.85$, $\frac{c_1}{L} = 0.30$, $t_1 = 0.80$.

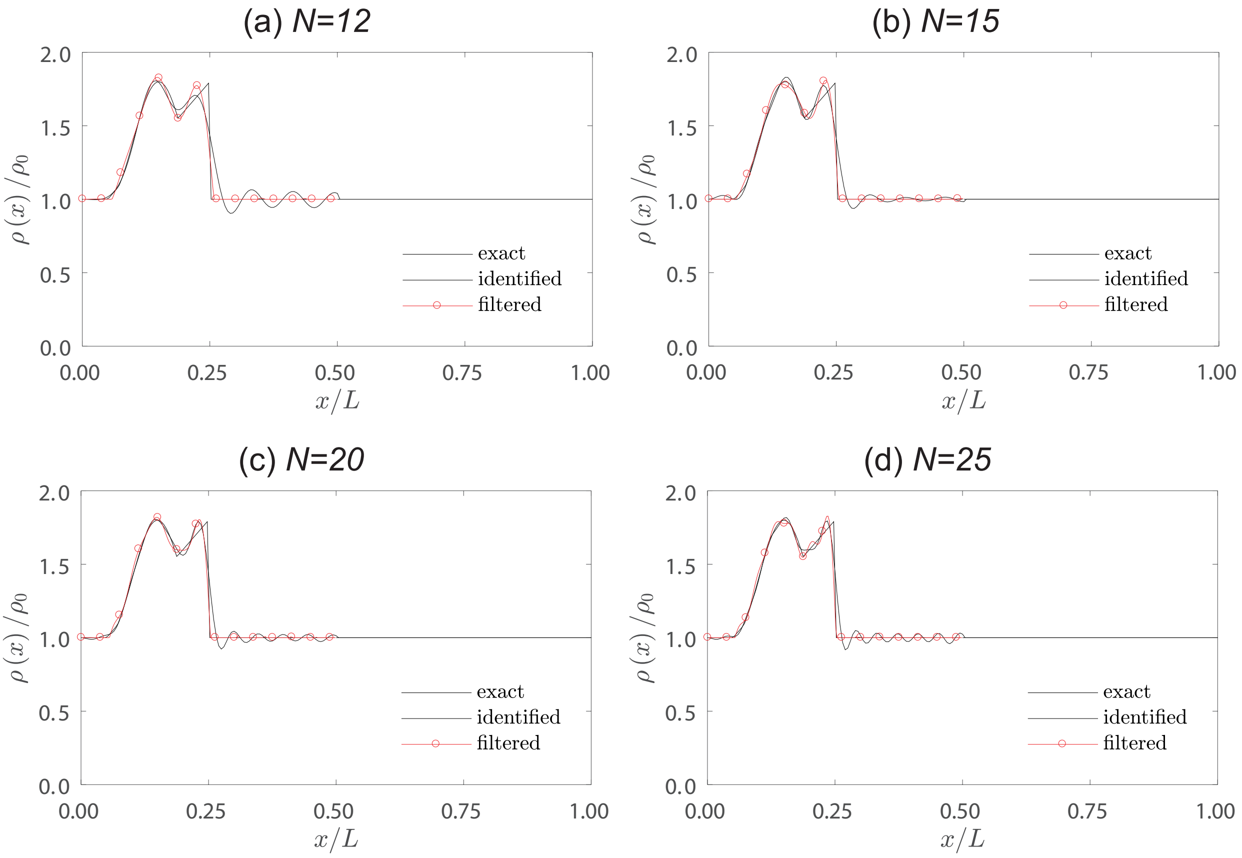

**Figure 4.14:** *Filter of the reconstruction of discontinuous overlapping mass changes as in* (4.24) *in* $\left[0, \frac{L}{2}\right]$*. Parameters:* $\frac{s}{L} = 0.15$*,* $t = 0.80$*,* $\frac{s_1}{L} = 0.25$*,* $t_1 = 0.80$*, with* $N = 12$ *(a),* $N = 15$ *(b),* $N = 20$ *(c),* $N = 25$ *(d).*

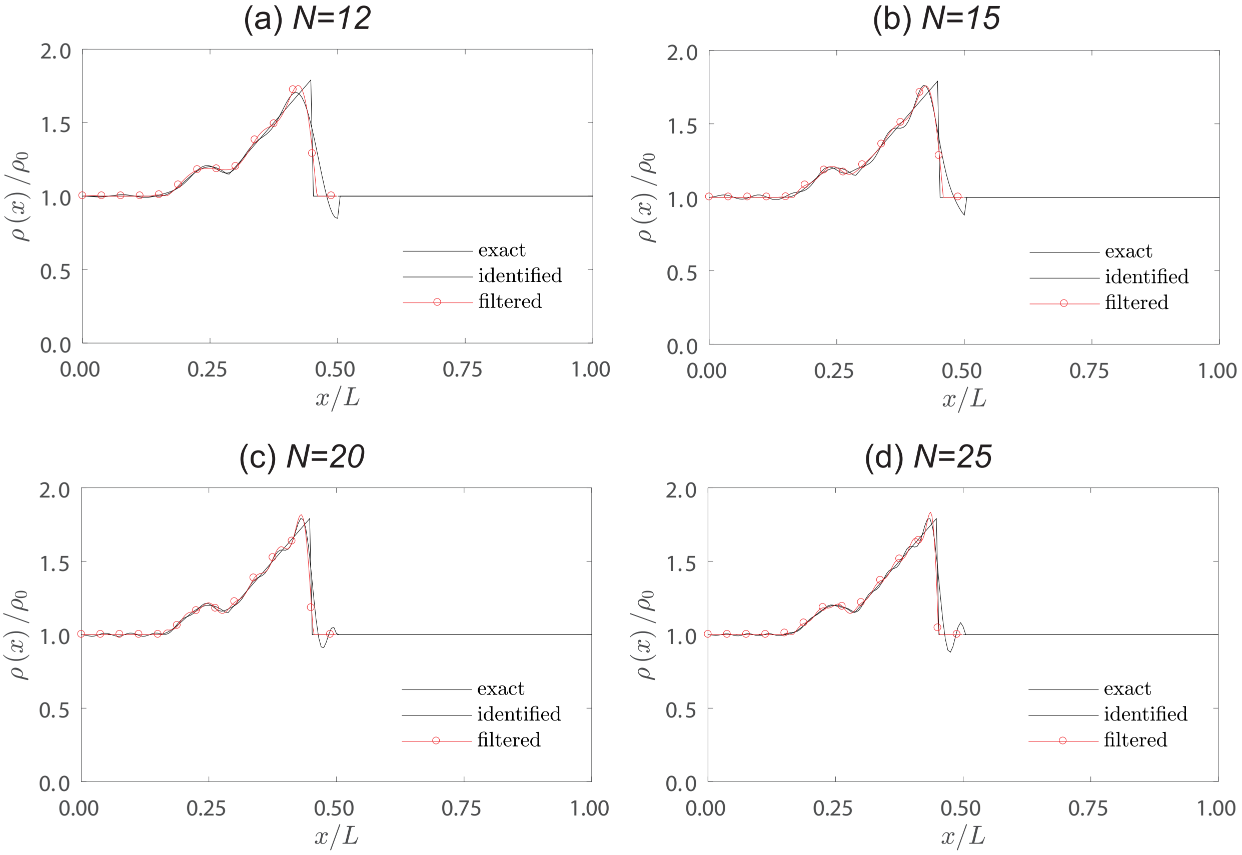

**Figure 4.15:** *Filter of the reconstruction of discontinuous overlapping mass changes as in* (4.24) *in* $\left[0, \frac{L}{2}\right]$*. Parameters:* $\frac{s}{L} = 0.25$, $t = 0.20$, $\frac{s_1}{L} = 0.45$, $t_1 = 0.80$, *with* $N = 12$ *(a),* $N = 15$ *(b),* $N = 20$ *(c),* $N = 25$ *(d).*

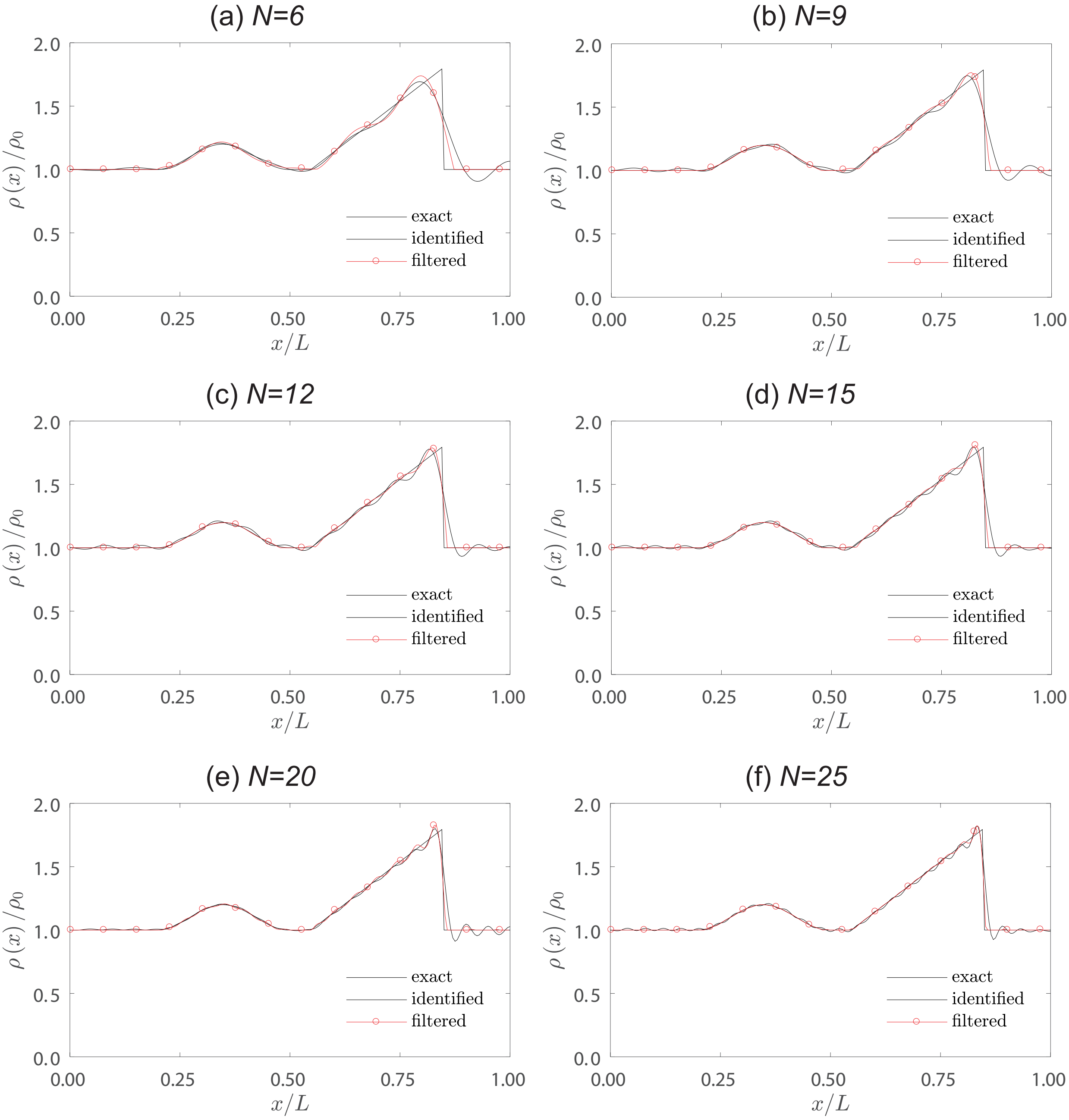

**Figure 4.16:** *Filter of the reconstruction of discontinuous overlapping mass changes as in* (4.24) *in* $[0, L]$. *Parameters:* $\frac{s}{L} = 0.35$, $\frac{c}{L} = 0.30$, $t = 0.20$, $\frac{s_1}{L} = 0.85$, $\frac{c_1}{L} = 0.30$, $t_1 = 0.80$, *with* $N = M = 6, 9, 12, 15, 20, 25$ *eigenfrequencies.*

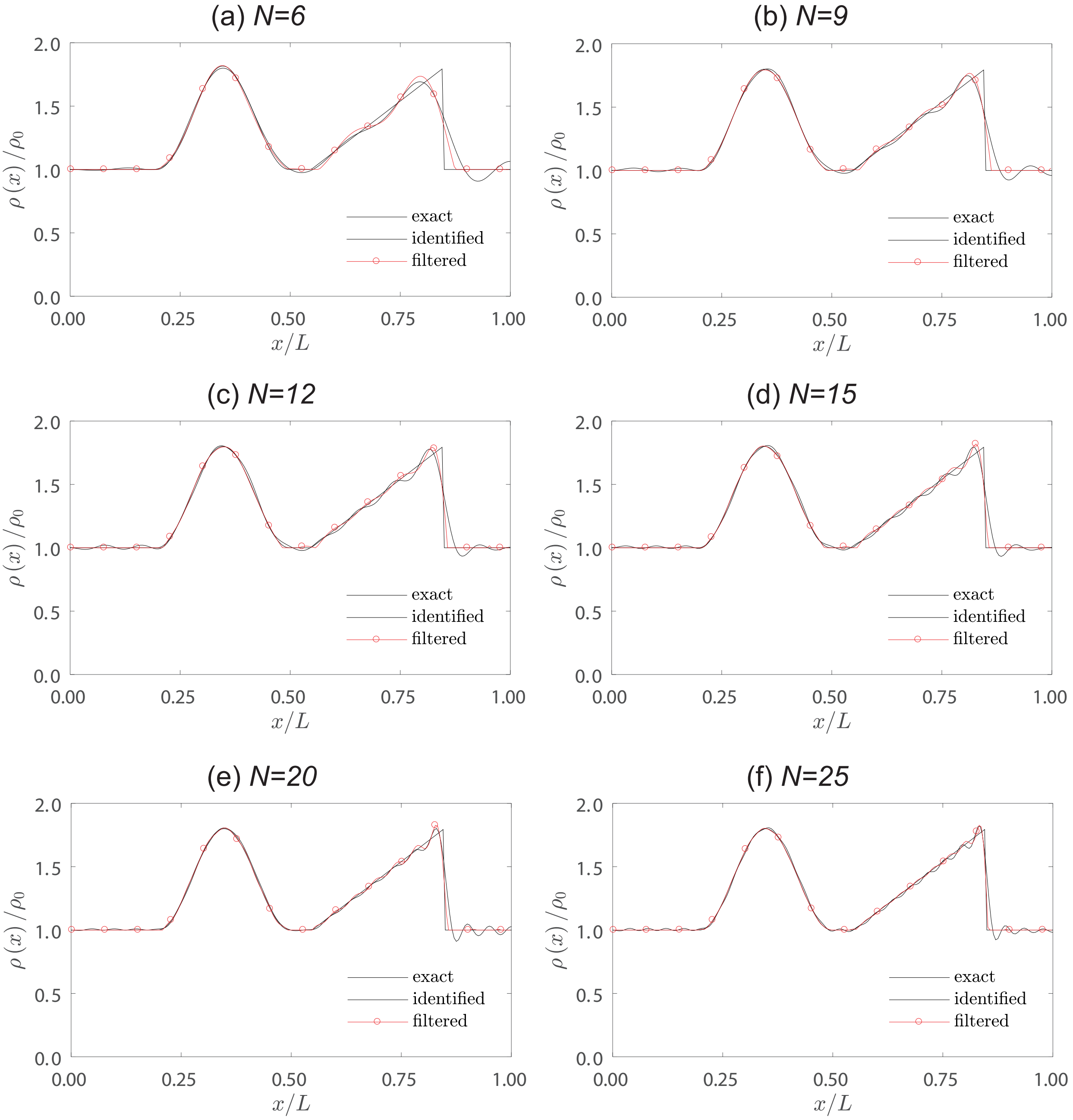

**Figure 4.17:** *Filter of the reconstruction of discontinuous overlapping mass changes as in* (4.24) *in* $[0, L]$. *Parameters:* $\frac{s}{L} = 0.35$, $\frac{c}{L} = 0.30$, $t = 0.80$, $\frac{s_1}{L} = 0.85$, $\frac{c_1}{L} = 0.30$, $t_1 = 0.80$, *with* $N = M = 6, 9, 12, 15, 20, 25$ *eigenfrequencies.*

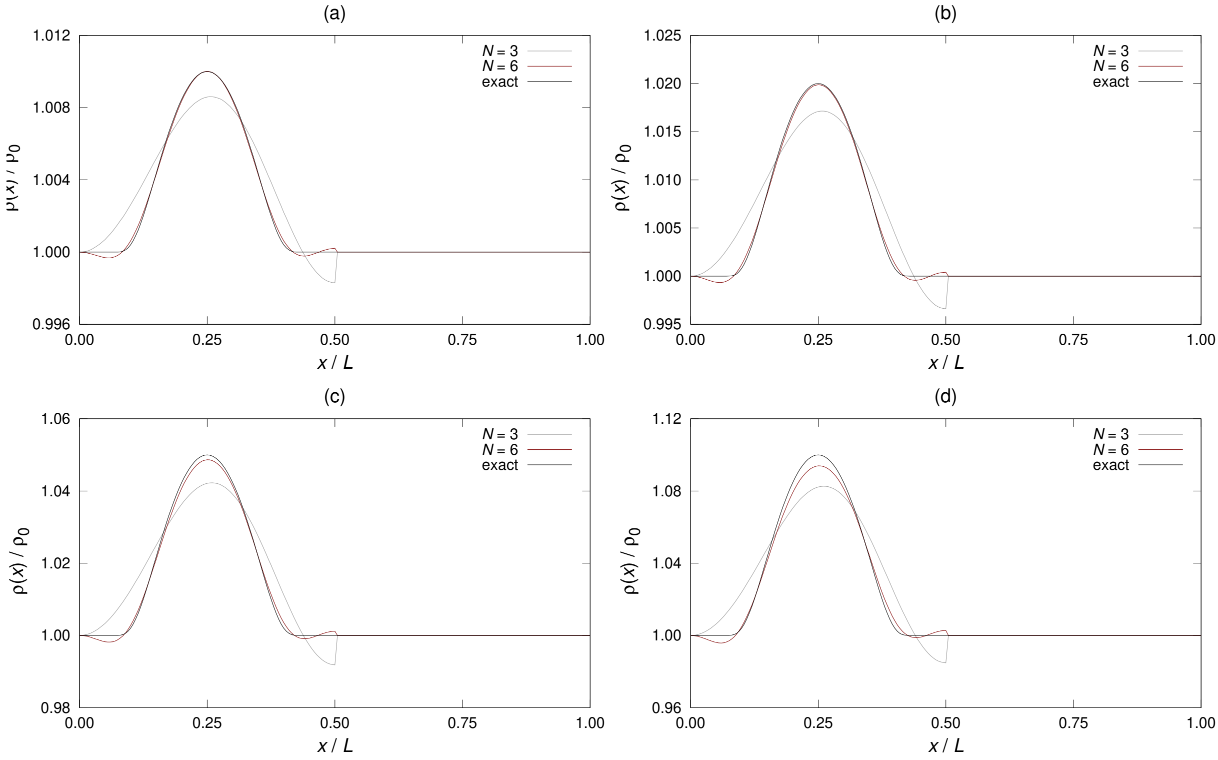

**Figure 4.18:** *First-order reconstruction of the mass variation* $r(x) = h_1(x)$*, with* $h_1(x)$ *as in* (4.94)*, with* $a_1 = 0.20$*,* $b_1 = 0.25$*,* $k_1 = 0.10$*, and* $t_1 = 0.01$ *(a),* $t_1 = 0.02$ *(b),* $t_1 = 0.05$ *(c),* $t_1 = 0.10$ *(d). Results for* $N = 3$*,* $N = 6$*.*

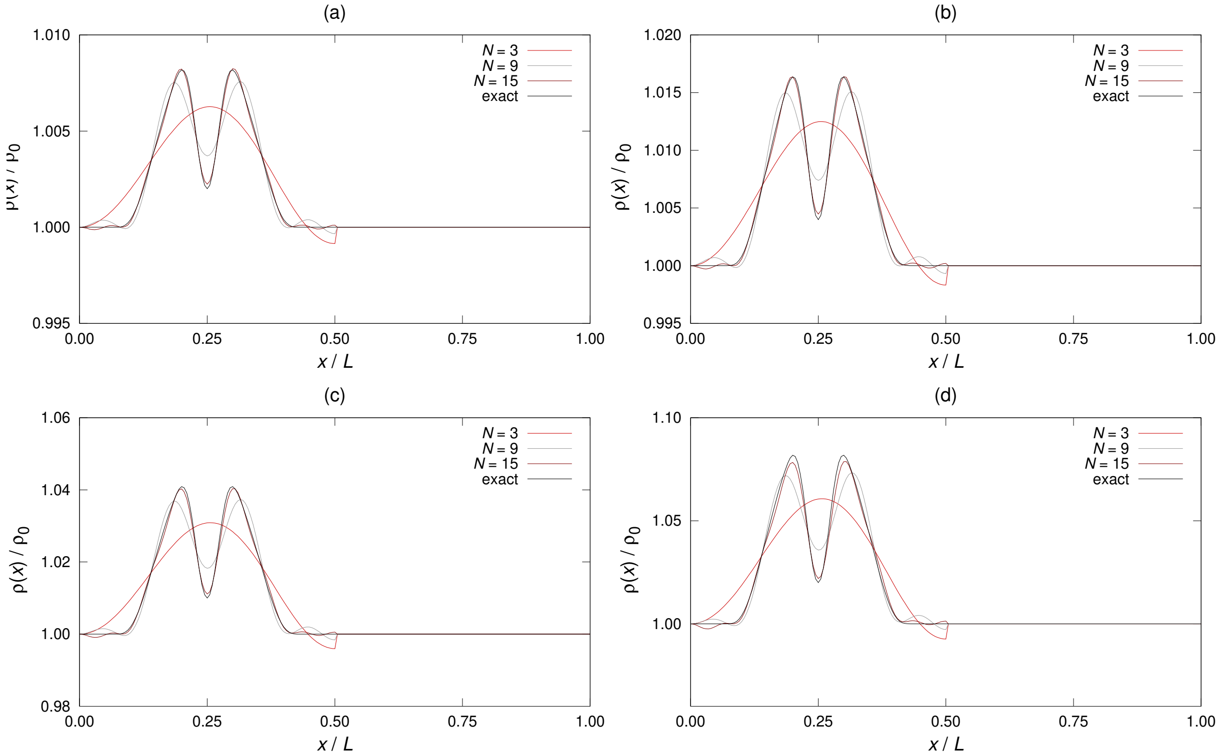

**Figure 4.19:** *First-order reconstruction of the mass variation* $r(x) = h_1(x) - h_2(x)$*, with* $h_1(x), h_2(x)$ *as in* (4.94)*, with* $a_1 = 0.20$*,* $a_2 = 0.10$*,* $b_1 = b_2 = 0.25$*,* $k_1 = k_2 = 0.10$*,* $t_2 = 0.8t_1$*, and* $t_1 = 0.01$ *(a),* $t_1 = 0.02$ *(b),* $t_1 = 0.05$ *(c),* $t_1 = 0.10$ *(d). Results for* $N = 3$*,* $N = 9$*,* $N = 15$*.*

# CHAPTER 5

# Conclusions

Nanosensors are gathering attention in the last decade due to necessity of measuring physical and chemical properties in industrial or biological systems at the sub-micron scale. One of the most representative examples of downscaling in sensoring systems is the nanomechanical resonator, which typically consists in one-dimensional vibrating structure with remarkable performance in detecting small adherent masses. The *mass sensing principle* for these systems is based on using the resonant frequency shifts caused by unknown additional masses attached on the surface of the sensor as data for the reconstruction of the mass variation.

In spite of its importance in applications, to our knowledge, a general formulation of the inverse problem of identifying distributed added mass attached on nanostructures, within the framework of generalized continuum mechanics theories, it has not been developed until now. The present thesis is a contribution on this topic.

Experimental results obtained by several research groups pointed out the need of considering size effects to model accurately the dynamic response of nanoscale components. Among the generalized continuum theories proposed in literature, the modified strain gradient theory by Lam et al. [53] seems to be an attractive formulation accounting for the scale effects present in nanostructures. Chapter 2 of this thesis was dedicated to a synthetic, self-contained illustration of this theory and to the deduction, starting from the three-dimensional version, of simplified one-dimensional models of nanobeams either in small axial or bending vibration, according to the approaches shown in [3] and [49].

In Chapter 3 we have investigated the inverse problem of determining additional distributed mass on an initially uniform nanobeam from finite number of lower resonant frequencies of the free axial vibration. Two main inverse problems are addressed.

In the first part of Chapter 3, we have considered the inverse problem of determining the mass distribution of a nanobeam from the knowledge of a finite number $N$ of lower resonant frequencies of the axial vibration under clamped ends, assuming that the mass is a small perturbation of the total mass of the nanoresonator. From a mathematical point of view, this problem belongs to the class of finite inverse eigenvalue problems for fourth-order differential operators of the Euler-Bernoulli type, and few general results are available, see the interesting theory proposed by Barnes [8].

In this thesis we propose a new method for solving this inverse problem, called the Generalized Fourier Coefficient method (GFCM) [26]. The method is based on an iterative procedure that produces an approximation of the unknown mass density as a generalized Fourier partial sum of order $N$, whose coefficients are calculated from the first $N$ resonant frequencies.

The generalized Fourier coefficients are evaluated on a suitable class of functions, each of which is - at every iteration- the gradient of the $n$th eigenvalue with respect to the mass variation. Therefore, the quantity of data required by the identification method to obtain good approximation of the mass coefficient depends on the smoothness of the coefficient. The results of an extensive series of simulations, even in presence of errors of the data, indicate that for smooth (e.g., continuous) coefficients the higher order Fourier contributions are less important and few first eigenvalues, $N$ less the 10 in the majority of simulations, provide sufficient data for good uniform approximations. When the mass variation is rough (e.g., discontinuous), some of the higher order Fourier coefficients are significant and eigenvalues corresponding to the higher modes will needed to capture the actual behavior, i.e., $N = 15 - 20$. In general, the smoother the coefficient, then more rapidly the method converges with small error in $L^\infty$-norm. Often, the first few iterates exhibit a good deal of oscillation. The rough the coefficient, the more pronounced was this behavior and the amplitude of the oscillation around the exact coefficient.

We have also provided a convergence theorem for the iteration scheme for a particular family of finite dimensional coefficients. The result holds under the assumption that the eigenvalues of the unperturbed and perturbed nanorod are close enough, and the mass variation is sufficiently small, see Section 3.5 for details.

In the second part of Chapter 3, we considered the more general inverse problem of determining a mass variation (on an axially vibrating nanobeam) not necessarily supported in half of the nanobeam axis. We proposed an extension of the above mentioned identification method based on the knowledge of a finite number of lower resonant frequencies belonging to two spectra corresponding to clamped-clamped and clamped-free end conditions. Roughly speaking, the information coming from one spectrum is equivalent to the a priori information on the support of the added mass. The mathematical aspects related to the convergence of the iterative method above can be extended to cover even this case. In brief, when the mass coefficient is regular, the first $N = 10$ resonant frequencies of both spectra allow for an accurate uniform approximation of the mass coefficient. In case of rough coefficients, a larger number of information is necessary to capture the target coefficient, say $N = 15 - 20$. We refer to Section 3.7.4 for more detailed description of the results; see also [24].

It is well known that real application of nanobeams often use bending vibration information to identify attached masses. Therefore, in Chapter 4 of this thesis we have extended the analysis of the inverse problem to the determination of distributed added mass in an initially uniform nanobeams under bending vibration. The GFCM was extended to bending vibration and the reconstruction method was based, as before, on a single partial spectrum for mass variation supported on half interval under supported-supported end conditions (Section 4.2), and on two partial spectra for genneral mass variation for nanobeams under supported-supported and supported-sliding end conditions (Section 4.3). The convergence of the iterative procedure can be proved as in the case of axial vibrations, and under the same assumptions of small and smooth mass variation.

For the bending case we have presented a new theoretical result that, hopefully, may help to advance in knowledge of this class of inverse eigenvalue problems with finite data. Referring to Section 4.5 for more details. In case of identification from one single spectrum, we proved that the reconstructed mass coefficient estimated at the first step of the iterative procedure converges pointwise to the target coefficient as the number of resonant frequencies tends to infinity. This result can be useful in applications, especially because the first-order approximation of the unknown added mass can be written in closed form in terms of the eigenfrequency shifts for initially uniform nanobeams.

We conclude this last section with some remarks on possible directions of future research which have been suggests by the analysis carried over in the present thesis.

i. In spite of the severe mathematical difficulties typical for this class of inverse eigenvalue problems with finite data, theoretical and numerical results show that it is possible to extract accurate approximation about the unknown coefficient in $L^2$ or even in $L^\infty$ norms. From the theoretical point of view, available results for second-order Sturm-Liuville operators show that this accurate approximation is possible only when an infinite amount of spectral data is available. We believe that this happens in our application of the GFCM since we have taken advantage of some a priori information about the unknown mass variation, such as the assumption of smallness and regularity of the mass coefficient, and we have chosen a suitable set of functions to represent the unknown coefficient. However, this does not explain the unexpected ability of the GFCM to reconstruct not necessarily small (smooth) mass variations, and it would be interesting to investigate further on this theoretical issue.

ii. Numerical reconstructions for rough coefficients showed pronounced Gibbs'-like phenomenon near the jump discontinuities. The combination of GFCM with least-squares based optimization filtering using additional information about the coefficient, such as the monotonicity which is available simply from the physics of the problem, shows to be very effective to reduce the undesirable oscillations around the target discontinuous coefficient. Development of the theoretical aspects of this combined technique would be of practical and theoretical interest.

iii. In this work, mass identification was performed only for special sets of boundary conditions. In case of axial vibration and mass variation with support in half of the axis and eigenvalues belonging to a single spectrum, for example, the boundary conditions used in Section 3.3 were of clamped ends. It can be shown that this choice (i) ensures that the family of functions with respect to which the generalized Fourier coefficients of the added mass are evaluated is a *basis* for mass distributions supported on half of the nanorod axis; and (ii) it allows finding a unique solution to the finite inverse problem linearized in a neighborhood of the unperturbed configuration of the referential nanobeam. These two properties play a crucial role in proving the convergence of the iterative method of identification. These properties follow from the particularly simple expression of the eigenfunctions of the uniform reference nanobeam (sine and cosine functions). For different choices of (symmetric) boundary conditions, it can be shown that the eigenfunctions are a combination of harmonic and hyperbolic functions, and properties (i) end (ii) have not yet been proved, to the best of our knowledge. Analogous considerations can be made for the reconstruction based on two distinct spectra. A preliminary set of encouraging numerical results obtained in [28] open up the prospective to a deeper theoretical investigation on this issue.

iv. In connection with the previous point (iii), it would be interesting, although not easy, to extend the present study to the reconstruction of the mass coefficient from *not* uniform unperturbed nanobeams. It is likely that, as for point (ii), new ideas and more abstract methods will be need to deal with this issue.

v. Experimental data on eigenfrequency changes induced by added mass in nanobeams are not numerous. Therefore, a further line of investigation consists in performing experimental test in conjunction with the interpretation based on suitable mechanical models able to take into account the size effects in nanostructures. Experiments would also be very useful to clarify the role of the boundary conditions and the actual possibility to assigning them in concrete applications.

The analysis of the above aspects (i)–(v), and a possible extension of our inverse methodologies to two-dimensional nanoresonators, seems to be a very demanding challenge that will require the development of refined skills in mathematics, mechanics, numerical analysis and experimental testing.

# Bibliography

[1] B. Akgoz and O. Civalek. Comment on ”Static and dynamic analysis of micro beams based on strain gradient elasticity theory” by S. Kong, S. Zhou, Z. Nie, and K. Wang, (International Journal of Engineering Science, 47, 487–498, 2009). *International Journal of Engineering Science*, 50:279–281, 2012.

[2] B. Akgoz and O. Civalek. Longitudinal vibration analysis of strain gradient bars made of functionally graded materials(FGM). *Composites: Part B*, 55:263–268, 2013.

[3] B. Akgoz and O. Civalek. Longitudinal vibration analysis for microbars based on strain gradient elasticity theory. *Journal of Vibration and Control*, 20:606–616, 2014.

[4] B. Akgoz and O. Civalek. Bending analysis of embedded carbon nanotubes resting on an elastic foundation using strain gradient theory. *Acta Astronautica*, 119:1–12, 2016.

[5] B. Arash, J. W. Jiang, and T. Rabczuk. A review on nanomechanical resonators and their applications in sensors and molecular transportation. *Applied Physics Reviews*, 2:021301, 2015.

[6] B. Arash and Q. Wang. Detection of gas atoms with carbon nanotubes. *Scientific Reports*, 3:Article number 1782, 2013.

[7] V. Barcilon. On the uniqueness of inverse eigenvalue problems. *Geophysical Journal of the Royal Astronautic Society*, 39:287–298, 1974.

[8] D. C. Barnes. The inverse eigenvalue problem with finite data. *SIAM Journal on Mathematical Analysis*, 22(3):732–753, 1991.

[9] J. Barros Neto. *An introduction to the theory of distributions*. Marcel Dekker, New York, 1973.

[10] A. Bilotta, A. Morassi, and E. Turco. The use of quasi-isospectral operators for damage detection in rods. *Meccanica*, 53:319–345, 2018.

[11] G. Borg. Eine Umkehrung der Sturm-Liouvilleschen Eigenwertaufgabe. Bestimmung der Differentialgleichung durch die Eigenwerte. *Acta Mathematica*, 78:1–96, 1946.

[12] A. Bouchaala. Size effect of a uniformly distributed added mass on a nanoelectromechanical resonator. *Microsystem Technologies*, 24(6):2765–2774, 2018.

[13] A. Bouchaala, A. H. Nayfeh, N. Jaber, and M. Younis. Mass and position determination in mems mass sensors: a theoretical and an experimental investigation. *Journal of Micromechanics and Microengineering*, 26(10):105009, 2016.

[14] L. Brand. *Vector and Tensor Analysis*. John Wiley and Sons, New York, USA, 1947.

[15] H. Brezis. *Analisi Funzionale*. Liguore Editore, Napoli, Italia, 1986.

[16] D. Calvetti, L. Reichel, and D.C. Sorensen. An implicitly restarted Lanczos method for large symmetric eigenvalue problems. *Electronic Transactions on Numerical Analysis*, 2:1–21, 1994.

[17] L. Caudill, P.A. Perry, and A.W. Schueller. Isospectral sets for fourth-order ordinary differential operators. *SIAM Journal of Mathematical Analysis*, 29(4):935–966, 1998.

[18] C.Q. Chen, Y. Shi, Y. St Zhang, J. Zhu, and Y.J. Yan. Size dependence of Young’s modulus in ZnO nanowires. *Physical Review Letters*, 96(7):Article number 075505, 2006.

[19] E. Cosserat and F. Cosserat. *Theory of Deformable Bodies, (Translated by D.H. Delphenich)*. Scientific Library, A. Hermann and Sons, Paris, 1909.

[20] R. Courant and D. Hilbert. *Methods of Mathematical Physics (first English edition)*. Interscience Publishers Inc., New York, 1966.

[21] S. Cuenot, S. Demoustier-Champagne, and B. Nysten. Elastic modulus of polypyrrole nanotubes. *Physical Review Letters*, 85(8):1690–1693, 2000.

[22] S. Cuenot, C. Frétigny, S. Demoustier-Champagne, and B. Nysten. Surface tension effect on the mechanical properties of nanomaterials measured by atomic force microscopy. *Physical Review B*, 69(16):Article number 165410, 2004.

[23] C. Davini, F. Gatti, and A. Morassi. A damage analysis of steel beams. *Meccanica*, 28:27–37, 1993.

[24] M. Dilena, M. Fedele Dell'Oste, J. Fernández-Sáez, A. Morassi, and R. Zaera. Identification of general added mass distribution in nanorods from two-spectra finite data. *Mechanical Systems and Signal Processing*, 134:Paper 106286, 2019.

[25] M. Dilena, M. Fedele Dell'Oste, J. Fernández-Sáez, A. Morassi, and R. Zaera. Mass detection in nanobeams from bending resonant frequency shifts. *Mechanical Systems and Signal Processing*, 116:261–276, 2019.

[26] M. Dilena, M. Fedele Dell'Oste, J. Fernández-Sáez, A. Morassi, and R. Zaera. Recovering added mass in nanoresonator sensors from finite axial eigenfrequency data. *Mechanical Systems and Signal Processing*, 130:122–151, 2019.

[27] M. Dilena, M. Fedele Dell'Oste, J. Fernández-Sáez, A. Morassi, and R. Zaera. Hearing distributed mass in nanobeam resonators. *International Journal of Solids and Structures*, 193–194:568–592, 2020.

[28] M. Dilena, M. Fedele Dell'Oste, A. Morassi, and R. Zaera. The role of boundary conditions in resonator-based mass identification in nanorods. *Mechanics of Advanced Materials and Structures*, accepted, 2020.

[29] M. A. Eltaher, M. A. Agwa, and F. F. Mahmoud. Nanobeam sensor for measuring a zeptogram mass. *International Journal of Mechanics and Materials in Design*, 12:211–221, 2016.

[30] K. Eom, H. S. Park, D. S. Yoon, and T. Kwon. Nanomechanical resonators and their applications in biological/chemical detection: Nanomechanics principles. *Physics Reports*, 503:115–163, 2011.

[31] A. C. Eringen. Linear theory of nonlocal elasticity and dispersion of plane-waves. *International Journal of Engineering Science*, 10(5):233–248, 1972.

[32] A. C. Eringen. Nonlocal polar elastic continua. *International Journal of Engineering Science*, 10(1):1–16, 1972.

[33] A. C. Eringen. *Microcontinuum field theories: I. Foundations and solids*. Springer Science & Business Media, 2012.

[34] A. C. Eringen and D. G. B. Edelen. Nonlocal elasticity. *International Journal of Engineering Science*, 10(3):233–248, 1972.

[35] N. A. Fleck and J. W. Hutchinson. Strain gradient plasticity. *Advances in Applied Mechanics*, 33:295–361, 1997.

[36] N. A. Fleck and J. W. Hutchinson. A reformulation of strain gradient plasticity. *Journal of the Mechanics and Physics of Solids*, 49:2245–2271, 2001.

[37] J. H. Ginsberg. *Mechanical and Structural Vibrations: Theory and Applications*. Wiley, 2001.

[38] G.M.L. Gladwell. *Inverse Problems in Vibration, 2nd edn*. Kluwer, Dordrecht, The Netherlands, 2004.

[39] A. Z. Hajjaj, N. Jaber, S. Ilyas, F. K. Alfosail, and M. Younis. Linear and nonlinear dynamics of micro and nano-resonators: Review of recent advances. *International Journal of Non-Linear Mechanics*, 119:103328, 2020.

[40] O. H. Hald. The inverse Sturm-Liouville problem and the Rayleigh-Ritz method. *Mathematics of Computation*, 32(143):687–705, 1978.

[41] O. H. Hald. The inverse Sturm-Liouville problem with symmetrical potentials. *Acta Mathematica*, 141:263–291, 1978.

[42] M. S. Hanay, S. Kelber, C. D. O'Connell, P. Mulvaney, J. E. Sader, and M. L Roukes. Inertial imaging with nanomechanical systems. *Nature Nanotechnology*, 10(4):339–344, 2015.

[43] H. Hochstadt. On inverse problems associated with Sturm-Liouville operators. *Journal of Differential Equations*, 17:220–235, 1975.

[44] H. Hochstadt and B. Lieberman. An inverse Sturm–Liouville problem with mixed given data. *SIAM Journal on Applied Mathematics*, 34(4):676–680, 1978.

[45] M. H. Kahrobaiyan, M Asghari, and M. T. Ahmadian. Strain gradient beam element. *Finite Elements in Analysis and Design*, 68:63–75, 2013.

[46] M. Kelleci, H. Aydogmus, L. Aslanbas, S. O. Erbil, and M. S. Hanay. Towards microwave imaging of cells. *Lab on a Chip*, 18:463–472, 2018.

[47] V. K. Khanna. *Nanosensors: Physical, Chemical, and Biological*. CRC Press, Boca Raton, FL, 2012.

[48] R. Knobel and B. Lowe. An inverse Sturm-Liouville problem for an impedance. *Z. Angew Math. Phys.*, 44:433–450, 1993.

[49] S. Kong, S. Zhou, Z. Nie, and K. Wang. Static and dynamic analysis of micro-beams based on strain gradient elasticity theory. *International Journal of Engineering Science*, 47:487–498, 2009.

[50] E. Kröner. Elasticity theory of materials with long range cohesive forces. *International Journal of Solids and Structures*, 3:731–742, 1967.

[51] J. Krumhansl. Some considerations of the relation between solid state physics and generalized continuum mechanics. In E. Kröner, editor, *Mechanics of Generalized Continua. IUTAM Symposia. Springer, Berlin Heidelberg*, pages 298–311, 1968.

[52] I. A. Kunin. The theory of elastic media with microstructure and the theory of dislocations. In E. Kröner, editor, *Mechanics of Generalized Continua. IUTAM Symposia. Springer, Berlin Heidelberg*, pages 321–329, 1968.

[53] D. C. C. Lam, F. Yang, A. C. M. Chong, J. Wang, and P. Tong. Experiments and theory in strain gradient elasticity. *Journal of the Mechanics and Physics of Solids*, 51:1477–1508, 2003.

[54] Z. L. Leibenzon. The inverse problem of the spectral analysis of ordinary differential operators of higher orders. *Trudy Moskov. Mat. Obsc.*, 15:70–144, 1966.

[55] X. Li, H. Yu, X. Gan, X. Xia, P. Xu, J. Li, M. Liu, and Y. Li. Integrated MEMS/NEMS resonant cantilevers for ultrasensitive biological detection. *Journal of Sensors*, 2009, DOI:10.1155/2009/637874, 2009.

[56] X. F. Li, G. J. Tang, Z. B. Shen, and K.Y. Lee. Resonance frequency and mass identification of zeptogram-scale nanosensor based on the nonlocal beam theory. *Ultrasonics*, 55:75–84, 2015.

[57] H.M. Ma, X.L. Gao, and J.N. Reddy. A microstructure-dependent Timoshenko beam model based on a modified couple stress theory. *Journal of the Mechanics and Physics of Solids*, 56(12):3379–3391, 2008.

[58] E. M. Miandoab, A. Yousefi-Koma, and H. N. Pishkenari. Nonlocal and strain gradient based model for electrostatically actuated silicon nano-beams. *Microsystem Technologies*, 21:457–464, 2015.

[59] R. D. Mindlin. Micro-structure in linear elasticity. *Archive for Rational Mechanics and Analysis*, 16:51–78, 1964.

[60] R. D. Mindlin. Second gradient of strain and surface-tension in linear elasticity. *International Journal of Solids and Structures*, 1:417–438, 1965.

[61] R. D. Mindlin and H. F. Tiersten. Effects of couple-stresses in linear elasticity. *Archive for Rational Mechanics and Analysis*, 11(5):415–448, 1962.

[62] H. Mohammadi and M. Mahzoon. Thermal effects on postbuckling of nonlinear microbeams based on the modified strain gradient theory. *Composite Structures*, 106:764–776, 2013.

[63] A. Morassi. Damage detection and generalized Fourier coefficients. *Journal of Sound and Vibration*, 302(1-2):229–259, 2007.

[64] A. Morassi, J. Fernández-Sáez, R. Zaera, and J. A. Loya. Resonator-based detection in nanorods. *Mechanical Systems and Signal Processing*, 93:645–660, 2017.

[65] A. Munawar, Y. Ong, R. Schirhagl, M. A. Tahir, W. S. Khan, and S. Z. Bajwa. Nanosensors for diagnosis with optical, electric and mechanical transducers. *RSC advances*, 9:6793–6803, 2019.

[66] T. Murmu and S. Adhikari. Nonlocal frequency analysis of nanoscale biosensors. *Sensors and Actuators A: Physical*, 173:41–48, 2012.

[67] S.K. Park and X.L. Gao. Bernoulli-Euler beam model based on a modified couple stress theory. *Journal of Micromechanics and Microengineering*, 16(11):2355, 2006.

[68] G. Romano, R. Barretta, M. Diaco, and F. Marotti de Sciarra. Constitutive boundary conditions and paradoxes in nonlocal elastic nanobeams. *International Journal of Mechanical Sciences*, 121:151–156, 2017.

[69] J. E. Sader, M. S. Hanay, A. P. Neumann, and M. L. Roukes. Mass spectrometry using nanomechanical systems: Beyond the point-mass approximation. *Nano Lett.*, 18:1608–1614, 2018.

[70] A.W. Schueller. Uniqueness for near-constant data in fourth-order inverse eigenvalue problems. *Journal of Mathematical Analysis and Applications*, 258:658–670, 2001.

[71] V. P. Smyshlyaev and N. A. Fleck. The role of strain gradients in the grain size effect for polycrystals. *Journal of the Mechanics and Physics of Solids*, 44:465–495, 1996.

[72] G. Talenti. Recovering a function from a finite number of moments. *Inverse Problems*, 3:501–517, 1987.

[73] J. Tamayo. Optomechanics to the rescue. *Nature nanotechnology*, 10:738–739, 2015.

[74] R. A. Toupin. Elastic materials with couple-stresses. *Archive for Rational Mechanics and Analysis*, 11(5):385–414, 1962.

[75] R. A. Toupin. Theories of elasticity with couple-stress. *Archive for Rational Mechanics and Analysis*, 17(2):85–112, 1964.

[76] B. Wang, J. Zhao, and S. Zhou. A microscale Timoshenko beam model based on strain gradient elasticity theory. *European Journal of Mechanics A-Solids*, 29:837–843, 2010.

[77] Q. Wang and B. Arash. A review on applications of carbon nanotubes and graphenes as nano-resonator sensors. *Computational Materials Science*, 82:350–360, 2014.

[78] H.F. Weinberger. *A First Course in Partial Differential Equations*. Dover Publications Inc., New York, USA, 1965.

[79] F. Yang, A.C.M. Chong, D.C.C. Lam, and P. Tong. Couple stress based strain gradient theory for elasticity. *International Journal of Solids and Structures*, 39:2731–2743, 2002.

[80] M. Zarepour, S. A. Hosseini, and M. Ghadiri. Free vibration investigation of nano mass sensor using differential transformation method. *Applied Physics A*, 123:181, 2017.

[81] B. Zhang, Y. He, D. Liu, Z. Gan, and L. Shen. Non-classical Timoshenko beam element based on the strain gradient elasticity theory. *Finite Elements in Analysis and Design*, 79:22–39, 2014.